

THÈSE

En vue de l'obtention du

DOCTORAT DE L'UNIVERSITÉ DE TOULOUSE

Délivré par :

Institut National Polytechnique de Toulouse (Toulouse INP)

Discipline ou spécialité :

Génie Mécanique, Mécanique des Matériaux

Présentée et soutenue par :

M. YVES BRESSON

le vendredi 1 juillet 2022

Titre :

On the importance of modelling the laser powder bed fusion process thermal history at different scales, to predict and enhance the quality of parts

---

Ecole doctorale :

Mécanique, Energétique, Génie civil, Procédés (MEGeP)

Unité de recherche :

Laboratoire Génie de Production de l'ENIT (E.N.I.T-L.G.P.)

Directeurs de Thèse :

M. LIONEL ARNAUD

M. MAHER BAILI

Rapporteurs :

M. CYRIL BORDREUIL, UNIVERSITE DE MONTPELLIER

MME EMMANUELLE ABISSET-CHAVANNE, ENSAM BORDEAUX

Membres du jury :

M. JEAN-YVES HASCOET, ECOLE CENTRALE DE NANTES, Président

M. AMÈVI TONGNE, ECOLE NATIONALE D'INGENIEURS DE TARBES, Membre

M. DAVID BETTAN, Halbronn, Invité

MI. LIONEL ARNAUD, ECOLE NATIONALE D'INGENIEURS DE TARBES, Membre

M. MAHER BAILI, ECOLE NATIONALE D'INGENIEURS DE TARBES, Membre

À mes parents

Remerciements

Tout d'abord, je souhaite remercier M. Lionel ARNAUD, Maître de Conférences HDR à l'École Nationale d'Ingénieurs de Tarbes (ENIT), pour avoir accepté de diriger cette thèse. Je lui suis extrêmement reconnaissant pour ces heures passées ensemble, son accompagnement, son aide et son soutien sans faille. Lionel m'a guidé tout au long de cette aventure. Ses efforts pour m'apprendre une rigoureuse démarche scientifique m'ont permis de grandir, en me montrant la voie vers l'autonomie et la réflexion. Grâce à Lionel, cette thèse ne fut pas qu'un parcours académique, ou un simple jalon vers l'insertion professionnelle, ce fut avant tout une aventure humaine.

Mes remerciements vont également à M. Maher BAILI, Maître de conférences à l'ENIT, pour ses conseils et son aide précieuse, notamment au moment de faire des choix à la fin de nombreuses réunions passionnées.

Je remercie M. Amèvi TONGNE, Maître de conférences à l'ENIT, pour son accompagnement et ses conseils. Son expertise m'a permis d'entrer dans le monde de la modélisation numérique et d'y évoluer.

Je n'aurais pu demander un meilleur encadrement, cette thèse s'est déroulée dans des conditions idéales, dont tous les étudiants souhaiteraient profiter.

Je remercie une nouvelle fois l'ensemble des membres du jury. Merci à M. Jean-Yves HASCOËT, Professeur à l'École Centrale de Nantes, pour m'avoir fait l'honneur de présider ce jury. Merci également à mes rapporteurs Mme Emmanuelle ABISSET-CHAVANNE, Professeure à l'École Nationale des Arts et Métiers de Bordeaux et M. Cyril BORDREUIL, Professeur à l'Université de Montpellier, pour avoir accepté d'évaluer ma thèse et pour leurs commentaires pertinents.

Je remercie l'ensemble des équipes de Halbronn et Repmo, ainsi que ceux qui sont partis depuis. Ils m'ont accueilli comme il se doit, m'ont soutenu et m'ont accompagné pendant ces quatre années. J'adresse tout particulièrement mes remerciements à Matthieu DUMINY, Manon FLAMAN, Quentin MANDOU et Damien TOMASEVIC. Leur bienveillance et leurs encouragements m'ont d'abord convaincu de tenter cette aventure, puis m'ont permis de rester motivé lors des moments difficiles. Merci également à Pierre HAENTJENS, qui a su être un manager à l'écoute et bienveillant. Merci à Léa et François pour leur bonne humeur à toute épreuve. J'ai également une pensée pour toutes les autres personnes du Groupe HRT avec qui j'ai pu travailler. Merci à David BETTAN, Directeur des Opérations et Bernard BETTAN, Président du Groupe HRT, pour avoir financé cette thèse et m'avoir gratifié de leur confiance.

Je remercie tous les membres du Laboratoire Génie de Production, en particulier tous ceux qui m'ont aidé et qui ont contribué à la réussite de ce projet : Antoine VEZIRIAN, Pierre SELVA et Eliane CASTA.

Je pense à mes amis que j'ai rencontrés à Tarbes, pour tous ces moments. Marine BÉDOUIN et Léopold STAMPFER d'abord, pour tous ces lundi où ils m'ont hébergé. Mais aussi Ayoub, Camille, Danilo, Ferhat, Louis, Maël, Martin, Rabab, Roger-Pierre, Yassin et tous les autres. Bien sûr, un merci particulier à Maylis pour ses encouragements, sa confiance et son accompagnement quotidien. Merci pour son écoute et ses conseils si précieux.

Enfin, toute ma gratitude va à ma famille, tout particulièrement à mes parents, ma sœur Enora et mon frère Philippe, pour m'avoir soutenu pendant cette aventure et avant elle. Travailler sur cette thèse pendant les confinements, entre autres, n'aurait pas été aussi agréable sans leur aide et leur rire. Merci à Delphine et Laurent, pour m'avoir hébergé chez eux durant toutes ces années. Merci à eux pour leur bienveillance et ces formidables moments passés parmi leurs proches. Merci à Georges pour son aide en traitements statistiques. Merci à mes cousins Axelle, Mathilde et Louis pour ces moments passés avec eux.

Merci à tous.

Juin 2022

Yves BRESSON

Table of contents

I. Introduction

1.1. Industrial context 2
1.2. Technological and scientific contexts 3
1.3. Manuscript organisation 4

II. Identifying main contamination factors of reactive powders

2.1. Introduction 9
2.1.1. Common parts defects 10
2.1.1.1. Internal defects 11
2.1.1.1.1. Porosity 11
2.1.1.1.2. Microstructure inhomogeneity 12
2.1.1.1.3. Microstructure impurities 13
2.1.1.1.4. Balling. 14
2.1.1.2. External defects. 14
2.1.1.2.1. Geometric dimensions 14
2.1.1.2.2. Surface quality 15
2.1.1.3. Process-induced defects 15
2.1.1.3.1. Anisotropy 15
2.1.1.3.2. Residual stresses 15
2.1.1.4. Summary 17
2.1.2. Powders used in the LPBF process 18
2.1.2.1. Mechanical and chemical powder manufacturing techniques 18
2.1.2.1.1. Mechanical manufacturing techniques 18
2.1.2.1.2. Chemical manufacturing techniques 18
2.1.2.2. Atomisation powder manufacturing techniques 20
2.1.2.2.1. Projection-based atomisation techniques 21
2.1.2.2.2. Centrifugal atomisation techniques 22
2.1.2.2.3. Spheroidisation atomisation techniques 22
2.1.2.3. Powder recycling strategies 23
2.1.2.3.1. Machine silo filling: virgin blend, continuous use, continuous refreshing 24
2.1.2.3.2. Powder drying effects. 25
2.1.2.4. Summary 26
2.1.3. Part and powder properties variations 27
2.1.3.1. Recycling process influence on part quality 27
2.1.3.1.1. Parts density 27
2.1.3.1.2. Tensile test results 27

2.1.3.1.3. Fatigue test results . . . 28
2.1.3.1.4. Parts oxidation . . . 28
2.1.3.2. Recycling process influence on powder properties. . . . 28
2.1.3.2.1. Powder particles size . . . 28
2.1.3.2.2. Powder flowability . . . 29
2.1.3.2.3. Powder oxidation . . . 29
2.1.3.3. Powder properties affecting the part quality . . . 30
2.1.3.3.1. Powders influence on parts density . . . 30
2.1.3.3.2. Powders influence on parts oxidation and dissimilarities . . . 31
2.1.3.4. Oxygen influence on part quality. . . . 31
2.1.3.5. Summary . . . 32
2.1.4. Materials used and specific oxidation mechanisms . . . 32
2.1.4.1. Materials used in this study. . . . 32
2.1.4.1.1. Al-Si10-Mg material . . . 32
2.1.4.1.2. Ti-6Al-4V material . . . 33
2.1.4.2. Oxidation mechanisms . . . 34
2.1.4.2.1. Metal oxidation and oxidation kinetics . . . 34
2.1.4.2.2. LPBF oxidation sources. . . . 36
2.1.4.3. Summary . . . 38
2.2. Identifying key oxidation factors . . . 40
2.2.1. Material and methods . . . 40
2.2.1.1. Material, machine and process conditions . . . 40
2.2.1.2. Design of experiment . . . 42
2.2.1.2.1. Samples and lattice geometries . . . 42
2.2.1.2.2. Procedure 1: recycling and heating. . . . 45
2.2.1.2.3. Procedure 2: recycling only . . . 45
2.2.1.3. Sampling and measurements . . . 47
2.2.2. Results . . . 47
2.2.2.1. Procedure 1 and Procedure 2 manufacturing . . . 47
2.2.2.2. Oxygen content. . . . 48
2.2.3. Discussions . . . 49
2.3. Limiting oxidation originating from heat . . . 50
2.3.1. Material and methods . . . 51
2.3.1.1. Material, machine and process conditions . . . 51
2.3.1.2. Design of experiment . . . 52
2.3.1.2.1. Samples geometries: calibration cantilever. . . . 52
2.3.1.2.2. Experiment 1: different scanned surfaces . . . 53
2.3.1.2.3. Experiment 2: interlayer cooling duration . . . 54
2.3.1.2.4. Optical measurements . . . 55

2.3.2. Results . . . 57
2.3.2.1. Experiment 1 results: different scanned surfaces . . . 57
2.3.2.2. Experiment 2 results: interlayer cooling duration . . . 60
2.3.3. Discussions . . . 63
2.4. Conclusions and perspectives . . . 65
2.5. References . . . 67

III. Simulation of beam supports damage and breakage

3.1. Introduction . . . 76
3.2. State of the art . . . 80
3.2.1. LPBF general modelling methods . . . 80
3.2.2. Supports design, modelling and optimisation . . . 82
3.3. Study case: hydraulic joint . . . 83
3.3.1. Description . . . 83
3.3.2. Numerical simulation using commercial codes . . . 87
3.3.2.1. Results of each software . . . 87
3.3.2.2. Example of simulation results with Simufact Additive . . . 88
3.4. The numerical models developed and experimental data . . . 91
3.4.1. Numerical method . . . 91
3.4.1.1. Models, meshing and process sequence . . . 91
3.4.1.2. Mechanical properties . . . 93
3.4.1.3. Considering the supports overlapping . . . 95
3.4.1.4. Overcoming buckling-based numerical instabilities: proposed solutions . . . 96
3.4.2. Numerical results and experimental comparison . . . 98
3.4.2.1. 3D-voxel elements simulation results . . . 98
3.4.2.2. 1D-beam elements simulation results . . . 99
3.4.2.3. Multi-supports set up: supports group's mechanical behaviour . . . 101
3.4.2.4. Individual beam support mechanical characterisation . . . 104
3.4.2.5. Beam supports mechanical sensibility . . . 106
3.5. Conclusions and perspectives . . . 107
3.6. References . . . 110

IV. Simulate the thermal history using a multiscale finite element method

4.1. Introduction . . . 118
4.2. State of the art . . . 119
4.2.1. Relation between thermal history and characteristics of parts . . . 119
4.2.2. Modelling methods . . . 119
4.3. Methodology . . . 121

4.3.1. General principles . . . 121
4.3.1.1. Parameter-driven approach . . . 121
4.3.1.2. Level definition . . . 122
4.3.2. Rules . . . 125
4.3.2.1. Definition of space and time domains . . . 125
4.3.2.2. Heat source modelling . . . 126
4.3.2.3. Boundary and initial conditions . . . 128
4.4. Study case . . . 128
4.4.1. Context, parameters, and levels . . . 128
4.4.2. Level 1 . . . 131
4.4.3. Level 2 . . . 133
4.4.4. Level 3 . . . 136
4.4.5. Level 4 . . . 138
4.4.6. Level 5 . . . 139
4.5. Discussions . . . 140
4.6. Conclusions and perspectives . . . 142
4.7. References . . . 143

V. Conclusions

5.1. Contributions . . . 148
5.2. Perspectives . . . 150

VI. Appendices

6.1. Parameters of the heat-incorporated experiment . . . 153
6.2. Scanning parameters of the spatter-limitation experiment . . . 155
6.3. Non-dispersive infrared method. . . . 156

List of Figures

Figure 2.1: Temporal evolution of publications in Web of Science database on the LPBF process. . . . 9
Figure 2.2: Main LPBF defect groups. . . . 11
Figure 2.3: Porosities within a small sample (a) and inside a powder particle (b). . . . 12
Figure 2.4: Assembly of three perpendicular optical metallographic images of as-built IN718 from [16]. . . . 13
Figure 2.5: Balling phenomenon from [36]. . . . 14
Figure 2.6: Illustration of the stress state after a unique laser scanning. . . . 16
Figure 2.7: Dispalcement and stress fields of a LPBF-manufactured pillar from [60]. . . . 16
Figure 2.8: Crack and delamination observed in LPBF and EBM processes. . . . 17
Figure 2.9: Illustration of the crushing process with a gyratory crusher (left) and a roll crusher (right) from [68]. . . . 18
Figure 2.10: Illustration of powder particle shapes from [67]. . . . 19
Figure 2.11: Overview of atomisation processes. . . . 21
Figure 2.12: Illustration of some powder manufacturing techniques from [87]. . . . 22
Figure 2.13: Particle size range for different applications [86]. . . . 23
Figure 2.14: Continuous aging recycling strategy [91]. . . . 24
Figure 2.15: Continuous use recycling strategy [94]. . . . 25
Figure 2.16: Continuous refreshing recycling strategy [91]. . . . 25
Figure 2.17: Connections between powder properties at different states, process parameters and part quality [95]. . . . 30
Figure 2.18: Al-Si phase diagram [128]. . . . 33
Figure 2.19: Ti-6Al-4V-adapted Ellingham diagram from [148]. . . . 36
Figure 2.20: Schematic representation of spatter formation mechanisms. . . . 37
Figure 2.21: Renishaw AM 400 system. . . . 41
Figure 2.22: Powder handling systems connected to powder bottles. . . . 42
Figure 2.23: Procedure 1 (recycling and heating) geometries: lattice and cubic samples (a), lattice pattern (b) viewed in QuantAM software, protection wall geometry (c). . . . 44
Figure 2.24: Procedure 2 (recycling only) sample supports and geometries. . . . 44
Figure 2.25: Procedure 1 (recycling and heating) steps. . . . 46
Figure 2.26: Procedure 2 (recycling only) steps. . . . 46
Figure 2.27: Procedure 1 (heating and recycling) manufactured lattices. . . . 48
Figure 2.28: DMP ProX320 LPBF system. . . . 51
Figure 2.29: Cantilever geometries used for both experiments. . . . 53
Figure 2.30: Experiment 1 disposition of cantilevers on a large build plate viewed in DMP Control software. . . . 54
Figure 2.31: Experiment 2 disposition of cantilever on a small build plate for both productions viewed in DMP Control software. . . . 55
Figure 2.32: Image preparation and analysis process using GIMP and ImageJ software. . . . 56
Figure 2.33: Final layer of the three cantilevers production. Dark particles are indicated wit arrows. . . . 57
Figure 2.34: DinoLite images of the 6 mm width cantilever. . . . 58

Figure 2.35: DinoLite images of the 12 mm width cantilever. 58
Figure 2.36: DinoLite images of the 24 mm width cantilever. 59
Figure 2.37: Images of both cantilevers after erasing the perspective using GIMP software. 60
Figure 2.38: No dwell time production analysis results using two grey scale threshold values. 61
Figure 2.39: 50 s dwell time production analysis results using two grey scale threshold values. 61
Figure 2.40: Production without dwell times at the end of two consecutive layers. 62
Figure 2.41: Production with 50 s dwell times at the end of two consecutive layers. 62
Figure 3.1: Illustration of supports teeth from [16].. 76
Figure 3.2: Example of support structure patterns from [2][16]. 77
Figure 3.3: Complex support structure example from [4]. Left side is a view of the file being prepared in 3DXPert software and right side is the manufactured part. 78
Figure 3.4: Examples of support meshing from two commercial codes. 79
Figure 3.5: Multiscale illustration of the process from [25].. 80
Figure 3.6: Temperature Gradient Mechanism described by [29].. 81
Figure 3.7: Original Keller's inherent strain method from [45] (translated from German) 82
Figure 3.8: Industrial hydraulic joint [84]. 84
Figure 3.9: Distortion of the part causing supports breakage with two different LPBF systems. 85
Figure 3.10: Position of broken supports (red) for each LPBF system. 86
Figure 3.11: Four commercial codes hydraulic block simulation displacement fields, zoom on the hydraulic joint arm. Simulated critical regions are indicated with a red arrow. 88
Figure 3.12: Comb-like structure in Simufact Additive used for the inherent strain vector calibration. 89
Figure 3.13: Hydraulic joint's simulation results on Simufact 90
Figure 3.14: Hydraulic joint Abaqus models with the build plate, voxel (a) and beam (b) supports. 91
Figure 3.15: MPC constraints between some supports and the build plate.. 92
Figure 3.16: 1D beam supports nodes with 0.5mm mesh size. 92
Figure 3.17: Stress-strain schematic diagram with evolution of the damage variable D from [103]. 94
Figure 3.18: Hydraulic joint STL file: zoom on overlapping supports region. 95
Figure 3.19: Simplified models of three beams, locked at the base, connected at the top, and a X-directed force applied at the top. 96
Figure 3.20: Simplified model (a) and deformed shapes (b & c) of an individual beam under compression. 97
Figure 3.21: 3D-voxel simulation results: stress and displacement fields. 98
Figure 3.22: Beam elements simulation results: stress and displacement fields.. 100
Figure 3.23: Multiple cone supports experimental and model set-up, as well as simulation results at the peak stress value.. 102
Figure 3.24: Multi-supports set up experimental (dashed) and simulated force-strain tensile test results with different stifness (elastic foundation: stiffness 16 kN/mm, and rigid foundation: stiffness 16.10^6 N/mm); and for both stifnesses, two values of the effective plastic displacement at the point of failure (EPDF) parameter.. . 103
Figure 3.25: Multi-supports set up experimental (dashed) and simulated force-strain tensile test results using artifically larger tensile strength and yield strength (+26%) and two values of the effective plastic displacement at the point of failure (EPDF) parameter. 104

Figure 3.26: Individual support set up (left) and inside the tensile test apparatus with the extensometer (right). . . 105
Figure 3.27: Individual beam support tensile test stress-strain results. 106
Figure 4.1: Illustration of the domains of three different scales. Dashed lines represent the size of the domains that a user may define for his application. All sizes are provided as illustration. 121
Figure 4.2: Absorbed energy Eabs for different types of heat generation: continuous (averaged) and discontinuous (instantaneous). The total absorbed energy E_{tot} is equivalent for both models. 123
Figure 4.3: Temperature field in the 1D semi-infinite body with two types of loading: averaged and discrete. . . . 124
Figure 4.4: Overlapping temporal domains of Level n and Level n+1.. 125
Figure 4.5: Hydraulic joint (a) and ABAQUS model with supports and build plate (b). 128
Figure 4.6: Fitted material properties from Parry *et al.* [8] used within the models.. 130
Figure 4.7: Level 1 map of maximum temperatures. 133
Figure 4.8: Level 1 temperature fields after heating macrolayer 33. 134
Figure 4.9: Level 2 islands randomly-generated sequence (supports and build plate are not shown for better clarity).135
Figure 4.10: Level 2 map of maximum temperatures.. 135
Figure 4.11: Level 2 zoom of maximum temperature. 136
Figure 4.12: Level 3 model. Temperature BC assigned to the bottom of the supports. The red surface in the zoom panel shows a line-heat source. 137
Figure 4.13: Level 3 temperature results.. 137
Figure 4.14: Level 4 model. Temperature boundary conditions are applied on the lower side. The red surface in the zoom panel shows a group of point-like heats sources. 138
Figure 4.15: Level 4 temperature results.. 139
Figure 4.16: Level 5 model. Temperature boundary conditions are applied on the lower side. The red surface in the zoom panel exhibit a point-like heat source. 139
Figure 4.17: Level 5 map of maximum filtered temperatures.. 140

List of Tables

Table 2.1: Defect categories identified in the literature . . . 10
Table 2.2: Powder size delivered by some gas and plasma atomisation process. . . . 23
Table 2.3: Ti-6Al-4V grade 5 and grade 23 element composition ranges according to ASTM standards [139][140]. . . 34
Table 2.4: Al-Si10-Mg chemical composition provided by the machine manufacturer.. . . . 40
Table 2.5: Manufacturing data of Procedure 1 (heating and recycling).. . . . 47
Table 2.6: Oxygen measurements from the samples of Productions 1, 3 and 5 of each procedure.. . . . 49
Table 2.7: Ti-6Al-4V powder chemical composition. . . . 51
Table 2.8: Analysis results with a common grey scale threshold value of 102. . . . 63
Table 2.9: Report of analysis results with adapted grey scale threshold values (87 for no-dwell time and 128 for 50 s dwell time productions). . . . 63
Table 3.1: 316L stainless steel powder characteristics.. . . . 83
Table 3.2: LPBF process 316L stainless steel material parameters of three different systems used in this study. Parameters were developped by the machine manufacturers.. . . . 85
Table 3.3: List of simulation software.. . . . 87
Table 3.4: Commercial codes hydraulic block simulation results. ”NC” stands for ”Not Communicated” information by the software provider.. . . . 87
Table 3.5: Mean 316L stainless steel mechanical properties from [88]-[100] and ASTM A666-15 Standard [101]. . . 94
Table 3.6: Displacements and relative errors of the 3D overlapping model and both 1D models with and without horizontal links. . . . 96
Table 3.7: Mechanical properties and number of broken supports for the different cone support sensibility cases. 107
Table 3.8: Mechanical properties and the number of broken supports with a dalayed damage behaviour for elements under compression solliciation.. . . . 107
Table 4.1: Parameters driven time and space domains of the simulation levels (D-S: discretization - scope). . . . 122
Table 4.2: Parameter values set to the models.. . . . 129
Table 4.3: Parameter consideration and corresponding levels used for the study case of the hydraulic joint. (□ averaged impact; ● simulated; - not considered at this level). . . . 130
Table 4.4: Computation duration for each level of the multiscale method.. . . . 141

Introduction

Table of contents

I. Introduction

1.1. Industrial context 2
1.2. Technological and scientific contexts 3
1.3. Manuscript organisation 4

Chapter I
Introduction

1.1. Industrial context

Halbronn-Repmo-TechniCN (HRT) group is a French company of approximately 120 persons. Its main office is located in Lognes (France, 77) and it has several sites across Europe.

Historically, Halbronn began the distribution of Japanese machine-tools in France in the 1960s. Its core activity is to sell the machines to the European industrials and accompany its customers in the control of their manufacturing processes.

In 2016, Halbronn created a division, Halbronn3D, which activity is to sell production machines (resins, polymers, and metals) of the American manufacturer 3DSystems.

In 2020, Halbronn acquired the Repmo-TechniCN group, which comprised the Repmo3D division. The activity of this division was to sell laser powder bed fusion (LPBF) and electron beam melting (EBM) machines of the American manufacturer General Electrics (GE) Additive. HRT group continued its additive journey selling machines manufactured by GE Additive.

Regarding the additive division Halbronn3D-Repmo3D, the machine and the raw material (powders) are provided by GE Additive. The software to prepare the manufacturing process is provided by Materialise company.

A large share of Halbronn3D-Repmo3D customers is in the dental and medical domains. These domains have widely adopted the LPBF technology in the past decade, and have constraining standards regarding the materials.

Numerous customers of the division are in the aeronautic and defense domains. Both are highly constrained by standards, but have accelerated their adoption of the technology during the last years.

Most of HRT customers are small or medium French companies (employing less than 250 persons), and do not have a specific AM department. Hence, these companies may need some technical supports.

To enable an optimised technical assistance to its customers, Halbronn and LGP laboratory in Tarbes identified several industrial challenges:

The machines sold tend to be larger, and the manufacturing paces tend to accelerate significantly. Hence, there is a need to use simulations before the manufacturing process to accelerate the designing processes and

prevent the trial errors method. It is expected that simulation results are reliable and fast to compute.

Indeed, the assumptions behind the simulations must be controlled, and their influence on the results errors should be estimated. Also, the computational durations for a full build plate should not last more than a few hours.

Regarding the standards, the medical and the aeronautic domains both are severely constrained with the chemical contents of the manufactured products. Indeed, the recycling processes of the powders are limited to a certain extent (usually between 4 and 15 recycling cycles) due to the excessive increase of the oxygen content.

Hence, the customers must not use the powder for their restrained applications and in most cases, the degraded powder is sold back at a low price, or even thrown away. The factors leading the oxygen increase must be identified and ways to prevent this degradation should be suggested to the end-user.

Since most of HRT customers are small or medium companies, the solutions proposed by the group should not need a specific expertise to be applied, nor excessively large supplementary expenses (such as a full characterisation campaign, or the need for expensive measurements).

1.2. Technological and scientific contexts

The advent and the growing adoption of the additive manufacturing processes in the last decades have revolutionised several industrial manufacturing domains and supply chains. The numerous advantages provided by the additive manufacturing have seduced industries previously using conventional methods for moulds inserts, implants, satellite and plane parts, for example

During the additive manufacturing (AM) process, the material is obtained with the part shape (near net-shape) from the process, with some variations due to the process parameters; although using subtractive techniques, the raw material is already in its final state, and the final shape is obtained from the process.

Hence, AM techniques enable a wide panel of part shapes which can be complex, and even impossible to obtain otherwise.

The AM technique investigated in this manuscript is the LPBF process, where thin metal powders layers (30 - 70 μm) are spread across a build plate, and scanned by high power laser source(s) (100 W - 1 000 W). The scanned powder particles melt, cool down, and solidify in a solid dense state. Repeating the processes of layering and scanning enable the user to manufacture parts in a few hours, days or weeks, depending on the machine and the size of the parts.

Common materials used with this process are stainless steels, titanium alloys, aluminium alloys, nickel-based alloys, cobalt-chromium alloys, and tool steels. More and more materials are developed to be suitable for this process, such as pure copper, copper alloys and alloys with specific physical or mechanical properties.

The process parameters are usually provided by the machine manufacturer, who ensures the manufacturing of dense parts (all of them above 99 %). The process parameters usually differ from the supports (structures below the parts, to connect them with the build plate), the bulk part (inside the part), the contours (the outskirts of the parts) and the overhang regions of the parts (regions nearly horizontal, or with a low angle), and the upper final surface.

The process takes place in an inert build chamber (an inert gas, often nitrogen or argon, fills the build chamber). Some materials react with oxygen, and the oxygen pick-up should be limited at minimum. Hence, the build chamber during the process has an oxygen content about 10 - 800 ppm.

After the manufacturing process, the loose powder around the parts on the build plate is recovered and recycled to be reused in the subsequent process. Generally, the recycling process consists solely on sieving the powder to separate excessively large particles from particles with sizes compliant regarding the requirements of the machine manufacturers, or those of the user.

In relation with the industrial challenges mentioned before, research problems have also been identified at

the start of this work:

- What is the main factor driving the contamination of the LPBF powders and parts?
- Is the contamination behaviour similar during processing and recycling?
- What parameters or phenomena must be considered during the simulation processes of the LPBF process?
- Which methods can be used to link phenomena occurring at microscale (i.e. melt pool scale) and those occurring at mesoscale or macroscale (i.e. layer scale or part scale), in the same simulation frame?

1.3. Manuscript organisation

This manuscript is organised as follow: an introduction of the industrial and scientific contexts, three independent chapters focusing on specific aspects of the LPBF process (namely, the oxidation behaviour, the simulation of the supports breakage, and the simulation of the thermal history); and finally, a global conclusion. Because the chapters are quite independent and focus on different aspects of the process, they comprise a literature section.

The introduction enables to introduce the company funding these works and its objectives. Also, it offers a brief presentation of the LPBF, which will be detailed in the next sections.

The first chapter links the powder properties with the properties of the parts, and for each of them, describe how they vary with time and use. This part is an aggregation of the results available in the literature. From this section, factors influencing the oxidation behaviour are identified. A design of experiment is performed to isolate the most influencing factor, and strategies to limit the contamination are tested.

The second chapter focuses on some assumptions used with commercial simulation codes, and show some limitations regarding the supports breakage with an industrial part. Some methods are proposed to enable the simulation of the supports breakage, and the deflection of the part after supports detachment. Some limitations are identified and discussed.

The last chapter focuses on the simulation of the thermal history of the process. From the first two chapters, a specific attention has been drawn to the thermal history experienced by the manufactured geometries. Limitations in the current methods regarding the integration of some process parameters are identified, and a new multiscale method is presented and applied to an industrial case study.

The conclusion provides an overall vision on the findings of those studies, and to summarise each of them, suggesting precise research perspectives.

Chapter II

Table of contents

II. Identifying main contamination factors of reactive powders

2.1. Introduction . . . 9
2.1.1. Common parts defects . . . 10
2.1.1.1. Internal defects . . . 11
2.1.1.1.1. Porosity . . . 11
2.1.1.1.2. Microstructure inhomogeneity . . . 12
2.1.1.1.3. Microstructure impurities . . . 13
2.1.1.1.4. Balling. . . . 14
2.1.1.2. External defects. . . . 14
2.1.1.2.1. Geometric dimensions . . . 14
2.1.1.2.2. Surface quality . . . 15
2.1.1.3. Process-induced defects . . . 15
2.1.1.3.1. Anisotropy . . . 15
2.1.1.3.2. Residual stresses . . . 15
2.1.1.4. Summary . . . 17
2.1.2. Powders used in the LPBF process . . . 18
2.1.2.1. Mechanical and chemical powder manufacturing techniques . . . 18
2.1.2.1.1. Mechanical manufacturing techniques . . . 18
2.1.2.1.2. Chemical manufacturing techniques . . . 18
2.1.2.2. Atomisation powder manufacturing techniques . . . 20
2.1.2.2.1. Projection-based atomisation techniques . . . 21
2.1.2.2.2. Centrifugal atomisation techniques . . . 22
2.1.2.2.3. Spheroidisation atomisation techniques . . . 22
2.1.2.3. Powder recycling strategies . . . 23
2.1.2.3.1. Machine silo filling: virgin blend, continuous use, continuous refreshing . . . 24
2.1.2.3.2. Powder drying effects. . . . 25
2.1.2.4. Summary . . . 26
2.1.3. Part and powder properties variations . . . 27
2.1.3.1. Recycling process influence on part quality . . . 27
2.1.3.1.1. Parts density . . . 27
2.1.3.1.2. Tensile test results . . . 27
2.1.3.1.3. Fatigue test results . . . 28

2.1.3.1.4. Parts oxidation 28
2.1.3.2. Recycling process influence on powder properties. 28
2.1.3.2.1. Powder particles size 28
2.1.3.2.2. Powder flowability 29
2.1.3.2.3. Powder oxidation 29
2.1.3.3. Powder properties affecting the part quality 30
2.1.3.3.1. Powders influence on parts density 30
2.1.3.3.2. Powders influence on parts oxidation and dissimilarities 31
2.1.3.4. Oxygen influence on part quality. 31
2.1.3.5. Summary 32
2.1.4. Materials used and specific oxidation mechanisms 32
2.1.4.1. Materials used in this study. 32
2.1.4.1.1. Al-Si10-Mg material 32
2.1.4.1.2. Ti-6Al-4V material 33
2.1.4.2. Oxidation mechanisms 34
2.1.4.2.1. Metal oxidation and oxidation kinetics 34
2.1.4.2.2. LPBF oxidation sources. 36
2.1.4.3. Summary 38
2.2. Identifying key oxidation factors 40
2.2.1. Material and methods 40
2.2.1.1. Material, machine and process conditions 40
2.2.1.2. Design of experiment 42
2.2.1.2.1. Samples and lattice geometries 42
2.2.1.2.2. Procedure 1: recycling and heating. 45
2.2.1.2.3. Procedure 2: recycling only 45
2.2.1.3. Sampling and measurements 47
2.2.2. Results 47
2.2.2.1. Procedure 1 and Procedure 2 manufacturing 47
2.2.2.2. Oxygen content. 48
2.2.3. Discussions 49
2.3. Limiting oxidation originating from heat 50
2.3.1. Material and methods 51
2.3.1.1. Material, machine and process conditions 51
2.3.1.2. Design of experiment 52
2.3.1.2.1. Samples geometries: calibration cantilever. 52
2.3.1.2.2. Experiment 1: different scanned surfaces 53
2.3.1.2.3. Experiment 2: interlayer cooling duration 54
2.3.1.2.4. Optical measurements 55
2.3.2. Results 57
2.3.2.1. Experiment 1 results: different scanned surfaces 57

2.3.2.2. Experiment 2 results: interlayer cooling duration 60
2.3.3. Discussions 63
2.4. Conclusions and perspectives 65
2.5. References 67

CHAPTER II

IDENTIFYING MAIN CONTAMINATION FACTORS OF REACTIVE POWDERS

2.1. Introduction

Laser powder bed fusion (LPBF) process is an additive manufacturing (AM) process making use of a high-power laser to selectively melt metal powder particles. The powder particles are spread as thin powder layers (20-70 µm thick) and sequentially added and molten by the laser beam.

The LPBF process has been the subject of numerous studies in the past decades. The evolution of the number of publications for this process using Web of Science database are shown in Figure 2.1. The request in Web of Science was: Topic= (selective laser melting OR SLM OR laser powder bed fusion OR LPBF).

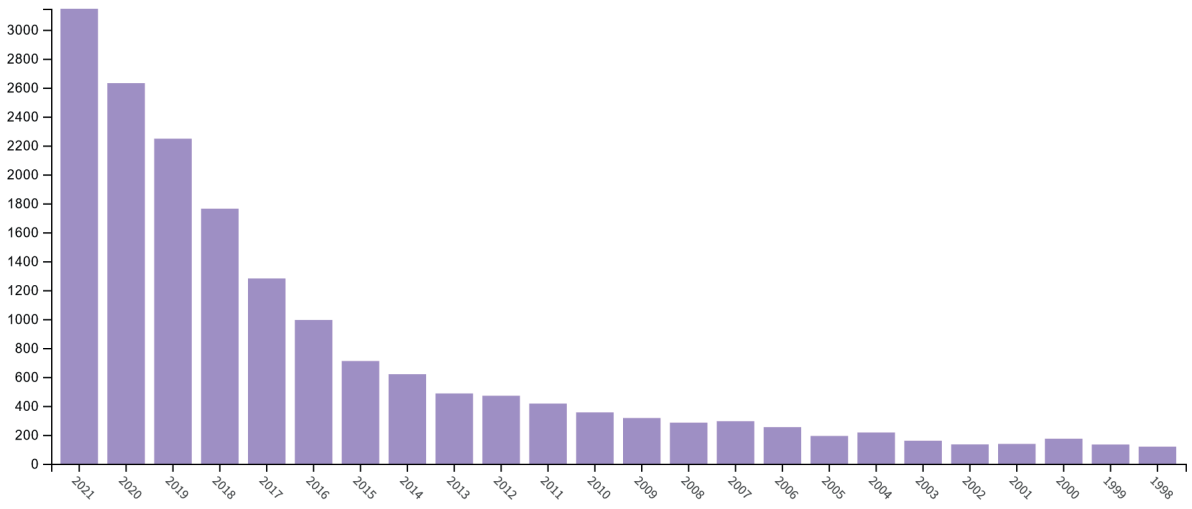

Figure 2.1: Temporal evolution of publications in Web of Science database on the LPBF process.

The process adoption in the industry is accelerating, and in a wide panel of applications. Manufactured parts become larger and larger, and production volumes are rapidly increasing too.

Powders are a key component of this process. They are at the root of its use and their understanding is critical to optimise the process. With rising production volumes, the volume of necessary powders also increases.

The unused powders are commonly recycled and used in subsequent productions. However, some powders may change with time and reuse, and become unsuitable for the LPBF process.

A major challenge is to understand how the powder can become improper to be used in the LPBF process and what actions can be launched to stop or to limit their ageing.

The literature survey will cover the following topics:

- Defects commonly encountered using the LPBF process;
- Powders manufacturing and recycling steps regarding the LPBF process;
- Parts and powders variation sources, focusing on powder ageing;
- Lastly, the oxidation mechanisms of two selected reactive materials commonly used in the LPBF process.

2.1.1. Common parts defects

During the LPBF process, the material changes phases from particulate to liquid (molten pool) and to solid (bulk part). Some defects can form during these fast transformations. According to Galy *et al.* [1], there are four main types of defects on aluminium LPBF parts. Malekipour *et al.* [2] proposed four defect categories and Grasso and Colosimo [3] proposed six of them. All these categories are listed in Table 2.1.

Focusing on aluminium alloys, Galy *et al.* [1], proposed hot cracking as one of the main defect categories. Hot cracking results from the lack of metal liquid supply during the process due to large solidification temperature ranges. As the authors mention, these defects are less susceptible to occur using casting aluminium alloys such as aluminium-silicon-magnesium alloys [1]. Since these alloys are mostly the ones proposed by the machine manufacturers [4]-[6], and other aluminium alloys are beyond the scope of this study, we chose not to discuss these specific defects.

Also, as discussed by Grasso and Colosimo [3], delamination phenomenon is linked with cracks caused by residual stresses. When these stresses magnitudes are excessively large, the previously manufactured layers tend to detach one from each other's [7]. Hence, these defects are incorporated with residual stress defects category.

Since some defect categories are similar, and to succinctly present them, they were all grouped in three main groups:

- Internal quality;
- External quality;
- Process-induced defects.

These groups are displayed in Figure 2.2.

Table 2.1: Defect categories identified in the literature

Galy *et al.* [1]	**Malekipour *et al.* [2]**	**Grasso and Colosimo [3]**
		Porosity
Porosity	Geometry dimension	Balling
Hot cracks	Surface quality	Geometric defects
Anisotropy	Microstructure	Surface defects
Surface quality	Mechanical properties	Residual stress, cracks and delamination
		Microstructure inhomogeneity and impurities

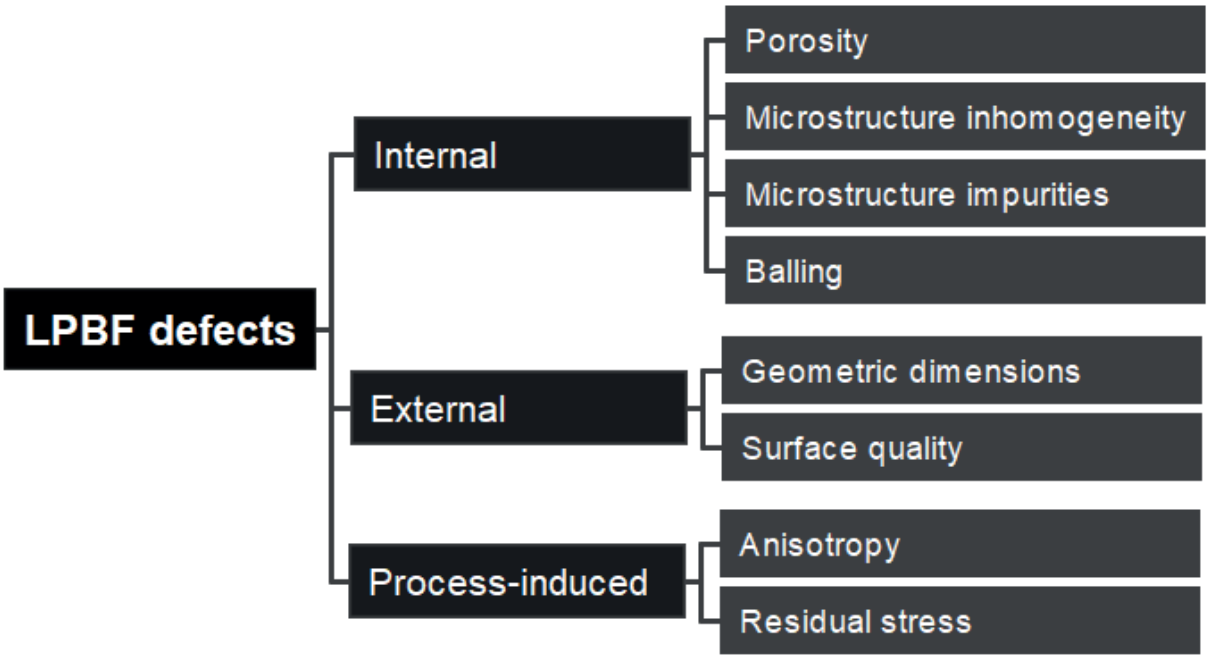

Figure 2.2: Main LPBF defect groups.

These groups are presented in the following sections.

2.1.1.1. Internal defects

2.1.1.1.1. Porosity

Porosity formation mechanisms are well-studied since a few decades since it impacts directly the conformity of the part and the LPBF adoption within the industry.

Porosities can be small: down to 10 µm according to Qiu *et al.* [8]; or extremely large: up to 1 580 µm according to Du Plessis *et al.* [9]. In some cases, with tuned parameters, the part can be almost fully dense: for instance, Stef [10] managed to produce a small part (2 mm * 2 mm * 3 mm) with a porosity level of 1.7 10^{-3} %. Porosity distribution within a small sample from [10] is shown in Figure 2.3(a).

The same study [10] identified five porosity formation mechanisms: lack of fusion, entrapped gas, keyhole coupled with matter ejection and denudation. Lack of fusion mechanism was found to be the principal porosity formation mechanism in [11]. Leung *et al.* [12][13] also found that spatter ejection can lead to open porosities. Studying Al-12Si material LPBF manufacturing, Li *et al.* [14] pointed moisture and hydrogen as a significant source of porosity.

Chen *et al.* [15] and Moussaoui *et al.* [16] identified powder particles containing porosities. These porosities inside the particles can be entrapped within the melt pool and be found in the manufacturing parts [64][65]. A scanning electron microscope image showing an internal powder porosity is shown in Figure 2.3(b).

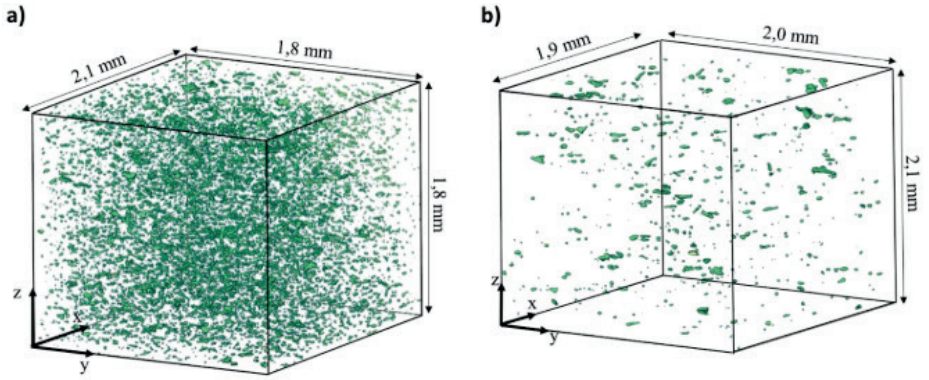

(a) 3D porosity distribution of samples measured with X-ray tomography from [10].

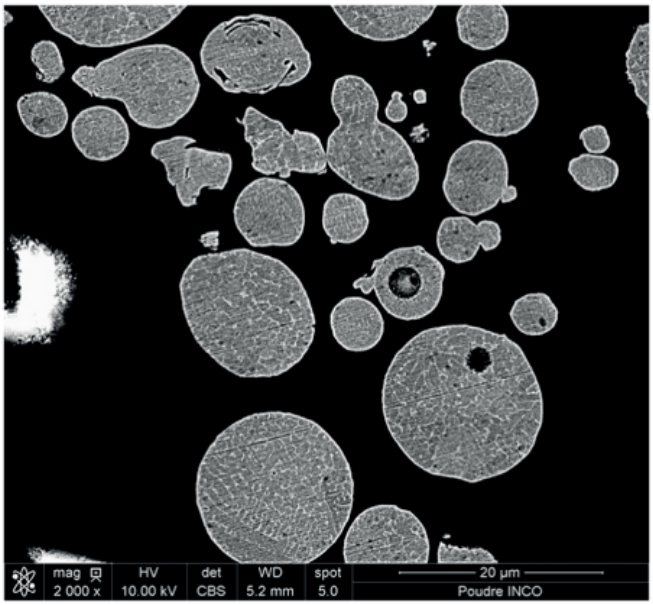

(b) SEM image of powders etched cross section with an internal porosity from [16].

Figure 2.3 : Porosities within a small sample (a) and inside a powder particle (b).

2.1.1.1.2. Microstructure inhomogeneity

According to Grasso and Colosimo [3], mechanical properties may suffer from heterogeneous microstructures of parts manufactured by LPBF. This manufacturing process generates specific microstructures that are not similar to wrought and cast processes [17] due to the fast solidifications, the directional heat transfers, the overlapping melt pools and the large heat gradients.

According to Sharratt [19], the microstructure of LPBF-manufactured parts has small columnar grains, oriented opposite to the heat flux. Moussaoui *et al.* [16] identified a columnar dendritic structure with several changes in dendrites orientations. For them, the grain growth can happen through multiple melt pools, due to the high temperature gradients. An optical metallographic image of an IN718 sample from [16] is shown in Figure 2.4.

Thijs *et al.* [18] observed three zones in the microstructure of Al-Si10-Mg: fine and coarse cellular structures inside the melt pool, and a heat affected zone around it. The cell sizes are thin (less than 1 µm) and they observed that the crystallographic orientations depend on the scanning directions.

Casati *et al.* [20] showed that the new grains solidification and formation follow an epitaxial growth (directed

by a surface): the grains grow perpendicular to the liquid-solid front. For them, it is possible to prevent the formation of texture by rotating the scanning direction from one layer to the next. They also identified that partially molten particles may lead to significant drop of the elongation at failure and premature failures.



Figure 2.4: Assembly of three perpendicular optical metallographic images of as-built IN718 from [16].

Sanaei and Fatemi [21] linked the fatigue behaviour of Ti-6Al-4V and 17-4PH specimens with internal defects and microstructures. It was shown that the internal defects had a major impact on the fatigue life, and in the case of Ti-6Al-4V, a hot isostatic pressing (HIP) treatment would reduce significantly the number of critical defects. Kahlin *et al.* [22] found that sub-surface (below the part's surface) defects impact the fatigue life of Ti-6Al-4V samples, and managed to improve greatly the fatigue performance with surface post-processing.

2.1.1.1.3. Microstructure impurities

According to Sharatt [23], there are two sources of impurities in the manufactured material composition: precipitation and contamination.

Precipitation may be used as a hardening post-treatment to enhance the material mechanical properties, increasing the yield strength. This technique has mainly been studied for nickel-based superalloys that display larger yield strength at high temperatures. Precipitates have been widely studied for IN625 [24][25], IN718 [26], IN100 [27] and 17-4 stainless steel [28] materials.

Contamination may be found under the form of oxides present on surface of the material. Multiple materials are concerned by these impurities: titanium alloys [29][30], aluminium alloys [31], nickel-based superalloys [32], stainless steels [33][34].

As mentioned by Casadebaigt [134], oxidation of the metal is not necessarily a default: under certain conditions, it can provide an interesting corrosion or wear resistance.

However, for some materials, the oxygen content is strictly defined in order for the material to be compliant with the industrial standards (i.e., for Ti-6Al-4V, ASTM F3001 [139] and ASTM F2924-12 [140]). Indeed, oxygen content has an important influence on the final material's performance. These variations may be detrimental for the final application.

It can reveal complex to remove the oxide layer of the base material [35], and it does not assure that the internal oxygen content complies with the standard ranges. Also, it seems that the oxidation of the material may be slowed down, but not stopped (the oxidation mechanisms of some materials will be discussed in Section 2.1.4.2).

2.1.1.1.4. Balling

In 2004, Kruth *et al.* [36] explained the balling phenomenon, leading the molten metal to spheroidise above the solid substrate instead of remaining a half-cylinder as shown in Figure 2.5. The authors explained that the surface tensions are responsible for this phenomenon since they while trying to spheroidise the liquid, they impede the molten metal to wet the underlying solid substrate. They also mention that specific laser parameters would prevent the issue to occur. The same year, Tolochko *et al.* [37] modelled the balling process and identified that a reduced layer thickness and an increasing melt length would enhance the risk of balling.

From Kruth *et al.* [38], the balling may lead to damaged surface quality. Li *et al.* [39] also mentioned this issue on manufactured parts, the risk of porosity formation around the formed metal balls and the scratching of the layering system from the contact with the metal balls. They found that two kind of balling phenomenon may occur, one of them leading to the formation of 500 µm large metal balls.

According to Li *et al.* [39], reducing the build chamber oxygen content level lower than 1 000 ppm (current machines oxygen levels are below 500 ppm) would diminish the risk for balling to occur. Also, using high energy densities would help to reduce this risk.

Studying the balling phenomenon on tungsten powders, Zhou *et al.* [40] observed that a remelting process (scanning the same area two times) would remelt the metal balls and yield better surfaces.

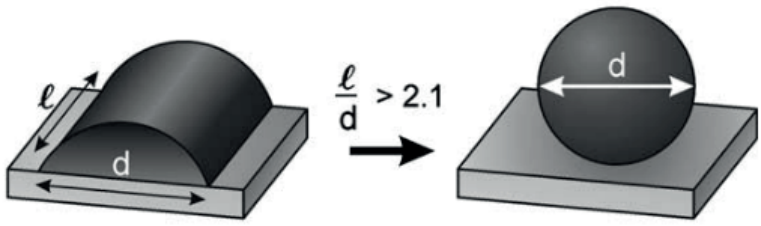

Figure 2.5: Balling phenomenon from [36].

2.1.1.2. External defects

2.1.1.2.1. Geometric dimensions

Due to the thermomechanical aspect of the LPBF process, the manufactured parts may suffer from shrinkage and warping phenomena.

According to Hong *et al.* [41], the staircase effect is induced by the material shrinkage. The staircase effect takes place during the manufacturing process: the newly-deposited top layer tends to shrink, dragging the underlying previously manufactured layers with it. Hence, the resulting surface is stepped.

Simchi *et al.* [42] used contouring strategies incorporating the beam compensation to consider the part shrinkage, improving the dimensional accuracy. Sharratt [44] mentioned that since the laser diameter was different from the melt pool width, a precise characterization of the melt pool width was necessary. Generally, this parameter is handled by the LPBF machine manufacturer which provides the process parameters.

Zhu *et al.* [43] modelled the shrinkage phenomenon of Cu-based material laser sintering. They mentioned that the shrinkage may be higher with increasing input energy since they are linked as Equation (2.1).

$$\Delta h = \alpha \frac{AP}{cpV\omega} \tag{2.1}$$

With Δh the height shrinkage of the manufactured layer, α is the linear coefficient of thermal expansion

(CTE), A is the absorption rate of the material, P is the laser power, c and p the material specific heat and density, respectively. V is the laser scan speed and ω is the scan line spacing.

According to Yasa *et al.* [46], contours are necessary for the geometrical accuracy of the production since they prevent edges elevations. The authors designate the surface tension effects as responsible for edge elevation phenomenon: the melt flow may be large enough to push the melt back while the laser scans forward.

According to Sharratt [44], rising the build plate temperature would diminish the geometric distortions. Thomas [45] offers design rules using supports, part orientations and minimum feature size to reduce the warping effects on LPBF parts.

2.1.1.2.2. Surface quality

The surface finish depends mainly on the orientation of the surface [3]. The staircase effect and the balling phenomenon presented before play an important role in the surface quality of LPBF components [39][41]. Inclined surfaces are mainly sensible to the staircase effect. Downfacing surfaces generally show poor surface quality [47], since they exhibit specific thermal history due to their thermal insulation.

The surface roughness influences the fatigue life of the manufactured component; hence it is requested to post-process the part to enhance the surface quality [48] for applications needing fatigue performance.

2.1.1.3. Process-induced defects

2.1.1.3.1. Anisotropy

In their study published in 2012, Kempen *et al.* [49] showed that LPBF-processed Al-Si10-Mg had mechanical properties (with tensile, Charpy and hardness tests) equivalent or better than the conventional cast material. Their study demonstrated a discrepancy of the elongation at break depending on the solicitation direction (XY or Z), hence reflecting an anisotropic behaviour for this characteristic. The density of the vertically-oriented samples (which was lower than the others) was pointed out as the main reason for such discrepancy.

The same authors in [50] found that the anisotropy in Al-Si10-Mg material may be lowered from changing the scanning strategy. They managed to reduce the crystallographic texture by rotating the direction of the laser paths (as compared with uni- or bidirectional scanning).

In [51], Prashanth *et al.* mentioned that either anisotropic or isotropic properties can be achieved with AlSi12 material from tuning the process parameters (i.e., the scanning direction and rotation, and the build plate temperature). They considered an anisotropy from the different behaviour of the vertically-manufactured samples through their length while tensile tested in a unique direction.

Giovagnoli *et al.* [52] showed that high temperature heat treatments reduce the anisotropic behaviour of Al-Si10-Mg with Charpy tests: although the as-built and annealed samples showed different results regarding the sample manufacturing orientation, the high-temperature heat-treated specimens provided more homogeneous results. The resulting microstructure is less heterogeneous with high-temperature heat-treatments than the microstructures of as-built and annealed samples.

Similar anisotropic behaviours have been noticed in other materials such as:

- Ti-6Al-4V [53][54];
- 316L stainless steel [54]-[56];
- IN718 [57].

2.1.1.3.2. Residual stresses

Kruth *et al.* [58] was one of the first studies studying the specific residual stresses formation within the LPBF process. They proposed the temperature gradient mechanism (TGM) and the following cool-down phase to

explain the formation of these stresses: locally (around the melt pool), the solid material is heated and tends to expand. However, the underlying solid impedes this expansion, generating compressive stresses that may exceed the yield strength (leading to plastic strains locally).

The cool-down phase concerns the upper layer which solidifies after the laser scanning. Due to the rapid cooling and solidification, the previously molten material tends to shrink, but this shrinkage is impeded by the surrounding solid (which was expanding in the TGM phase).

From these two phases (TGM and cool-down), there remain tensile stresses at the previous melt pool areas and compressive stresses in the solid around these previous melt pools. An illustration of the stress fields after the laser scanning is shown in Figure 2.6.

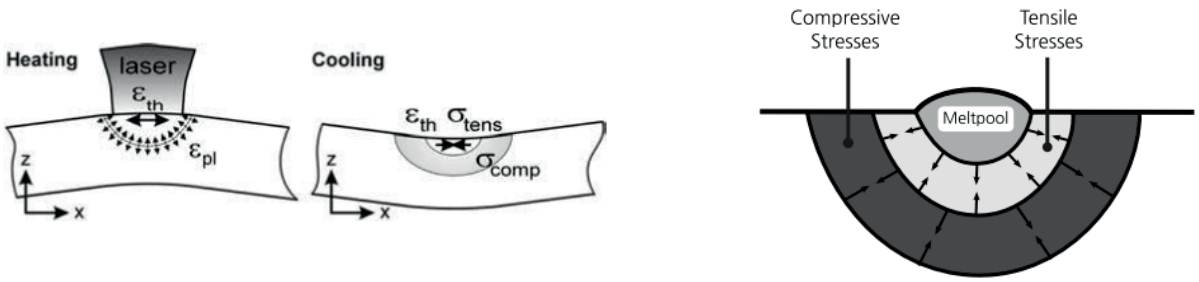

(a) TGM and cool-down phase from [58]. (b) Final stress state after laser scanning from [60].

Figure 2.6: Illustration of the stress state after a unique laser scanning.

Vrancken [59] and Parry [60] both studied the residual stresses formation within the LPBF process. From these works, the overall resulting stress fields are known: the upper surface suffers from horizontal tensile stresses, while the centre of the part suffers from compressive stresses in every direction. The borders of the part suffer from vertical tensile stresses, resulting from the tensile forces at the top surface and the connection with the build plate. Displacement and residual stress fields computed for a small pillar (10 mm * 10 mm * 20 mm) are shown in Figure 2.7.

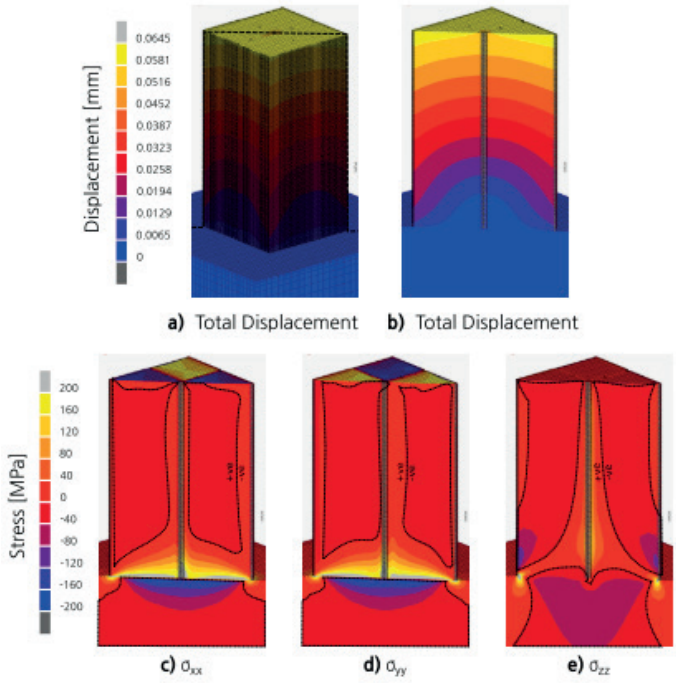

Figure 2.7: Dispalcement and stress fields of a LPBF-manufactured pillar from [60].

As discussed, the stresses magnitudes may exceed the yield strength, leading to plastic strains and distortion, but they also can exceed the ultimate tensile strength of the material. Cracks and delamination can then appear, which are major flaws during the process [61]. Examples of crack and delamination are shown in Figure 2.8 for electron beam melting (EBM) process.

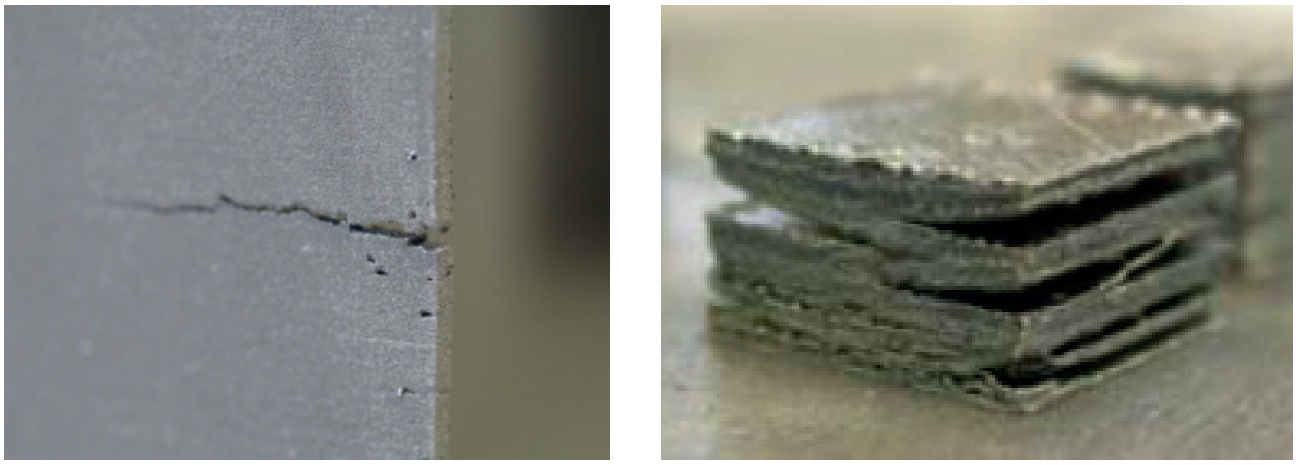

(a) Crack on thin Ti-6Al-4V wall from [60]. (b) EBM layers delamination from [61].

Figure 2.8: Crack and delamination observed in LPBF and EBM processes.

According to Vrancken [59] and Ali *et al.* [62], one of the most important factors to reduce the residual stress magnitudes is to increase the build plate temperature. Also, heat treatments are to be used after the manufacturing process to reduce drastically the residual stresses within the parts [63].

2.1.1.4. Summary

Several types of defects have been observed in the literature. For most of them, reliable solutions have already been suggested:

Porosities can be handled by tuning the process parameters and specific HIP post-process. Heat treatments are effective to erase the microstructural textures. The balling phenomenon may be handled by limiting the oxygen content in the chamber and scanning at higher energy densities. Design guide lines and mechanical post processes are used to limit the geometric and surface defects. The anisotropic properties of the parts may be influenced by the process parameters, and, regarding the residual stresses, rising the build plate temperature may help lowering their magnitudes and avoid cracks risks.

Most of these defects are related to the complex thermal history, material specificities, and instabilities of the melt pool during the laser beam scan.

However, for some materials, the oxidation phenomenon can represent a major flaw since the industrial standards limit strictly the chemical composition.

Ageing and reuse of the powders seem to have a strong influence on the oxidation of some materials. Hence, in the next section, powder manufacturing and recycling processes will be presented.

2.1.2. Powders used in the LPBF process

There are several methods to manufacture metal powders. Understanding these methods and resulting powder properties can help choosing the right powder for the right application, and also to prevent the generation of defects that can hardly be erased afterwards.

Regarding the powder manufacturing market a few years ago (in 2015), additive manufacturing represented a small portion of the market share: 0.0047% according to [66]. However, with the upcoming of new large systems (consuming more powder material for larger manufactured parts) and the increasing use of AM in the industry, this portion rises fast.

2.1.2.1. Mechanical and chemical powder manufacturing techniques

Powder manufacturing techniques are divided into three groups, depending on the nature of the energy used for the production: mechanical processes, chemical processes and physical processes.

2.1.2.1.1. Mechanical manufacturing techniques

Common mechanical processes (mechanical milling) to manufacture powders are the grinding and the crushing processes [67]. Angelo and Subramanian [68] describe these processes:

During the grinding process, particles are launched against each other, making them collide and break into smaller particles.

Crushing makes use of additional systems, such as a gyratory crusher, or a roll crusher, both are displayed in Figure 2.9. Crushing process is mostly used for ceramic materials such as metal oxides. Crushing enables the breakage of bulk materials into powders as a preliminary step.

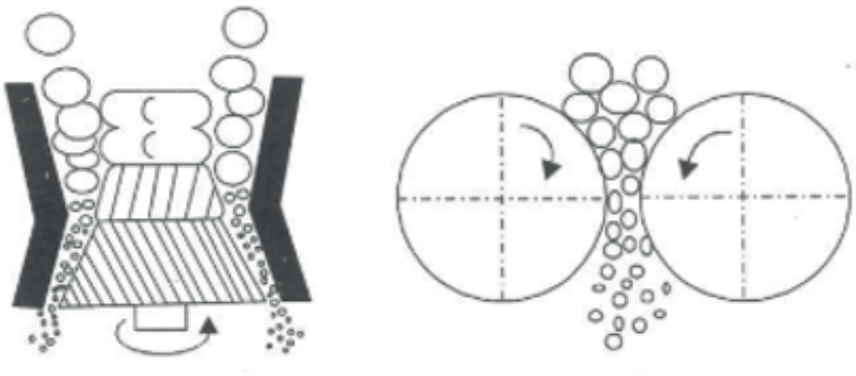

Figure 2.9 : Illustration of the crushing process with a gyratory crusher (left) and a roll crusher (right) from [68].

In the case of the LPBF process, these methods cannot be directly used since the resulting powders are of angular shape [67]. Until now, it is recommended by LPBF machine manufacturers to use spherical powders with a smooth surface, and milled powders are not compliant with these prerequisites.

Hence, mechanical powder manufacturing techniques may not be suitable for the LPBF process in the author knowledge.

2.1.2.1.2. Chemical manufacturing techniques

There are several chemical processes that can be used to produced metal powders. These powders differ from their purity, size, shape and by the nature of the metal which can be treated. These processes differ also from the resulting powder shapes, an illustration of different shapes from is displayed in Figure 2.10.

Electrolysis process:

From [67], the electrolysis process can treat only pure metals using these as anodes. Indeed, the metal in its molten state is used as an electrolyte that can conduct the electrical current. Resulting particles are of dendritic, bar or needle shape.

Owing to the requirement to use pure metals and the resulting particle shape, this process looks inadequate for the LPBF process.

Reduction process:

The reduction process is one the most widely used and the oldest metal powder manufacturing technique [68]. Compatible materials with this process are titanium, nickel, copper, cobalt, and many others. However, powders manufactured from this process are usually porous. Hence, this process is inadequate with the LPBF process since the porosities from the powder can be retrieved in the manufactured parts.

Thermal decomposition:

The thermal decomposition of carbonyls (nickel, cobalt or iron) produces fine powders of high purity [68]. In the case of iron, the iron pentacarbonyl is produced projecting high pressure carbon monoxide on heated porous metal. Carbonyl is then decomposed at approximately 200 °C at atmospheric pressure to generate spherical iron powders of high purity. Nickel powders manufactured by thermal decomposition are usually porous and irregular in shape (hence, not recommended for the SLM process).

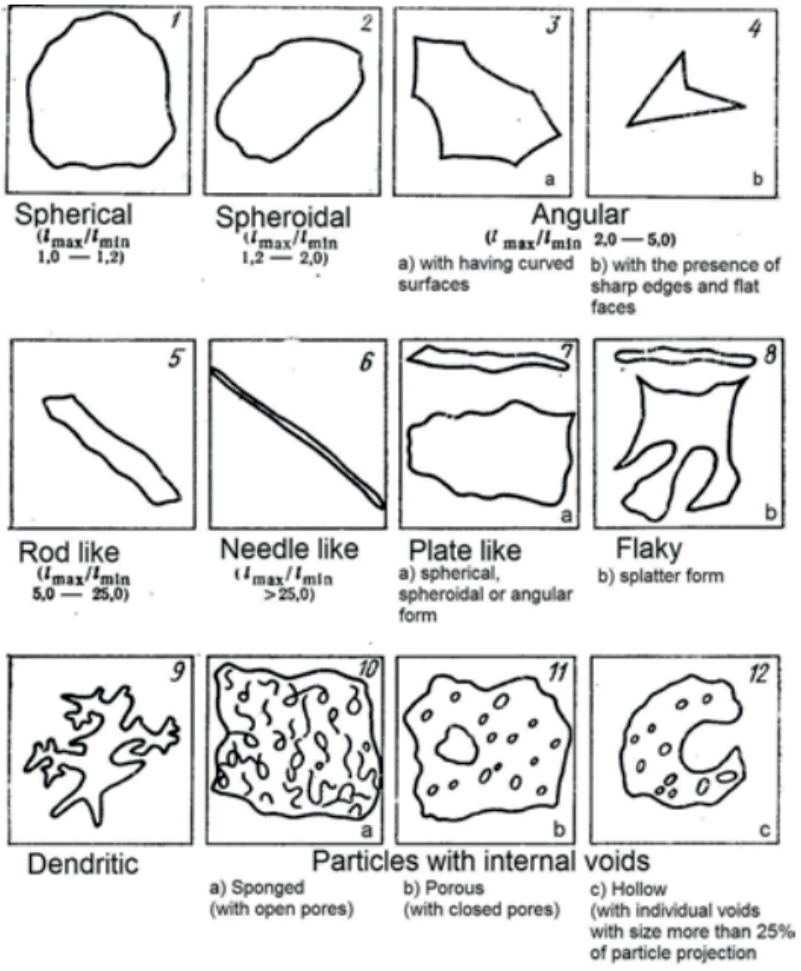

Figure 2.10: Illustration of powder particle shapes from [67].

FFC Cambridge process:

The FFC Cambridge process is one of the mostly used for the titanium material. An oxidised anode of the material has its oxides being reduced in an electrolytic media at high temperature (800 - 1 000 °C). The oxygen present in the media reacts with the carbon atoms of the anode, producing carbon monoxide and dioxide [69].

Hydride-DeHydride process, HDH:

Metal hydrides decomposition is used to manufacture powders of reactive materials (notably titanium) since powders are delivered with high purity [68]. There are two main chemical transformation steps: the metal is transformed into hydrides and grinded mechanically into smaller particles, then it is decomposed into metallic powder. The second step is performed placing the hydride in a vacuum atmosphere and heating it at the temperature of hydride transformation.

Some chemical processes can be used in terms of purity to manufacture LPBF powders, notably thermal decomposition and HDH processes. However, only specific materials can be treated with those processes, and a specific care should be brought regarding the shape and the size of the particles to comply with the machine manufacturer prerequisites and the AM standards. Also, none of these processes deliver both dense and spherical powder particles.

Assuming the need for dense, spherical and low contaminated powders to be used in the LPBF process [66] [131], none of the chemical processes are directly suitable for the LPBF process in the author knowledge.

Some other manufacturing processes exist, such as the carbonyl process (used for nickel and iron powders) [67], the electrolytic deposition (used for iron and copper production) [68], the granulation-sintering-deoxygenation (GSD) method for titanium powders and its alloys [86], or the arc-spraying based atomisation process [87], although these methods are not common in the AM research fields.

Common techniques, however, are grouped under the «Atomisation» label and are presented in the next section.

2.1.2.2. Atomisation powder manufacturing techniques

Atomisation is currently growing in Europe, in North America and in China: transatlantic partnerships are settled and factories implanted [70]-[74].

In most cases, the atomisation-based process consists in breaking a thread of molten metal using water, pressurised gas or plasma [67]. Molten metal drops solidify before touching the surface of the atomisation system. There are three groups of atomisation methods: projection techniques, centrifugal techniques and spheroidisation techniques. An overview of atomisation processes is displayed in Figure 2.11.

Atomisation processes can treat every metal that can be molten (preferentially with a low melt point) [68]. Very high melting point materials such as tungsten or molybdenum are not turned into powders using atomisation processes. These are not common metals in the LPBF process.

With atomisation, the particle size distribution (PSD) depends on the nature of the material and the atomisation process [67].

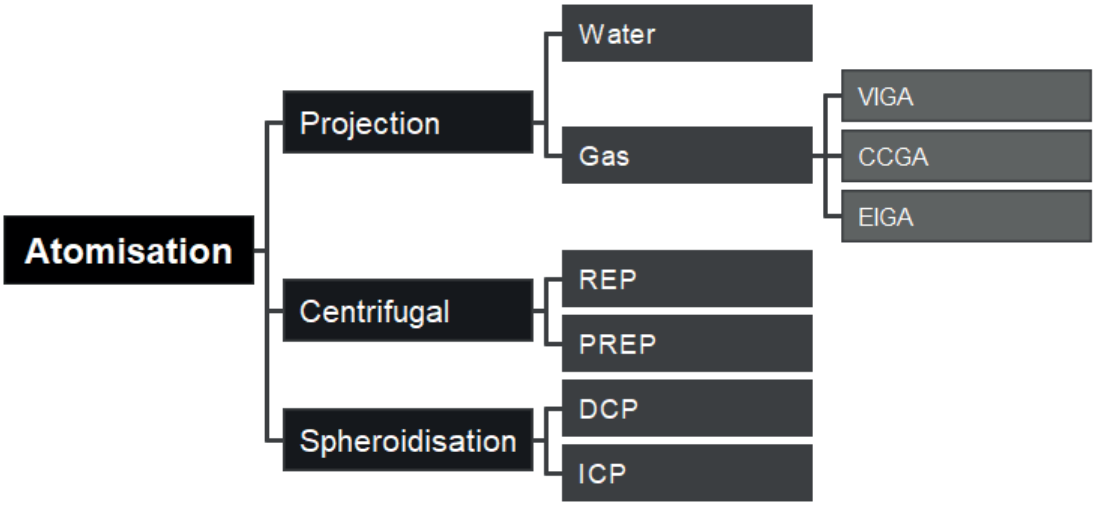

Figure 2.11: Overview of atomisation processes.

2.1.2.2.1. Projection-based atomisation techniques

Water atomisation

With this process, the molten metal thread is broken using water jets [68]. This process is considered highly productive [67][76], and able to treat ferrous and non-ferrous metals.

It is the most affordable atomisation process; however, it cannot treat reactive materials (i.e., titanium and its alloys) and resulting powders particles have an angular shape and high oxygen contents.

Gas atomisation:

Gas atomisation consists in breaking the molten metal thread using high-speed gas (air, nitrogen, argon or helium) [68]. Regarding the gas choice, Baitimerov *et al.* [77] observed that air-atomised powders comprised significantly more oxygen than argon-atomised powders.

Materials that can be treated using these processes are alloys of Ti, Al, Co and Ni, special steels and precious metals [76]. There is an order of magnitude of difference regarding from gas atomisation to water atomisation regarding the cooling durations. It explains the better sphericity of the gas-atomised particles.

It is necessary to compare gas and water-atomised powders quality (presence of satellites, surface quality, sphericity) regarding LPBF powder requirements. For instance, Hedberg [80] found that the oxide nature in the oxide layer of 316L stainless steel powder particles vary according to the atomisation process (Si element in the case of water atomisation, Mn element in the case of gas atomisation). Gas atomisation is more expensive than water atomisation according to [68].

Several versions of the gas atomisation are available:

Vacuum induction melting combined with inert gas atomisation (VIGA):

This process can be used to manufacture powders of non-reactive materials [67], and the resulting particle size is comprised between 15 and 150 µm [78].

Cold crucible gas atomisation (CCGA):

During the CCGA process, the metal is first melt within a crucible before being sent towards the atomisation nozzle [75]. Resulting powder has high sphericity and a fine granulometry.

Electrode induction melting gas atomisation (EIGA):

With the EIGA process, a metal bar is molten with contact-less induction [75]. Once at its molten state, it falls freely within the atomisation chamber. Since there are no contact with exterior matter, the process yields

powder of high purity and can treat reactive metals such as titanium [67]. EIGA processed powders have a granulometry comprised between 1 and 500 µm according to [79].

2.1.2.2.2. Centrifugal atomisation techniques

Rotating electrode process (REP):

During REP process, part of a rotating electrode is molten using an electric arc [67]. Centrifugal forces break the molten metal thread and metal liquid drop solidify slowly, in a spherical shape [68].

Resulting particles have high quality surface (smooth) and the PSD is comprised between 50 and 400 µm [67]. This process can be used to treat reactive materials such as titanium [68].

Plasma rotating electrode process (PREP):

PREP process is similar to REP process, changing the source of heat (electric arc in REP process) into a plasma arc [67]. Resulting powders have low contamination and the yielded granulometry is below 100 µm [79].

An illustration of some of these techniques is shown in Figure 2.12.

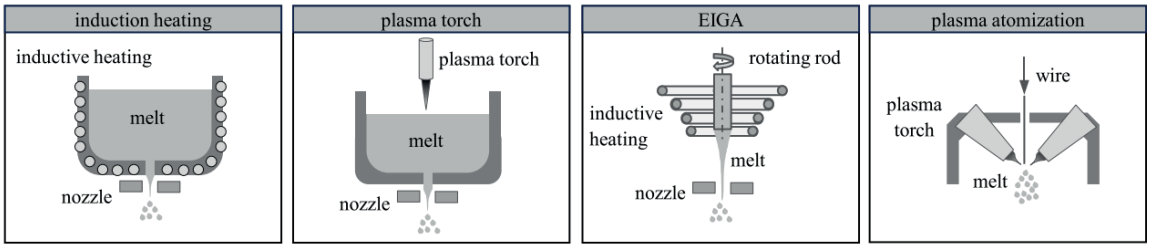

Figure 2.12: Illustration of some powder manufacturing techniques from [87].

2.1.2.2.3. Spheroidisation atomisation techniques

Direct current plasma (DCP):

Plasma atomisation is one of the most used process for manufacturing the industry and research LPBF powders. Plasma atomised powders have smoother surfaces [83] and have a better sphericity than gas atomised powders, but they are also more expensive [82].

In the case of the DCP process, the raw material is on wire form [67][75]. Plasma torches delivering high temperature inert gas (argon) at high velocity melt and atomise the metal wire [81]. Atomising a solid metal wire in place of breaking a molten metal thread is favourable to prevent any contact between the molten metal and any solid element, limiting the contamination. Using a heated gas slows the particles cooling, providing a better sphericity.

With this process, the PSD can be controlled with the wire speed [67][81], and fine granulometries are usually produced (1 to 200 µm according to [67], up to 300 µm according to [81]). Resulting particles are highly spherical, with low oxygen contents [67][75].

Inductively coupled plasma (ICP):

A plasma torch melts the raw material, and the following cooling is controlled [84]. The raw material can be of various types, such as powder (that can be previously manufactured, for instance) [75]. The ICP process is commonly used after Hydride-DeHydride process to treat titanium powders [83].

This process generates a lot of satellite particles, but using it as a treatment enables a better sphericity and to erase internal porosities [83]. According to [67], powders flowability are improved as well as their apparent density while being layered.

The particle size ranges delivered by some gas and plasma atomisation process are listed in Table 2.2. A schematic illustration of the ranges required for the LPBF process is shown in Figure 2.13 (LPBF process is

mentioned as «Selective Laser Melting»). Only a share of the particles produced by these techniques are suitable in size for the LPBF process, explaining partially the high cost of these powders. Indeed, powders go through several sieving processes to isolate those with suitable sizes, other particles are used for another process as illustrated in Figure 2.13, or remelted to generate suitable particles.

Table 2.2: Powder size delivered by some gas and plasma atomisation process.

Process	Type of heat source	Particle size range
VIGA	Gas	15 - 150 µm
EIGA	Gas	1 - 500 µm
REP	Gas	50 - 400 µm
PREP	Plasma	Inf. 100 µm
DCP	Plasma	1 - 200 µm

Plasma atomisation techniques seem to have numerous advantages regarding manufactured powders (high purity, smooth particle surfaces, high sphericity, PSD covers the range used by LPBF process), but they are economically more expensive than the other processes.

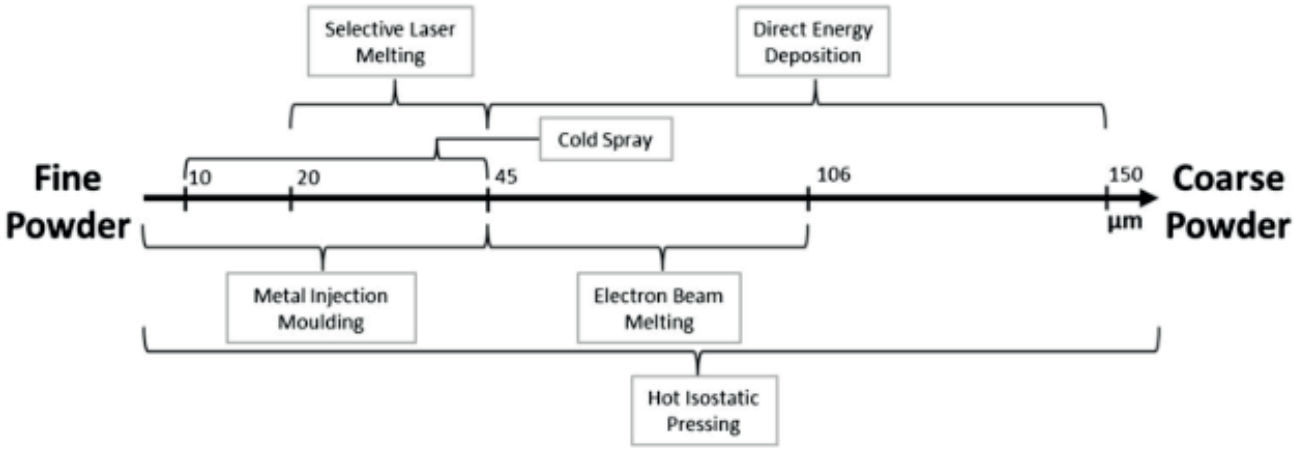

Figure 2.13: Particle size range for different applications [86].

2.1.2.3. Powder recycling strategies

According to Powell *et al.* [88], a large number of powder can be retrieved from production chamber and reused, Petrovic [89] estimated 95 to 98% of unfused powders can be reused. Lutter-Günther [91] found that the volume of fused material (parts and supports) impacts the number of recycling cycles, however they did not consider parts or powders' quality.

Barclift *et al.* [85] demonstrated that using reused powders at a certain degree (depending on the material and the manufactured parts geometries) one can achieve significant cost savings. However, they considered that remaining powder would be contaminated and advised to fill at most the build plate to reduce the number of unused powder. It is then necessary to limit the contamination of unused powders to reduce the material cost.

Regarding the condensates, Asgari *et al.* [90] observed that they were larger than powder particles (both new and reused), hence these unwanted particles may be separated from the powder particles with sieving.

Hence, the recycling process has multiple objectives, including removing spatter and condensate particles, and providing powders of similar quality as the fresh powder used in the first cycle. If powder characteristics were to change, they should not impact the final parts quality.

Great efforts from the researchers and industrials have been done to develop methodologies enabling multiple recycling cycles and find the configuration leading to the minimum variations of both powders and parts qualities.

2.1.2.3.1. Machine silo filling: virgin blend, continuous use, continuous refreshing

Virgin blend / Collective aging

In their white-paper [92], Okello and Samper (GE Additive) present the virgin blend method to rejuvenate used powders. It is similar to strategy B (collective aging) presented by Lutter-Günther *et al.* [91] and also similar to the strategy proposed by Derimow and Hrabe [148]. Renishaw [93] presented a similar method as Lutter-Günther *et al.* [91], although no fresh powder is added at any time. If no fresh powder can be used, less manufacturing productions can be performed.

It consists in putting aside the used powder (labelling it «n-use») and to fill the machine with fresh powder. Once there is not enough fresh powder for the next production, the powder labelled «n-use» is blended with the insufficient remaining powder in the silo.

The process can then be repeated while labelling the separated powder with «n+1 label». The process stops when reaching a predefined number of reuse cycles, or when there are insufficient powder numbers for the next build. The collective aging strategy is displayed in Figure 2.14.

To perform this method, the user does not need to extract the powder from the silo at each iteration. However, once there is not enough powder in the machine and there is a need to fill with the used powder, the steps of extracting the powder from the silo and mixing it with the used powder can be time-consuming.

Also, since the powder set aside must not be incorporated until there is an insufficient number of powder within the silo, specific infrastructure for the (possibly long-time) storage should be provided. The step of mixing the used and fresh powder seems to have effects on the measured oxygen content, however Powell *et al.* [88] mentioned the need to further investigate the effects of mixing virgin and recycled powders.

This method provides advantages regarding the tracking of the powder state, which is mandatory for specific applications such as aeronautics.

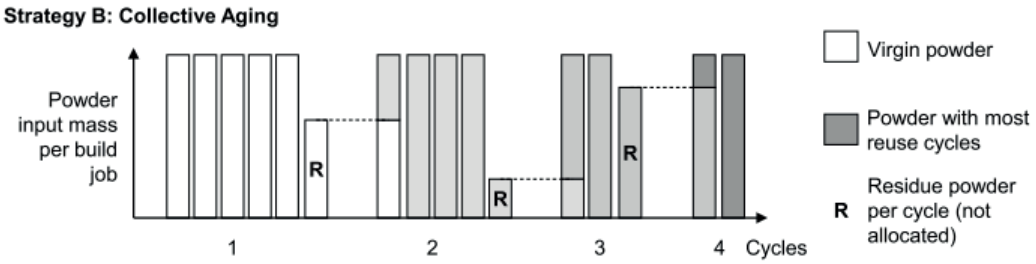

Figure 2.14: Continuous aging recycling strategy [91].

Continuous use

The method presented by Jacob [94] is similar as the strategy D presented by Vock *et al.* [95]. It consists in adding the sieved reused powder at the top of the silo without mixing. Hence, the powder at the top of the silo is always the most used at the beginning of the production. The continuous use strategy after three builds is shown in Figure 2.15.

This method is simple since it does not require to extract unused powder from the machine (to be mixed), however, it is not possible to keep track of the powder state through the multiple cycles.

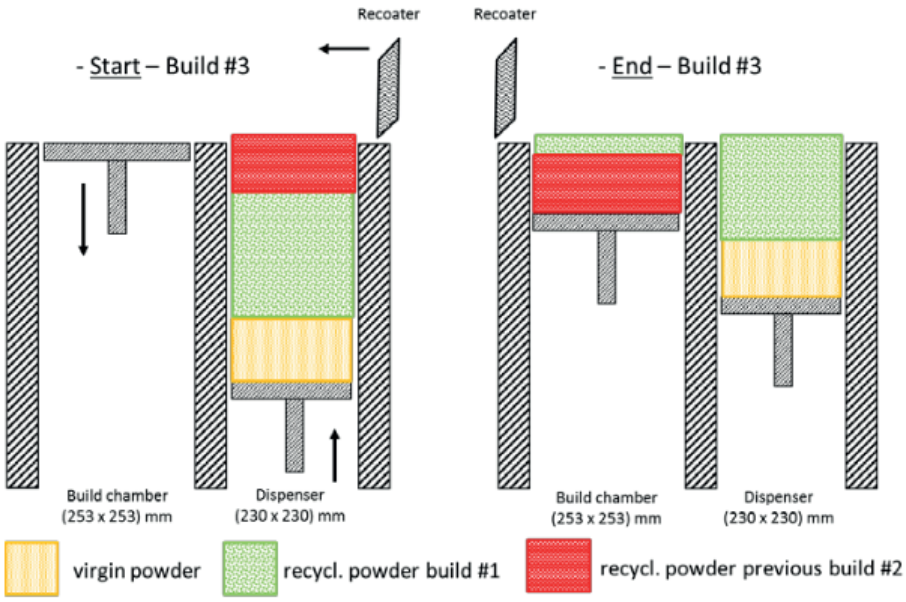

Figure 2.15: Continuous use recycling strategy [94].

Continuous refreshing

The continuous refreshing strategy is presented by Lutter-Günther *et al.* [91]. In the continuous refreshing strategy, the used powder is blended with the remaining powder within the silo and virgin powder is added to fill the silo. The process is shown in Figure 2.16.

The authors of [91] assume that the powder in the silo that has not been used should be considered aged. Hence, the powder at the top of the silo is always virgin at the beginning of the production.

This approach reduces the aging process and virgin powder is always the first to be used at the beginning of the production. However, it is time-consuming to extract use and un-used powders to mix them together.

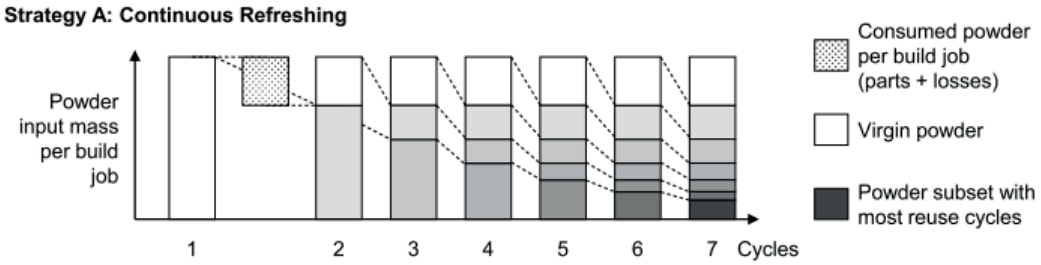

Figure 2.16: Continuous refreshing recycling strategy [91].

2.1.2.3.2. Powder drying effects

Recent studies have shown that the drying of powders have favourable effects on the parts quality, and some others incorporate the drying process within the recycling strategy [76].

Indeed, Riener *et al.* [96] observed excellent density and mechanical resistance of samples with dried powders. They suggest to always dry the powder beforehand, even the fresh one.

In [97], Cordova *et al.* proposed two drying strategies prior to melt the Al-Si10-Mg powders: the first one consisted in drying the powder under vacuum externally, at 70 °C during 18h. The second strategy took place inside the AM machine, it consisted in scanning the powder at low power (90W) before effectively melting it. According to the authors, the resulting densities of all specimens were acceptable.

Comparing moisturized, air-dried and vacuum-dried powders effects on four different materials (Al-Si10-Mg, Ti-6Al-4V, IN718 and Scalmalloy), Cordova *et al.* [98] observed that the results were material-dependent with a particular sensitivity of Al-Si10-Mg with moisture. Indeed, the oxygen content rose significantly for this material (compared with the dried conditions).

For all materials, the moisturized powders did not flow using the Hall-flow method. The authors explained that two phenomena were taking place to explain the loss in flowability: particles agglomerate together, and hydrogen bonds formed between the moisturized particles.

Similar flowability results were observed by Bauer *et al.* [99] with two moisturized powders (Al-Si10-Mg0.6 and Al-Si10-Mg0.45): the flowability decreases significantly (measured with a rotating drum). However, when drying the powders under vacuum at 25 °C during 4h, the moisturized powders flowability enhanced significantly.

According to [98], in the case of the Al-Si10-Mg, the moisture presence between the powder particles helps the oxide layer thickness growth, explaining the oxygen content rise. Also, even if no difference was observed regarding the density of samples made from air-dried (150 °C - 20 min) and vacuum-dried (85 °C - 12h), the authors advise to use vacuum-drying treatments since it may be useful to prevent the contamination of the powders.

Using a specific method where the IN718 powder is sieved and dried (drying conditions were not provided), Ardila *et al.* [100] concluded that the recycling does not alter the powder properties significantly. This conclusion may be attributed to both the recycling methodology and the subject material (IN718), which do not seem to be altered by recycling process [101]-[103].

Hence, depending on the material, the powder drying seems to have positive effects regarding powder reuse. It seems that moisture impedes the flowability of powders (for all materials) and that the drying process would help reduce the moisture on particles' surface.

Also, according to Cordova *et al.* [98], the humidity present between powder particles seems to favour the oxide layer growth in the case of Al-Si10-Mg. However, no indication regarding the moment of contamination (during the scanning, the powder layering, handling, sieving, or all of those indistinctly) is available.

Several drying conditions were proposed in these studies, and almost all of them seem to yield better results than in no-drying conditions. Further studies regarding the optimal drying conditions are still necessary. Also, in the industry, drying is not common in the recycling processes. Incorporating drying processes may yield beneficial results in the industry.

2.1.2.4. Summary

Several techniques can be used to produce metal powders, however, due to specific LPBF requirements regarding the powder particles, the most reliable techniques are in the atomisation group.

For reactive materials which may be contaminated, plasma atomisation is more appropriate since resulting powder particles are of high purity. However, these techniques are more expensive than gas atomisation techniques. Hence, using plasma-atomised powders, the initial oxygen contents of the particles should be lower, and may result in increased reuse potential.

Regarding the recycling of the powders, the main objectives are to remove condensate and spatter particles from the used powder, which should be of similar quality as fresh powder afterwards. The recycling steps mainly consist in retrieving the powder from the feeders, sieving it, and filling the machine silo either with the recycled powder, fresh powder, or a mix. The selection of the filling powder represents the recycling strategy.

Recycling strategies presented in this section make compromise between simplicity (cost), tracking of the powder reuse state, and number of thrown away powders, hence, limiting the cost.

It also appears that drying the powders before any productions may reduce significantly the ageing process: the powders seem to be less contaminated. Hence, the oxygen present in the moisture may play a significant role in the ageing process.

However, it cannot be identified at which step (from the recycling process or the manufacturing process) the powder suffers the most from contamination. Indeed, the manufacturing process is under inert atmosphere, but generate spatters which might be oxidized and retrieved within the recycled powder. Also, during the extraction, the sieving and the machine filling, the powder may be exposed to ambient atmosphere and moisture. Hence, it is not possible yet to tell if one of these steps is the main oxidation site of the powder material.

2.1.3. Part and powder properties variations

The variations of parts quality regarding the recycling process are discussed in this section. Also, since the powder properties variations are impacted by the recycling process, and they may impact the parts' quality, the different variations are also listed.

The analysis is done from a material-driven fashion since results may differ significantly considering the studied material.

Also, studies considering other metal AM processes, such as the EBM process, may help understand different variations observed in the LPBF process. Hence, several of these studies were also considered in this analysis.

2.1.3.1. Recycling process influence on part quality

2.1.3.1.1. Parts density

After 30 cycles of Ti-6Al-4V EBM-manufacturing, Ghods *et al.*. [104] observed that multiple recycling of powders has no effects on parts porosity. In their study, the porosity was measured by μ-computed tomography on small cylinders (diameter 6 mm, 11 mm height), and neither the distribution of pores nor the pores size was impacted.

On the contrary, Tang *et al.* [105] found that using Ti-6Al-4V powders for 21 recycling cycles and EBM manufacturing, the density lowered from 99.55% to 98.89%. These observations were measured using Archimedes' method.

From 12 recycling cycles of using Ti-6Al-4V in LPBF, Seyda *et al.* [106] found that the overall porosity is reduced (from 0.11% to 0.05%, measured by optical microscope) but pores size were larger.

On the contrary, using 316L powder for 15 cycles [107] and INVAR36 with fresh and one-year old powder [13], both studies found that the density decreased with aged powders.

Using fresh and moisturized Al-Si10-Mg powders, Riener *et al.* [96] shown an important impact of humidity on the manufactured parts density. Hence, moisture pick-up during the recycling process should be prevented for this alloy.

Findings seem contradictory between studies using the same material and processes, as in [104] and [105]. The different measurement techniques may be the reasons for the discrepancy in the observed results.

Regarding the other studies, it cannot be told whether the density variation results are material-dependent, or also recycling-process-dependent, since not all processes conditions were strictly similar.

2.1.3.1.2. Tensile test results

Regarding stainless steel materials, Jacob *et al.* [94] observed no variations of the mechanical properties of

17-4PH material after 11 cycles and Delacroix *et al.*. [107] observations were similar after 15 cycles with 316L.

Weiss *et al.* [108] could not conclude of the influence of recycling after 10 cycles on the mechanical properties of Al-Si10-Mg material although Del Re *et al.* [110] (after 9 cycles) and Fiegl *et al.* [109] (with long-term reused powder) observed lowered mechanical resistances. Riener *et al.* [96] found that samples made from moisturized powders have low mechanical resistances compared to samples from virgin and dried powders.

Del Re *et al.* [110] estimated that recycling had no major impact on Al-Si10-Mg samples ductility after 9 cycles. For Ti-6Al-4V, Quintana *et al.* [115] observed no significant impact of recycling on ductility, even though they concluded that the mechanical resistances increased with powder reuse (up to 31 cycles).

Overall, it is not clear whether the material strength diminishes in the case of Al-Si10-Mg, but it seems that there are no variations in the case of stainless steels (316L and 17-4PH) and Ti-6Al-4V mechanical strengths seem to enhance with increasing number of recycling cycles.

2.1.3.1.3. Fatigue test results

Del Re *et al.* [110] also studied the fatigue resistance of Al-Si10-Mg samples after 9 cycles and concluded that the fatigue resistance strength decreased by 10%.

For Ti-6Al-4V samples EBM-manufactured, Popov *et al.* [112] noticed that the fatigue resistance was better using fresh powder than 69-times recycled powders.

On the contrary, Carrion *et al.* [111] found that the Ti-6Al-4V fatigue results were better for samples made of used powders (the number of cycles cannot be identified) than those made of fresh powder. Considering also as-built conditions, no differences were observed between samples made of used and fresh powders.

Regarding the impact of recycling on the fatigue resistance, more studies are needed to draw general conclusions.

2.1.3.1.4. Parts oxidation

Popov *et al.* [112] measured an increase of oxygen content in Ti-6Al-4V EBM-manufactured parts from 0.116% to 0.336% after 69 cycles. The measures were done by «combustion test» which is assumed to be Inert Gas Fusion method (IGF) [113]. It is worth noting that these values are higher than Ti-6Al-4V grade 5 [140].

Carrion *et al.* [111] also used IGF to measure the oxygen contents of Ti-6Al-4V ELI LPBF-manufactured and noticed an increase from 0.10% to 0.12%. The limit for this material is 0.13% [139].

O'leary *et al.* [114] LPBF-manufactured small cubes and measured the oxygen of both the powder and the samples (Ti-6Al-4V grade 23) and noticed that while the powder remained below the 0.13% limit through the five cycles, the samples were above this limit since the first cycle.

On the contrary, Quintana *et al.* [115] observed a rising oxygen content in the Ti-6Al-4V ELI powder (from 0.09% to 0.13% through 31 cycles) but did not observe any correlation between the number of cycles and the oxygen content of parts (from 0.11% to 0.13%). The authors measured the oxygen content with IGF method.

It seems that oxidation is a major issue regarding the recycling of Ti-6Al-4V considering the standards. The processed material has to respect the industrial standards, otherwise the manufacturing process is considered flawed and the loss can reveal costly for the user.

2.1.3.2. Recycling process influence on powder properties

2.1.3.2.1. Powder particles size

For 17-4PH material, although Jacob *et al.* [94] did not observe variations of particles size, Slotwinski *et al.* [116]

concluded that particles agglomerate, and the general trend of the PSD was toward the right (hence, a rise in the global particle size). Recycling 15 times the 316L powder material, Delacroix *et al.* [107] found an increase of the PSD.

The same observations were made for these materials:

- Al-Si10-Mg [108][110];
- IN718 [100][102];
- Ti6Al4V [106][114].

2.1.3.2.2. Powder flowability

Processing IN718 material with the Direct Metal Laser Deposition process (DMLD, a metal AM process using powders), Carroll *et al.* [117] noticed a better flowability of powders after recycling, using Hall Flow measurements.

Jacob *et al.* [94] had similar observations for 17-4PH, measuring the flowability with Hall Flow Funnel and Hausner Ratio methods.

From visual analysis, Seyda *et al.* [106] also observed a better flowability of Ti-6Al-4V powders. It was validated by Carrion *et al.* [111], measuring the flowability with a powder rheometer and concluding a better flowability of recycled powders.

According to Seyda *et al.* [106], since there are fewer fine particles after recycling, there may be a simultaneous reduction of adhesion and friction between particles.

2.1.3.2.3. Powder oxidation

Recycling 316L powder material for 15 cycles, Delacroix *et al.* [107] noted an increase in powder oxygen content. Gruber *et al.* [149], had similar observations with EBM IN718 powders.

Mellin *et al.* [118] noted that Hastelloy X fresh and recycled powders were contaminated with oxygen on particles surface.

In the case of Ti-6Al-4V, LPW study case [119] noted an oxygen rise of 200ppm after 10 cycles, Quintana *et al.* [115] measured an elevation of oxygen from 0.10% to 0.13% of grade 23 (0.13% is the limit). The authors explain that it may be due to the presence of spatter particles. Sun *et al.* [120] observed such a rise in oxygen content of powders after 30 cycles of EBM processes and recycling that it was above the grade 5 limit (0.20%).

Regarding Al-Si10-Mg, Maamoun *et al.* [121] concluded that almost the same oxygen content can be found in fresh and 18-times recycled powders. On the contrary, Cordova *et al.* [131] observed that the oxygen content doubled after 6 cycles. Weiss *et al.* [108] recycled the Al-Si10-Mg powder 10 times and noticed a small increase of oxygen content from 850 ppm to 900 ppm.

Raza *et al.* [155] used the Al-Si10-Mg powder for 30 months led to an increase of oxygen content from 500 ppm to 1 250 ppm. The oxide layer thickness grew from 4 nm to 38 nm.

According to Riener *et al.* [96], which compared moisturized, dried and fresh powders, the humidity has a strong impact on powders oxygen content (from 692 ppm to 759 ppm in their case). It is possible that the humidity measured on the powder particles may evaporate during the process due to the vacuum process, or from the build plate heating. However, since this evaporation is not certain, the humidity must be removed in the recycling processes.

Variations of powder size, flowability and oxidation with recycling do not look material-dependent. It seems that with reuse, the small particles are removed (potentially in the chamber atmosphere, during the powder handling, or agglomerating one to the others), and the largest particles tend to be larger.

The sieving process is then mandatory to remove too large particles. Since the powder coarsens, it appears that the flowability enhances. It can be due to less interactions (reduction of adhesion and friction [106]) of small particles.

Finally, all powders seem to oxidise while being recycled. This aspect is an important issue, since some recycled powders (and manufactured parts) chemistry may not comply with the standards.

2.1.3.3. Powder properties affecting the part quality

2.1.3.3.1. Powders influence on parts density

In their review, Vock *et al.* [95] link powder properties with the part's, revealing the complex connections between the powder at different state (from particle state to the powder bed state) and the process parameters resulting in different part quality. The illustration of these connections is shown in Figure 2.17.

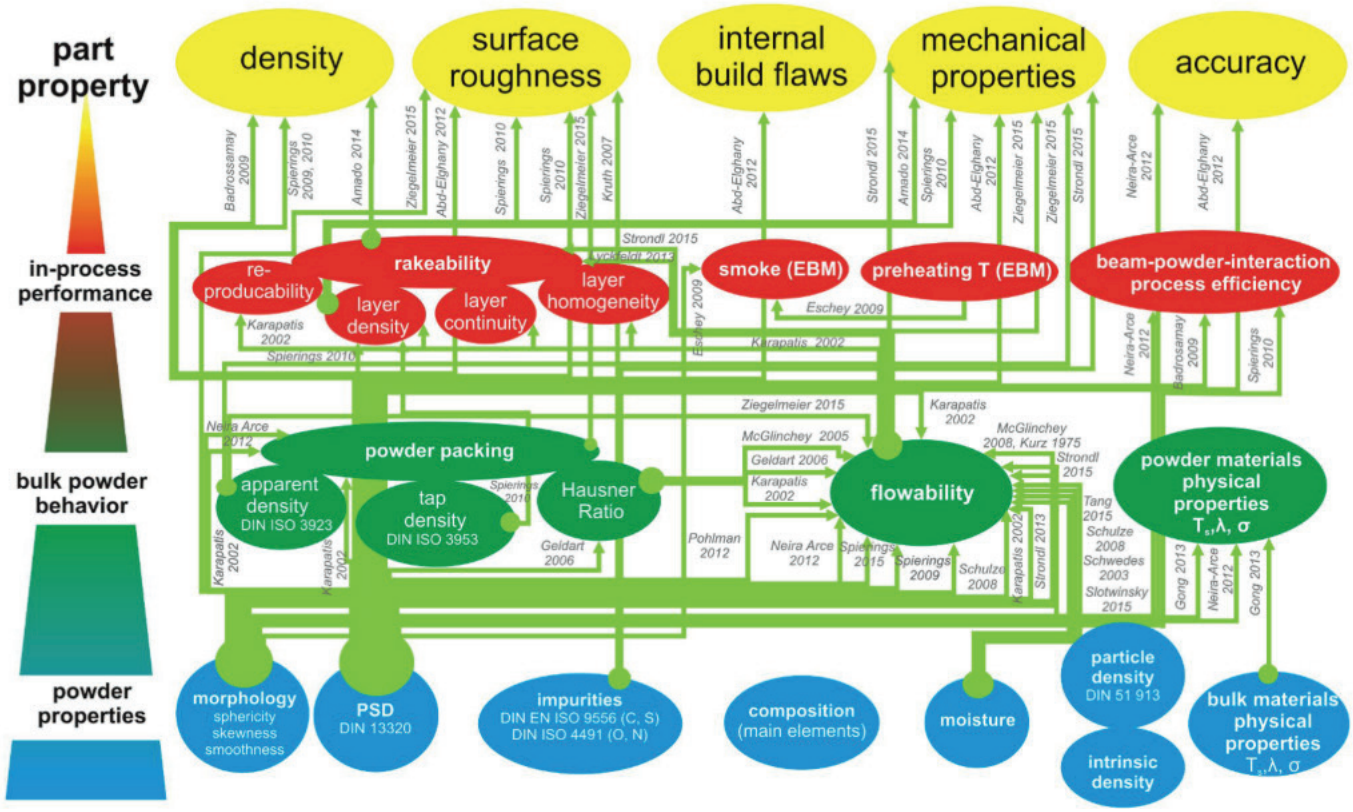

Figure 2.17: Connections between powder properties at different states, process parameters and part quality [95].

Using three different 316L powders, Spierings and Levy [123] noticed that using the same process parameters do not result in sufficiently dense parts. However, tuning the laser parameters (from the energy density point of view, Equation (2.2)), they managed to achieve densities higher than 99%.

$$E_d = \frac{P_{laser}}{v_{scan} \,.\, d_{hatch} \,.\, t_{layer}} \tag{2.2}$$

From Equation (2.2), P_{laser} is the laser power (W), v_{scan} the scan speed (mm/s), d_{hatch} the hatch distance between two consecutive vectors (mm) and t_{layer} the layer thickness (mm). However, in their study, Prashanth *et al.* [122] showed that the energy density parameter cannot be used directly to validate a process parameters configuration but should be used as an estimation tool.

In a similar approach to Spierings and Levy [123], Gu *et al.* [124] used three powders (of Ti-6Al-4V material in this case) and observed that using the process parameters set, significant porosity levels were obtained. However, when varying the process parameters for each powder, nearly-dense parts were feasible.

The authors also noted that for tuned process parameters and identical process parameters, the resulting ultimate tensile strength and the yield strength were similar.

Hence, the powder has a strong impact on the parts density, but these properties must be coupled with process parameters since different powders may yield similar results by tuning the scanning parameters.

However, it is assumed that most powders considered in these studies were suitable for the LPBF process. Indeed, according to Gong *et al.* [64] and Tammas-Williams *et al.* [65], internal porosities within the powder particles can be retrieved in the manufactured parts since the porosities cannot escape the fast-solidifying melt pool.

2.1.3.3.2. Powders influence on parts oxidation and dissimilarities

Comparing three different AlSi7Mg powders, Muñiz-Lerma *et al.* [125] found that the absence of fine particles limits the water adsorption, and may limit the parts contamination.

Small particles have a higher surface to volume ratio than larger particles [68]. Hence at constant oxide layers thicknesses (few nanometres thick) there would be more impact on these smaller particles since there are relatively more contaminant elements compared with the metal elements.

Although O'leary *et al.* [114] validated the powders chemistry as complying with Ti-6Al-4V ELI standard, the resulting parts had too high oxygen contents.

Similarly, when Tang *et al.* [105] measured the oxygen levels of the Ti-6Al-4V parts and powders, both oxygen contents increased, but not in the exact same quantities, although the measuring method was identical (IGF).

Hence, apart from the powder oxygen content and the number of fine particles which may carry relatively more oxygen than larger particles, there does not seem to be powder characteristics that lead to part's oxidation.

However, it seems that validating Ti-6Al-4V powders as compliant with grade 23 standard, one should be aware that the resulting part chemistry may be flawed. Hence, the most relevant practice seems to be:

- First, thoroughly validating the part's chemistry (in terms of contaminant contents);
- Then, if possible, since the measures is expensive, validate the chemistry of the recycled powders.

2.1.3.4. Oxygen influence on part quality

Dietrich *et al.* [87] inspected the ability to manufactured aluminium powders suitable for the LPBF process, and mentioned that both oxygen and hydrogen has a strong negative impact on density with these materials.

Some more results are available for oxygen's influence on Ti-6Al-4V. Oxygen doesn't seem to influence parts density or toughness [126], however:

- Parts tensile strengths rise [87][126];
- Parts elongation decrease [87][126];
- Vickers hardness rises [87];
- Parts fatigue strengths decrease [126].

The mechanical properties of Ti-6Al-4V with different oxygen levels have been studied in the literature and it seems that the overall characteristics are enhanced when the oxygen content increases. However, the elonga-

tion and the fatigue strength decrease, representing a great risk.

The elongation of Ti-6Al-4V has minimum standard value that the final material should comply with, and the fatigue strength should be considered regarding the final application requirements.

2.1.3.5. Summary

The recycling process influences both the part and powder properties. Major part characteristics (density and mechanical properties) seem to be influenced, however, depending on the studied material, some results seem contradictory. Also, regarding the fatigue characterisation, more studies are needed to draw general conclusions.

On the contrary, powder variations with recycling seem to be more homogeneous in the material perspective. It was also demonstrated that powder property variations had an impact on part characteristics. Hence, the powder variations from recycling need to be limited to prevent major variations on parts quality.

Also, it was found that the link between powder and part oxidation was not clear: when the powder is oxidised, the oxygen content of the part also rises but not necessarily in the same proportions. Hence, thorough validation of the part oxygen content should be performed for Ti-6Al-4V material at least (since it was demonstrated that this material may exceed the standard oxygen values).

The oxidation mechanisms will be presented in the following section for two reactive materials commonly used with LPBF process: Al-Si10-Mg, and Ti-6Al-4V.

2.1.4. Materials used and specific oxidation mechanisms

2.1.4.1. Materials used in this study

2.1.4.1.1. Al-Si10-Mg material

Al-Si10-Mg (also known as A360.0) is an age-hardening cast aluminium alloy [127]. Aluminium-silicon alloys have the eutectic point at 12.6% [128] and are divided in three groups, depending on the silicon content: hypoeutectic (<12% Si), eutectic (12-13% Si) and hypereutectic (14-25% Si) [129]. Al-Si phase diagram is shown in Figure 2.18.

Because the Si content is close to the eutectic point, the solidification range of the alloy is small (the liquidus is close to the solidus) making the material suitable for LPBF process [127].

These alloys are widely used in the automotive industry [129], aerospace and conventional manufacturing industries [127]. They have an excellent machinability, good thermal and electrical conductions and have a low density [129]. They also have a good weldability and an excellent corrosion resistance [127].

Compared to other common materials used in the LPBF process, they have a relatively low cost [127][130]. The magnesium content enabling the precipitation of Mg_2Si provides significantly better mechanical characteristics [127]-[129].

Al-Si alloys have a high affinity with oxygen, generating an oxide layer on the melt pool surface [127][131].

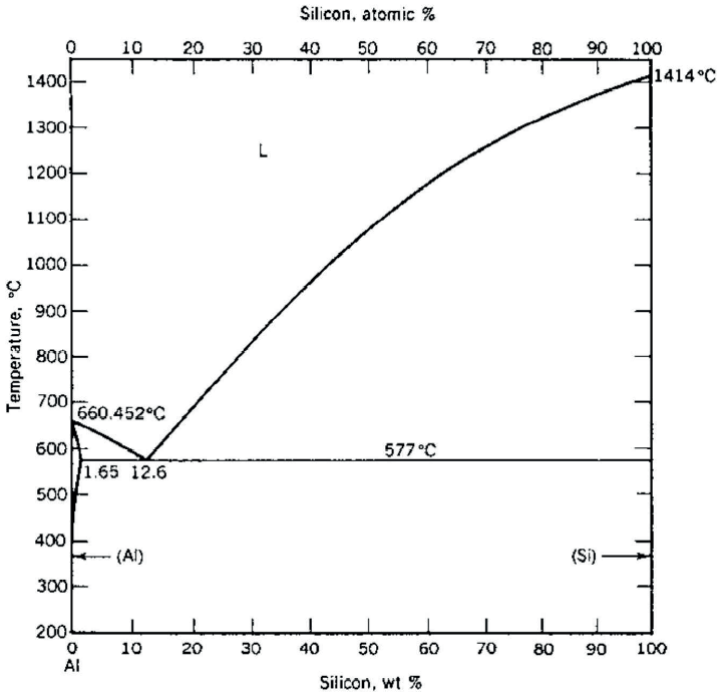

Figure 2.18 : Al-Si phase diagram [128].

2.1.4.1.2. Ti-6Al-4V material

Amongst the most abundant metal element on earth, titanium ranks fourth behind aluminium, iron and magnesium [132]. Pure titanium has two distinct phases separated by the allotropic transformation occurring at the temperature known as Transus β, at 882 °C [133]:

- α-phase (lower temperatures), a hexagonal pseudo-compact phase structure.
- β-phase (higher temperatures), a centred cubic phase structure, stable up to the melting temperature.

Due to its TiO_2 passivation film, titanium and its alloys have a better corrosion resistance than stainless steels' [132]. However, above 600 °C, oxygen diffusion through the film is too fast and the oxide layer becomes excessively large [6]. Hence, titanium alloys applications are usually limited to temperature ranges below 550 °C.

Commercially pure (CP) titanium grades are mostly used in applications where high strength levels are not mandatory [132]. Alloying elements are then used to enhance pure titanium properties [134].

Since these alloying elements vary the Transus β temperature, they are classified as follow: α-genes (i.e., Al, O, N, C), β-genes and neutral. α-genes elements lead to the formation of a α+ β domain. Lower oxygen and nitrogen concentrations lead to better ductility, a better corrosion resistance and an increased toughness according to [135]. Also, according to [136], aluminium and vanadium prevent the effects of oxygen on mechanical properties, compared to pure titanium.

Ti-6Al-4V (or TA6V) is the most widely used titanium alloy, especially for spatial, automotive, and chirurgical applications [135]. Titanium is part of the bioinert elements [137] due to its non-toxic chemistry [133].

Ti-6Al-4V has a α+β microstructure and its aluminium content stabilizes the α phase [134]. ASTM B265-20a [138] provides chemical compositions of Ti-6Al-4V grade 5 and grade 23 (also called Extra Low Interstitial elements, ELI). These alloys differ from the maximum oxygen content (1300 ppm for grade 23, 2000 ppm for grade 5). ASTM F3001 [139] specifies the requirements for grade 23 produced by additive manufacturing (AM) techniques. Table 2.3 lists the elements ranges for both grade 23 and grade 5 alloys in AM [139][140].

Titanium has a high affinity with oxygen, the resulting oxidation product being TiO_2 [132]. Oxygen solubility

within titanium is large compared to other elements, for which most of the oxygen content is located on the oxide layer and not in the metal. On the contrary, titanium α phase may contain a large number of oxygen [134]. According to [132], oxygen solid solubility in titanium rises to 14.5%.

Table 2.3: Ti-6Al-4V grade 5 and grade 23 element composition ranges according to ASTM standards [139] [140].

	C	Fe	N	O	Al	V	H	Other (each)	Other (total)	Ti
Min Gr. 5 & 23					5.5	3.5				Base
Max Gr 5	0.1	0.3	0.05	0.2	6.75	4.5	0.015	0.10	0.40	Base
Max Gr 23	0.08	0.25	0.05	0.13	6.5	4.5	0.012	0.10	0.40	Base

2.1.4.2. Oxidation mechanisms

2.1.4.2.1. Metal oxidation and oxidation kinetics

Oxidation phenomenon discussed here relates to dry corrosion phenomenon: two electrochemical reactions, i.e., oxidation of the metal and reduction of the corrosion agent [142].

The oxidation mechanism is split in two different steps: the oxygen diffusion within the metal, and the formation of the oxide layer [141]. The formation of the oxide layer begins with oxide patches on the surface of the metal. These oxide islands expand laterally and form a thin oxide layer on the surface of the metal [134]. As the oxide layer grows, an oxygen-rich layer, called α-case, forms within the base metal [132].

Generally, the oxide layer formation follows these steps [143]:

1. Oxygen chemical adsorption;
2. Oxide germination;
3. Surface oxide growth;
4. In-depth oxide growth.

The last step takes place by diffusion of ions and electrons through the oxide layer towards the metal. Overall, the oxidation process reflects the loss of electrons by the metal or the oxide formation resulting from the reaction of the metal and the surrounding oxygen [134].

In the case of titanium material, the underlying metal is considered to be at the equilibrium with the oxide layer (of tetragonal rutile crystal structure [132]) above [134].

Several parameters influence the oxide layer formation and oxygen dissolution within the metal: i.e., the temperature, the alloy chemical composition, the microstructure and the partial pressure of oxidising gas. Other secondary parameters are also in play regarding the oxidation mechanisms [134].

In the case of Ti-Al alloys, since aluminium forms a dense and thermally stable α-Al_2O_3 oxide, it lowers the diffusion rates, and the resulting scale is made of TiO_2 (not stable at high temperatures) and Al_2O_3 underneath the TiO_2 rutile surface oxide layer [132][134].

Assuming the dissolve oxygen content within the metal is negligible (not verified for all metals), the oxidation kinetics of a metal consists in the temporal evolution of its oxide layer thickness [134].

For titanium, since the solubility of oxygen within the metal is high, there are two simultaneous behaviours: the oxide layer's growth and the diffusion within the metal.

Several mathematical relations were proposed to adjust experimental kinetic oxidation: Casadebaigt *et al.* [141] identified the oxidation kinetics for the bulk LPBF Ti-6Al-4V metal (Equation (2.3)).

$$\frac{\Delta W}{A} = \sqrt{k_p\, t} \tag{2.3}$$

$$k_p = k_p^0 \exp\left(-\frac{E_a}{RT}\right) \tag{2.4}$$

with ΔW the weight gain, A the surface area, t is time, k_p is the parabolic rate constant following an Arrhenius law defined in Equation (2.4) [141][144]. E_a is the activation energy, R the gas constant, T the reaction temperature and k_p^0 a constant. It is worth noting that the weight gain of bulk titanium in Equation (2.3) is proportional to the square root of time.

The oxide layer growth depends on the oxygen diffusion within the oxide layer [145], and when the temperature rises, the elements diffusion rise [134].

To compare the oxides relative stability of titanium and aluminium metals, one can use the Ellingham diagram [142]. These diagrams consider the equilibrium temperature between a metal, its oxide and oxygen. The reaction is thermodynamic and depends on the sign of the standard free enthalpy $\Delta_r G_T^\circ$.

Ellingham diagrams show the evolution of the standard free enthalpy of oxidation reaction of pure metals [142]. The considered reaction in place uses one mole of oxidising agent, as:

$$\frac{2m}{x} M + [X_2] \rightleftharpoons \frac{2}{x} M_m\, X_x \tag{2.5}$$

The standard free enthalpy $\Delta_r G_T^\circ$ at temperature T is expressed as:

$$\Delta_r G_T^\circ = \Delta_r H_T^\circ - T\, \Delta_r S_T^\circ \tag{2.6}$$

with $\Delta_r H_T^\circ$ the standard enthalpy of the oxidation reaction, and $\Delta_r S_T^\circ$ the standard entropy of the reaction. To draw the Ellingham curves, the standard enthalpy and entropy variation with temperature are neglected (Ellingham approximation) [142], hence the Ellingham curves are straight lines expressed as:

$$\Delta_r G_T^\circ = \Delta_r H_{298}^\circ - T\, \Delta_r S_{298}^\circ \tag{2.7}$$

Slope changes in the Ellingham diagram represent a change in the physical state. In abscissa axis is shown the temperature and in ordinates $\Delta_r G_T^\circ$ values. The stability of metal oxides reduces with temperatures rise since the lower the position on the diagram, the more stable is the oxide.

According to Cordova [146], from the Ellingham diagram, Al-Si10-Mg may contain MgO, Al_2O_3 and SiO_2 oxides (ordered from the most to the least thermodynamically stable).

From the diagram displayed in Figure 2.19, it can be seen that titanium and aluminium oxides are close in terms of stability, hence these two metals can be considered close regarding their affinity with oxygen.

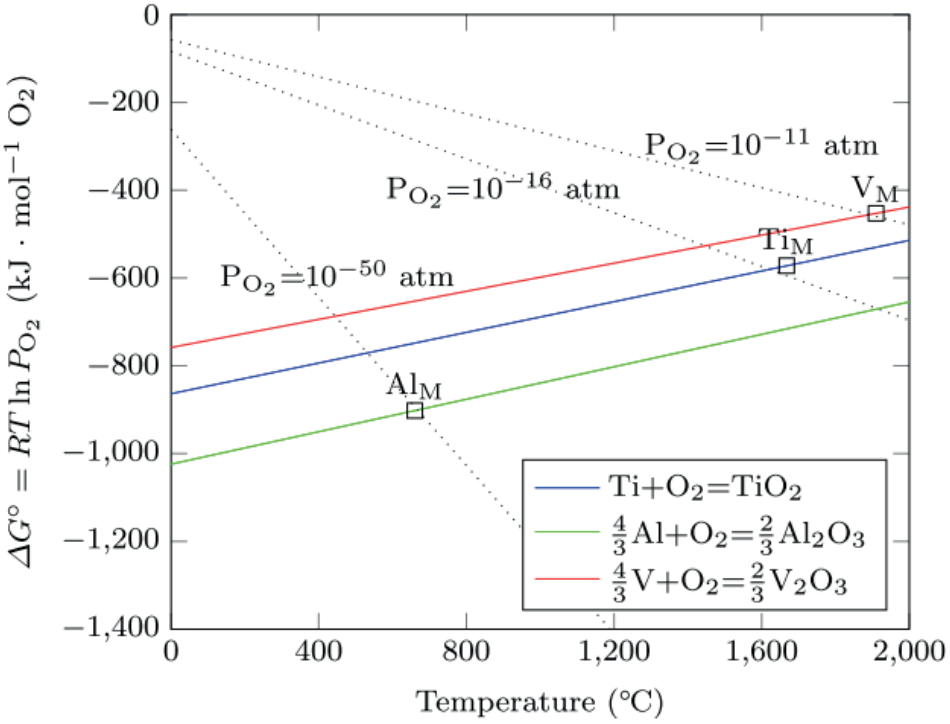

Figure 2.19 : Ti-6Al-4V-adapted Ellingham diagram from [148].

It can be concluded that time, temperature, surrounding oxygen content (and for titanium, diffused oxygen content) have major impacts on the oxidation kinetics of a metal. Titanium and aluminium seem to have close affinity with oxygen since their oxides are close in stability in Ellingham diagrams.

2.1.4.2.2. LPBF oxidation sources

Derimow & Hrabe [148] mentioned that powder oxidation may be attributed to numerous factors outside the manufacturing system (powder handling, exposure to atmosphere, humidity) and within the manufacturing system (background temperature, proximity to melted parts and build chamber atmospheres) and that «a critical understanding of key factors influencing oxidation and oxidation rate is needed» [148].

Powder particles oxide layer and ambient humidity

Regarding the LPBF process, there are several sources of oxygen (ambient moisture, remaining humidity in the chamber) and several sources of heat (build plate heating, laser beam, surrounding heated parts, falling spatters). These components seem to drive the material oxidation process.

Tarabay *et al.* [147] showed that larger powder particles are less sensitive to oxygen than smaller particles. The greater sensitivity with oxygen from smaller powder particles may be explained by their larger specific surface.

Casadebaigt [134] showed that the powder particles suffer different oxidation kinetics (first parabolic, the oxidation kinetics increase when the particles break, and finally they decrease as there are less non-oxidized metal surface) than the raw material (parabolic only).

For Gruber *et al.* [149], the oxidation is caused by the oxygen present in the chamber atmosphere and the assimilation of oxides and hydroxides. Li *et al* [14] showed that the powder particles have a moisture layer on their surface that can be efficiently reduced by drying.

These factors are closely related to humidity and already present and growing oxide layer on the powder particle surface. It is necessary to understand the extent of humidity impact on the oxidation process of LPBF powders.

Spatters formation, size and distribution

Simonelli *et al.* [150] found that spatters comprised a large number of oxides (material dependent) and assumed that these spatters were oxidized while ejected in the chamber atmosphere. Gasper *et al* [152] assumed the oxidation of spatters of IN718 (a nickel-based superalloy) may come from the already oxidized melt pool surface, at the origin of the spatters. In another study on Hastelloy X, Gasper *et al* [153] estimated that spatters may absorb oxygen while flying in the chamber atmosphere.

Also, with Hastelloy X, Schwerz *et al.* [154] investigated spatters redeposition and found that they had a bimodal size distribution with modes at 30 and 90 µm. In the case of Al-Si10-Mg, Lutter-Günther *et al.* [151] showed that these spatters were a lot more oxidized than the powder particles (2 110 ppm of oxygen compared to 870 ppm), and that the spatter size was between 20 and 120 µm. Gasper *et al.* [152] found spatters of size comprised between 28 and 86 µm for IN718 material and estimated that almost 50% of the spatters were comprised in the Particle Size Distribution (PSD) of their powder.

Hence, some spatters may go through the sieving mesh (usually between 60 and 100 µm) and be scanned in the next manufacturing processes.

Using a large quantity of Al-Si10-Mg during 30 months, Raza *et al.* [155] observed a significant increase in spatters content of aged powders. Also, the measured oxygen content rose from 500 ppm to 1 250 ppm. Since the spatters cannot be separated from the powder particles, the rise of oxygen content may be partly explained by the spatter presence, as Lutter-Günther *et al.* [151].

Gasper *et al* [152] identified seven types of spatters and threes spatter formation mechanisms: melt-ejection, hot-entrained and cold-ejection. The schematic representation of these mechanisms is displayed in Figure 2.20. A similar mechanism as hot-entrained spatters identified by [152] was found by Leung *et al.* [12]. In this study, it is observed that powder particles passing through the laser beam agglomerate and form a spatter particle.

Also, according to [156], increasing the laser energy would lead to larger recoil pressure and more spattering phenomena. From the same study, other parameters such as the beam diameter, the number of lasers used, the powder material, the chamber pressure, the scanning patterns and the type of inert gas may lead to spatter generation. A schematic representation of melt-pool-generated spatters is shown in Figure 2.20.

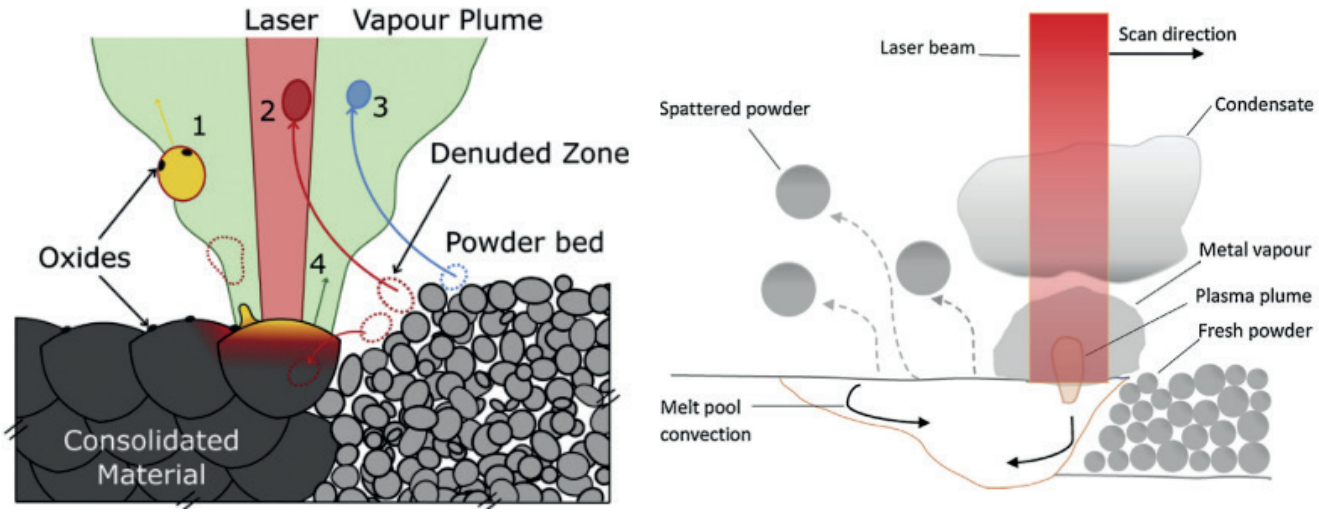

(a) Melt-ejection (1), hot-entrained (2), cold-ejection (3) spatter formation mechanisms [152].

(b) Melt-pool ejection spatters [156].

Figure 2.20: Schematic representation of spatter formation mechanisms.

According to [157], Al-12Si powder generates less spatters than 316L (stainless steel material), due to the significantly larger thermal conductivity of aluminium compared to the steel thermal conductivity. Hence, they

assumed that the 316L powder melts, evaporates and the vapor pressure on the melt pool leads to spatters generation.

This assumption agrees with Leung *et al.* [12] observations where scanning under overhang conditions yield more spatters as compared with conditions using an underlying solid material. Hence, the ability to conduct heat away from the melt pool area may help reducing the number of generated spatters.

To diminish the spattering phenomenon, Khairallah *et al.* [158] proposed and simulated with promising results the impact of a pre-sintering process before scanning, as in the electron beam melting (EBM) process, another AM metal powder bed fusion process.

Anwar *et al.* [159] quantified the spatter distribution in the case of Al-Si10-Mg and observed that larger spatters fall near the part while smaller may fall far from the part. The majority of the spatters landed near the part, following the gas flow direction.

Chien *et al.* [160] had similar conclusions: the overall landing site was 10 to 20 cm long from the part following the gas flow direction, but the majority of largest spatters felt in the first 25 mm. In terms of spatter volume, a large share of the spatters falls within the first 50 mm.

Schwerz *et al.* [154] observed that the stripe direction influences the spatters orientation, considering the gas flow direction. They also found that the layer thickness has an impact on the quantity of generated spatters and their distribution.

The gas flow seems to have an important impact by removing the spatters from the build plate surface [161] and the resulting atmosphere purity inside the chamber influences the oxidation of the spatter particles [162].

In conclusion, it seems that the spatters are a type of particles generated during the LPBF process, and which may be highly oxidised. These particles have a large particle size distribution, and for a significant share of them, is comprised within the actual powder PSD.

There are numerous identified mechanisms of spatter generation, and several process parameters seem to influence their generation and distribution, including the gas flow and the energy provided by the laser source.

Considering oxidation results obtained by Gasper *et al.* [152] and Schwerz *et al.* [154], discussed in Section 2.1.4.2.2, it is assumed that remaining spatters may lead to overly oxidised powders in average.

Hence, since their size is comprised within the powder's PSD, these spatter particles may be found in subsequent production: highly oxidised particles among powder particles of high quality (melted all the same during the process), and generate defects.

There may be efficient ways to limit the spatter generation, as the one proposed by Khairallah *et al.* [158], but it is first required to verify that these spatters are a main contributor of the overall oxidation observed while using aged LPBF powders.

2.1.4.3. Summary

Two common reactive materials and oxidation mechanisms were presented. It appears that Ti-6Al-4V oxidation happens following two mechanisms: diffusion of oxygen within the base metal and oxide layer growth. It was found that the oxidation of LPBF-manufactured Ti-6Al-4V was similar to conventional Ti-6Al-4V. However, the powders seem to have different oxidation kinetics than the bulk material.

From the presented oxidation mechanisms, it appears that oxygen sources, temperatures and time play a significant role in the oxidation kinetics. These were linked with the LPBF process: ambient atmosphere (and at a lesser degree, the quasi-inert machine atmosphere), and the humidity on powder particles represent oxidation sources. Build plate heating and laser scanning rise the temperature of the powder particles, especially, melt pool ejecta (and overall spatters) may be particularly oxidized.

The studied spatter formation and distribution were also discussed in this section, and it appears that most spatters fall near the scanned parts (first 25-50 mm).

In the following study, the role of the temperatures in the oxidation of powders will be investigated. The objective is to identify whether the oxidation occurs during the manufacturing process or during the recycling process.

Such identification can help understand the most influencing factors in the oxidation of powder particles and help reduce their ageing for extending their use life.

2.2. Identifying key oxidation factors

From the literature review section, the time, oxygen and heat, coupled together, were identified as main contributors of the oxidation phenomenon.

In the LPBF process, the oxygen sources are:

- The ambient atmosphere humidity, during powder handling and storing;
- The residual oxygen in the quasi-inert chamber atmosphere (from few to hundreds of ppm);
- The humidity present on the particles surface (from condensation).

The heat sources are:

- The build plate (up to few hundreds of degrees Celsius);
- The high-power laser heat source.

The objective of this section is to identify the influence of the heat factor on the oxygen level increase. Powders were handled and sieved similarly; however, the thermal history was very different from a procedure to the next.

Regarding the observations from the literature, we have considered that the oxygen pick-up measurements need to be operated on bulk specimens instead of powder specimens.

Solid specimens were chosen because it is almost impossible to manipulate powders from build chamber to the vacuum of the microscope without exposition to oxygen. Indeed, some studies found a discrepancy of oxygen content from the powder to the part which cannot be explained and anticipated.

Reactive materials are necessary for this experiment. Indeed, the objective is to observe changes in oxygen pick-up evolution. If the material studied were not sensible enough to oxygen, the oxygen pick-up may not be observed.

From the literature, aluminium and titanium are both very sensitive to oxygen and are close in terms of oxide stability. Hence, it is assumed that conclusions drawn in our test for one material may be similar to other. Because titanium alloys are very expensive, and considering that a full tank of material was to be wasted, we have chosen aluminium powders.

2.2.1. Material and methods

2.2.1.1. Material, machine and process conditions

The selected material for this study was Al-Si10-Mg. This material is commonly used with the LPBF process and its properties are ensured by the machine manufacturer under predefined manufacturing conditions [163].

The powder was bimodal with modes at 20 µm and 63 µm. The chemical composition from [163] can be found in Table 2.4. The powder used in this study was virgin. This state will be mentioned as «fresh powder» in the following.

Table 2.4: Al-Si10-Mg chemical composition provided by the machine manufacturer.

El.	Al	Si	Mg	Fe	N	O	Ti	Zn	Mn	Ni	Cu	Pb	Sn
wt.%.	Bal.	9-11	0.25-0.45	<0.25	<0.20	<0.20	<0.15	<0.10	<0.10	<0.05	<0.05	<0.02	<0.02

The machine used for this experiment was a Renishaw AM400 from the CEF3D research facility, shown in Figure 2.21(a). The machine is equipped with one 400 W laser of beam diameter 70 µm.

The manufacturing volume is of 230 mm * 230 mm * 285 mm. The gas flow comes from the right of the

build plate and crosses the build plate to be collected on the left side of the build chamber. Feeders are placed behind and in front of the build plate, enabling the powder in excess to fall down into two inert bottles. The build chamber is shown in Figure 2.21(b).

These bottles can be unclipped during the manufacturing process to retrieve the powder in excess, without interrupting the production. One bottle connected to a machine feeder is displayed in Figure 2.22(a).

A vacuum step before the manufacturing process removes the air within the build chamber, and argon gas is filled within the machine, until oxygen level is below 1 000 ppm.



(a) Machine.

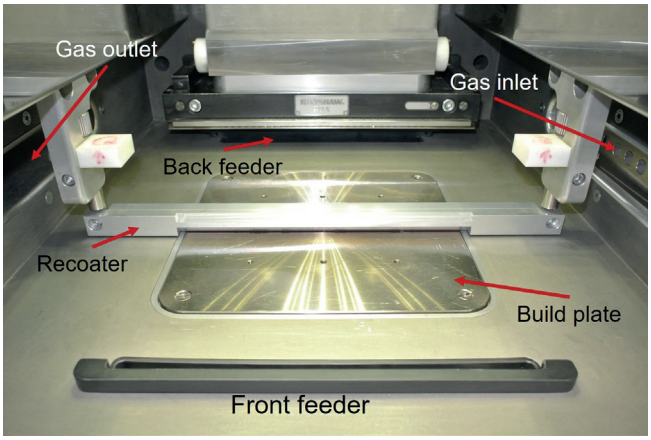

(b) Build chamber.

Figure 2.21: Renishaw AM 400 system.

The powder falls from a silo placed above the machine and is layered using a silicon recoating system. The powder volume in the silo (33kg of Al-Si10-Mg maximum) is not sufficient to fill the 285 mm height of powder within the build chamber. Hence, supplementary powders, and the powder in excess in the feeder bottles can be injected back in the silo.

At the end of the manufacturing process, the build plate is elevated at the initial level, and the user can push the remaining powder (under inert atmosphere) into the feeders and interact with the part through a glove access.

Then, the user can unclip the feeders' bottles which are now sealed: they do not interact with the ambient atmosphere. The bottles can be clipped to the sieving station and unsealed after filling with inert gas. Then the powder flows within the station, as in Figure 2.22(b). The sieve mesh is of 80 µm, to remove largest particles assumed to be spatters.

Another bottle is connected below the sieving station, receiving the recycled powder. Once filled, this bottle is used to fill the silo as in Figure 2.22(c).

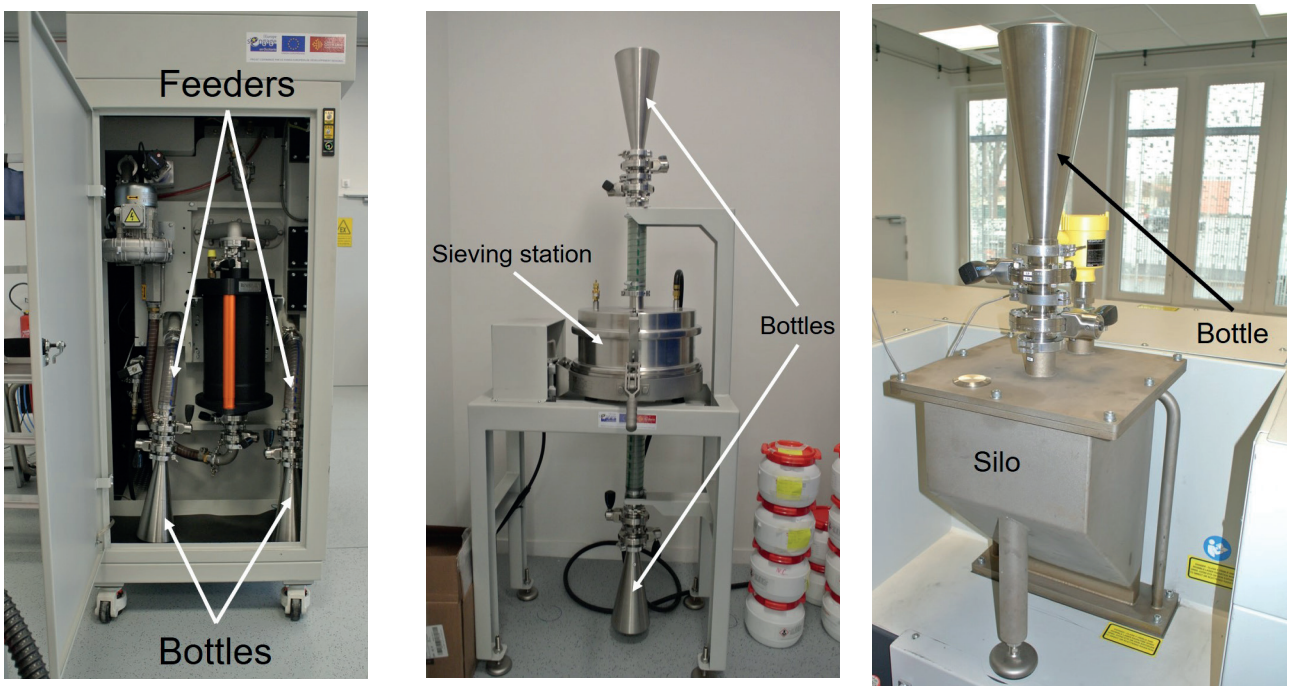

(a) Powder bottle connected to a feeder.

(b) Powder bottles connected to the sieving station.

(c) Powder bottle connected to the machine silo.

Figure 2.22: Powder handling systems connected to powder bottles.

Hence, using this system, the contact of powder with the ambient atmosphere should be limited, since the atmosphere in the machine and the sieving station is inert, and the powder handling is done with the use of sealed bottles that prevent at most contact with the atmosphere. However, it is not possible to prevent any contact with oxygen while opening/closing the bottles.

The files needed for the manufacturing process were prepared with Catia, Magics and QuantAM 5.1.0.84 software.

2.2.1.2. Design of experiment

As mentioned, two experiment scenarios will be launched in this study: one including both oxygen and heat sources, the other containing only the oxygen sources. Less heat will be injected in the system for the second experiment.

One constraint with the first experiment was to enable the heat of the maximum volume through the build plate heating and the laser scanning, but also, to recover the maximum number of powder which will be recycled and reused in subsequent steps.

Hence, we needed a geometry for this experiment that maximises the contact surface of scanned matter while using a minimum of unmelted powder volume for subsequent steps.

We chose to use a grid geometry with a cross-like pattern, and to enable similar scanning for all layers.

2.2.1.2.1. Samples and lattice geometries

After first trials, a geometry was validated for full production. The lattice is shown in Figure 2.23(a) and its pattern is shown in Figure 2.23(b). Each square cell within the lattice has its sides of 3.6 mm to enable the powder flow. The lattice had a small angle around the vertical direction to preserve the recoating system from any crash.

As it can be seen from Figure 2.23(b), the lattice is an open geometry, hence the mesh cannot prevent the powder from falling by the sides with the build plate elevation at the end of the production. The build plate is elevated to recover the surrounding powder, but the powder inside the lattice should be isolated. Hence, a protection wall has been added at the lattice border. The protection wall geometry is displayed in Figure 2.23(c).

The lattice height was of 285 mm, manufactured with 9 501 powder layers, and a duration of nearly 159 h.

As discussed, the oxygen measurement should be performed on bulk specimens. Hence, three small samples of size 20 mm * 20 mm * 10 mm were added in front of the lattice. The samples volume is minimal to get three oxygen values for each sample (samples are cut before measurement).

The samples were supported by numerous cone-supports, as displayed in Figure 2.24(a). Indeed, it was chosen to use support geometries since samples may be contaminated while being scanned directly on the build plate surface.

Also, it is commonly assumed that the residual oxygen in the chamber is mostly absorbed during the first scanned layers. Hence, supports heigh was set at 10 mm, assuming it would be enough to lower significantly the residual oxygen content within the chamber.

For every layer, the lattice geometry was scanned before the samples, and the samples were scanned from left to right. Scanning and supports parameters are listed in Appendix 6.1.

For every production, the residual powder in the machine (on the sides of the build plate, and on the walls) has been vacuumed, not to be used again.

Using these geometries for the experiment incorporating the heat factor, it was possible to scan a relatively small volume of powder distributed across the entire surface, while having a maximum exchange surface between the scanned regions and the powder.

In the experiment removing the heat factor, only the samples were present, not the lattice nor the exterior wall.

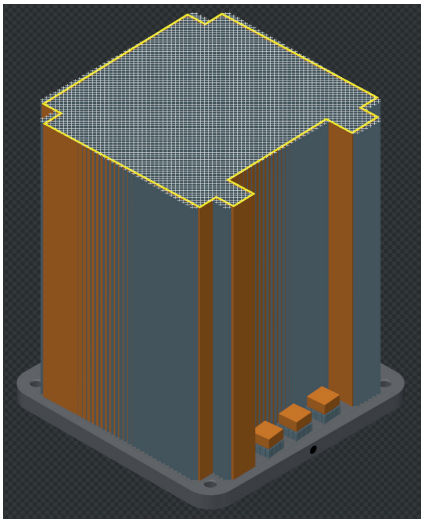

(a) Procedure 1 geometries (lattice and samples).

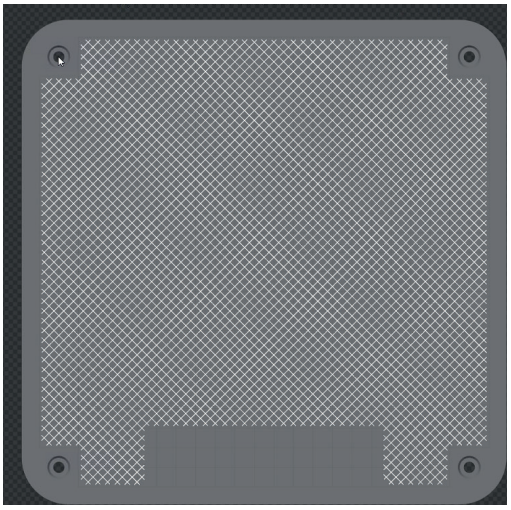

(b) Lattice pattern viewed from above.

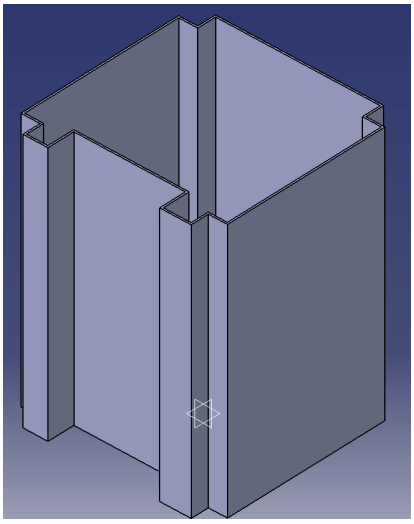

(c) Protection wall designed to prevent internal powder from falling by the sides.

Figure 2.23: Procedure 1 (recycling and heating) geometries: lattice and cubic samples (a), lattice pattern (b) viewed in QuantAM software, protection wall geometry (c).

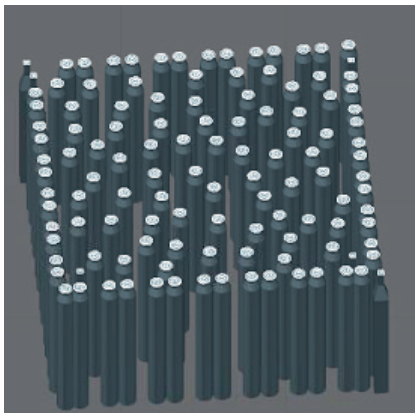

(a) Sample supports.

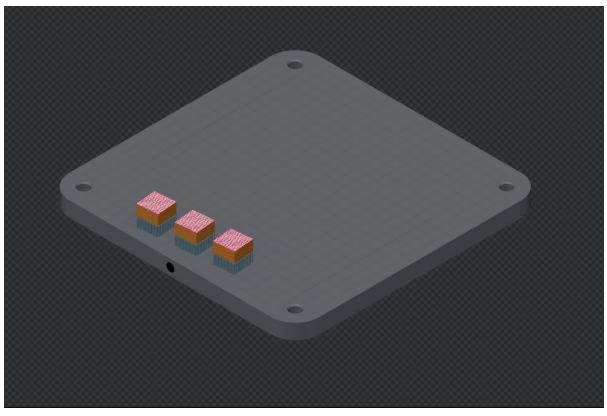

(b) Procedure 2 samples.

Figure 2.24: Procedure 2 (recycling only) sample supports and geometries.

2.2.1.2.2. Procedure 1: recycling and heating

As recommended by the machine manufacturer for Al-Si10-Mg material, the build plate was heated at its maximum temperature value of 170 °C.

For the first production of this procedure, to enable the entire lattice fabrication, fresh powder was added during the manufacturing process without interrupting the machine. Hence, 37 kg of powder were used in the first production.

For the other productions, the powder from the feeders was recovered, and placed back in the silo during the manufacturing process without interruption and without sieving. It was considered that the powder in the feeders came from the powder in excess while layering.

Hence, it is assumed that the powder had not been exposed to the heat of the build plate or the laser. Since it had not been exposed to heat, and it had not been sieved before being reinjected, this powder was considered as «same-state» powder as the powder remaining in the silo.

For the first production, after extracting the build plate, the powder in the chamber, and the powder in the feeders (both for sieving), the powder in the silo was extracted and put aside. This powder was fresh powder that would not be used again in this study.

After the first production, it was difficult to retrieve the powder from the lattice: it was stuck and would not flow easily. For the next productions, small teeth were added below the lattice structure to help the air insert itself and make the powder flow.

For the next productions, n°2 to n°5, there was not enough powder to manufacture the entire lattice. Indeed, after each production, less powder remained for the next production owing to the lattice manufacturing. Hence, these productions were stopped when there was no more powder in the silo and in the feeder: all the powder was located in the build volume.

For all productions, the subsequent recycling steps were similar: the powder to be reused (from the build volume and the feeders in Production 1, from the entire machine for the others) was connected to the sieving station. The powder in contact with the atmosphere was limited at most since the bottles are sealed when unconnected.

Once sieved, the powder is collected in another bottle and used to fill the machine silo. The complete procedure is displayed in Figure 2.25.

2.2.1.2.3. Procedure 2: recycling only

In this procedure, the build plate heating was never activated. The manufacturing process was interrupted and considered in two stages: the manufacturing of the samples stage, and the layering stage.

The first stage consisted in manufacturing the samples entirely (through the 20 mm height). The production geometries are shown in Figure 2.24(b).

Then the production was interrupted, the build plate elevated and the surrounding powder placed into the feeders. The feeders were emptied and the powder within was set apart, not to be used again in this study. Finally, the build plate was extracted from the machine and a new build plate was placed to start the job once again.

However, in this relaunched job, no scanning nor build plate heating took place. The powder was layered on the build plate, and the powder in excess felt down into the feeders. The powder in the feeders was placed back into the silo, as it were for the other experiment. When the production was ended, the powder was retrieved and sieved.

This stage ended when the powder filled completely the build volume, or when there was no more powder in the feeders.

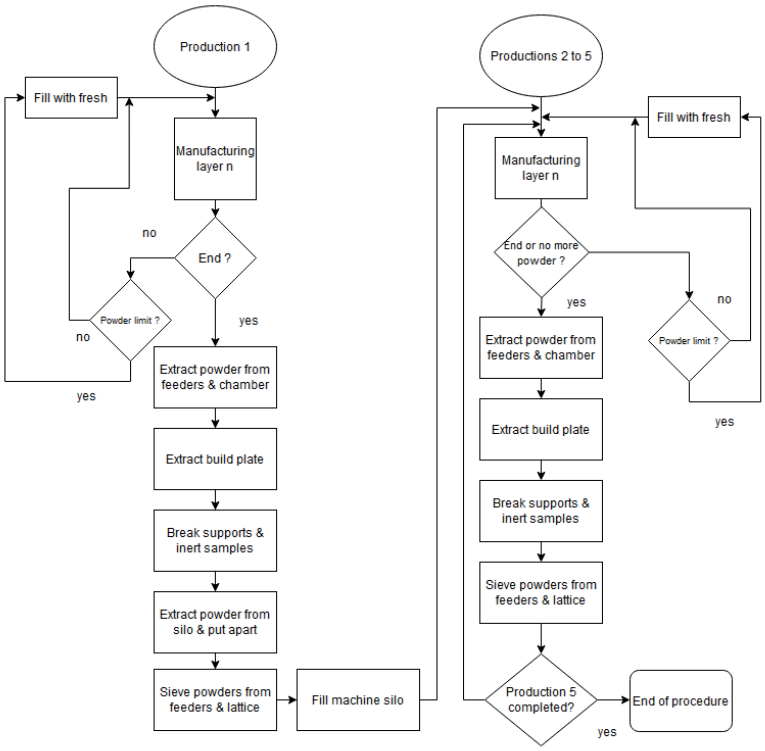

Figure 2.25: Procedure 1 (recycling and heating) steps.

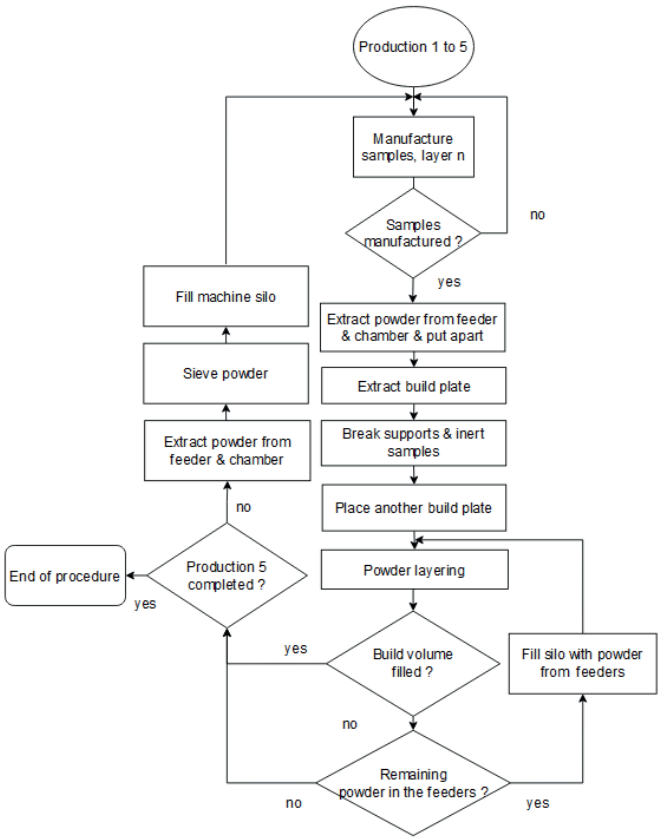

Figure 2.26: Procedure 2 (recycling only) steps.

At the end of the process, the powder within the build volume was pushed within the feeders (still under inert atmosphere), and the same procedure as the other experiment took place for the recycling: bottles were unclipped, connected to the sieving station, sieved, collected in another bottle, and the machine silo was filled. This procedure was repeated for a total of five productions. The complete procedure is displayed in Figure 2.26.

2.2.1.3. Sampling and measurements

For both procedures, when the build plate was extracted (see Figure 2.25 and Figure 2.26), the supports under the samples were broken outside the machine, and the samples were sealed in bottles in an inert atmosphere. Hence, the samples were in the open air for a few minutes before being placed under a protective inert argon atmosphere.

Then, the oxygen content of the samples was measured by EAG Laboratory in Toulouse, equipped with a LECO ONH836, using the Inert Gas Fusion (IGF) Non-Dispersive Infrared (IGF-NDIR) technique:

First, the LPBF-manufactured sample is cut in small portions (0.25 g each) which are placed in an ethanol solution until analysis. Then, one portion is placed in a calibrated graphite crucible and melted using Joule's effect (the furnace reaches a temperature between 2 500 °C and 2 900 °C).

A non-dispersive infrared cell absorbs the CO_2 gas delivered by the melting of the sample under inert helium atmosphere. The measuring method was described in a document provided by EAG laboratory in Appendix 6.3.

The measurement procedure is repeated three times for each sample provided, and the average value is provided.

2.2.2. Results

2.2.2.1. Procedure 1 and Procedure 2 manufacturing

The manufacturing durations for the first production was higher than 6 days (158 h 40 min).

While using the powder to manufacture the lattice and the samples, a significant number of powder was consumed. The global manufacturing durations, as well as the number of layers and the volume of silo filled are listed in Table 2.5.

As a recall, during the first manufacturing process (Production 1 in Table 2.5), 4 kg of fresh powder was added during the process without interruption. In the other productions, no fresh powder was added, however, powder collected from the feeders were added, assuming that they were powder in excess and not in contact with the heat.

Altogether the machine manufacturing duration was about 13 days and 19 h (331 h). Considering the extraction, sieving, filling treatments, and the working days, the procedure lasted approximately a month.

Table 2.5: Manufacturing data of Procedure 1 (heating and recycling).

	Production 1	Production 2	Production 3	Production 4	Production 5
Inital powder quantity (% silo volume)	121%	72%	43%	24%	4%
Number of layers	9501	6737	4704	2593	720
Duration	158 h 50 min	79 h 40 min	52 h 11 min	31 h 33 min	8 h 48 min

Photos of lattices after manufacturing are shown in Figure 2.27.



(a) Production n°1: lattice and samples.

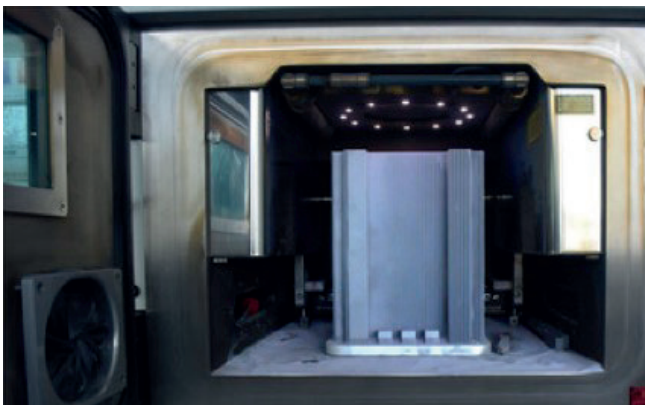

(b) Production n°1 in the build chamber.

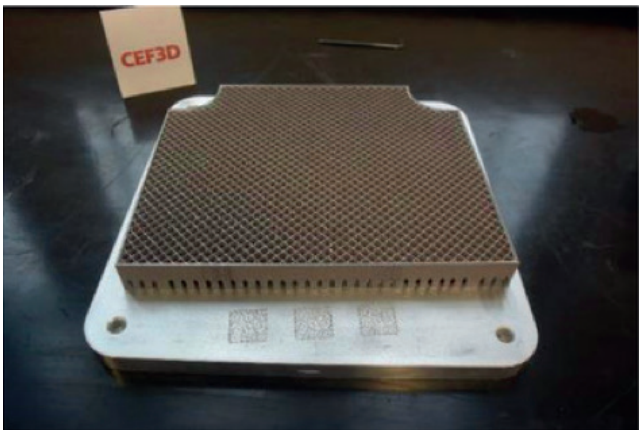

(c) Production n°5 extracted from the machine. Samples have been detached.

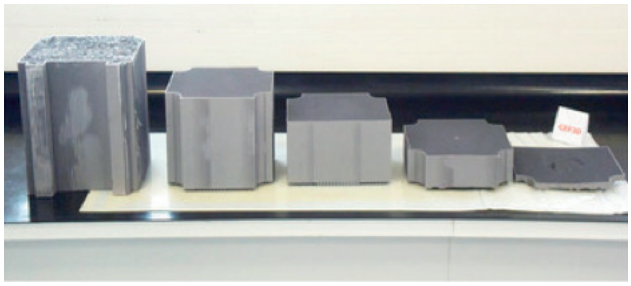

(d) All lattices of Procedure n°1.

Figure 2.27 : Procedure 1 (heating and recycling) manufactured lattices.

For Procedure 2, the data were very similar from one production to another. Indeed, each of the first stage production (Figure 2.26) where the samples were fabricated were about 19.98 mm and lasted 2 h 10 min.

Then, for the second stage, all the powder of the silo was emptied and the silo was filled back (from the feeders, without sieving) until the entire build volume was full of powder, or until there remained no more powder in the feeders to fill the silo. This stage took between six and four hours, decreasing from the loss of powder. In total, procedure 2 lasted a little more than a week due to the sieving durations after each iteration.

2.2.2.2. Oxygen content

For both procedures, the samples from production n°1, 3 and 5 were sent to the laboratory for IGF analysis.

The analysis method is detailed in Section 2.2.1.3.

The averaged values (from three measurements each) provided by the laboratory are listed in Table 2.6. From the laboratory, the measurement errors were about 5%.

Table 2.6: Oxygen measurements from the samples of Productions 1, 3 and 5 of each procedure.

	Production 1	Production 3	Production 5
Procedure 1: recycling and heating (ppm)	500 ± 25	550 ± 28	620 ± 31
Procedure 2: recycling only (ppm)	460 ± 23	450 ± 23	470 ± 24

2.2.3. Discussions

From oxygen measurement results listed in Table 2.6, an increase of the oxygen content can be observed for the first procedure, while the oxygen content remains relatively constant for the second procedure.

Hence, it seems that scanning the lattice and heating the build plate in a production affect the oxygen content of the sample manufactured in the subsequent scanning.

It is worth noting that the initial oxygen levels for both procedures were different (500 and 460 ppm). However, the conclusion is based solely on the evolution of the oxygen content through the entire procedures.

The only present heat sources for the first procedure were the build plate (170 °C during the entire productions), and the laser scanning, with parameters provided by the machine manufacturer, listed in Appendix 6.1.

It is assumed that the oxygen sources were the moisture on the particles due to condensation, the humidity in the ambient atmosphere (even though the contact of powders with the atmosphere was limited using the sealed bottles), the residual oxygen within the quasi-inert chamber atmosphere, the machine pipes (i.e., filters), and potentially some inaccessible volumes (the volume below the build plate for instance).

It is assumed that heating the powder accelerates the oxide layer growth, absorbing oxygen from the moisture present on the particles surface. In this case, drying the particles before the manufacturing process would have had a beneficial impact, as observed in the literature.

Given that the Procedure 1 samples were scanned after the lattice, they also may have been contaminated by spatters generated by the scanning of the lattice. Samples may also contaminate one another.

Limiting further the oxygen sources can be done by drying the powder and the filters. Also, scanning sacrificial volumes before the parts (first layers) may help diminish the oxygen content within the chamber. Also, limiting the inaccessible volumes such as the volume below the build plate may be helpful.

Limiting the heat accumulation may not be trivial: reducing the build plate temperature may affect the residual stresses formation. Changing the orientation of the parts to limit the scanned surface at each layer may help reducing the heat accumulation. Also, scanning at locations of spatters deposition represents a risk. Hence, it is necessary to understand the spatter deposition distribution.

In conclusion, it seems that heat due to the scanning has a major influence on the oxidation of LPBF powders. With these results, it seems that the repetitive high-temperature heating due to the laser scanning leads to a continuous contamination of the powder, and not the handling nor sieving of the powders (ambient temperatures), since it was assumed it would lead to an accumulation of humidity on the particles, absorbed during the subsequent scanning.

Also, thorough recycling process (sieving under inert atmosphere, limiting contact with the ambient atmos-

phere) seems to help limiting the oxidation of reactive powders. Also, drying the powders before manufacturing may have a beneficial influence on limiting the oxidation.

2.3. Limiting oxidation originating from heat

From the previous section findings (see Section 2.2.2.2), it was concluded that heat has a major influence on the oxidation of LPBF manufactured samples. Two heat sources were identified: build plate heating (remained constant at 170 °C) and the laser scanning.

From these two heat sources, several affected features are assumed regarding the powder contamination:

- Powder heated by the build plate;
- Powder heated by the contact with scanned regions;
- Spatters ejected from melt pools and entrained (as illustrated in Figure 2.20).

The powder heated by the build plate was heated at 170 °C, which is significantly lower than the local temperature of the laser scanned regions (aluminium melt point is approximately at 660 °C). Also, it is assumed that the heat from the build plate is dissipated through the build volume height, since the powder conductivity is significantly lower than the conductivity of the bulk material (see Chapter 3 for more details).

Hence, it is assumed that the effects of the laser scanning are dominant before the effects of the build plate heating.

The effects of the laser heating are heating the powder beside the scanned regions, and generating spatters. Experimentally isolating these two phenomena is hardly achievable: it would require to find a combination of parameters (scanning, process, geometry, material parameters) that do not yield spatters, but with the same heat provided.

Indeed, from the literature, spatters tend to deposit close to the scanned regions, and may have a wide range of size and shapes. Hence, it may be difficult to isolate the spatters from heated powder while observing the powder around the specimens.

From small finite element simulations of a large Ti-6Al-4V cubic part being manufactured, it appeared that the powders significantly heated were located at the border of the part. The powder was considered as a homogeneous solid body with specific material properties.

Few millimitres away from the part, the powder temperature was significantly reduced compared to the scanned regions temperatures. These observations were made with powder conductivities 1/100 the conductivity of the solid material, and also with powder conductivities equal to the conductivity of the solid material. For each simulation, the powder density was considered 60% the density of the solid, and the heat capacity was set equal to the material.

If a large extent of the powder was at similar temperatures as the scanned regions, it may have been assumed that a large number of powder was significantly heated and contaminated. Here, from the simulation results, we assumed that the heat from the scanned regions does not affect a large number of the surrounding powder, and it may not lead to significant contaminations of the powder.

Hence, it is assumed that the heat from the part's conduction into the powder is negligible, and may not lead to significant powder contamination. Hence, spatters are assumed to be the main contributors of the powder's contamination.

Since the oxidation seems to have a strong link with the thermal history, two strategies are proposed to reduce contaminated powders around the scanned surface:

- Reduce the scanned surface at each layer;
- Provide cooling time to scan on cool homogeneous substrate.

In this context, «contaminated powders» are considered only to be spatters. These two strategies are based on the assumption that higher temperature levels yield more contaminated powders.

Indeed, spatters ejected from the melt pool may originate from the interaction of melt pools with high pressure gas flow, and the vapor flux may rise with the temperature [164]. Also, entrained particles may be more contaminated with higher temperatures (regarding the oxidation kinetics, as discussed in Section 2.1.4).

The next part of this study will challenge these two strategies for simple case studies using different geometries and Ti-6Al-4V material.

2.3.1. Material and methods

2.3.1.1. Material, machine and process conditions

The material used in this study was Ti-6Al-4V grade 23 provided by Tekna. The powder size distribution was bimodal with modes at 15 and 45 µm. The chemical composition provided by Tekna is listed in Table 2.7.

Table 2.7: Ti-6Al-4V powder chemical composition.

Ti	Al	V	Fe	O	N	H	C	Y
Bal.	6.0-6.5%	3.5-4.5%	<0.25%	<0.13%	<0.03%	<0.012%	<0.08%	<0.005%

The machine used in this study was a DMP ProX320 from 3D SYSTEMS. The machine and its chamber are shown in Figure 2.28.



(a) Exterior view. (b) Machine chamber at the end of a production.

Figure 2.28: DMP ProX320 LPBF system.

The machine has two powder tanks, on each side of the build plate. The build volume of the machine is of 275 mm * 275 mm * 420 mm. As the Renishaw AM400, a vacuum process is first performed, and argon gas fills the build chamber.

In this study the state of the powder used was unknown since it has been recycled several times before. The recycling process is similar to the Renishaw, however the powder is in contact with air at room temperature when the chamber is opened.

The files used for the manufacturing process were prepared using 3DXPert and DMP Control software.

Process parameters for Ti-6Al-4V with 30 μm layer thickness provided by the machine manufacturer are listed in Appendix 6.2.

2.3.1.2. Design of experiment

To test the two previously mentioned strategies about limiting the powder contamination, two different experiments were performed.

For each experiment, the same base geometry was used: a cantilever commonly used for the calibration of Simufact software. The calibration was originally performed for simulations introduced in Chapter 2.

In the first experiment, three geometries were manufactured with varying the geometry width. Hence, the scanned surface for all geometries was different.

In the second experiment, a unique cantilever geometry was used in two productions. However, one production did not use interlayer cooling delays, while the other made use of a significant cooling time between each layer.

All these experiments are based on the assumption that contaminated powders changed in colour: as mentioned in Diamanti *et al.* [165], the colour of titanium oxides vary with the oxide layer thickness, due to optical interferences in this layer. Also, burned particles (fully black) can be found, these are considered contaminated also.

2.3.1.2.1. Samples geometries: calibration cantilever

From previous tests, it was observed that calibration cantilever geometries produce a large number of burned particles. For simplicity, these particles will be called spatters.

The geometries are shown in Figure 2.29.

The cantilever geometry with 12 mm width is the standard geometry for calibration step recommended by MSC for Simufact software calibration. As explained in Chapter 2, Simufact is used for the simulation of residual stresses and distortions in LPBF.

This geometry was chosen because, after a few tries using other geometries without noticing much spatter, a large number of dark particles surrounding this part (12 mm width) were present.

All cantilevers produced in this study were manufactured directly on the build plate, without any supporting structure, as recommended for Simufact calibration.

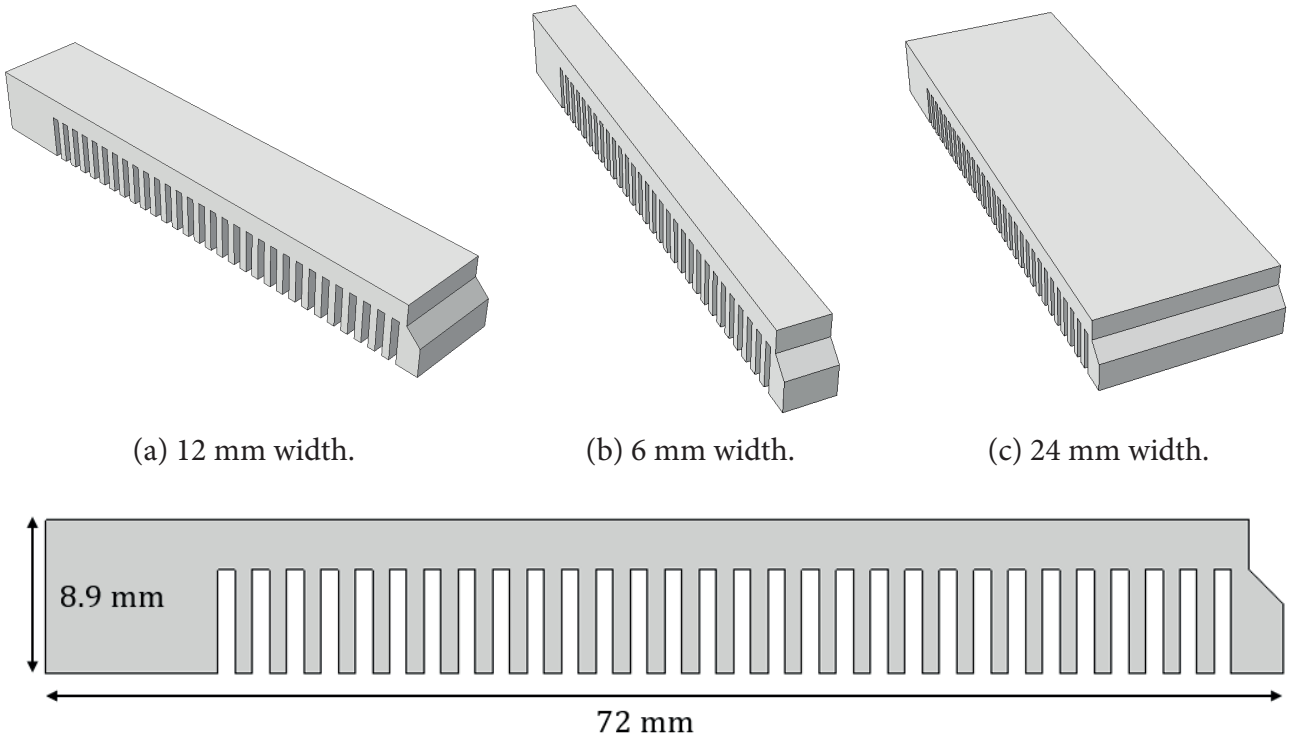

(a) 12 mm width. (b) 6 mm width. (c) 24 mm width.

(d) All cantilever profiles.

Figure 2.29: Cantilever geometries used for both experiments.

2.3.1.2.2. Experiment 1: different scanned surfaces

In the first experiment, three different geometries of the cantilever were produced in the same production. The objective is to observe the influence of the cantilever width (hence, the influence of the surface scanned) on the quantity of surrounding spatters.

The parts were positioned at the same level regarding the gas flux, and sufficiently far one from another. Hence, the spatters generated from one part cannot be mistaken with spatters generated by the two others. The disposition of the cantilevers on the build plate is shown in Figure 2.30.

All geometries were of equal height (8.9 mm); hence, the production was of 296 layers 30 μm each. All optical measurements were performed on the last layer for each geometry.

It is common to use finely tuned parameters for the last layer of a geometry, to yield smooth surfaces. However, in our case, the last layer parameters were set equal as the other layers.

Before the scanning, for every production, the spreading system came from the right side of the build plate. The observed spatters were generated during the scanning of the last layer, and not from the previous layers (before scanning, the recoated layer was homogeneous).

The last layer spatters distribution did not seem different than the distribution of the previous layers.

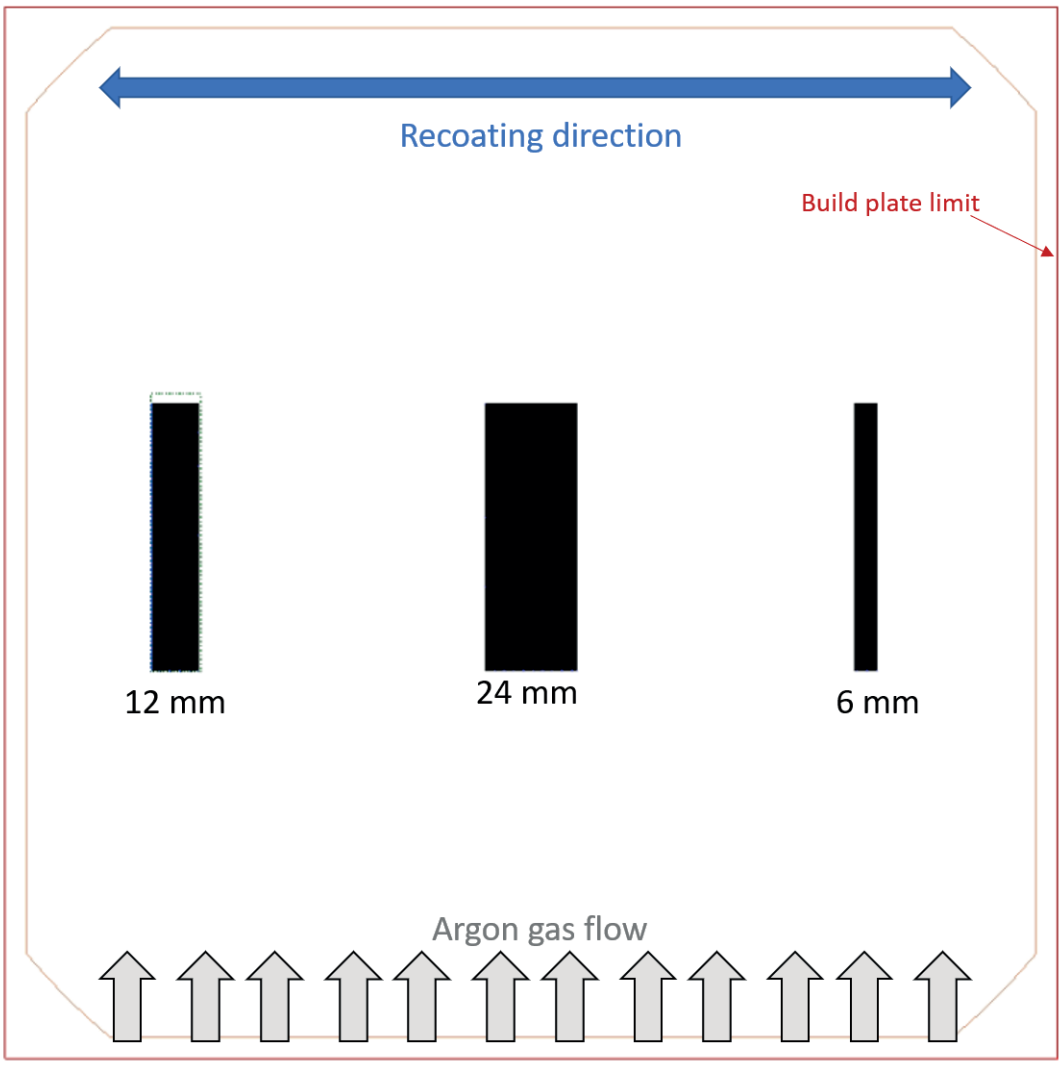

Figure 2.30: Experiment 1 disposition of cantilevers on a large build plate viewed in DMP Control software.

2.3.1.2.3. Experiment 2: interlayer cooling duration

In the second experiment, two productions were performed: during the first production, the cantilever of 12 mm width was manufactured with no dwell-time (no artificial cooling duration between two consecutive layers). Hence, the cooling duration between two consecutives consisted in the recoating process which lasts between 2 and 3 seconds. The manufacturing of entire one layer (scanning of all geometries, and layering) lasted between 8 and 10 s, depending on the layer owing to the varying geometry, see Figure 2.29(d)).

During the second production, a dwell time of 50 s was added, hence, the manufacturing of one layer was as follow: 8 to 10 s of scanning, 50 s of cooling (nothing happened), 2 to 3 s of layering.

For both productions, the build plate used was smaller than the one used for Experiment 1 (same height, of 40 mm, but a surface of 200 mm * 150 mm instead of 275 mm * 275 mm).

Regarding Experiment 2, except the dwell time, no variations were included from one production to another. The disposition of the cantilever on the build plate for each production is shown in Figure 2.31.

All geometries were of equal height (8.9 mm); hence, the production was of 296 layers 30 µm each. All measurements were performed on the last layer for each geometry.

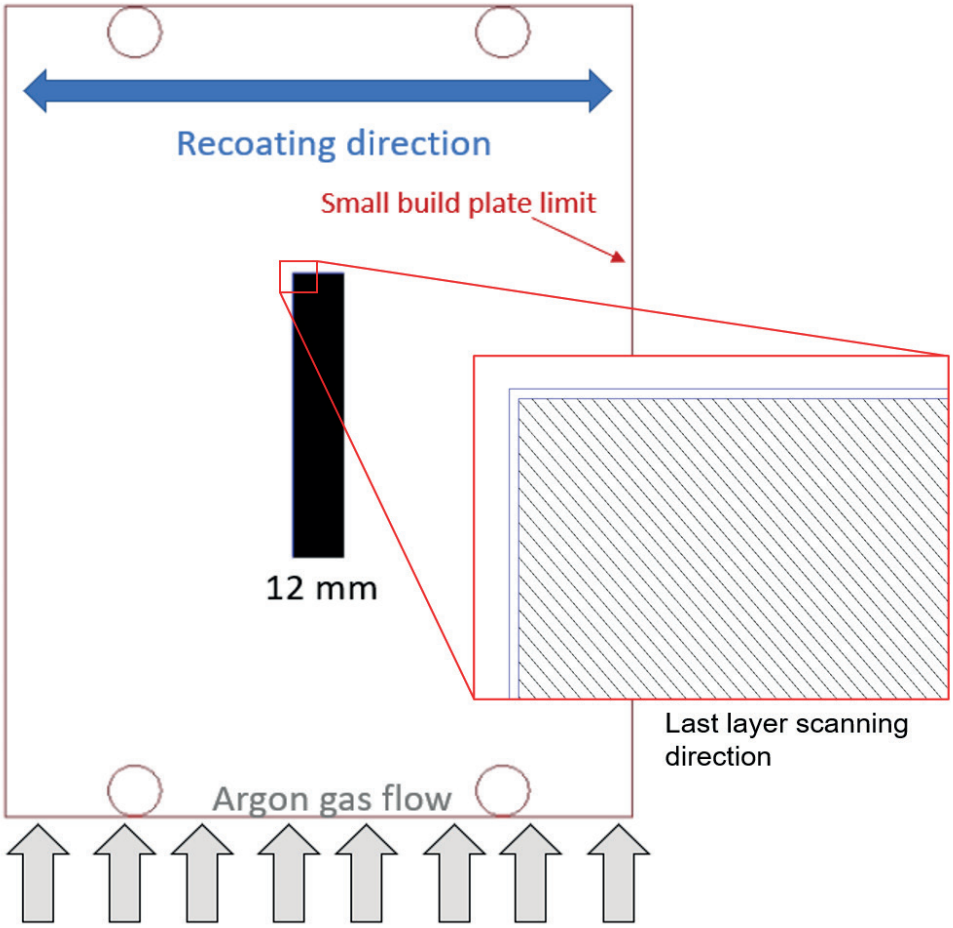

Figure 2.31: Experiment 2 disposition of cantilever on a small build plate for both productions viewed in DMP Control software.

2.3.1.2.4. Optical measurements

All deposited particles assimilated to spatters particles were black, no colour can be seen with naked eye and iSight camera (as shown in Figure 2.32).

At the end of every manufacturing process, before the build plate was elevated and the powder removed, rulers were placed around the cantilevers and pictures of them were taken with a standard 8M pixels iSight camera and a 5M pixels DinoLite device (ref. AM7515MT8A) of magnification between 700x and 900x.

The pictures from the camera were manually treated in GIMP software to erase the perspective from the image. Then, the images were treated in ImageJ software: they were transformed from RVB format to 8-bit format. The scale was set from the ruler and thresholds were manually set to retrieve the darker particles from the image. All thresholds were noted and placed with the results.

Then, the results from the «Particle analysis», providing the ratio of particles detected using the given threshold to the image size.

The full process is displayed in Figure 2.32.

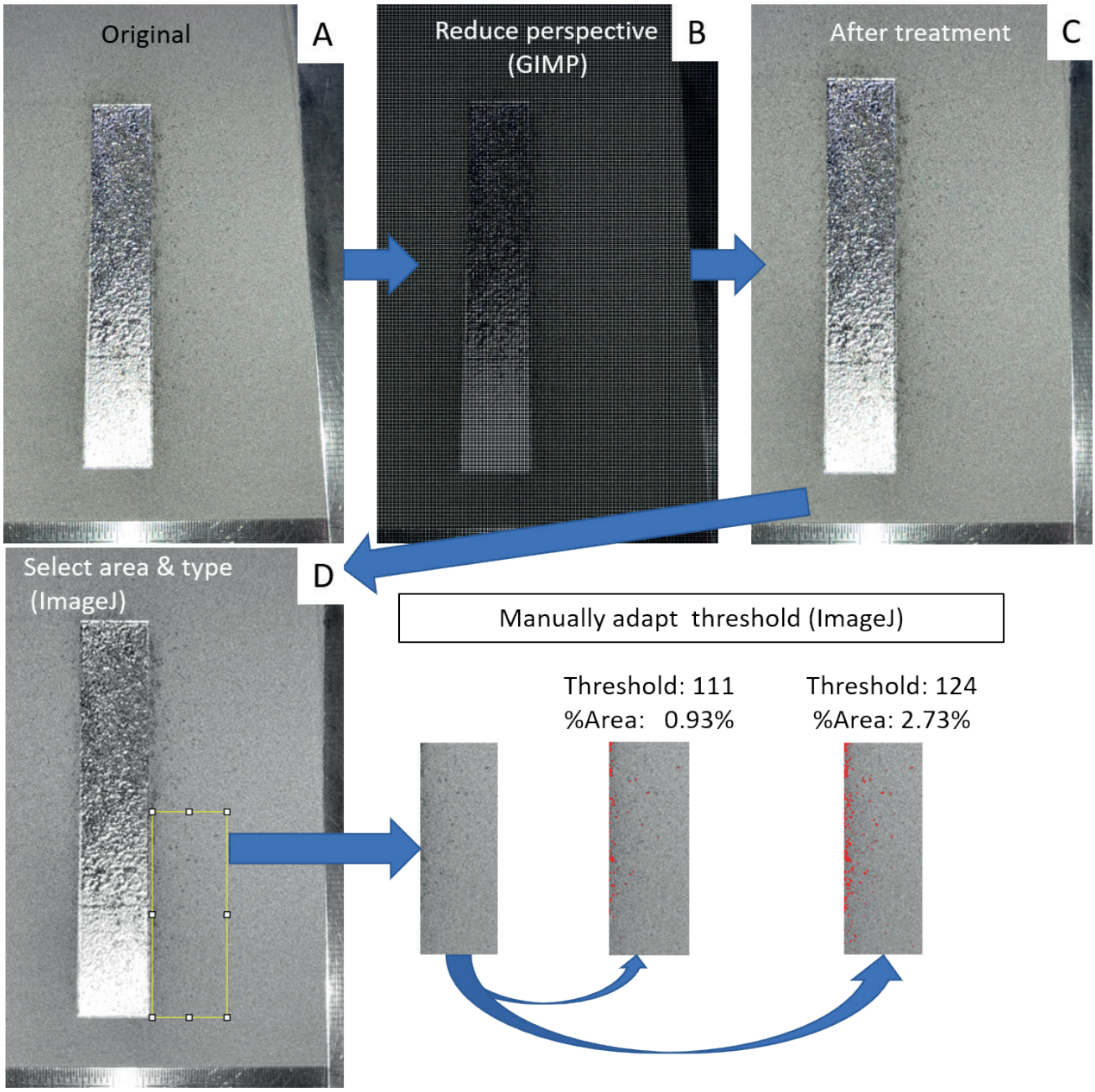

Figure 2.32: Image preparation and analysis process using GIMP and ImageJ software.

From Figure 2.32, image A is the original picture taken with the camera. Two rulers and a cantilever are shown. In image B, the picture is opened in GIMP software and the grids are used with the software perspective tool to erase the perspective. Image C is the result of such process.

Image D is the picture opened in ImageJ which type has been changed from RVB to 8-bits (to greyscale). From this image, a rectangle at a location neat the part's edge is defined and analysed using both thresholds and Particle Analysis tools. The surface ratio of the darker particles is shown on the right for two threshold values.

All images in the results section have been treated and analysed the same way. Due to different light expositions while taking the photo, the darkness level is not similar for all images. Hence, different thresholds are needed.

2.3.2. Results

2.3.2.1. Experiment 1 results: different scanned surfaces

The last layer of the production containing the three cantilevers can be seen in Figure 2.33.

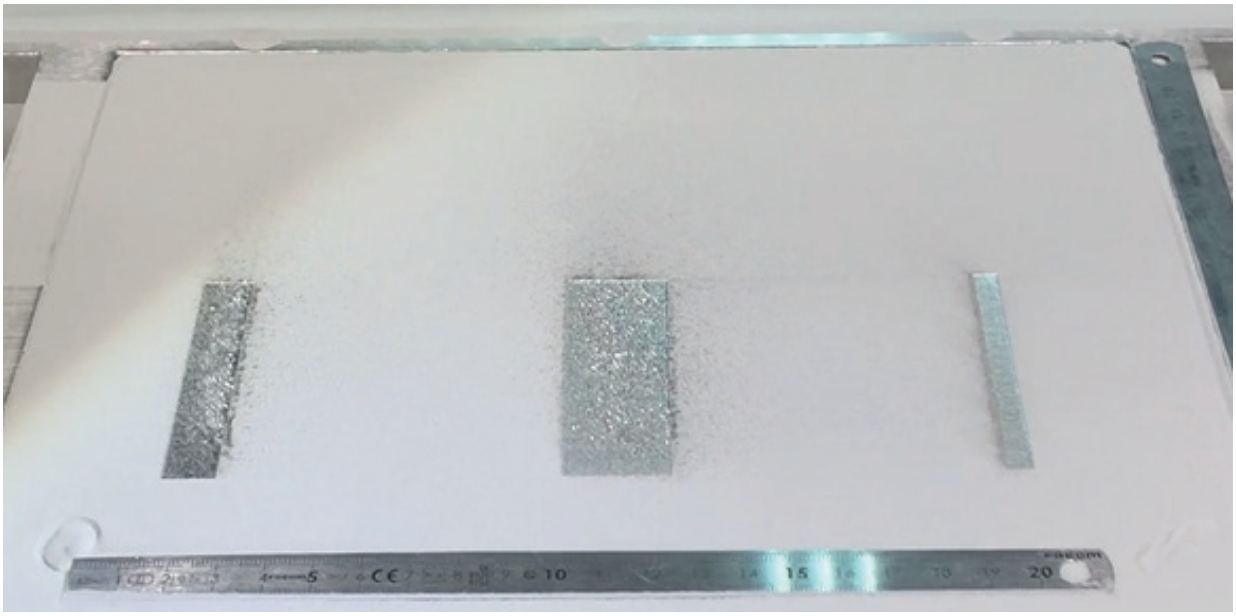

(a) Entire build plate.

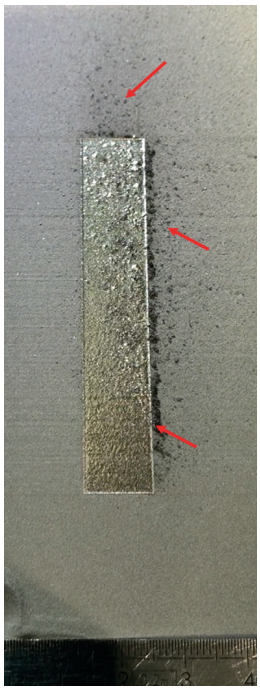

(b) Cantilever 12 mm width.

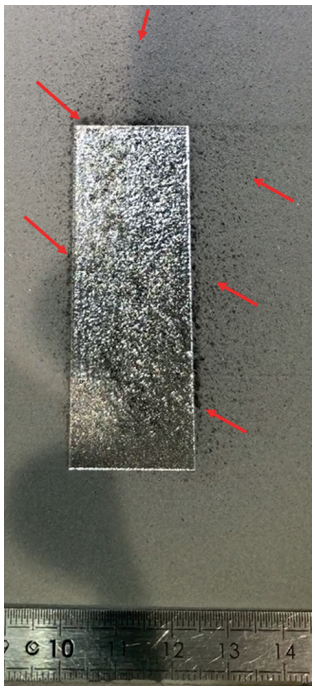

(c) Cantilever 24 mm width.

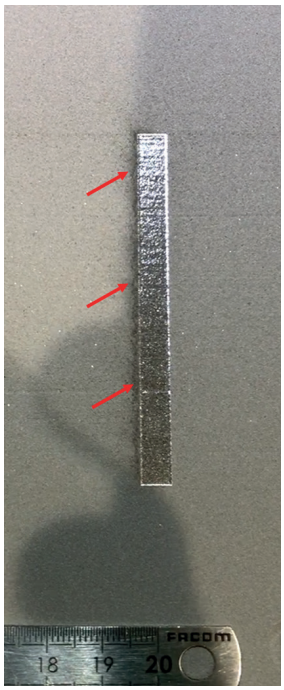

(d) Cantilever 6 mm width.

Figure 2.33: Final layer of the three cantilevers production. Dark particles are indicated wit arrows.

Several images taken around the cantilevers are shown in Figure 2.34 to Figure 2.36.

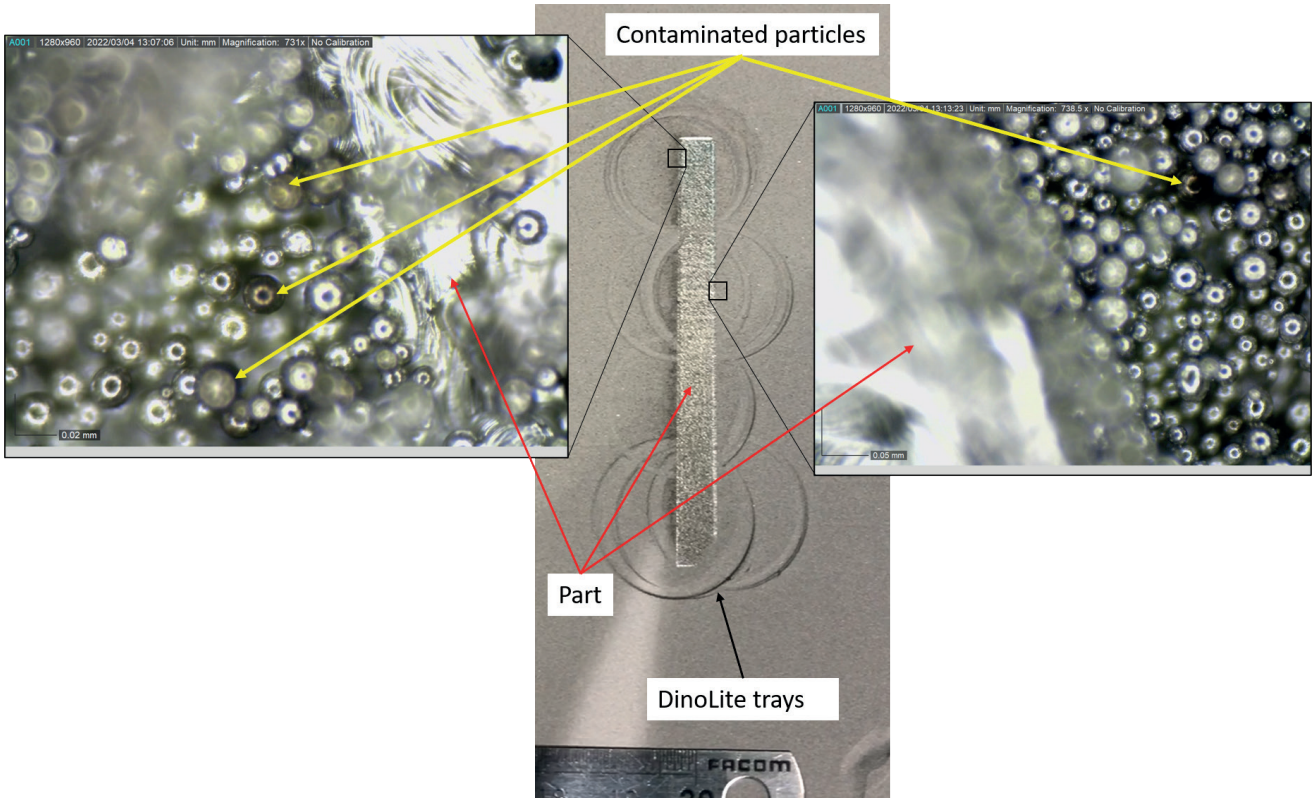

Figure 2.34: DinoLite images of the 6 mm width cantilever.

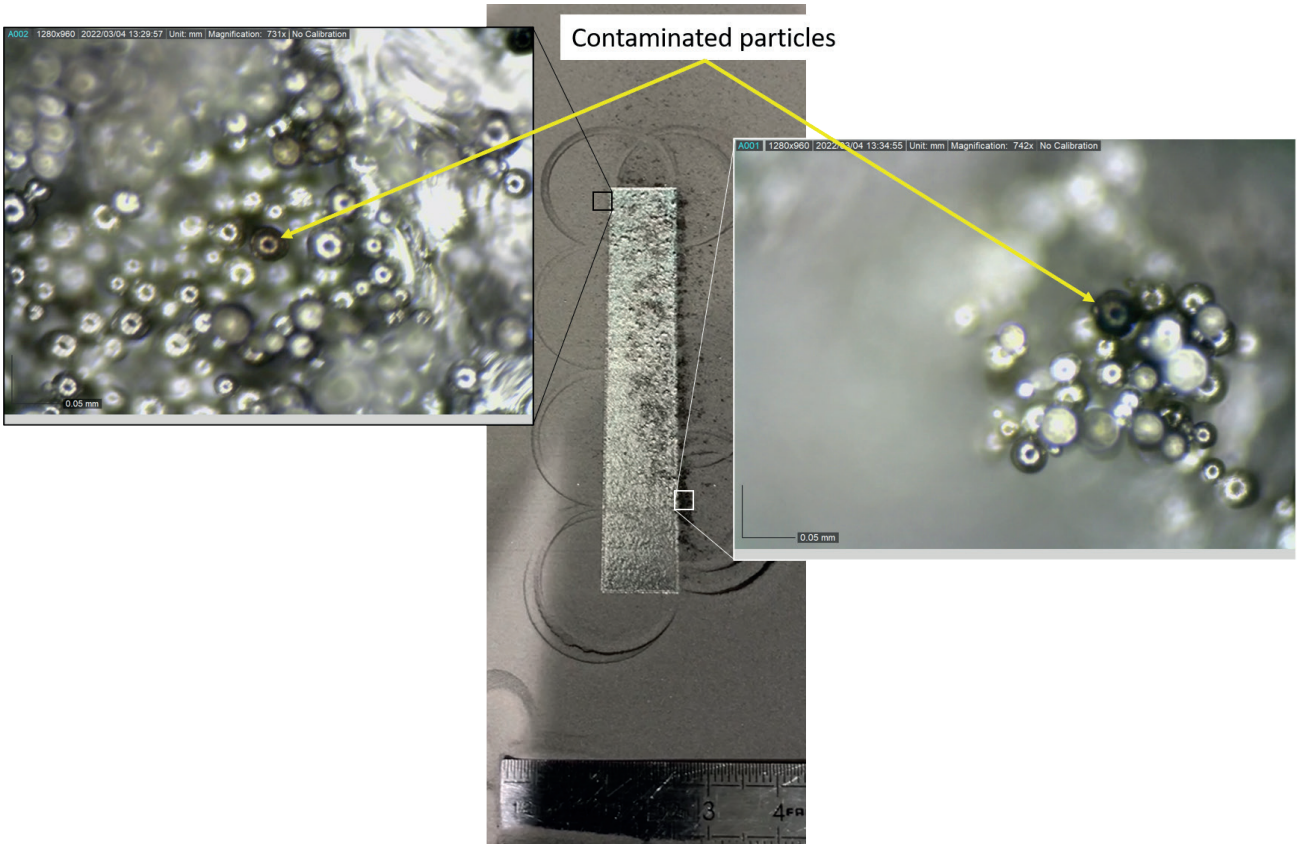

Figure 2.35: DinoLite images of the 12 mm width cantilever.

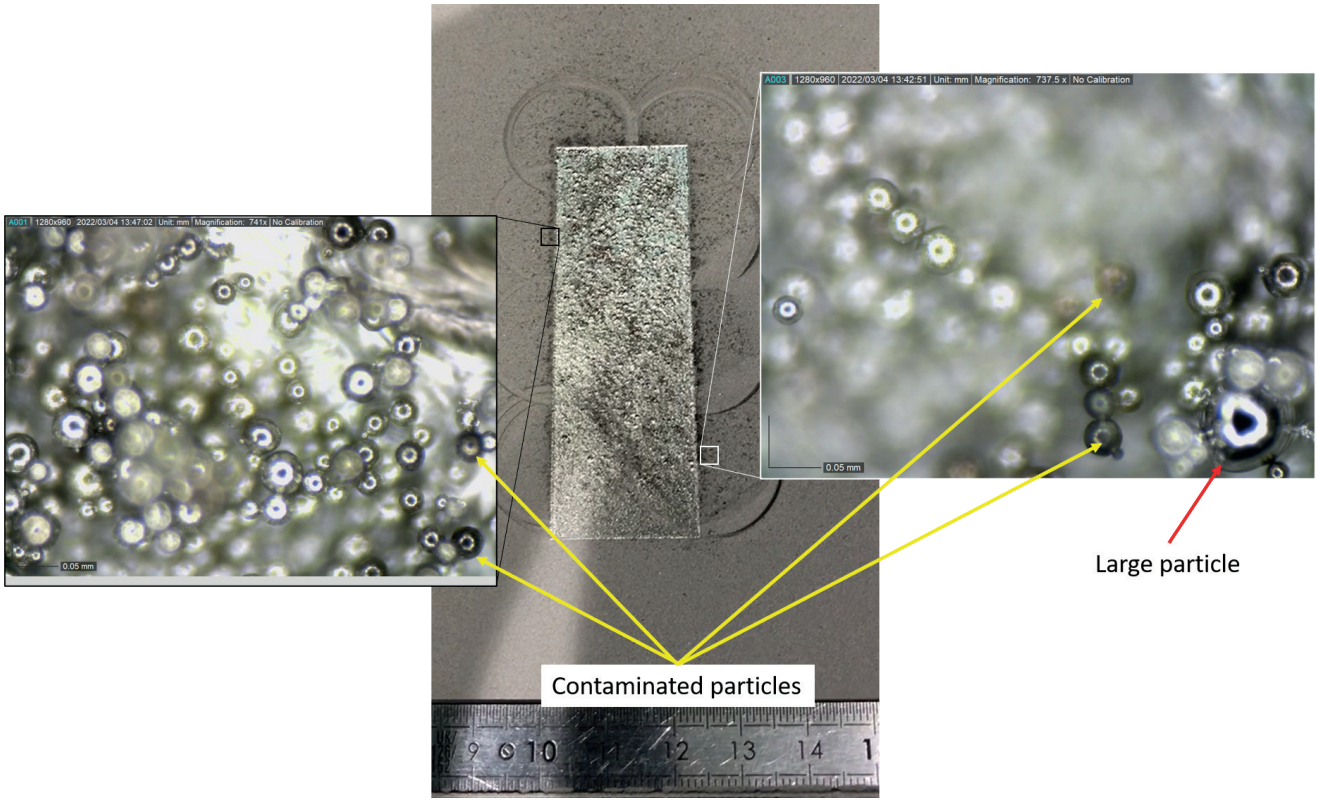

Figure 2.36: DinoLite images of the 24 mm width cantilever.

From Figure 2.33, it can be seen that the number of dark particles increases with the width of the cantilever. Also, dark particles seem to fall farer from the cantilever with an increasing cantilever width: in Figure 2.33(d), the 6 mm width cantilever have dark particles at its border, while some dark particles are located a few millimetres away from the cantilevers 12 mm and 24 mm in Figure 2.33(b) and (c). It seems that largest dark particles are located near the 12 mm cantilever, compared with the other two. A large number of spatters can also be observed on the surface of the parts.

Also, the cantilever 24 mm have dark particles on each side (more on the right side) and above, while the other two cantilevers seem to have a greater distribution on a specific side (right side for 12 mm cantilever in Figure 2.33(b) and left side for cantilever 6 mm in Figure 2.33(d)).

For all cantilevers images, it seems that there are more dark particles above than beneath. This is explained by the gas flux which comes from below.

Also, the preferred side of the spatter depositions for the 12- and 6-mm cantilevers may be explained either by the gas flux which may come inwards (from the exterior to the interior) due to perturbations, or by the laser incidence angle which may generate spatters with a preferred angle. However, the 24 mm cantilever was placed in the centre of the build plate, and it seems that there are more particles on the right side. This observation may deny the assumption of the laser angle and put forward the assumption of an misoriented gas flux.

Hence, it appears that the size of the scanned surface has an important influence on the number of generated spatters in the powder. The reasons for a preferential side of spatters deposition are still to explore.

Owing to large discrepancies in brightness levels and some shadows hindering the measurements, it was not possible to analyse thoroughly the images for all three cantilevers using ImageJ software.

From Figure 2.34 to Figure 2.36, several contaminated particles are present around the parts. These are distinguishable from their dark or yellow colour. Dark particles may be particles burnt from the scanning, and they seem to be of equivalent size of standard powder particles. Yellow particles are also displayed, these particles may have been heated without burning, hence leading to the layer thickness growth.

It is assumed that black particles were severely heated, and yellow particles have been heated to a limited extent compared to «burnt» black particles.

Also, a large particle has been observed in Figure 2.36, which has the same colour as the standard powders. Hence, it is assumed that this particle was already present in the fresh powder (from the provider). It may have managed to go through the sieves during the previous sieving process.

2.3.2.2. Experiment 2 results: interlayer cooling duration

Spatters may lead to severe defects within the parts such as large porosities if they cannot be entirely melted. Treated images from GIMP (to erase the perspective) are shown in Figure 2.37.

The analysis results using ImageJ software are displayed in Figure 2.38 and Figure 2.39. It can be seen from these two figures that the brightness at the instant of the picture were different, explaining the need for different threshold values between these two figures. However, as a comparison, a threshold value of 102 was used in both cases.

For the production with no dwell time, in Figure 2.38, a threshold value of 87 looks more appropriate for every corner. In the case of the 50 s dwell time production, in Figure 2.39, a threshold value of 128 seems more appropriate for every corner, except the lower left corner which seems to overestimate the spatters content.

Results for these two productions using the same threshold values are listed in Table 2.8, and results with threshold values that seem more appropriate are listed in Table 2.9.

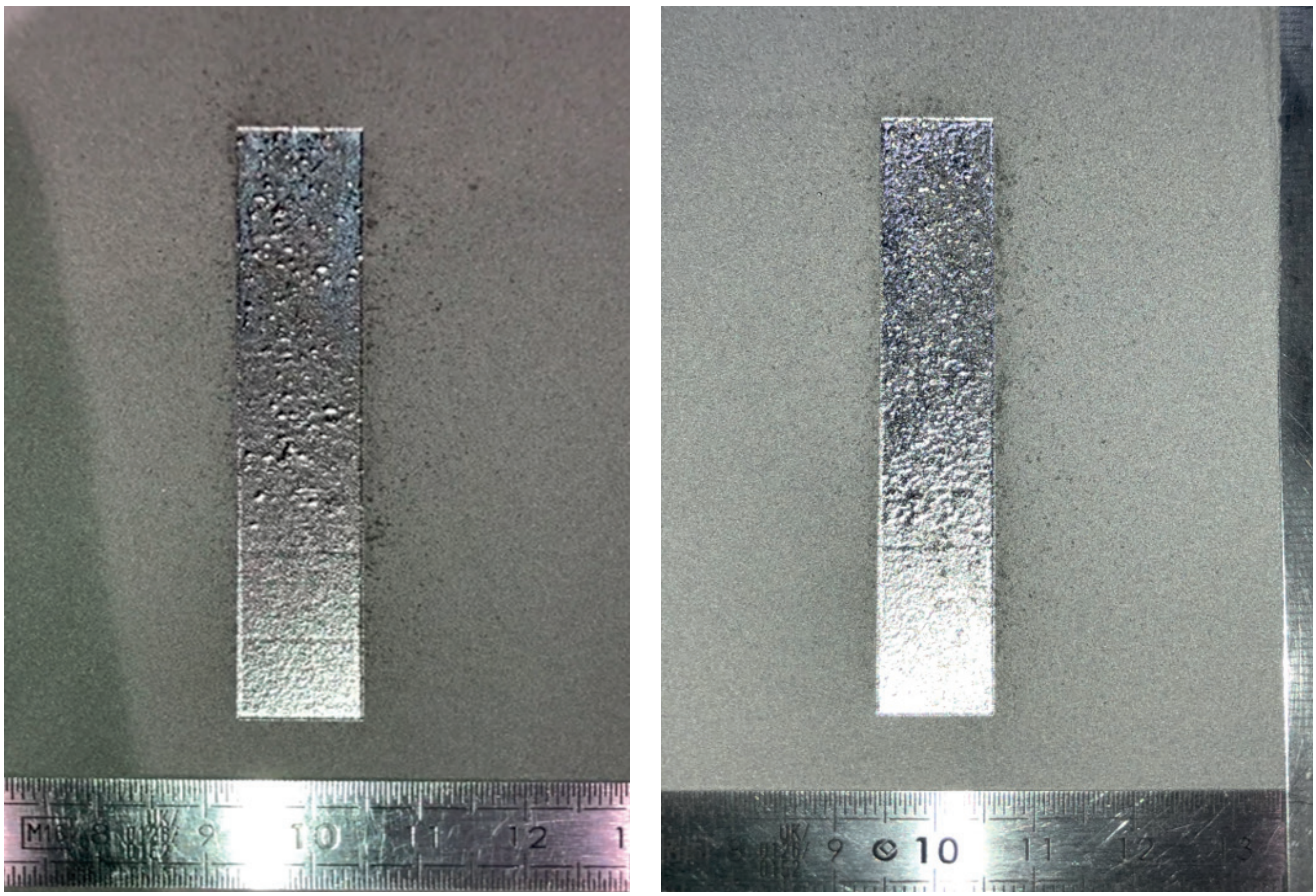

(a) No dwell time. (b) 50 s dwell time.

Figure 2.37 : Images of both cantilevers after erasing the perspective using GIMP software.

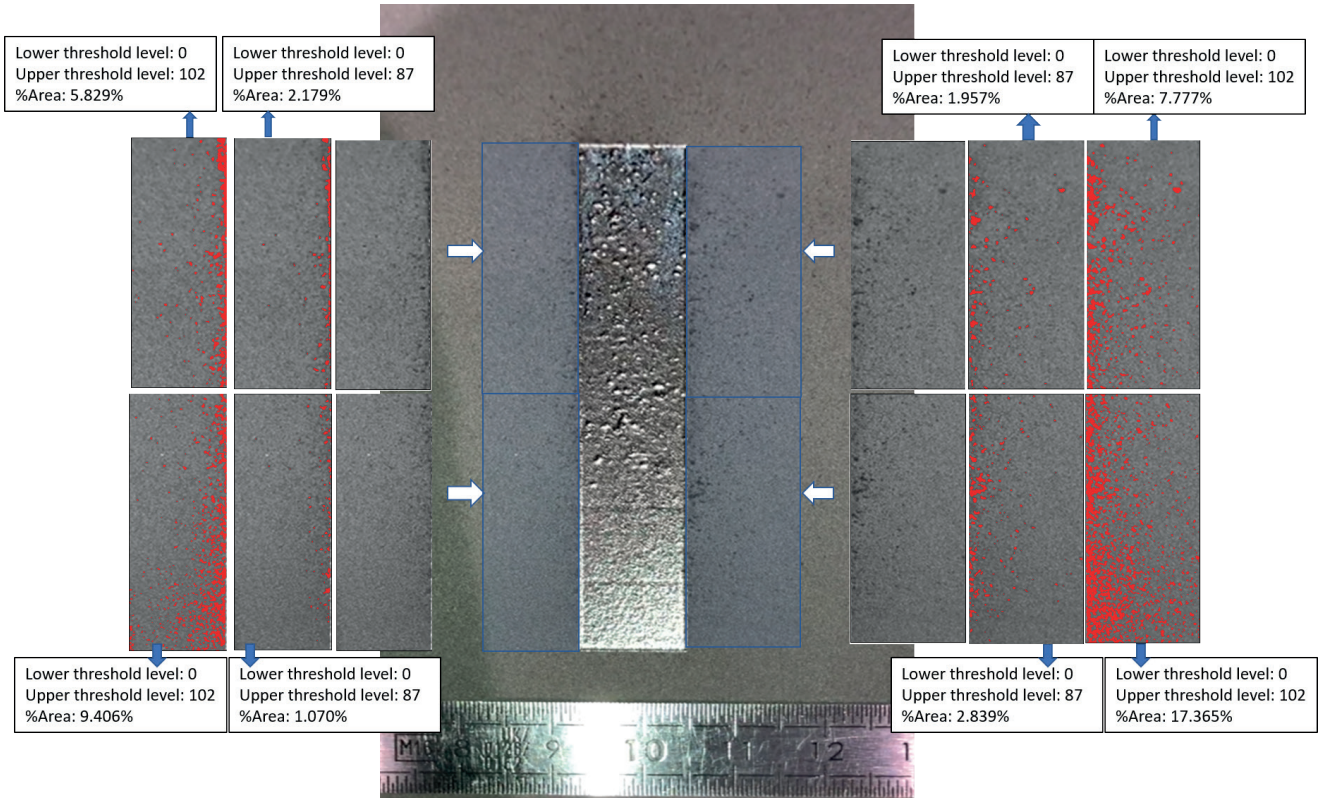

Figure 2.38: No dwell time production analysis results using two grey scale threshold values.

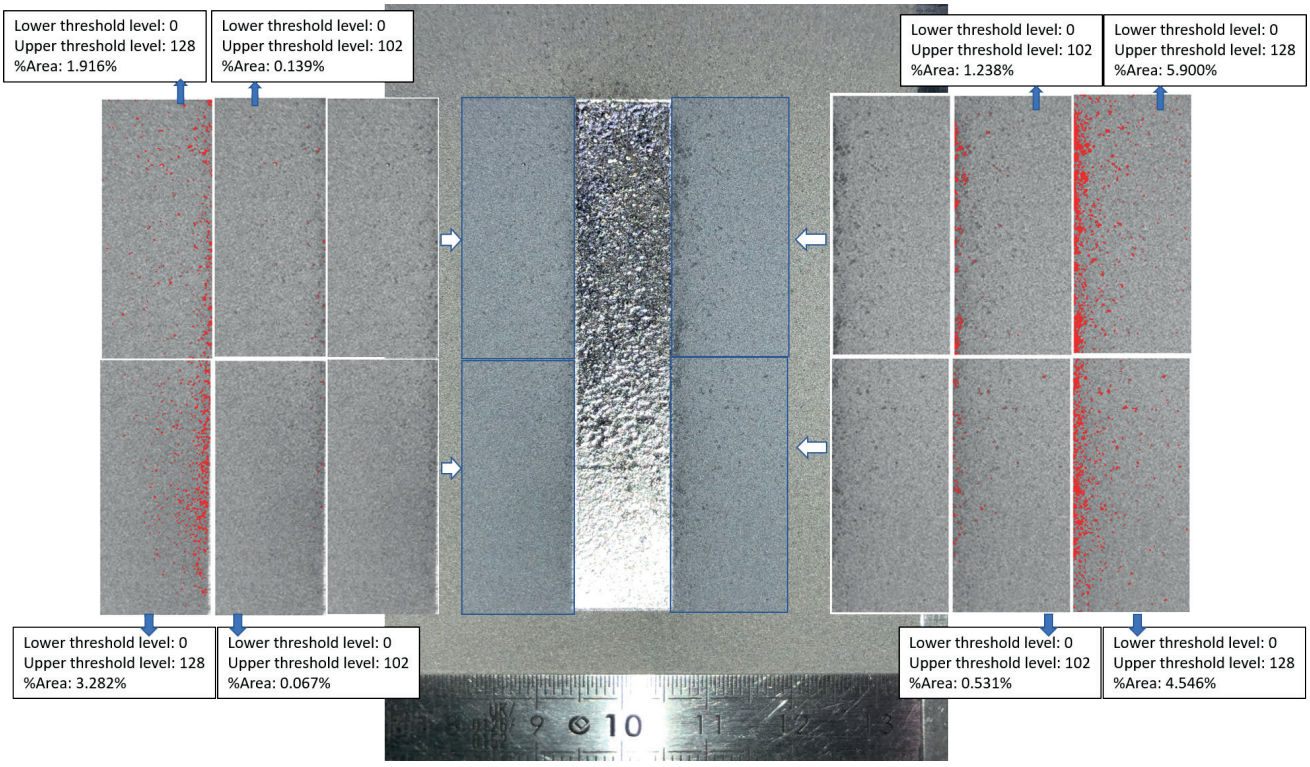

Figure 2.39: 50 s dwell time production analysis results using two grey scale threshold values.

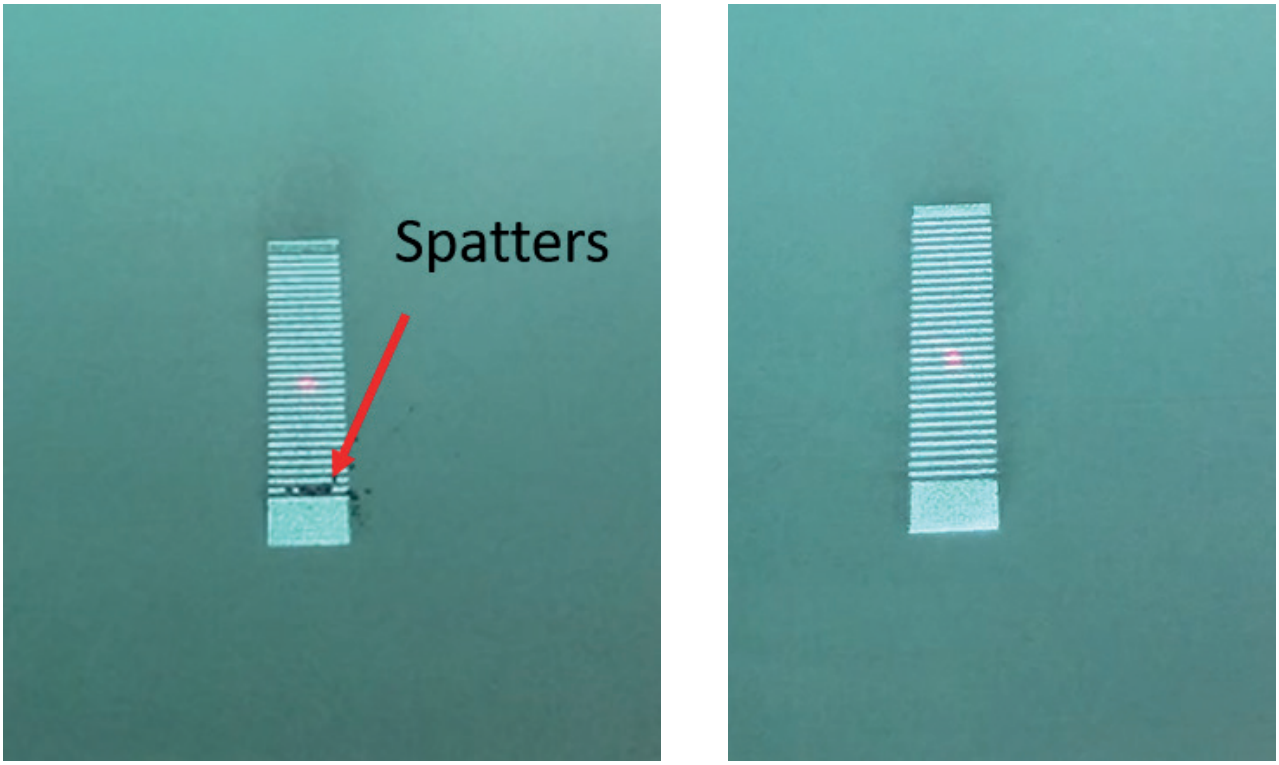

(a) Layer 104. (b) Layer 105.

Figure 2.40: Production without dwell times at the end of two consecutive layers.

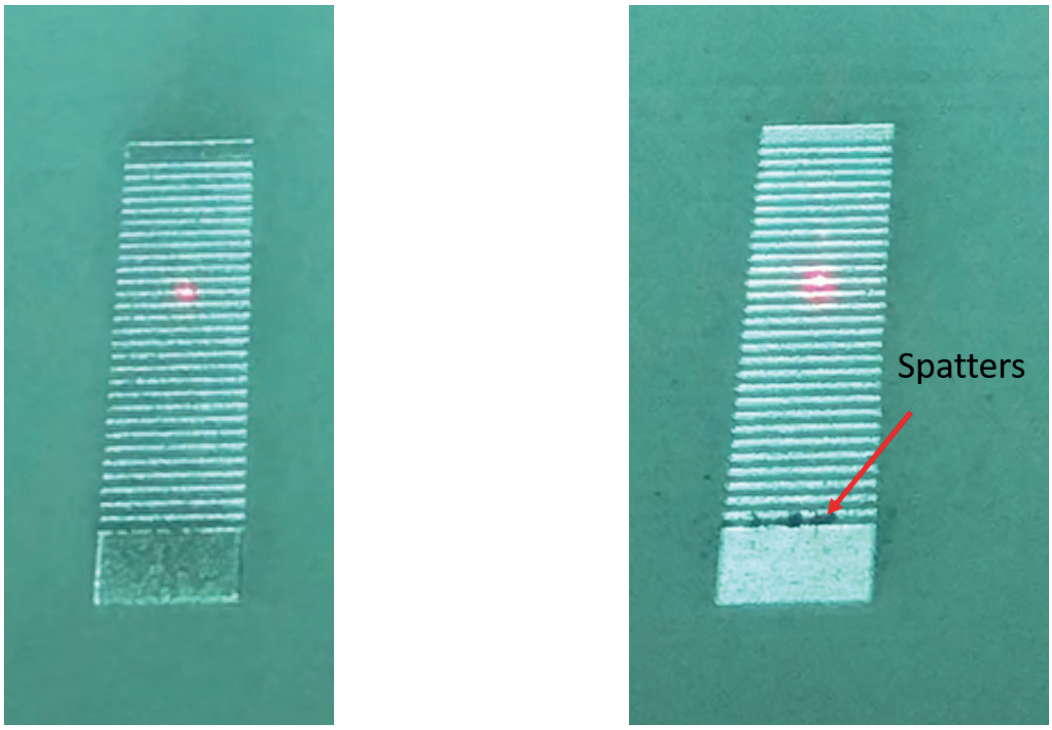

(a) Layer 19. (b) Layer 20.

Figure 2.41: Production with 50 s dwell times at the end of two consecutive layers.

During the two productions of the unique cantilevers (12 mm width), specific spatter generations have been observed for both productions. Pictures of the corresponding layers and also another neighbour layer are shown in Figure 2.40 and Figure 2.41. Red dots on the figures are the laser indication light, it is turned off during the layering process (all pictures were taken during the layering process).

From these figures, it appears that a large number of spatters may be generated and deposited close to the part or directly on its surface. However, these spatters are not observed at every layer, the rotating scanning strategy varying the length of scanning stripes may explain the generation of spatters and their absence in subsequent step.

Table 2.8: Analysis results with a common grey scale threshold value of 102.

	Corner below left	Corner upper left	Corner below right	Corner upper right
No dwell time	9.406 %	5.829 %	17.365 %	7.777 %
50 s dwell time	0.067 %	0.139 %	0.531 %	1.238 %

Using the same grey scale threshold value (Table 2.8), it appears that ImageJ software detects a significantly larger number of dark particles in the no-dwell time production. This is explained by the darker contrast in the image compared with the 50 s dwell time production image.

Hence, the values can hardly be compared one from another. However, in both cases, the software detects more spatters on the right side of the cantilever. Preferred sides of spatter deposition were also observed in the Experiment 1 with three cantilever geometries.

Table 2.9: Report of analysis results with adapted grey scale threshold values (87 for no-dwell time and 128 for 50 s dwell time productions).

	Corner below left	Corner upper left	Corner below right	Corner upper right
No dwell time	1.070%	2.179%	2.839%	1.957%
50 s dwell time	3.282%	1.916%	4.546%	5.900%

Regarding more adapted grey scale threshold values in Table 2.9, it appears that the production which used dwell times between layers may generate more spatters than the other production.

Although the no-dwell time surface ratio values do not reflect a preferred landing side for spatters in Table 2.9, looking at Figure 2.37(a), it seems that there is a discrepancy between left and right side: more spatters may be present on the right side.

Hence, it looks difficult to quantify precisely the number of generated spatters using this method. From the images in Figure 2.37, it is not trivial to determine which cantilever has generated the greater number of spatters.

2.3.3. Discussions

From these two experiments, several observations have been made. First, the number of generated spatter is strongly influenced by the scanned surface. The larger the scan surface, the greater the number of generated spatters. An important consideration is to determine if the generation of spatters is proportional to the scanned surface, or if below a certain threshold limit, the number of spatters decreases rapidly.

Also, in the first experiment, for both the 12- and 24-mm cantilevers, spatters seem to deposit preferentially on the right side. A stronger emphasis was found for the 12 mm cantilever, which was located on the left of the build plate, than for the 24 mm cantilever, in the centre.

In the second experiment, two 12 mm cantilevers were produced in the centre of their respective production. Comparing the last layers in Figure 2.33(b) and Figure 2.37, it can be observed that more spatters were generated at the side of the cantilever in Experiment 1, than the two others. Also, it seems that the preferential side

is more visible in the Experiment 1 than in Experiment 2.

These two experiments were distinguished the position of the 12 mm cantilever (left side in Experiment 1, centre in Experiment 2) and the dwell times: in Experiment 1, the layer duration was between 45 and 48 s, in Experiment 2, the layer durations were between 10-12 s in one case, 1min-1min2s in the other.

Since the layer duration, and hence the cooling duration, of Experiment 1 was comprised between those of Experiment 2, it does not seem like a possible explanation of the number of spatter generated.

Also, in Experiment 1, the 6 mm cantilever placed on the right side of the build plate had a preferential side of spatters deposition, which was opposite to the 12- and 24-mm cantilevers.

Two assumptions are proposed to explain these discrepancies, both concern the location of the cantilever on the build plate.

It is first assumed that even though the gas flux is assumed to be straight at the gas inlet, it may rebound on the opposite surface of the machine and may be misdirected. The resulting gas flux over the build plate may not be perfectly straight, but a complex addition result of the misoriented gas fluxes and the straight flux from the gas inlet. Measurements regarding the gas flux are planned with an industrial partner.

Also, the gas over the edges of the build plate may be more inclined to be perturbated by exterior perturbations than the gas flux at the centre, explaining why the strong influence of the position on the preferred sides.

The incidence angle of the laser may explain both the discrepancy of generated spatters and preferred side of deposition. Indeed, strong evaporation fluxes may form from the high local temperatures, entraining the particles. The scanning direction influences the direction of flying spatters as mentioned in the literature.

These entrained particles may encounter the laser beam while they are on the left side of the 6 mm cantilever, and on the right side of the 12 mm cantilever of Experiment 1. In this regard, they would melt and fall beneath this location.

Also, with a low incident angle of the laser, maybe more particles would be susceptible to encounter the laser beam in their flight than with a vertical laser beam.

Overall, from Experiment 1, it can be concluded that a larger scanned surface leads to a greater number of generated spatters. However, regarding spatters generated in Figure 2.40 and Figure 2.41, it seems that two identical layers (the same geometry of identical size) may generate very different spatters phenomena. Because the only parameter that has changed between these consecutive layers is the scanning direction (due to the rotation between consecutive layers), the scanning direction coupled with the scanned surface may influence the spatters generation.

Hence, this parameter would be important to consider while choosing an orientation for a part, given that the more spatters are generated, the higher the risk of defects (porosity and surface roughness) and also the risk of contamination.

Some contaminated particles may be isolated from their colour: from the DinoLite images, it appeared that some particles are yellow and other dark, while most particles (assumed to be standard powder) were grey.

From Experiment 2, it was not possible to determine confidently which case generated more spatters. Indeed, from the production with no dwell time, and the one with 50 s of cooling time between each layer, it can hardly be told visually, or using thresholds in ImageJ software, which cantilever have produced a greater number of spatters.

The layer duration in the first case was approximately 10 s (scanning and layering), while the other was ap-

proximately one minute (scanning, dwell time and layering). Hence, either the dwell time does not affect the number of generated spatters, or this cooling duration of 50 s was not sufficient. However, such a considerable dwell time is inacceptable economically since it increases significantly the overall manufacturing duration.

In this experiment, it was also observed that spatters are generated at specific layers (see Figure 2.40 and Figure 2.41). This phenomenon was attributed to the scanning strategy: with the rotation of the scanning strategy at each layer, the vectors are longer or shorter and the different thermal history may generate different number of spatters.

In every case, the particles were pushed by the gas fluxes, leading to a greater number of spatters on the upper side of the images than on the down sides.

Hence, from this study, it can be concluded that the size of the scan region has a strong influence on the spatter generation. Their deposition, as demonstrated in the literature, depends on the gas flux direction, and it is assumed that a combination of the part location on the build plate, the scanning direction, and the resulting gas flow direction may lead to a specific spatter distribution.

2.4. Conclusions and perspectives

A literature survey considering LPBF manufactured parts defects categories was performed. Regarding the microstructure impurities, in the case of reactive materials, a too large oxygen content may lead to invalid parts. This is especially a problem for Ti-6Al-4V grade 23, an alloy mainly used for medical applications.

The literature survey considered the powder manufacturing processes, and the variations of parts and powders with recycling processes, since it is known that while ageing, the oxygen content of reactive alloys rises. The oxidation mechanisms were also considered.

From the literature, it was concluded that several factors affect the oxidation kinetics, hence the oxygen content of powders and parts. The main factors are the heat and the oxygen sources, and several sources of both factors have been identified.

However, the specific moment of the oxidation of powders remained quite unknown. A first study was performed to determine if the powders can be contaminated without heat (i.e., without scanning and build plate heating).

With five recycling cycles, no specific rise in the oxygen content was found without heat, although a significant rise was observed when manufacturing a large lattice structure, to heat the surrounding powder.

It was concluded that the powder was mostly contaminated from the heat induced by the process.

In this regard, two strategies were formulated to limit the contamination in the LPBF process:

- Reduce the scanned surface at every layer;
- Provide dwell times (cooling times between consecutive layers).

Two experiments were performed to test these hypotheses. In the first one, three similar geometries with different scanned surfaces were manufactured. In the second experiment, the same geometry was produced twice, incorporation dwell times in one case, and no dwell times in the other.

First, from the second experiment, it was found that spatters generations were not identical from one layer to another. This behaviour was attributed to the difference in thermal history due scan vectors of different sizes. Indeed, the stripes in the scanning strategy were rotated at every layer from an angle of 115°.

Then, coloured particles (yellow and black) were observed using a DinoLite portable microscope. It was assumed that the change in colour reflects the growth of the oxide layer (yellow particles) or particles burnt during the process (black particles). Since these particles were of equivalent size as the grey particles (assumed non-contaminated particles), these particles may pass the filter of the sieving process. Indeed, the sieve mesh may not be able to block them. Hence, a specific isolation process based on the particles colour may be considered. Detailed chemical characterisations of these particles may be useful.

With the first experiment, it was shown that the larger the scanned surface, the greater the number of generated spatters in the powder. This finding may affect the orientation of the parts for medical applications. Indeed, since a larger scanned surface is prone to generate more spatters, the risk of spatters-originated defects within the parts is higher, and so is the contamination risk, assuming spatters are oxidized.

Different spatter generation behaviours were observed between two consecutive layers at two different productions, it is then assumed that the rotating angle of the scanning direction is responsible. Hence, both the scanned surface and the scanning direction may play a major role in the generation of spatters.

It was already known from the literature that the flying direction of the spatters was led by the scanning direction. Observations from this study suggest that the scanning direction also influences the generation of spatters.

From the second experiment, it cannot be determined which of the cases generated more spatters, from the «no-dwell time» and the «50 s dwell time» productions. Hence, it was assumed that either the dwell time had no influence on the generation of spatters, or the dwell time used here was not sufficient (the layer duration was multiplied by six using 50 s dwell time).

Finally, a preferential side for spatter landing was observed for every specimen. This behaviour seemed to be highly dependent on the location on the build plate. It is assumed that the gas flow over the build plate is not purely straight, and may be perturbed.

Measurements of the gas flow above the build plate are to be performed soon. Researchers [160] already demonstrated that these gas flow directions within the build chamber can be complex and influence the spatter deposition.

Overall, these studies showed the major influence of the heat on the oxidation of LPBF reactive powders. Based on this finding, a strategy to limit the contamination of the powders was identified as promising using variations of the same geometry and observing the number of generated spatters. More tests to validate this strategy are required.

The local thermal history seems to play an important role in the formation of spatters, as seen during the experiments where large spatters were observed on specific layers only.

Recycling processes adapted to the applications should be designed regarding the material and the standards. Indeed, the sieving and drying processes on their own may not be sufficient to effectively limit the number of contaminated powders in the subsequent productions.

2.5. References

[1] Galy, C., Le Guen, E., Lacoste, E. & Arvieu, C. Main defects observed in aluminum alloy parts produced by SLM: From causes to consequences. Addit. Manuf. 22, 165–175 (2018).

[2] Malekipour, E. & El-Mounayri, H. Common defects and contributing parameters in powder bed fusion AM process and their classification for online monitoring and control: a review. Int. J. Adv. Manuf. Technol. 95, 527–550 (2018).

[3] Grasso, M. & Colosimo, B. M. Process defects and in situ monitoring methods in metal powder bed fusion: A review. Meas. Sci. Technol. 28, (2017).

[4] GE Additive. Powder selection. GE Additive website https://www.ge.com/additive/powders-overview.

[5] 3D Systems. Metal Materials for 3D Printers and Additive Manufacturing. 3D Systems website https://www.3dsystems.com/materials/metal.

[6] EOS. Additive Manufacturing With Aluminum. EOS website https://www.eos.info/en/additive-manufacturing/3d-printing-metal/dmls-metal-materials/aluminium-al.

[7] Zäh, M. F. & Lutzmann, S. Modelling and simulation of electron beam melting. Prod. Eng. 4, 15–23 (2010).

[8] Qiu, C., Adkins, N. J. E. & Attallah, M. M. Microstructure and tensile properties of selectively laser-melted and of HIPed laser-melted Ti-6Al-4V. Mater. Sci. Eng. A 578, 230–239 (2013).

[9] Du Plessis, A. *et al.* Laboratory X-ray tomography for metal additive manufacturing: round robin test. Addit. Manuf. 30, (2019).

[10] Stef, J. Fusion Laser Selective de poudres de TA6V : microstructure et mécanismes de formation des porosités en lien avec les paramètres du procédé SLM et les propriétés structurales. Thèse de Doctorat de l'Université de Bordeaux (2018).

[11] Stef, J. *et al.* Mechanism of porosity formation and influence on mechanical properties in selective laser melting of Ti-6Al-4V parts. Mater. Des. 156, 480–493 (2018).

[12] Leung, C. L. A. *et al.* In situ X-ray imaging of defect and molten pool dynamics in laser additive manufacturing. Nat. Commun. 9, 1–9 (2018).

[13] Leung, C. L. A. *et al.* The effect of powder oxidation on defect formation in laser additive manufacturing. Acta Mater. 166, 294–305 (2019).

[14] Li, X. P., O'Donnell, K. M. & Sercombe, T. B. Selective laser melting of Al-12Si alloy: Enhanced densification via powder drying. Addit. Manuf. 10, 10–14 (2016).

[15] Chen, G. *et al.* A pore morphological study of gas-atomized Ti-6Al-4V powders by scanning electron microscopy and synchrotron X-ray computed tomography. Powder Technol. 330, 425–430 (2018).

[16] Moussaoui, K., Rubio, W., Mousseigne, M., Sultan, T. & Rezai, F. Effects of Selective Laser Melting additive manufacturing parameters of Inconel 718 on porosity , microstructure and mechanical properties. Mater. Sci. Eng. A 735, 182–190 (2018).

[17] Song, B. *et al.* Differences in microstructure and properties between selective laser melting and traditional manufacturing for fabrication of metal parts: A review. Front. Mech. Eng. 10, 111–125 (2015).

[18] Thijs, L., Kempen, K., Kruth, J. P. & Van Humbeeck, J. Fine-structured aluminium products with controllable texture by selective laser melting of pre-alloyed AlSi10Mg powder. Acta Mater. 61, 1809–1819 (2013).

[19] Sharratt, B. M. Non-Destructive Techniques and Technologies for Qualification of Additive Manufactured Parts and Processes: A Literature Review. Dep. Natl. Def. Canada 55, 91–127 (2015).

[20] Casati, R., Lemke, J. & Vedani, M. Microstructure and Fracture Behavior of 316L Austenitic Stainless Steel Produced by Selective Laser Melting. J. Mater. Sci. Technol. 32, 738–744 (2016).

[21] Sanaei, N. & Fatemi, A. Analysis of the effect of internal defects on fatigue performance of additive manufactured metals. Mater. Sci. Eng. A 785, 139385 (2020).

[22] Kahlin, M. *et al.* Improved fatigue strength of additively manufactured Ti6Al4V by surface post processing. Int. J. Fatigue 134, 105497 (2020).

[23] Sharratt, B. M. Non-Destructive Techniques and Technologies for Qualification of Additive Manufactured Parts and Processes: A Literature Review. Dep. Natl. Def. Canada 55, 91–127 (2015).

[24] Dubiel, B. & Sieniawski, J. Precipitates in Additively Manufactured Inconel 625 Superalloy. Materials (Basel). 12, 1144 (2019).

[25] Keller, T. *et al.* Application of finite element , phase-field , and CALPHAD-based methods to additive manufacturing of Ni-based superalloys. Acta Mater. 139, 244–253 (2017).

[26] Amato, K. N. *et al.* Microstructures and mechanical behavior of Inconel 718 fabricated by selective laser melting. Acta Mater. 60, 2229–2239 (2012).

[27] Bi, G., Sun, C. N., Chen, H. chi, Ng, F. L. & Ma, C. C. K. Microstructure and tensile properties of superalloy IN100 fabricated by micro-laser aided additive manufacturing. Mater. Des. 60, 401–408 (2014).

[28] AlMangour, B. & Yang, J. M. Understanding the deformation behavior of 17-4 precipitate hardenable stainless steel produced by direct metal laser sintering using micropillar compression and TEM. Int. J. Adv. Manuf. Technol. 90, 119–126 (2017).

[29] Karlsson, J., Norell, M., Ackelid, U., Engqvist, H. & Lausmaa, J. Surface oxidation behavior of Ti – 6Al – 4V manufactured by Electron Beam Melting (EBM ®). J. Manuf. Process. 17, 120–126 (2015).

[30] Takahashi, T., Minamino, Y., Hirasawa, H. & Ouchi, T. High-Temperature Oxidation and Its Kinetics Study of Ti-Al and Ti-V Alloys in Air. Mater. Trans. 55, 290–297 (2014).

[31] Tang, M. & Pistorius, P. C. Oxides, porosity and fatigue performance of AlSi10Mg parts produced by selective laser melting. Int. J. Fatigue 94, 192–201 (2017).

[32] Jia, Q. & Gu, D. Selective laser melting additive manufactured Inconel 718 superalloy parts: High-temperature oxidation property and its mechanisms. Opt. Laser Technol. 62, 161–171 (2014).

[33] Chasoglou, D., Hryha, E. & Nyborg, L. Effect of process parameters on surface oxides on chromium-alloyed steel powder during sintering. Mater. Chem. Phys. 138, 405–415 (2013).

[34] Haines, M. P., Peter, N. J., Babu, S. S. & Jägle, E. A. In-situ synthesis of oxides by reactive process atmospheres during L-PBF of stainless steel. Addit. Manuf. 33, 101178 (2020).

[35] Guillén, T. *et al.* Removal of the α-Case layer from precision-cast cellular TiAl6Nb7 to be used for biomedical applications. Adv. Eng. Mater. 11, 680–684 (2009).

[36] Kruth, J. P. *et al.* Selective laser melting of iron-based powder. in Journal of Materials Processing Technology vol. 149 616–622 (2004).

[37] Tolochko, N. K. *et al.* Balling processes during selective laser treatment of powders. Rapid Prototyp. J. 10, 78–87 (2004).

[38] Kruth, J. P., Levy, G., Klocke, F. & Childs, T. H. C. Consolidation phenomena in laser and powder-bed based layered manufacturing. CIRP Ann. - Manuf. Technol. 56, 730–759 (2007).

[39] Li, R., Liu, J., Shi, Y., Wang, L. & Jiang, W. Balling behavior of stainless steel and nickel powder during selective laser melting process. Int. J. Adv. Manuf. Technol. 59, 1025–1035 (2012).

[40] Zhou, X., Liu, X., Zhang, D., Shen, Z. & Liu, W. Balling phenomena in selective laser melted tungsten. J. Mater. Process. Technol. 222, 33–42 (2015).

[41] Hong, W., Lee, Y. T. & Gong, H. A study of the staircase effect induced by material shrinkage in rapid prototyping. Rapid Prototyp. J. 11, 82–89 (2005).

[42] Simchi, A., Petzoldt, F. & Pohl, H. On the development of direct metal laser sintering for rapid tooling. J. Mater. Process. Technol. 141, 319–328 (2003).

[43] Zhu, H. H., Lu, L. & Fuh, J. Y. H. Study on shrinkage behaviour of direct laser sintering metallic powder. Proc. Inst. Mech. Eng. Part B J. Eng. Manuf. 220, 183–190 (2006).

[44] Sharratt, B. M. Non-Destructive Techniques and Technologies for Qualification of Additive Manufactured Parts and Processes: A Literature Review. Dep. Natl. Def. Canada 55, 91–127 (2015).

[45] Thomas, D. The Development of Design Rules for Selective Laser Melting. Ph.D. Thesis (University of Wales Institute, Cardiff (2012).

[46] Yasa, E., Deckers, J., Craeghs, T., Badrossamay, M. & Kruth, J.-P. Investigation on occurence of elevated edges in selective laser melting. 27 (2009).

[47] Triantaphyllou, A. *et al.* Surface texture measurement for additive manufacturing. Surf. Topogr. Metrol. Prop. 3, (2015).

[48] Kahlin, M. *et al.* Improved fatigue strength of additively manufactured Ti6Al4V by surface post processing. Int. J. Fatigue 134, 105497 (2020).

[49] Kempen, K., Thijs, L., Van Humbeeck, J. & Kruth, J. P. Mechanical Properties of AlSi10Mg Produced by Selective Laser Melting. Phys. Procedia 39, 439–446 (2012).

[50] Thijs, L., Kempen, K., Kruth, J. P. & Van Humbeeck, J. Fine-structured aluminium products with controllable texture by selective laser melting of pre-alloyed AlSi10Mg powder. Acta Mater. 61, 1809–1819 (2013).

[51] Prashanth, K. G., Scudino, S. & Eckert, J. Defining the tensile properties of Al-12Si parts produced by selective laser melting. Acta Mater. 126, 25–35 (2017).

[52] Giovagnoli, M. *et al.* On the Anisotropic Impact Behavior of an Additively Manufactured AlSi10Mg Alloy in Different Heat Treatment Conditions. J. Mater. Eng. Perform. (2022).

[53] Chen, L. Y. *et al.* Anisotropic response of Ti-6Al-4V alloy fabricated by 3D printing selective laser melting. Mater. Sci. Eng. A 682, 389–395 (2017).

[54] Mertens, A. *et al.* Mechanical properties of alloy Ti-6Al-4V and of stainless steel 316L processed by selective laser melting: Influence of out-of-equilibrium microstructures. Powder Metall. 57, 184–189 (2014).

[55] Ronneberg, T., M. Davies, C. & A. Hooper, P. Revealing relationships between porosity, microstructure and mechanical properties of laser powder bed fusion 316L stainless steel through heat treatment. Addit. Manuf. 189, 100820 (2019).

[56] Suryawanshi, J., Prashanth, K. G. & Ramamurty, U. Mechanical behavior of selective laser melted 316L stainless steel. Mater. Sci. Eng. A 696, 113–121 (2017).

[57] Chlebus, E., Gruber, K., Kuznicka, B., Kurzac, J. & Kurzynowski, T. Effect of heat treatment on microstructure and mechanical properties of Inconel 718 processed by selective laser melting. Mater. Sci. Eng. A 639, 647–655 (2015).

[58] Mercelis, P. & Kruth, J. P. Residual stresses in selective laser sintering and selective laser melting. Rapid Prototyp. J. 12, 254–265 (2006).

[59] Vrancken, B. Study of Residual Stresses in Selective Laser Melting. PhD Thesis; KU Leuven Arenberg Doctoral School Faculty of Engineering Science (2016). doi:10.1007/s11277-005-0744-1.

[60] Parry, L., Ashcroft, I., Bracket, D. & Wildman, R. D. Investigation of Residual Stresses in Selective Laser Melting. Thesis University of Nottingham (2018).

[61] Kahnert, M., Lutzmann, S. & Zaeh, M. F. Layer formations in electron beam sintering. Proc. 18th Solid Free. Fabr. Symp. 88–99 (2007) doi:10.3386/w2977.

[62] Ali, H., Ma, L., Ghadbeigi, H. & Mumtaz, K. In-situ residual stress reduction, martensitic decomposition and mechanical properties enhancement through high temperature powder bed pre-heating of Selective Laser Melted Ti6Al4V. Mater. Sci. Eng. A 695, 211–220 (2017).

[63] Li, C., Liu, Z. Y., Fang, X. Y. & Guo, Y. B. Residual Stress in Metal Additive Manufacturing. Procedia CIRP 71, 348–353 (2018).

[64] Gong, H., Rafi, K., Gu, H., Starr, T. & Stucker, B. Analysis of defect generation in Ti-6Al-4V parts made using powder bed fusion additive manufacturing processes. Addit. Manuf. 1, 87–98 (2014).

[65] Tammas-Williams, S., Withers, P. J., Todd, I. & Prangnell, P. B. Porosity regrowth during heat treatment of hot isostatically pressed additively manufactured titanium components. Scr. Mater. 122, 72–76 (2016).

[66] Dawes, J., Bowerman, R. & Trepleton, R. Introduction to the Additive Manufacturing Powder Metallurgy Supply Chain. Johnson Matthey Technol. Rev. 59, 243–256 (2015).

[67] Popovich, A. & Sufiiarov, V. Metal Powder Additive Manufacturing. New Trends 3D Print. (2016) doi:10.5772/63337.

[68] Angelo, P. C. & Subramanian, R. Powder Metallurgy : Science, Technology and Applications. (2015).

[69] Bertolini, M. *et al.* The FFC Cambridge Process for Production of Low Cost Titanium and Titanium Powders. Key Eng. Mater. 436, 75–83 (2010).

[70] Sandvik. Sandvik to invest in metal powder plant in Sandviken, Sweden. https://www.materials.sandvik/en/news-media/news-and-stories/archive/2018/02/sandvik-to-invest-in-metal-powder-plant-in-sandviken-sweden/ (2018).

[71] Eramet. Eramet : Aubert & Duval et PyroGenesis signent un accord de partenariat technique et commercial pour la distribution de poudres titane par atomisation plasma. Communiqué de presse 30–31 http://www.eramet.com/communiques-de-presse/eramet-aubert-duval-et-pyrogenesis-signent-un-accord-de-partenariat-technique (2019).

[72] CNPC. CNPC nears completion of facility for AM metal powder production. http://www.cnpcpowder.com/news/corporate/118.html (2018).

[73] Tekna. Aperam and Tekna are announcing the signature of a Memorandum of Understanding (MoU) on industrial cooperation regarding spherical powder manufacturing of Nickel Superalloys and Steels dedicated to new advanced manufacturing technologies. 1–5 http://www.tekna.com/news/aperam-and-tekna-are-announcing-the-signature-of-a-mou-on-industrial-cooperation-regarding-spherical-powder-manufacturing-of-nickel-superalloys-and-steels (2019).

[74] Tekna. Tekna officially inaugurated the expansion of its second plant. 1–5 www.tekna.com/news/tekna-officially-inaugurated-the-expansion-of-its-second-plant 1/5 (2019).

[75] Deborde, A. L'atomisation de poudres d'alliages de titane. MetalBlog https://metalblog.ctif.com/2018/11/26/latomisation-des-alliages-de-titane/ (2018).

[76] Seyda, V. Werkstoff- und Prozessverhalten von Metallpulvern in der laseradditiven Fertigung. PhD Thesis (Springer Berlin Heidelberg, 2018). doi:10.1007/978-3-662-58233-6.

[77] Baitimerov, R. *et al.* Influence of powder characteristics on processability of AlSi12 alloy fabricated by selective laser melting. Materials (Basel). 11, 1–14 (2018).

[78] Böhler. Additive Manufacturing Powder. https://www.bohler.fr/media/ST036E_AMPO_Additive-Manufacturing.pdf (2018).

[79] Carpenter Additive. Methods of AM metal Powder production. https://www.carpenteradditive.com/technical-library/powder-production/ (2016).

[80] Hedberg, Y. Stainless Steel in Biological Environments – Relation between Material Characteristics , Surface Chemistry and Toxicity. KTH Royal Institute of Technology (2014).

[81] Raymor AP&C. Raymor AP & C : Leading the way with plasma atomised Ti spherical powders for MIM. Powder Injection Moulding International December 57 (2011).

[82] Clayton, J. Optimising metal powders for additive manufacturing. Met. Powder Rep. 69, 14–17 (2014).

[83] Seyda, V., Herzog, D. & Emmelmann, C. Relationship between powder characteristics and part properties in laser beam melting of Ti-6Al-4V, and implications on quality. J. Laser Appl. 29, 022311 (2017).

[84] Tekna. Our ICP Technology | Tekna. 1–7 www.tekna.com/our-icp-technology (2019).

[85] Barclift, M., Joshi, S., Simpson, T. & Dickman, C. Cost Modeling and Depreciation for Reused Powder Feedstocks in Powder Bed Fusion Additive Manufacturing. Proceeding 27th Annu. Int. solid Free. Fabr. Symp. 2007–2028 (2016) doi:10.7748/nr.2.2.13.s3.

[86] Sun, P., Fang, Z. Z., Zhang, Y. & Xia, Y. Review of the Methods for Production of Spherical Ti and Ti Alloy Powder. Jom 69, 1853–1860 (2017).

[87] Dietrich, S., Wunderer, M., Huissel, A. & Zaeh, M. F. A New Approach for a Flexible Powder Production for Additive Manufacturing. Procedia Manuf. 6, 88–95 (2016).

[88] Powell, D., Rennie, A. E. W., Geekie, L. & Burns, N. Understanding powder degradation in metal additive manufacturing to allow the upcycling of recycled powders. J. Clean. Prod. 268, 122077 (2020).

[89] Petrovic, V. *et al.* Additive layered manufacturing: Sectors of industrial application shown through case studies. Int. J. Prod. Res. 49, 1061–1079 (2011).

[90] Asgari, H., Baxter, C., Hosseinkhani, K. & Mohammadi, M. On microstructure and mechanical properties of additively manufactured AlSi10Mg_200C using recycled powder. Mater. Sci. Eng. A 707, 148–158 (2017).

[91] Lutter-Günther, M., Gebbe, C., Kamps, T., Seidel, C. & Reinhart, G. Powder recycling in laser beam melting: strategies, consumption modeling and influence on resource efficiency. Prod. Eng. 12, 377–389 (2018).

[92] Okello, A. & Samper, V. Effective Powder Reuse Strategies. GE Addit. White Paper. 1–14 (2021).

[93] Renishaw. Investigating the effects of multiple re-use of Ti6Al4V powder in additive manufacturing. Renishaw White Paper. 1–10 (2016) doi:10.6028/jres.119.018.

[94] Jacob, G., Brown, C. U., Donmez, M. A., Watson, S. S. & Slotwinski, J. Effects of powder recycling on stainless steel powder and built material properties in metal powder bed fusion processes. NIST Advanced Manufacturing Series 100-6 http://nvlpubs.nist.gov/nistpubs/ams/NIST.AMS.100-6.pdf (2017).

[95] Vock, S., Klöden, B., Kirchner, A., Weißgärber, T. & Kieback, B. Powders for powder bed fusion: a review. Prog. Addit. Manuf. 0, 0 (2019).

[96] Riener, K., Oswald, S., Winkler, M. & Leichtfried, G. J. Influence of storage conditions and reconditioning of AlSi10Mg powder on the quality of parts produced by laser powder bed fusion (LPBF). Addit. Manuf. 39, (2021).

[97] Cordova, L., Bor, T., Campos, M. & Tinga, T. Drying strategies to reduce the formation of hydrogen porosity in Al alloys. EasyChair Prepr. 973, 8–10 (2019).

[98] Cordova, L., Bor, T., de Smit, M., Campos, M. & Tinga, T. Measuring the spreadability of pre-treated and moisturized powders for laser powder bed fusion. Addit. Manuf. (2020).

[99] Bauer, D. M. *et al.* Investigations of aging behaviour for aluminium powders during an atmosphere simulation of the LBM process. Powder Metall. 60, 175–183 (2017).

[100] Ardila, L. C. *et al.* Effect of IN718 recycled powder reuse on properties of parts manufactured by means of Selective Laser Melting. Phys. Procedia 56, 99–107 (2014).

[101] Gruber, K., Smolina, I., Kasprowicz, M. & Kurzynowski, T. Evaluation of Inconel 718 Metallic Powder to Optimize the Reuse of Powder and to Improve the Performance and Sustainability of the Laser Powder Bed Fusion (LPBF) Process. Materials (Basel). 14, (2021).

[102] Renderos, M., Girot, F., Lamikiz, A., Torregaray, A. & Saintier, N. Ni Based Powder Reconditioning and Reuse for LMD Process. Phys. Procedia 83, 769–777 (2016).

[103] Choi, H., Kim, S., Goto, M. & Kim, S. Effect of powder recycling on room and elevated temperature damage tolerability of Inconel 718 alloy fabricated by laser powder bed fusion. Mater. Charact. 171, (2021).

[104] Ghods, S. *et al.* Powder reuse and its contribution to porosity in additive manufacturing of Ti6Al4V. Materialia 15, (2021).

[105] Tang, H. P. *et al.* Effect of Powder Reuse Times on Additive Manufacturing of Ti-6Al-4V by Selective Electron Beam Melting. JOM 67, 555–563 (2015).

[106] Seyda, V., Kaufmann, N. & Emmelmann, C. Investigation of Aging Processes of Ti-6Al-4V Powder Material in Laser Melting. Phys. Procedia 39, 425–431 (2012).

[107] Delacroix, T., Lomello, F., Schuster, F., Maskrot, H. & Garandet, J.-P. Influence of powder recycling on 316L stainless steel feedstocks and printed parts in laser powder bed fusion. Addit. Manuf. 50, 102553 (2022).

[108] Weiss, C., Haefner, C. L. & Munk, J. On the Influence of AlSi10Mg Powder Recycling Behavior in the LPBF Process and Consequences for Mechanical Properties. Jom (2022) doi:10.1007/s11837-021-05080-4.

[109] Fiegl, T., Franke, M., Raza, A., Hryha, E. & Körner, C. Effect of AlSi10Mg0.4 long-term reused powder in PBF-LB/M on the mechanical properties. Mater. Des. 212, 110176 (2021).

[110] Del Re, F. *et al.* Statistical approach for assessing the effect of powder reuse on the final quality of AlSi10Mg parts produced by laser powder bed fusion additive manufacturing. Int. J. Adv. Manuf. Technol. 97, 2231–2240 (2018).

[111] Carrion, P. E., Soltani-Tehrani, A., Phan, N. & Shamsaei, N. Powder Recycling Effects on the Tensile and Fatigue Behavior of Additively Manufactured Ti-6Al-4V Parts. Jom 71, 963–973 (2018).

[112] Popov, V. V., Katz-Demyanetz, A., Garkun, A. & Bamberger, M. The effect of powder recycling on the mechanical properties and microstructure of electron beam melted Ti-6Al-4 V specimens. Addit. Manuf. 22, 834–843 (2018).

[113] Holt, B. D. & Goodspeed, H. T. Determination of Nitrogen, Oxygen, and Hydrogen in Metals by Inert Gas Fusion. Anal. Chem. 35, 1510–1513 (1963).

[114] O 'leary, R., Setchi, R., Prickett, P., Hankins, G. & Jones, N. An Investigation into the Recycling of Ti-6Al-4V Powder Used Within SLM to Improve Sustainability. SDM'2015 2nd Int. Conf. Sustain. Des. Manuf. 1–12 (2015) doi:10.1016/j.surfcoat.2006.07.216.

[115] Quintana, O. A., Alvarez, J., Mcmillan, R., Tong, W. & Tomonto, C. Effects of Reusing Ti-6Al-4V Powder in a Selective Laser Melting Additive System Operated in an Industrial Setting. Jom 70, 1863–1869 (2018).

[116] Slotwinski, J. A. *et al.* Application of physical and chemical characterization techniques to metallic powders. AIP Conf. Proc. 1581 33, 1184–1190 (2014).

[117] Carroll, P. A., Brown, P., Ng, G. & Scudamore, R. The effect of powder recycling in direct metal laser deposition on powder and manufactured part characteristics. http://eprints.lancs.ac.uk/59645/ (2006).

[118] Mellin, P. *et al.* COPGLOW and XPS investigation of recycled metal powder for selective laser melting. Powder Metall. 60, 223–231 (2017).

[119] LPW. LPW TECHNOLOGY Case Study 05: Powder degradation. vol. 44 https://www.lpwtechnology.com/wp-content/uploads/2016/09/LPW-Case-Study-05.pdf (2015).

[120] Sun, Y., Aindow, M. & Hebert, R. J. The effect of recycling on the oxygen distribution in Ti-6Al-4V powder for additive manufacturing. Mater. High Temp. 35, 217–224 (2018).

[121] Maamoun, A. H., Elbestawi, M., Dosbaeva, G. K. & Veldhuis, S. C. Thermal post-processing of AlSi10Mg parts produced by Selective Laser Melting using recycled powder. Addit. Manuf. 21, 234–247 (2018).

[122] Prashanth, K. G., Scudino, S., Maity, T., Das, J. & Eckert, J. Is the energy density a reliable parameter for materials synthesis by selective laser melting? Mater. Res. Lett. 5, 386–390 (2017).

[123] Spierings, A. B. & Levy, G. Comparison of density of stainless steel 316L parts produced with selective laser melting using different powder grades. Solid Free. Fabr. Proc. 342–353 (2009).

[124] Gu, H. *et al.* Effects of powder variation on the microstructure and tensile strength of Ti-6Al-4V parts fabricated by selective laser melting. Int. J. Powder Metall. 51, 35–42 (2015).

[125] Muñiz-Lerma, J., Nommeots-Nomm, A., Waters, K. & Brochu, M. A Comprehensive Approach to Powder Feedstock Characterization for Powder Bed Fusion Additive Manufacturing: A Case Study on AlSi7Mg. Materials (Basel). 11, 2386 (2018).

[126] Dietrich, K. *et al.* The influence of oxygen on the chemical composition and mechanical properties of Ti-6Al-4V during laser powder bed fusion (L-PBF). Addit. Manuf. 32, (2020).

[127] Kempen, K. Expanding the materials palette for Selective Laser Melting of metals. PhD Thesis Katholieke Universiteit Leuven (2015).

[128] Totten, G. E. & MacKenzie, D. S. Handbook of Aluminum: Volume 1 - Physical Metallurgy and Processes. (Marcel Dekker, Inc., 2003).

[129] Le, V. D. Etude de l 'influence des hétérogénéités microstructurales sur la tenue en fatigue à grand nombre de cycles des alliages d'aluminium de fonderie. Thèse de doctorat Ecole Nationale Supérieure d'Arts et Métiers (2016).

[130] Benoist, V. Développement d'une méthodologie pour la fabrication additive dans un contexte de fabricaion de pièces métalliques par usinage. (Université de Toulouse, 2020).

[131] Cordova, L., Campos, M. & Tinga, T. Revealing the Effects of Powder Reuse for Selective Laser Melting by Powder Characterization. Jom 71, 1062–1072 (2019).

[132] Lütjering, G. & Williams, J. C. Titanium - 2nd Edition. (2007).

[133] Regniere, M. Impact du conditionnement de poudres de Ti6Al4V sur le procédé de fusion sélective la-ser. Thèse de Doctorat de l'Université de Lyon (2018).

[134] Casadebaigt, A. Etude de l'oxidation à chaud d'échantillons en alliage TA6V élaborés par fabrication additive. Conséquences sur les propriétés mécaniques. Thèse de doctorat de l'université de Toulouse (2020).

[135] Boyer, R., Welsch, G. & Collings, E. W. Materials Properties Handbook: Titanium Alloys. (ASM International, 1994).

[136] Oh, J. *et al.* Oxygen Effects on the Mechanical Properties and Lattice Strain of Ti and Ti-6Al-4V. Met. Mater. Int. 17, 733–736 (2011).

[137] P. Laheurte, W. Elmay, F. Prima et T. Gloriant. Titane et alliages des matériaux de choix pour les applications médicales. Techniques de l'ingénieur Métaux et alliages, matériaux magnétiques et multimatériaux, base documentaire : TIB357DUO, ref. article : M4781 (2017).

[138] ASTM. ASTM B265-20a - Standard Specification for Titanium and Titanium Alloy Strip, Sheet, and Plate. 12 (2020) doi:10.1520/B0265-20A.

[139] ASTM. ASTM F 3001 - Standard Specification for Additive Manufacturing Titanium-6 Aluminum-4 Vanadium ELI (Extra Low Interstitial) with Powder Bed Fusion. (2014).

[140] ASTM. ASTM F2924-12 -- Specification for additive manufacturing Titanium-6 Aluminum-4 Vanadium with powder bed fusion. (2012).

[141] Casadebaigt, A., Hugues, J. & Monceau, D. Influence of Microstructure and Surface Roughness on Oxidation Kinetics at 500–600 °C of Ti–6Al–4V Alloy Fabricated by Additive Manufacturing. Oxid. Met. 90, 633–648 (2018).

[142] Sarrazin, P., Galerie, A. & Fouletier, J. Les mécanismes de la corrosion sèche - Une approche cinétique. (2000).

[143] Baïlon, J.-P. & Dorlot, J.-M. Des Matériaux. (Presses Internationales Polytechnique, 2000).

[144] Xiao, J. Etude de la cinétique d'oxydation et contraintes résiduelles de l'Inconel 600 sous air humide. Ph.D Université Paris-Sud (Université Paris-Sud, 2015).

[145] Beranger, G. & Lacombe, P. Contribution a l'etude de la cinetique de l'oxydation du zirconium α et de la diffusion de l'oxygene dans le metal sous-jacent a l'oxyde. J. Nucl. Mater. 16, 190–207 (1965).

[146] Cordova, L. Exploring the influence of powder properties and handling on the selective laser melting process. Ph.D University of Twente (University of Twente, 2020).

[147] Tarabay, J., Peres, V. & Pijolat, M. Oxidation of stainless steel powder. Oxid. Met. 80, 311–322 (2013).

[148] Derimow, N. & Hrabe, N. Oxidation in Reused Powder Bed Fusion Additive Manufacturing Ti-6Al-4V Feedstock: A Brief Review. Jom 73, 3618–3638 (2021).

[149] Gruber, H., Henriksson, M., Hryha, E. & Nyborg, L. Effect of Powder Recycling in Electron Beam Melting on the Surface Chemistry of Alloy 718 Powder. Metall. Mater. Trans. A Phys. Metall. Mater. Sci. 50, 4410–4422 (2019).

[150] Simonelli, M. *et al.* A Study on the Laser Spatter and the Oxidation Reactions During Selective Laser Melting of 316L Stainless Steel , AlSi10Mg , and Ti-6Al-4V. Metall. Mater. Trans. A (2015) doi:10.1007/s11661-015-2882-8.

[151] Lutter-Günther, M. *et al.* Spatter formation during laser beam melting of AlSi10Mg and effects on powder quality. Procedia CIRP 74, 33–38 (2018).

[152] Gasper, A. N. D. *et al.* Spatter and oxide formation in laser powder bed fusion of Inconel 718. Addit. Manuf. 24, 446–456 (2018).

[153] Gasper, A. N. D. *et al.* Oxide and spatter powder formation during laser powder bed fusion of Hastelloy X. Powder Technol. 354, 333–337 (2019).

[154] Schwerz, C. *et al.* In-situ detection of redeposited spatter and its influence on the formation of internal flaws in laser powder bed fusion. Addit. Manuf. 47, 102370 (2021).

[155] Raza, A. *et al.* Degradation of AlSi10Mg powder during laser based powder bed fusion processing. Mater. Des. 198, (2021).

[156] Anwar, A. Bin & Pham, Q. Selective laser melting of AlSi10Mg : Effects of scan direction , part placement and inert gas flow velocity on tensile strength. J. Mater. Process. Tech. 240, 388–396 (2017).

[157] Gunenthiram, V. *et al.* Experimental analysis of spatter generation and melt-pool behavior during the powder bed laser beam melting process. J. Mater. Process. Technol. 251, 376–386 (2018).

[158] Khairallah, S. A. *et al.* Controlling interdependent meso-nanosecond dynamics and defect generation in metal 3D printing. Science. 368, 660–665 (2020).

[159] Anwar, A. Bin & Pham, Q. C. Study of the spatter distribution on the powder bed during selective laser melting. Addit. Manuf. 22, 86–97 (2018).

[160] Chien, C.-Y., Le, T.-N., Lin, Z.-H. & Lo, Y.-L. Numerical and experimental investigation into gas flow field and spattering phenomena in laser powder bed fusion processing of Inconel 718. Mater. Des. 210, 110107 (2021).

[161] Ferrar, B., Mullen, L., Jones, E., Stamp, R. & Sutcliffe, C. J. Gas flow effects on selective laser melting (SLM) manufacturing performance. J. Mater. Process. Technol. 212, 355–364 (2012).

[162] Raza, A., Pauzon, C., Hryha, E., Markström, A. & Forêt, P. Spatter oxidation during laser powder bed fusion of Alloy 718: Dependence on oxygen content in the process atmosphere. Addit. Manuf. 48, (2021).

[163] Renishaw. AlSi10Mg-0403 powder for additive manufacturing. Renishaw data sheet https://www.renishaw.fr/fr/fiches-techniques-fabrication-additive--17862 (2015).

[164] Khairallah, S. A., Anderson, A. T., Rubenchik, A. & King, W. E. Laser powder-bed fusion additive manufacturing: Physics of complex melt flow and formation mechanisms of pores, spatter, and denudation zones. Acta Mater. 108, 36–45 (2016).

[165] Diamanti, M. V., Del Curto, B. & Pedeferri, M. P. Interference colors of thin oxide layers on titanium. Colour Res. Appl. 33, 221–228 (2008).

Chapter III

Table of contents

III. Simulation of beam supports damage and breakage

3.1. Introduction 76
3.2. State of the art 80
3.2.1. LPBF general modelling methods 80
3.2.2. Supports design, modelling and optimisation 82
3.3. Study case: hydraulic joint 83
3.3.1. Description 83
3.3.2. Numerical simulation using commercial codes 87
3.3.2.1. Results of each software 87
3.3.2.2. Example of simulation results with Simufact Additive 88
3.4. The numerical models developed and experimental data 91
3.4.1. Numerical method 91
3.4.1.1. Models, meshing and process sequence 91
3.4.1.2. Mechanical properties 93
3.4.1.3. Considering the supports overlapping 95
3.4.1.4. Overcoming buckling-based numerical instabilities: proposed solutions 96
3.4.2. Numerical results and experimental comparison 98
3.4.2.1. 3D-voxel elements simulation results 98
3.4.2.2. 1D-beam elements simulation results 99
3.4.2.3. Multi-supports set up: supports group's mechanical behaviour 101
3.4.2.4. Individual beam support mechanical characterisation 104
3.4.2.5. Beam supports mechanical sensibility 106
3.5. Conclusions and perspectives 107
3.6. References 110

CHAPTER III

SIMULATION OF BEAM SUPPORTS DAMAGE AND BREAKAGE

3.1. Introduction

An important characteristic of the Laser Powder Bed Fusion (LPBF) process is its requiring of supports anchoring the parts to the build plate surface [1]. Supports used during the process have three main functions [2] [3].

- Anchoring the over-hanged surfaces to the build plate.
- Reducing part's distortion.
- Conducting heat away from the upper material.

Most of the time, supports are structures between the parts and the build plate, manufactured with the part during the LPBF process. Often, they are connected to the parts with teeth (as illustrated in Figure 3.1) to ease the removal process. They are to be present in sufficient number on overhanging regions, namely regions inclined with an angle below 45° with the horizontal plane [15][16].

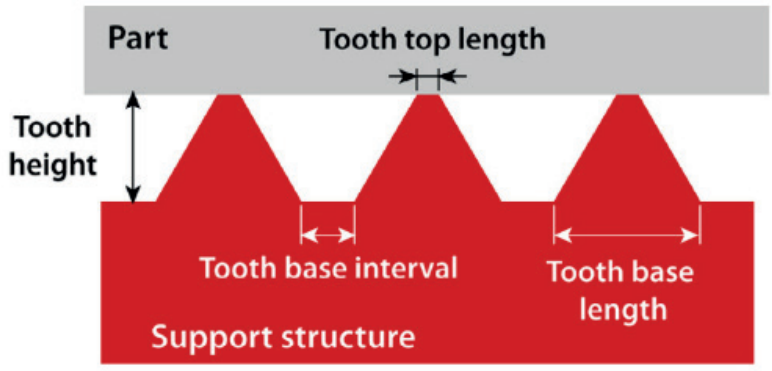

Figure 3.1: Illustration of supports teeth from [16].

Sufficient number of supports are required; however, their manufacturing should use as little time as possible, and spend the minimum powder material. Also, their design should ease the removing process, without damaging the part. Supports geometries are mostly linked to the engineers' experiences. Some of them are easier to remove, others consume less material, others are faster to produce.

Numerous supports geometries could be used. Most of them are presented in the works conducted by Jiang [2], Calignano [16], and Leary [17]. Some examples of support patterns are displayed in Figure 3.2.

Some supports are rarely seen in industrial applications (lattice, cellular, «Y» and «IY» types for instance), while others, such as «Beam» type, «Block» type or «Contour» type are common in the industry.

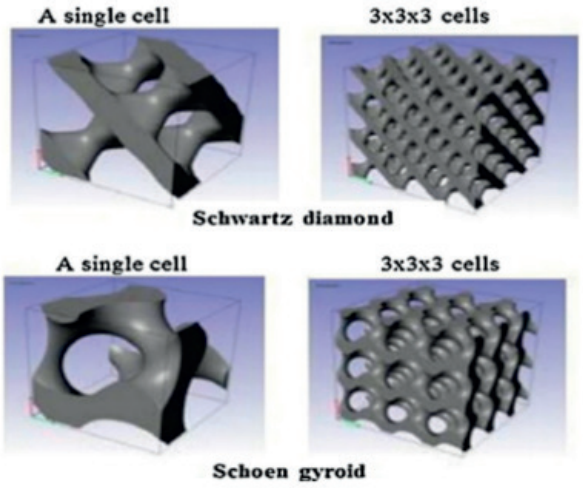

(a) Lattice type.

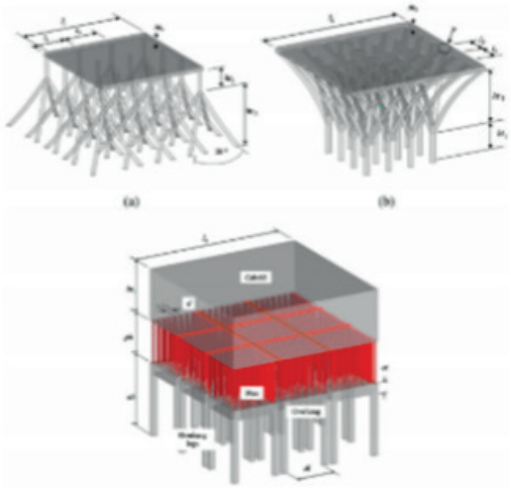

(b) «Y», «IY» and Beam types.

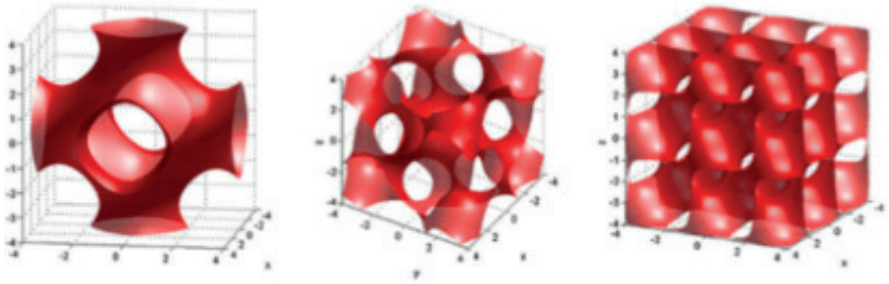

(c) Cellular type.

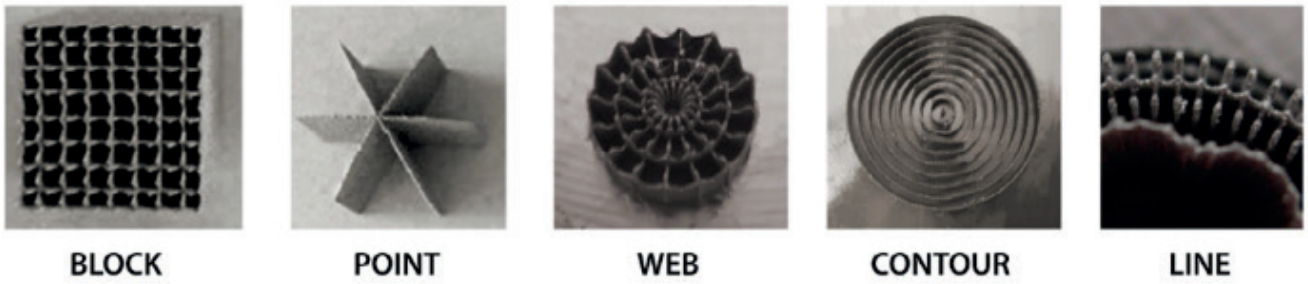

(d) Common supports types.

Figure 3.2: Example of support structure patterns from [2][16].

Although the generation of supports can be helped by most industrial software, they are usually tuned by the user to withstand the process stresses, and the structure can become complicated due to the part's shape and

the user experience, as illustrated in Figure 3.3 showing a part supported by Halbronn's engineering team in Ti-6Al-4V for a previous PhD research work [4]. Also, most of the time, case-by-case supplementary constraints are to be considered, such as the proximity of other parts on the build plate.

Since supports manufacturing requires scanning time, post-processing steps and consumes material, it generates non-negligible costs [5]. For instance, in the configuration displayed in Figure 3.3, the supports manufacturing time represented nearly 12% of the total manufacturing time [4]. Recent machine manufacturers [6]-[7] and a few studies have been focusing on ways to avoid or to minimize their usage [8]-[9] and the mechanical post-processing steps [10]-[14].

Supports could help prevent the occurring of parts deformation, warping and cracking [18] which are part of the main four LPBF defect types (including porosity [19]).

The following study will focus on beam-like (also named cone or strut-like) supports, commonly used in the industry.

These types of supports are often used by Halbronn's customers to prevent major warpage at specific locations. Indeed, these supports may be combined with «wall-supports» to resist the intense reaction forces that develop within some part's regions. Also, these supports could be used alone, as a «forest-like» support structure, enabling both a flexible and tough structure. Indeed, with the multiplication of the cone supports, which can bend before breaking, if the structure is dense enough, from user-experience, it may prevent warping efficiently in numerous cases.

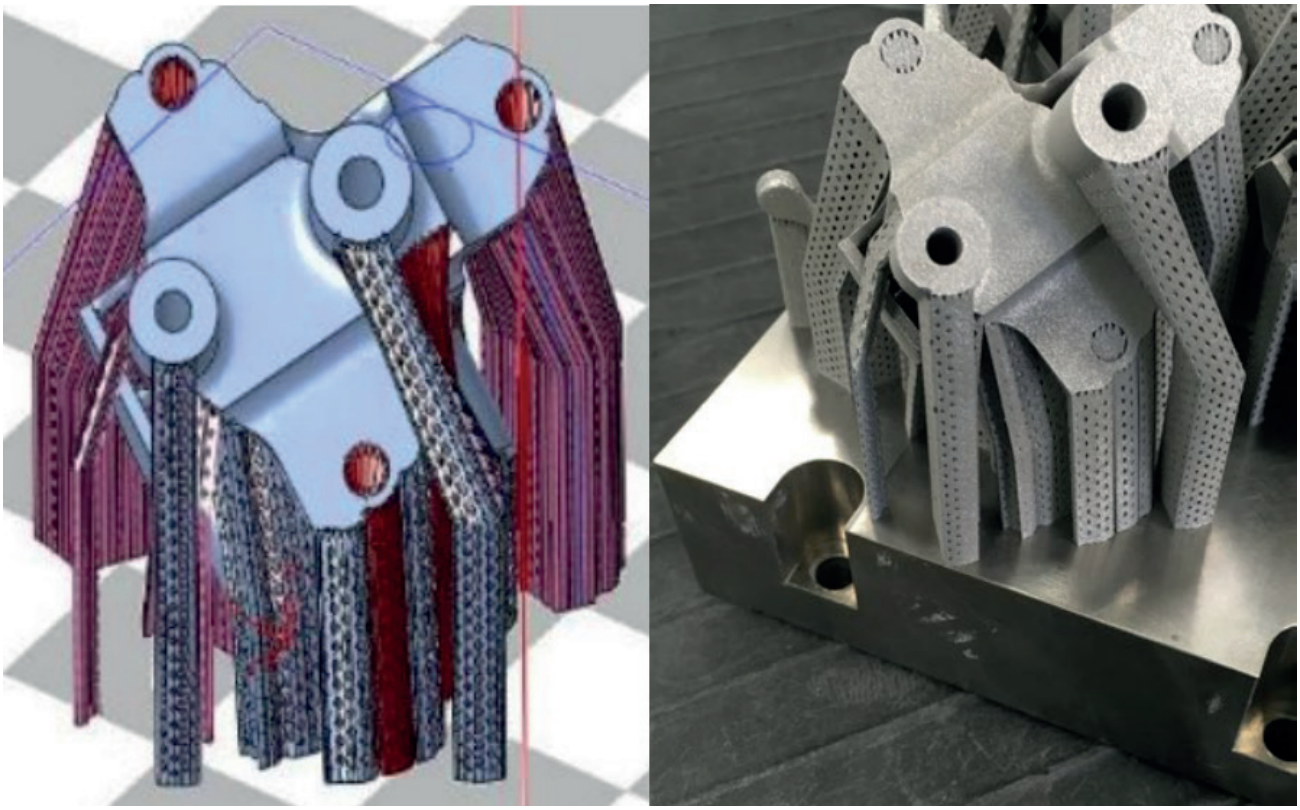

Figure 3.3: Complex support structure example from [4]. Left side is a view of the file being prepared in 3DXPert software and right side is the manufactured part.

In addition, standard process parameters optimized for this class of supports have been used, provided by the machine manufacturer.

Several commercial codes are conceived to estimate the deformation and residual stress distributions along with the manufactured parts. Some of them (Inspire [20], Amphyon [21], Netfabb [22], Simufact Additive [23], ESI Additive Manufacturing [24]) have been tested in this study on an industrial part.

The various models are based on different approaches (such as 3D-modelling, homogenised structures, plate elements, etc.) and most of them try to precisely model the supports and their distortion, as illustrated in Figure 3.4. However, none of these software is able to model the supports breakage and the continuation of manufacturing with some fractured supports. Detached-like Netfabb supports on Figure 3.4 are not detached from a real fracture: it is due to a display error caused by the meshing.

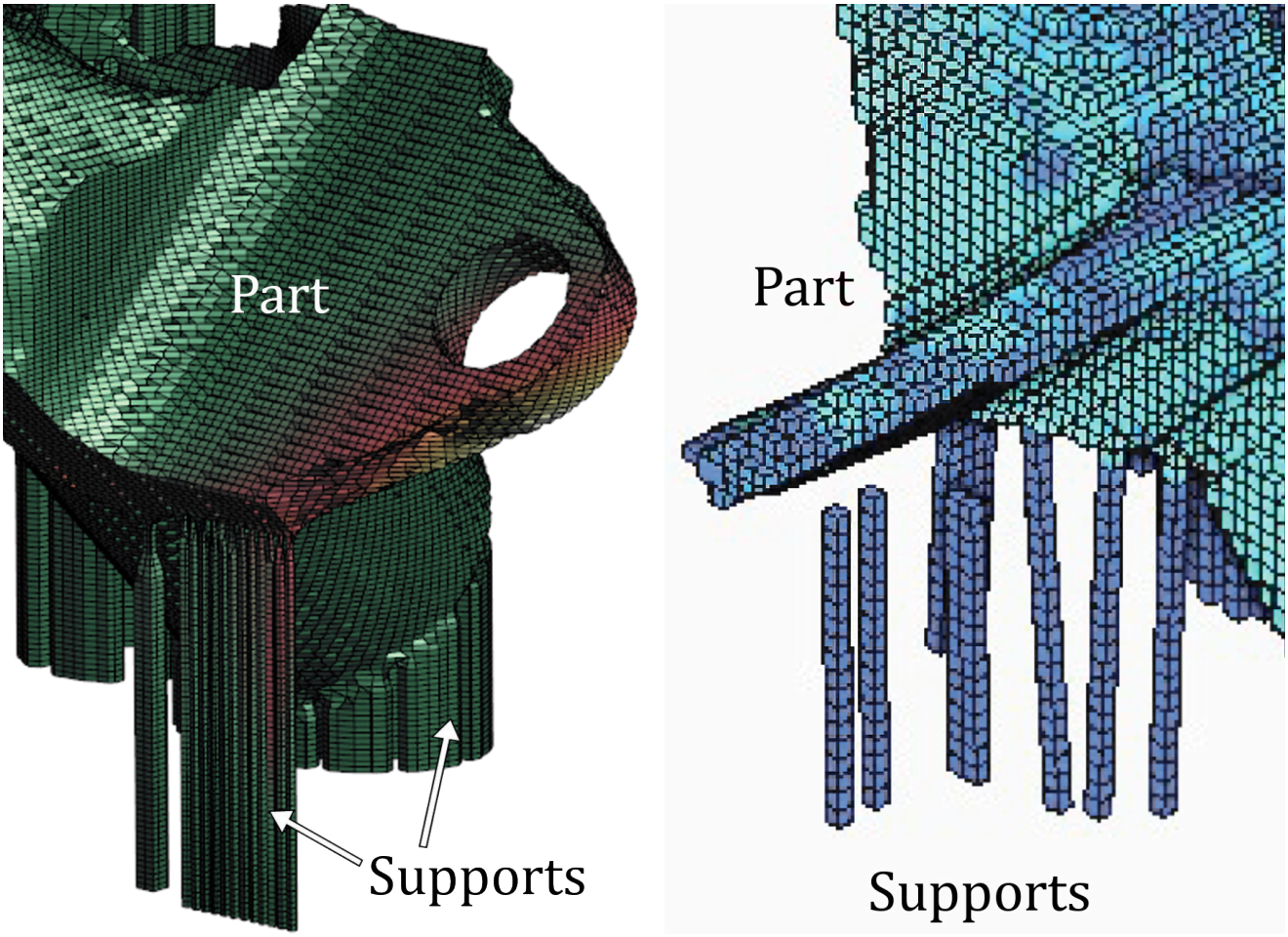

(a) Amphyon's supports distortion results. (b) Netfabb's supports distortion results.

Figure 3.4: Examples of support meshing from two commercial codes.

It is commonly accepted that the damage of the supporting structure generally leads to failure of the part's manufacturing. However, the cone supports' fracture in a dense tree-like structure could happen on multiple occasions without degrading the part. This study aims to simulate the damage and fracture of the supports used in additive manufacturing and to evaluate the final result.

The numerical model developed in this work predicts supports fracture using beam elements and voxel elements to mesh supports and parts. Thus, the study is decomposed as follow: Section 3.2 refers to the literature regarding both the modelling and optimisation processes in LPBF with a specific focus on supports. In Section 3.3, a practical industrial case is presented and simulated using current commercial codes. Distortion results regarding the supports and the narrowing area at the interface with the part are discussed. In Section 3.4, a novel modelling approach for cone supports is presented using one-dimensional beam elements in Finite Element (FE) analysis. Numerical results and parameters are discussed in Section 3.5.

3.2. State of the art

3.2.1. LPBF general modelling methods

Considering LPBF process numerical modelling, several spatial and temporal discrete levels could be used and even combined in multiscale frameworks [25]-[28], as illustrated in Figure 3.5. In these types of modelling, all parameters are considered: the powder individual particles or the whole powder bed, laser-matter interaction at microscale, whole layers, including scanning strategy, such as the scanning patterns, etc. A complete description of multiscale strategies will be presented in the next chapter of this manuscript. The work presented in this chapter concentrates solely on modelling part-scale deformations developed during the process.

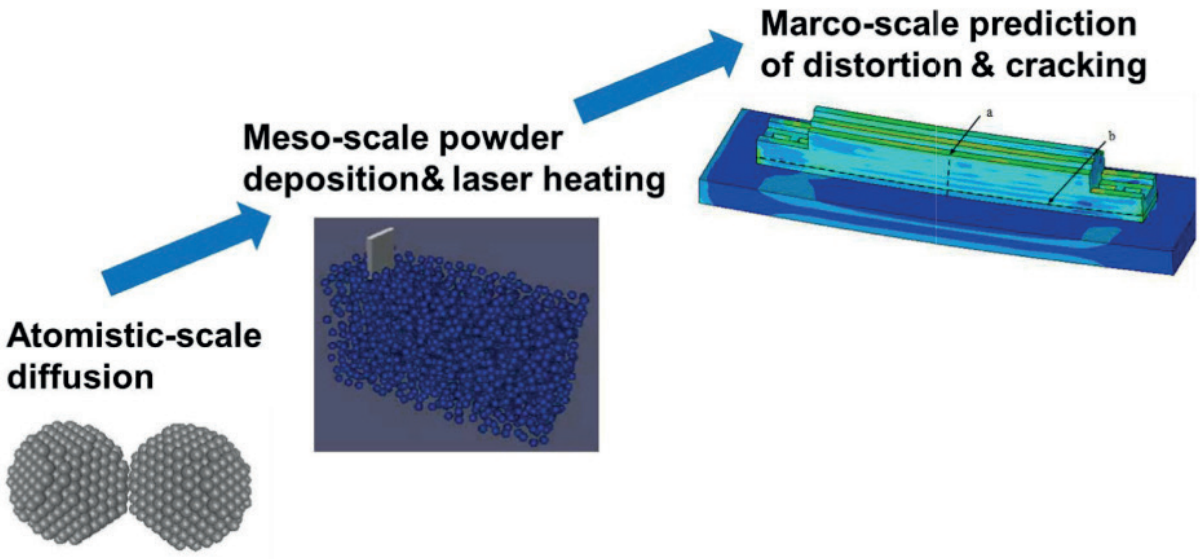

Figure 3.5: Multiscale illustration of the process from [25].

As discussed by [29]-[31], thermal distortions and residual stresses are consequences of the process complex thermal history. The Laser Powder Bed Fusion (LPBF) process involves extremely fast heating / cooling phases that reach magnitudes in the order of 10 K/µs to 20 K/µs [32].

To generate the residual stress fields, two main mechanisms are consecutively taking place [29]: the elasto-plastic expansion of the heated material, and its shrinkage. The whole process is known as the Temperature Gradient Mechanism (TGM), and is illustrated in Figure 3.6 from [29].

First, while the laser scans the powder layer, the surrounding solid material's temperature rise without exceeding the melting temperature. Hence, the material expands, its mechanical strength drops while an intense temperature gradient takes place. The temperature gradient comes from the quasi-instantaneous heating while conduction drives heat away slowly in comparison.

Then, while the surrounding body remains relatively cold it hinders the expansion of the hotter areas. From this phenomenon, compressive strains are generated. These strains may be plastic locally since the hot material strength has dropped.

The second mechanism results from the shrinkage of the material while it cools down. The upper - previously hot - material tends to shrink but the surrounding material hinders its displacement. From these two phases, it results tensile strains in the previously hot material, and compressive strains from the heat phase at the surrounding areas.

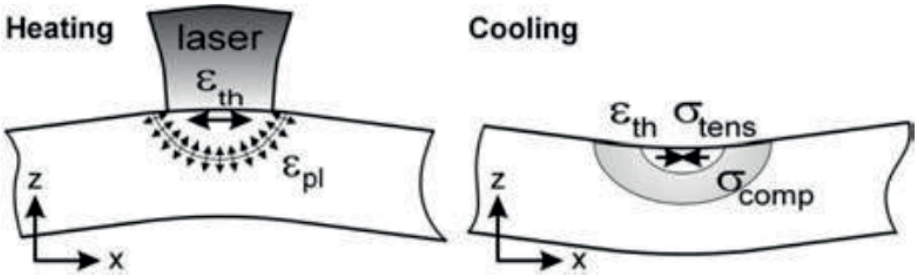

Figure 3.6: Temperature Gradient Mechanism described by [29].

Hence, numerous studies have developed sophisticated thermomechanical models to capture the impacts of those thermal loadings on mechanical residual stresses and deformations [33]-[38]. Several numerical methods, such as quiet elements method or inactive elements method, could be used to model the LPBF process, as described by [39].

The quiet elements method makes use of the elements yet not present in the actual manufacturing, i.e. the elements of the upper layers. While simulating the heating of a specific layer, the elements above are present, but their thermal and mechanical properties are weakened in such a way they seem to not being involved in the model. A drawback of this method is that it could be challenging to find new suitable characteristics to make them seem passive while not causing numerical instabilities [40].

The inactive elements approach allows to «delete» these elements and activate them while being scanned only. Hence, the computation should be faster since at the beginning, a very little number of elements are present within the model. However, with an increasing number of steps, there are also an increase of solver initialisations [40], and matrices creations [39].

Michaleris [40] mixed these approaches in a hybrid quiet inactive element method to mitigate each method's drawbacks. Moreover, whereas the physical layer thickness ranges in the order of tens of microns, it is a common approach to model thicker layers (macro layers) to reduce computational times [41]. Hence, in the numerical modelling process, it is possible to activate the elements one by one, in a layer-wise fashion or macro layer by macro layer.

A method first developed for the welding process in the 70s is referred to as the «inherent strain (IS) method» [43]. This method allows a significant reduction of the computational effort.

This method inspired the multiscale one developed for the LPBF process by Keller and Ploshikhin in 2014.

First, a thermal microscale model allowed to calibrate the Goldak heat source parameters, equations (3.8) and (3.9) [42][45]. The parameters a_r, a_f, b, c are the geometrical parameters to be tuned, η is the energy absorption coefficient. The simulated melt pool is compared with the melt pool size from experimental measurements.

The second model is at mesoscale: a thermomechanical resolution of the layer manufacturing. From this level, an inherent strain vector is computed by averaging the components of the strain distributions [44].

The inherent strain is then applied into each newly-activated macrolayer at the last level: macroscale. The method is illustrated in Figure 3.7.

Numerous works have used such methods to simulate metal AM processes, based on the inherent strain approach: some of them advanced limitations and others proposed some improvements [44]-[48]. These inherent strain-based methods are used in recent studies which simulate and even optimise the supports used in LPBF [49]-[52].

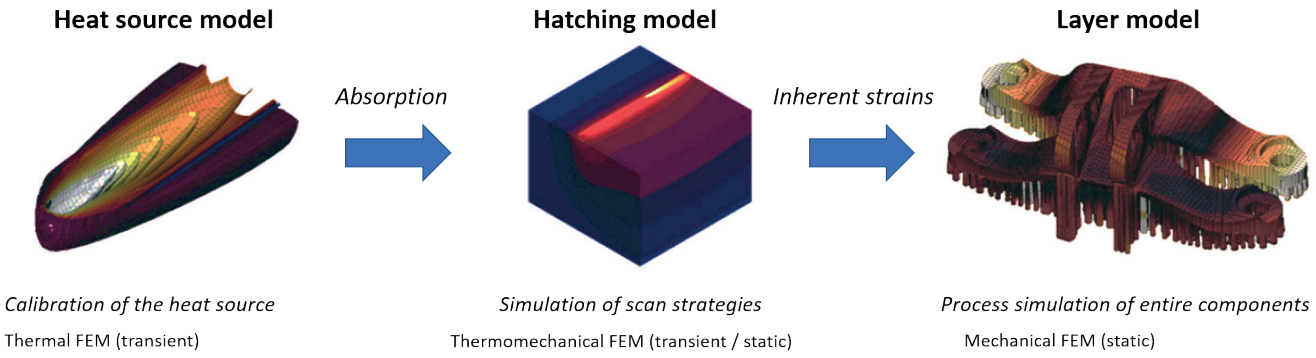

Figure 3.7: Original Keller's inherent strain method from [45] (translated from German)

$$\dot{q}(\vec{r},t) = \frac{6\sqrt{3}\,\dot{Q}}{bc\pi}\, e^{-3\left(\frac{y^2}{b^2}+\frac{z^2}{c^2}\right)} \begin{cases} \frac{f_f}{a_f}\, e^{\frac{(x-vt)^2}{a_f^2}} ; x - v_x t > 0 \wedge x - v_x t < a_f \\ \frac{f_r}{a_r}\, e^{\frac{(x-vt)^2}{a_r^2}} ; x - v_x t > 0 \wedge x - v_x t < a_r \end{cases} \tag{3.8}$$

$$f_f = \frac{2}{1 + a_r/a_f} \quad ; \quad f_r = \frac{2}{1 + a_f/a_r} \; ; \quad \dot{Q} = \eta P \tag{3.9}$$

3.2.2. Supports design, modelling and optimisation

Supports modelled by finite elements can be modelled completely as in [14][50], with a mesh size of tens of microns yielding hundred thousand elements, or partially, as in [51], where a small portion has been precisely discretised and simulated, then served as the basis for a homogenisation technique (asymptotic homogenisation method in this case).

The connection area between supports and parts (the teeth) often need to be optimised [53]. It could be modelled by a very thin mesh size to represent the residual stresses finely at these locations. For instance, Cao et al. [14][54] have been using almost 200 000 brick-type elements to simulate the machining process of a few beam-supports.

Also, since the supports' scanning strategies and geometries are different from the parts, it is assumed that the support material properties might vary. Some studies have been considering tensile testing supports of different geometries [17][18][55] to characterise their behaviour. However, there is still a lack of data that could help AM-engineers to design supports, and standard methods to test these structures repetitively are still required.

Well-developed AM process studies can also be found in patents. Many provide methods regarding supports such as their positioning [56]-[58], their geometry [57][59]-[68], methods to break them easily [69] or to design them in an effective heat diffusion fashion [70][71]. Numerous parameters have an impact on supports integrity, such as scanning parameters [9][72][73] and parts orientations [8][74][75].

Some supports optimization researches [76]-[78] showed that the ability of the supports to diffuse heat out from upper layers could improve parts overall fatigue performance [79].

Several studies have focused on comparing and selecting geometries based on objective function or experimental testing [3][16][19][53][80]. Recent works have designed supports using topological optimization [49][50][81] and taking into account supports crack risk during manufacturing [52][82].

Hence, supports are the subject of numerous research since the last decade, and there is still a lack of understanding regarding their behaviour during the process. In particular, several research works have developed optimization frameworks regarding the support's geometries and weight reduction. But a few tried to anticipate

the supports breakage and the subsequent part distortion [83].

It is common that a few supports break away from the part without ceasing the build or invalidating the part, especially because the supports breakage would generally happen while scanning a layer far above the fracture site, or even during the final cool down of the build.

3.3. Study case: hydraulic joint

3.3.1. Description

The part used in this study is a hydraulic joint used in the aeronautic field to channel oil fluids into aircraft components. The part has been topologically optimised, taking into account all lifetime forces, including machining forces, in a previous work [84]. The topological optimization led to a weight reduction from 210 g to less than a 100 g and 75% hydraulic performance improvements.

The initial and final geometries are shown in Figure 3.8. Only one part has been placed on the build plate, and its supporting can be seen in Figure 3.8(c). Its orientation has been chosen mainly to avoid the use of internal supports within the oil pipes. The beam supports geometries as well as their positioning are user-defined. There are 354 supports in total and the total manufacturing height is 66.8 mm.

Several Additive Manufacturing machines and materials have been tested to manufacture this hydraulic joint. The same observation was made with every configuration: some supports broke under the hydraulic joint arm.

The resulting manufacturing using both a Renishaw AM 400 machine and a GE MLab 200R are displayed in Figure 3.9. The material used in these cases is 316 L stainless steel powder provided by the machine manufacturers (particle size of 15-45 µm, the chemical composition from the providers [85][86] is detailed in Table 3.1).

Table 3.1: 316L stainless steel powder characteristics.

Elements	Fe	Cr	Ni	Mo	Mn	Si	N	O	P	C	S
Mass (%)	Bal.	16-18	10-14	2-3	≤2	≤1	≤0.1	≤0.1	≤0.045	≤ 0.03	≤ 0.03

The manufacturing process has been considered successful, however, in the case of the Renishaw system, 13 supports located under the arm of the hydraulic joint had broken, as shown by green circles in Figure 3.9. Supports detachment caused the part to warp a little and to collide smoothly with the layering system, even though the manufacturing process completed. The manufacturing parameters are listed in Table 3.2.

In the case of the GE system, 44 beam supports detached from the part, even though the manufacturing process completed. The detached beam supports are shown in white circles in Figure 3.9. The position of broken supports for each LPBF system are displayed in red in Figure 3.10.

Hence, the results differ significantly regarding the manufacturing system, although in each case the manufacturing process completed. Such discrepancy has important consequences regarding the simulation process since it looks necessary to calibrate the material parameters depending on the machine used for production.

Also, in can be seen from Figure 3.9 that almost every support broke at the tooth location (for every system) except three neighbour supports on the GE MLab 200R system. Due to their location, it is assumed that the supports broke from tensile solicitations.

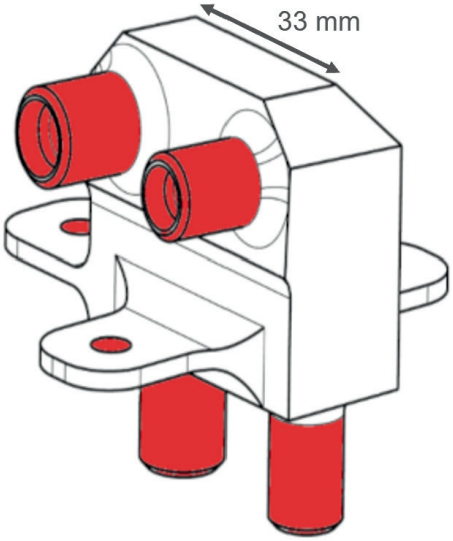

(a) Initial part (functional surfaces in red).

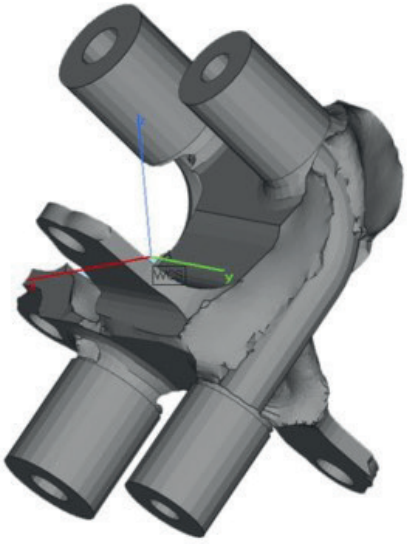

(b) Topologically optimised part.

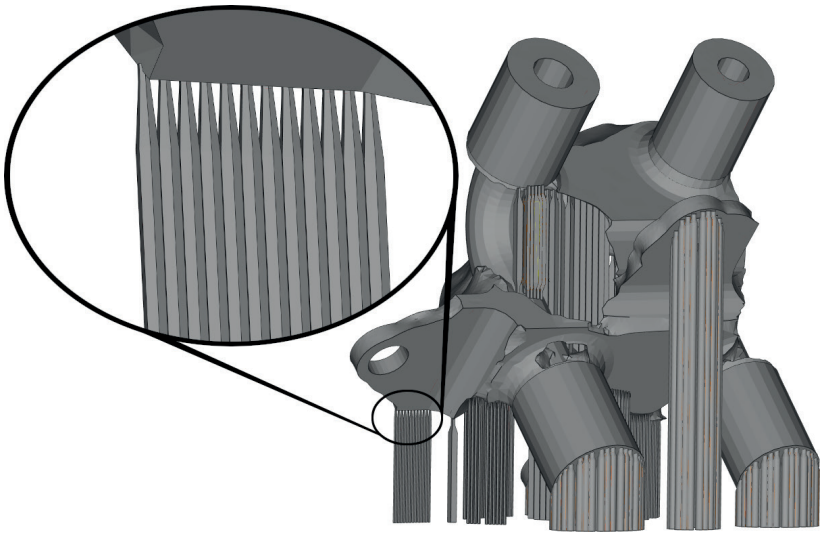

(c) Part and its supports (zoom in the tooth area).

Figure 3.8: Industrial hydraulic joint [84].

While the precise instant of the rupture cannot be defined precisely, it is assumed that the smooth collision occurred hundreds of layers above the supports.

This could be explained by the cumulative thermal shrinkage effect during the build-up of the component. The shrinkage of later printed layers results in an additional stress of the layers below. This, in turn, would lead to supports breakage when exceeding their ultimate tensile stress.

The supports that broke away in Figure 3.9 had two diameters: twelve of them (circled in Figure 3.8(c)) had a diameter of 0.20 mm and one of them (standing alone in Figure 3.9) had a diameter of 0.50 mm. Those diameters were among the standard dimensions proposed by the Renishaw QuantAM® build-preparation software.

Table 3.2: LPBF process 316L stainless steel material parameters of three different systems used in this study. Parameters were developed by the machine manufacturers.

Parameter	AM400	MLab 200R	ProX300
Layer thickness	50 µm	30 µm	40 µm
Beam diameter	70 µm	75 µm	70 µm
Preheating temperature	170°C	-	-
Bulk part			
Laser power	195 W	140 W	172 W
Scanning speed	750 mm/s	1 000 mm/s	1 800 mm/s
Cone supports			
Laser power	195 W	140 W	172 W
Scanning speed	750 mm/s	1 000 mm/s	1800 mm/s
Contours			
Laser power	110 W	130 W	-
Scanning speed	200 mm/s	1 300 mm/s	-

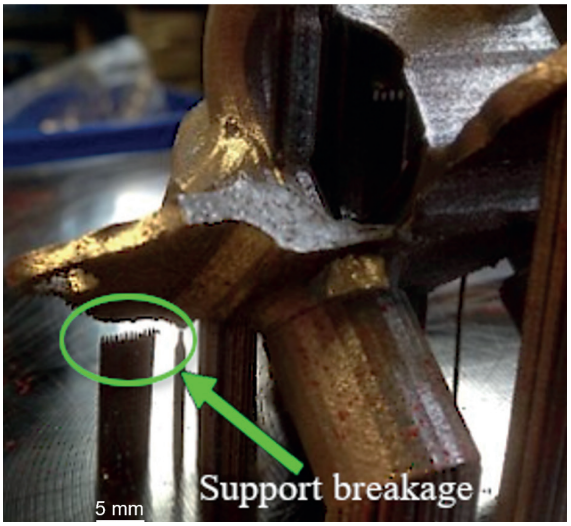

(a) Renishaw AM400 front view.

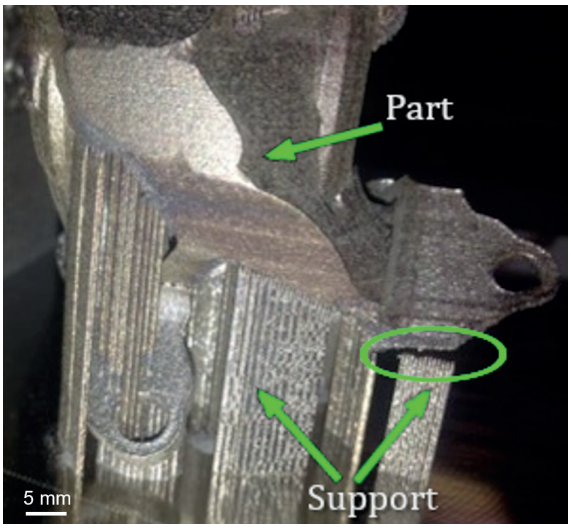

(b) Renishaw AM400 rear view.

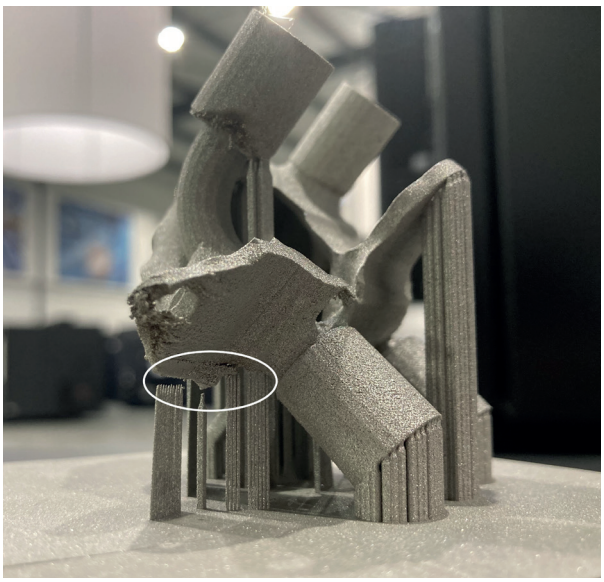

(c) GE MLab 200R side view

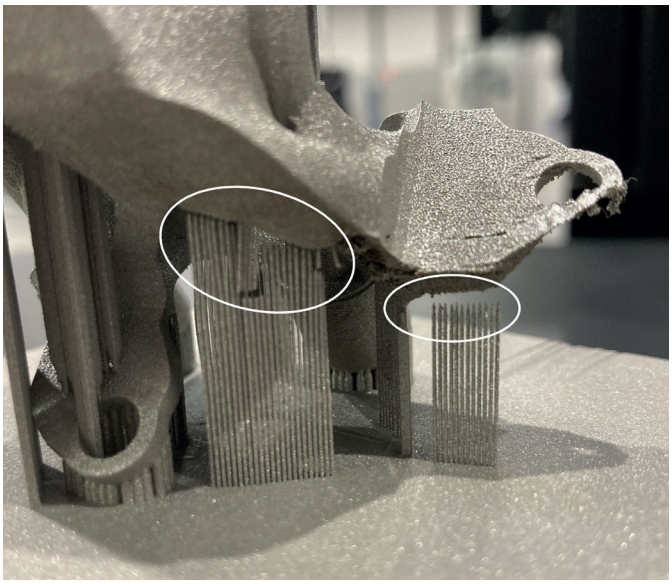

(d) GE MLab 200R rear view

Figure 3.9: Distortion of the part causing supports breakage with two different LPBF systems.

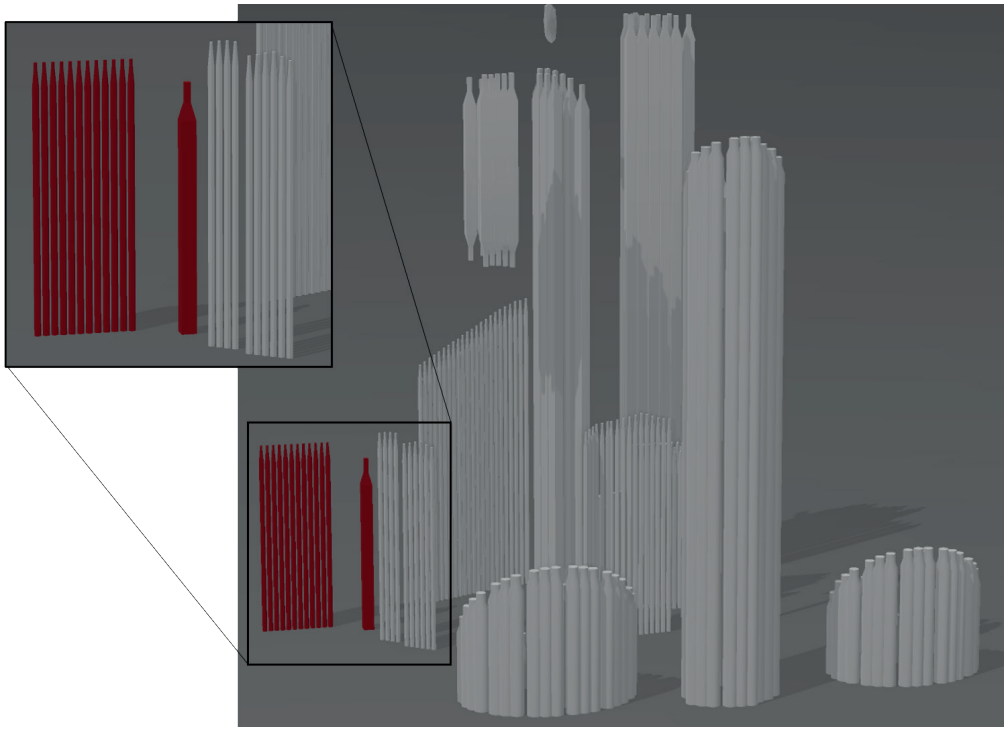

(a) Fractured supports location on Renishaw system.

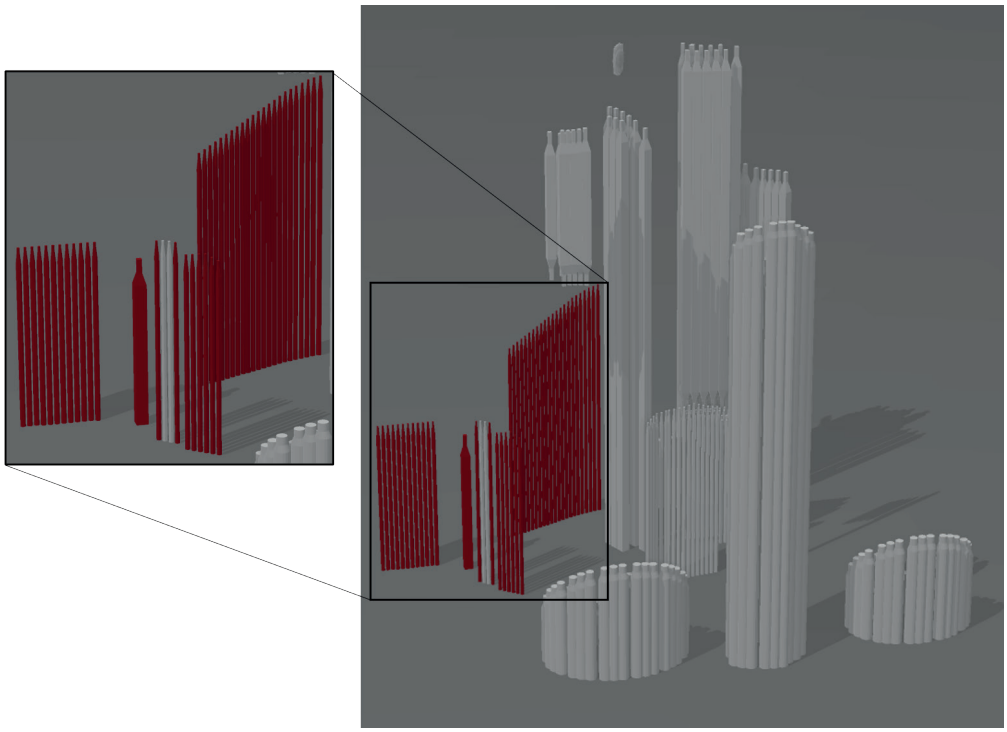

(b) Fractured supports location on GE system.

Figure 3.10: Position of broken supports (red) for each LPBF system.

3.3.2. Numerical simulation using commercial codes

3.3.2.1. Results of each software

The above mentioned additively manufactured part has been simulated using five commercial codes: Netfabb, Amphyon, Inspire, ESI Additive Manufacturing and Simufact. A list of all the LPBF software in our knowledge is presented in Table 3.3.

Table 3.3: List of simulation software.

Software	Owner
Simufact Additive	MSC SOFTWARE, HEXAGON
Inspire Print 3D	ALTAIR
Simulia	DASSAULT SYSTEMS
Amphyon	ADDITIVE WORKS
Netfabb	AUTODESK
GENOA 3DP	ALPHASTAR
ANSYS Additive Print	ANSYS
NX Fabrication Additive	SIEMENS
ESI Additive Manufacturing	ESI GROUP

Due to the specificity of each software, it was not possible to compare the simulation results using the same meshing strategy or the same computation time. Hence, these simulations were not meant to quantitatively compare the software, but to illustrate obtained results from each of these commercial codes currently available.

The global results of each software are displayed in Table 3.4. The deformation results of each software are illustrated in Figure 3.11. They range from 0.68 mm to 2.53 mm, which is relatively wide in terms of discrepancy. Nearly each code predicted high deformation magnitudes in the area where the supports experimentally broke away.

Only Amphyon software could finely mesh the supports and deliver fast results. It was done using another type of mesh than the standard cubic voxels.

Table 3.4: Commercial codes hydraulic block simulation results. "NC" stands for "Not Communicated" information by the software provider.

Code	Max displacement	Non cubic voxels	Computation time
Amphyon	1.75 mm	Yes	<10 min
Netfabb	2.53 mm	No	NC
Inspire	0.68 mm	No	<10 min
ESI	2.17 mm	No	NC
Simufact	1.37 mm	No	21 min

Hence, several AM software are able to simulate the parts distortion. Most of them predict accurately the defects' location and the global deformation as well as local plasticity. However, none of them explicitly model the supports damage or their breakage, which is an important consideration to prevent the whole build interruption.

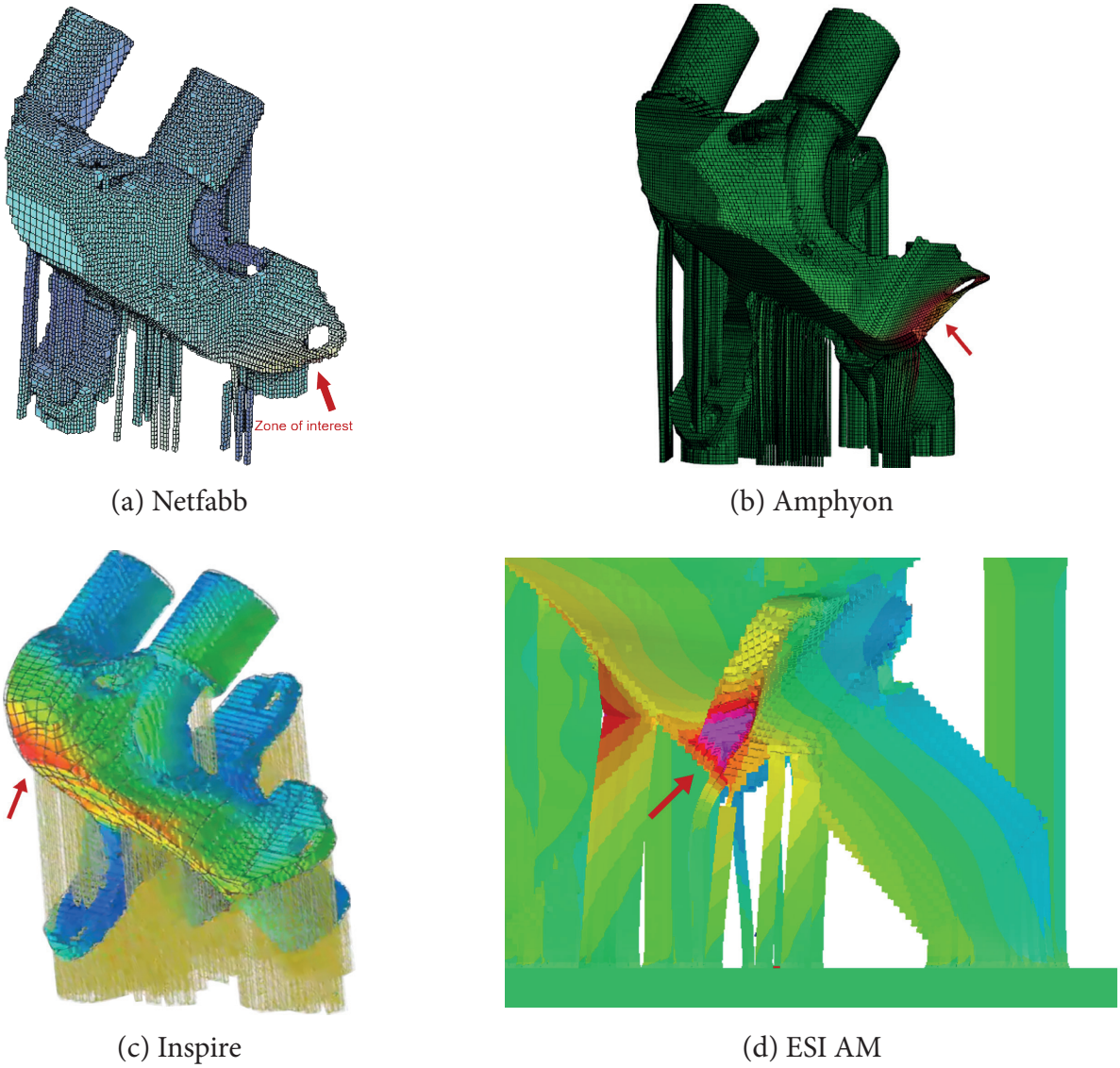

(a) Netfabb (b) Amphyon

(c) Inspire (d) ESI AM

Figure 3.11: Four commercial codes hydraulic block simulation displacement fields, zoom on the hydraulic joint arm. Simulated critical regions are indicated with a red arrow.

3.3.2.2. Example of simulation results with Simufact Additive

For availability reasons, only Simufact Additive could have been thoroughly tested for the following of this manuscript. Originally, Simufact engineering was acquired by MSC Software in 2015. Simufact engineering's main activity was focused on its welding and forming simulation tools. Simufact additive was based on MARC solver from MSC Software and launched on market in 2017.

Simufact Additive offers two resolution methods: a fully-mechanical resolution, and a thermomechanical resolution. The first one is based on the inherent strain method developed by Keller [43], however the first two simulation steps (for heat source calibration and inherent strain definition) are neglected and replaced by an experimental calibration step: the manufacturing of two comb-like structure placed at 90° one another on the build plate, as illustrated in Figure 3.12.

This calibration step takes two types of input: the material used for the calibration, and the displacement measured on the manufactured structure after it has been cut from the build plate.

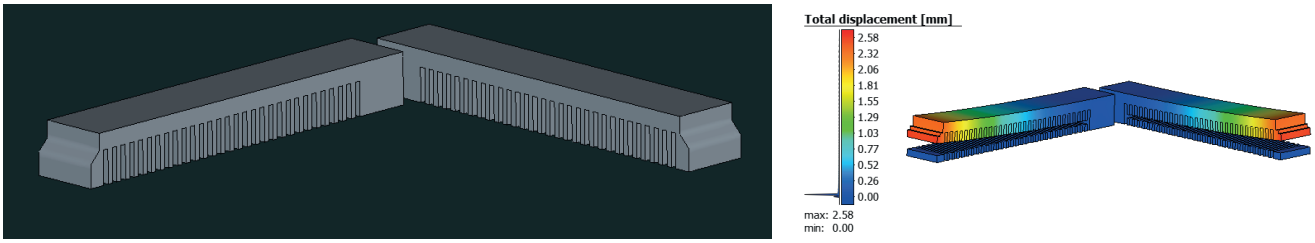

(a) Comb-like structure. (b) Final calibration results.

Figure 3.12: Comb-like structure in Simufact Additive used for the inherent strain vector calibration.

The comb-like structure for the calibration was manufactured on the GE MLab200R machine, and has provided similar results as the Renishaw AM400 machine. Five measures of the displacement value were taken and the mean values are displayed in Equation (3.10).

An initial inherent strain vector is provided and the software modifies its value to reduce the error between the simulated displacement and the measured one. Typically, a tolerance criterion of 1% for the error and a maximum number of converging steps of 200 are used. In this case, nine steps were required to calibrate the inherent strain vector.

For 316L, the standard material from Simufact was used and both the initial and the final inherent strain vectors are shown in Equation (3.11).

$$\bar{u}_X = 2.33\ mm \quad ; \quad \bar{u}_Y = 2.34\ mm \tag{3.10}$$

$$\varepsilon_{init} = \begin{pmatrix} -0.005 \\ -0.003 \\ -0.03 \end{pmatrix} \quad ; \quad \varepsilon_{calib} = \begin{pmatrix} -0.003252 \\ -0.003249 \\ -0.03 \end{pmatrix} \tag{3.11}$$

Then, the part is imported, the same material used for the calibration and the calibrated inherent strain vector are set. It is suggested to use the same mesh size as the calibration step (1mm in our case). A voxel mesh is then generated. By the end of the simulation, the results on the voxels and on the part are available. Only the mesh results are shown here since the part's results come directly from the voxel results by a field transformation which is not communicated. The results for the displacement and stress fields are displayed in Figure 3.13.

From Figure 3.13, it can be seen that the maximum predicted displacements and stresses are located at the right location regarding the actual part's manufacturing. Also, the software was able to predict a possibility of collision with the layering system, which happened on both cases. However, the software could not tell if the supports would break away, and the consequences regarding the manufacturing process.

In this case, there were minor collisions with the layering systems, however the manufacturing process continued, but finally the part was rejected. However, there are some cases where very few supports break away, and the part is not flawed.

The aim of the following study is to be able to model the supports damage, their breakage, and to follow the ongoing displacement of the part, such that it would be possible to predict the possible process interruption.

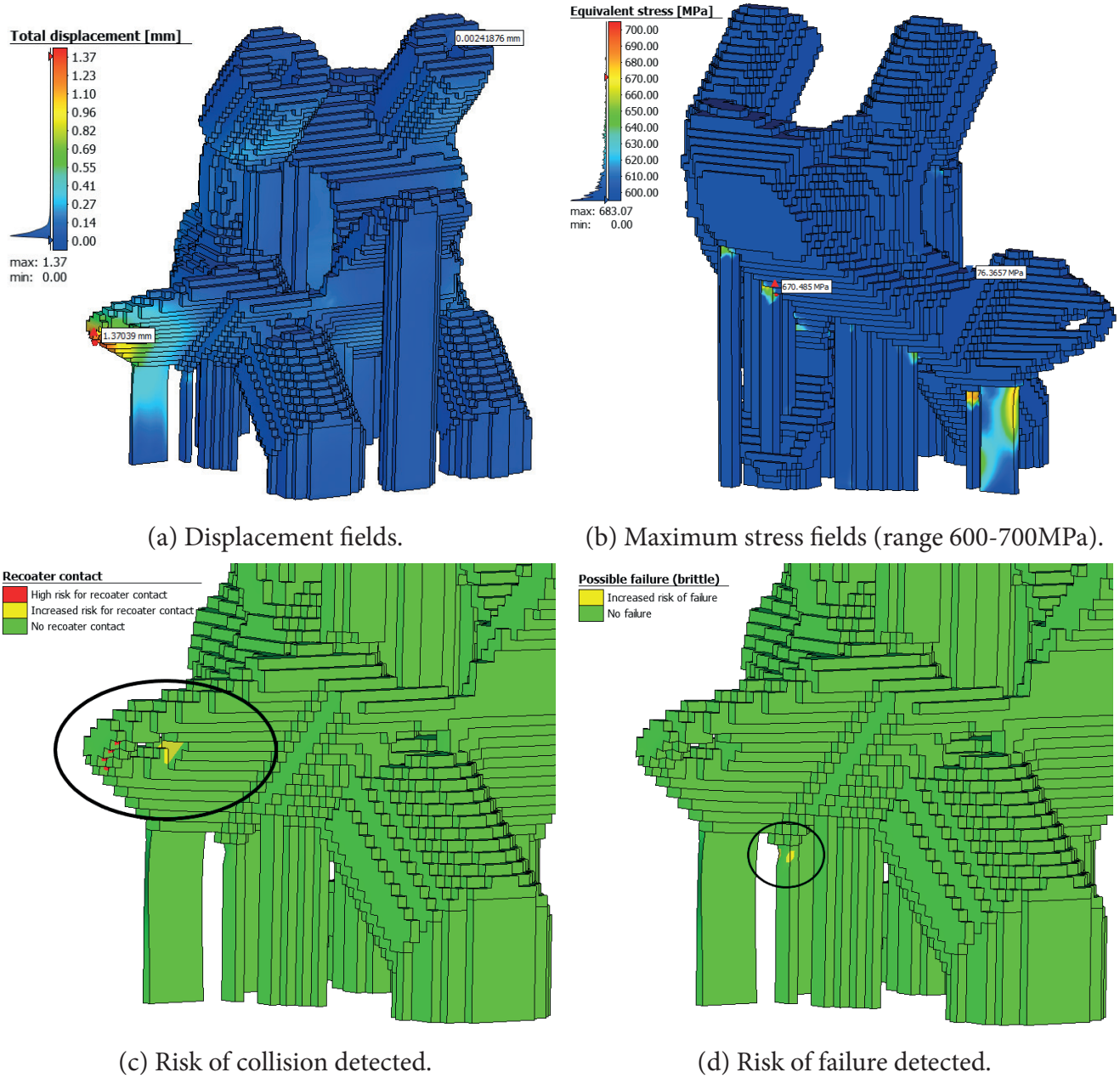

(a) Displacement fields.

(b) Maximum stress fields (range 600-700MPa).

(c) Risk of collision detected.

(d) Risk of failure detected.

Figure 3.13: Hydraulic joint's simulation results on Simufact

3.4. The numerical models developed and experimental data

3.4.1. Numerical method

3.4.1.1. Models, meshing and process sequence

The numerical model consisted of an assembly of several instances: a build plate, the supports, and the hydraulic joint (the part). The build plate is a rectangular instance of dimensions 70.9 mm × 53.9 mm × 20 mm meshed with 153 360 ABAQUS C3D8-type (brick) elements. The hydraulic joint is meshed using cubic voxel elements before being imported in ABAQUS software: 203 736 C3D8-type voxel elements were used. The part's mesh size is set to 0.5 mm, which corresponds to the thickness of ten physical layers (50 µm each). This layer's bundling will be mentioned as a macro layer in the next sections.

Two models were created with different meshing strategies for the supports:

The first model employed 0.5 mm length Abaqus C3D8-type voxel elements (see Figure 3.14(a)) to mesh the supports. This way, 47 857 elements were added to model the support structures.

The voxels could not represent the narrowing at the zone linking the supports to the part (the tooth area). Section and material properties were homogeneous throughout the supports. This is due to the difficulty of identifying the voxels corresponding to the support's teeth, which are merged with the supports core and the part while using such mesh length.

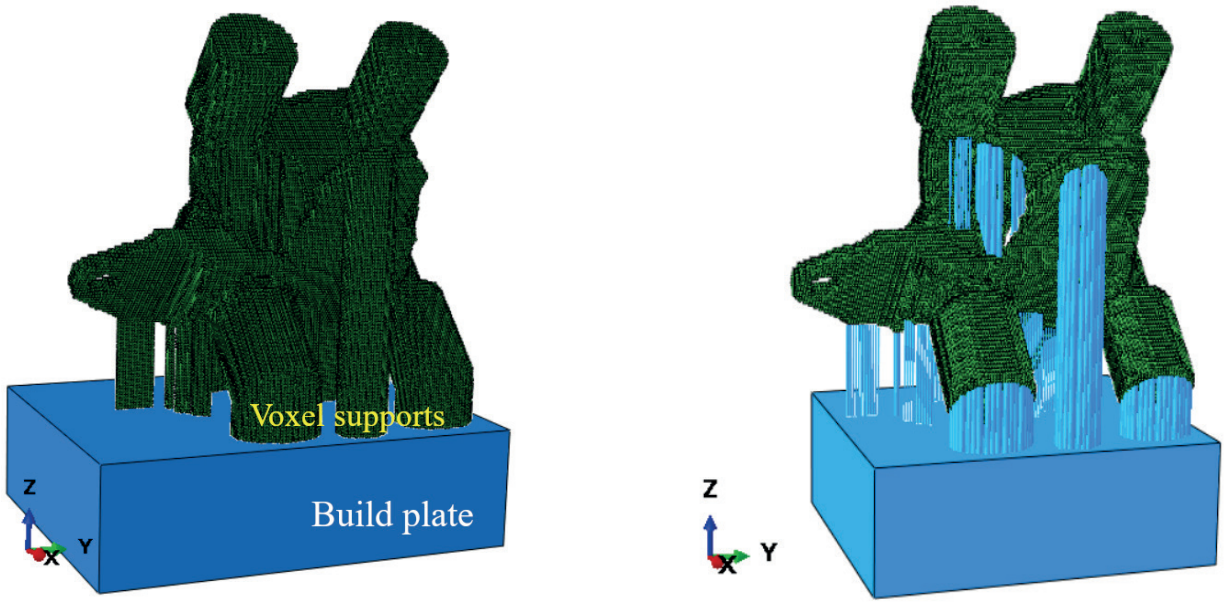

(a) Voxel supports. (b) Beam supports.

Figure 3.14: Hydraulic joint Abaqus models with the build plate, voxel (a) and beam (b) supports.

The second model consisted of meshing the supports with Abaqus B31-type beam elements (see Figure 3.14). Multi-Point Constraints (MPC) are used to connect the supports' ends to the build plate and the hydraulic joint (see Figure 3.15 and Figure 3.16).

As the voxel elements could not represent the geometrical narrowing at the tooth area, 1D elements have been implemented with a uniformly reduced section to model the narrowing at the tooth area. It is the scope of future studies to use progressive section reduction at these locations instead of a uniformly reduced section..

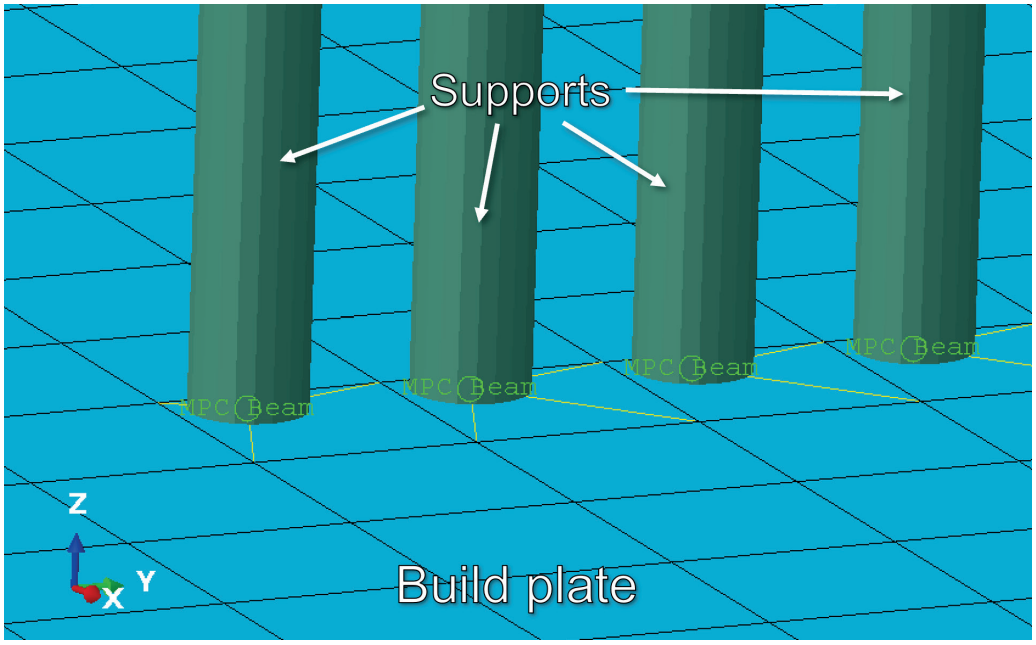

Figure 3.15: MPC constraints between some supports and the build plate.

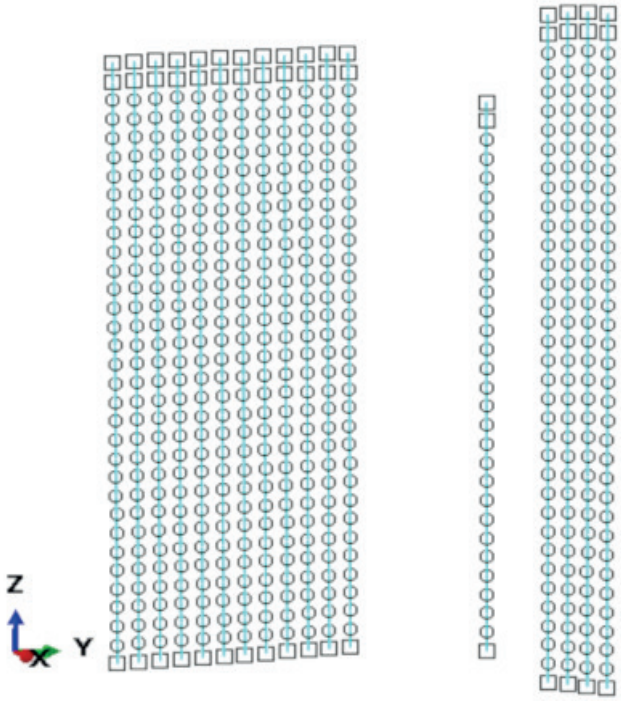

Figure 3.16: 1D beam supports nodes with 0.5mm mesh size.

The models were developed using ABAQUS/Standard, and the model generation was fully automated using python scripts. The main python script, handling the most important phases of the model construction contained nearly 800 lines of code, and the model was generated within five minutes using all the necessary files.

In the case of the voxel supports model, when the part is imported, the supports are already present and linked to the part's voxels. Hence, in this model, both the parts and the supports are imported from the file used for the manufacturing process (see Figure 3.9).

In the case of the beam supports model: the python script allowed to import the part (hydraulic joint), generate the build plate, mesh both of them and generate the 354 beam supports within ABAQUS. The beam

supports are generated according to the manufactured supports (see Figure 3.9).

For both models, the script cut the instances in 0.5 mm thick layers. For each layer, specific steps are generated, loads and interactions (i.e., activations) are set automatically.

The same loading type as the inherent strain method was used: by varying the layer temperature, there is a shrinkage due to the Coefficient of Thermal Expansion (CTE), hence, the resolution was fully mechanical:

User-defined thermal strains were applied by incrementally varying the temperature fields. Using a linear Coefficient of Thermal Expansion (CTE), these temperature variations drove thermal-induced strains. In this study, the CTE value was set to 18 K^{-1} [87].

In the inherent strain method, the CTE value corresponds to the inherent strain vector computed from the thermomechanical mesoscale model (see Section 3.2.1) and the temperature variation is equal to 1K. Here, the approach is similar, but the CTE value is the one of the physical materials and the temperature variation is defined to imitate the part cooling. Full sequence of activation/deactivation and cooling is then described:

The first simulation step in ABAQUS consisted of deactivating the hydraulic joint and the supports. Then, at each further step, a novel macro layer was activated at the material melting temperature (1 673 K).

To simplify the study, no thermal equation was solved: the cooling process was simulated by setting consecutive temperature drop steps. Hence, at each step, each already activated macro layer was cooled by 153 K until it reaches the room-ambient temperature. Numerical thermal studies detailed in the next chapter indicated that nine steps were required for the layer temperature to reach the room-ambient temperature (293 K). The choice of a constant temperature increment was made for simplifications.

The full sequence is reported in the following python-like code block:

```
### variable initialisation ###
last_layer = False
ambient_temperature = 293.
melt_temperature = 1673.
temperature_increment = 153.33
### process begins ###
While last_layer == False:
  for element in model :
    if (element.temperature - ambient_temperature) > 1 :  # if the element is not at ambient temperature yet
      element.temperature = element.temperature - temperature_increment
  new_layer = activate_new_layer()  # predefined function which activates a new layer above the others and returns the layer elements
  new_layer.set_temperature(temperature=melt_temperature)  # function that modifies the temperature of the whole layer variable
  last_layer = check_last_layer()  # predefined function that returns True if last layer of the model
```

3.4.1.2. Mechanical properties

Regarding the mechanical properties, literature values were used since 316L material mechanical characteristics have been well studied for the LPBF process. Mean values from literature are listed in Table 3.5 [88]-[100].

Since the thermal history is not computed in this study (the model is fully mechanical), the material parameters are temperature-independent. This behaviour could be improved in a future study, specifically, the temporal aspect is not considered (to introduce the viscoplasticity for instance).

It can be seen from Table 3.5 that the fracture strain A% parameter taken from the average literature values is less than the standard specified value [101]. It can be explained by the fact that the standard value was set for conventional annealed and cold-worked austenitic stainless steels, although the literature values were measured as-built from LPBF specimens. Hence, it is expected that the as-built LPBF-manufactured specimens are more

fragile than conventional 316L.

Table 3.5: Mean 316L stainless steel mechanical properties from [88]-[100] and ASTM A666-15 Standard [101].

Characteristics	Literature	ASTM Standard
Young Modulus E	180 GPa	-
Yield strength R_e	496 MPa	170 MPa
Tensile strength R_m	614 MPa	485 MPa
Fracture strain A%	34%	40%

A damage model was also incorporated, to observe the potential breakages. A ductile damage initiation criterion [102] was defined for predicting the onset of damage in every models. Its value corresponded to the fracture strain (34%) mentioned in Table 3.5.

A displacement damage evolution was used to link the damage as a function of the plastic displacement after damage initiation. The damage varied linearly with the deformation (*Linear Softening* in ABAQUS). The effective plastic displacement at the point of failure parameter $\bar{u}_f^{pl}$ [103] was set to 0.05 mm for an element length of 0.5 mm. This parameter is linked to the element damage variable $\dot{d}$ as in Equation (3.12) [103]. Another tangible option would have been to use an exponential evolution of the damage variable as in Equation (3.13) [103]. This option has not been tested but it may allow a more instantaneous behaviour of the beam's breakage.

$$\dot{d} = \frac{L\dot{\varepsilon}^{pl}}{\bar{u}_f^{pl}} \tag{3.12}$$

$$d = \frac{1 - \exp\left(-\alpha\left(\bar{u}^{pl} / \bar{u}_f^{pl}\right)\right)}{1 - \exp(-\alpha)} \tag{3.13}$$

Where L is the characteristic length of the element (equal for all elements throughout the model) and $\dot{\varepsilon}^{pl}$ is the equivalent plastic strain variable. Then, when $L\dot{\varepsilon}^{pl}$ equals $\bar{u}_f^{pl}$ value, the degradation is completed.

A schematic representation of the stress-strain diagram with evolution of the damage variable is shown in Figure 3.17 from [103]. In this figure, σ_{y0} is the yield stress (614 MPa in our case), $\bar{\varepsilon}_0^{pl}$ is the equivalent plastic strain at the onset of damage (34% in our case) and $\bar{\varepsilon}_f^{pl}$ is the equivalent plastic strain when the damage is complete (damage variable equals 1), hence it is the equivalent plastic strain at failure.

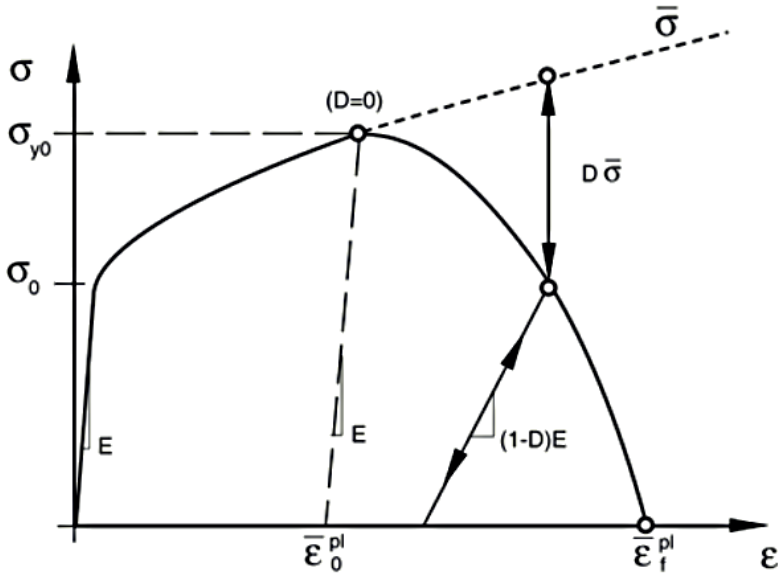

Figure 3.17: Stress-strain schematic diagram with evolution of the damage variable D from [103].

Elements are deleted from the simulation once the damage variable is equal to 1. These damage parameters were kept constant for all element sizes presented in the following sections.

3.4.1.3. Considering the supports overlapping

As illustrated in Figure 3.18 representing the STL file of the hydraulic joint with its supports, some of them overlap at their base, stiffening the structure.

We first tried to estimate the importance of these overlaps on the mechanical strength of the structure. To do so, three simplified models were created (see Figure 3.19), each of them used three beams (without teeth): the first one is a 3D model for which each beam overlap with the next, the second one is a 1D model with the three beams only, not overlapping, and the last one is a 1D model with the three beams and horizontal 1D connections to link the beams together. The three models are displayed in Figure 3.19.

The 1D beam elements were assigned the same section as the ones of the 3D model. For each of these models, the last node of the beams was tied to the others, as if the beams were connected to the same plane. A force along a specific direction was then applied to the last node of the middle beam.

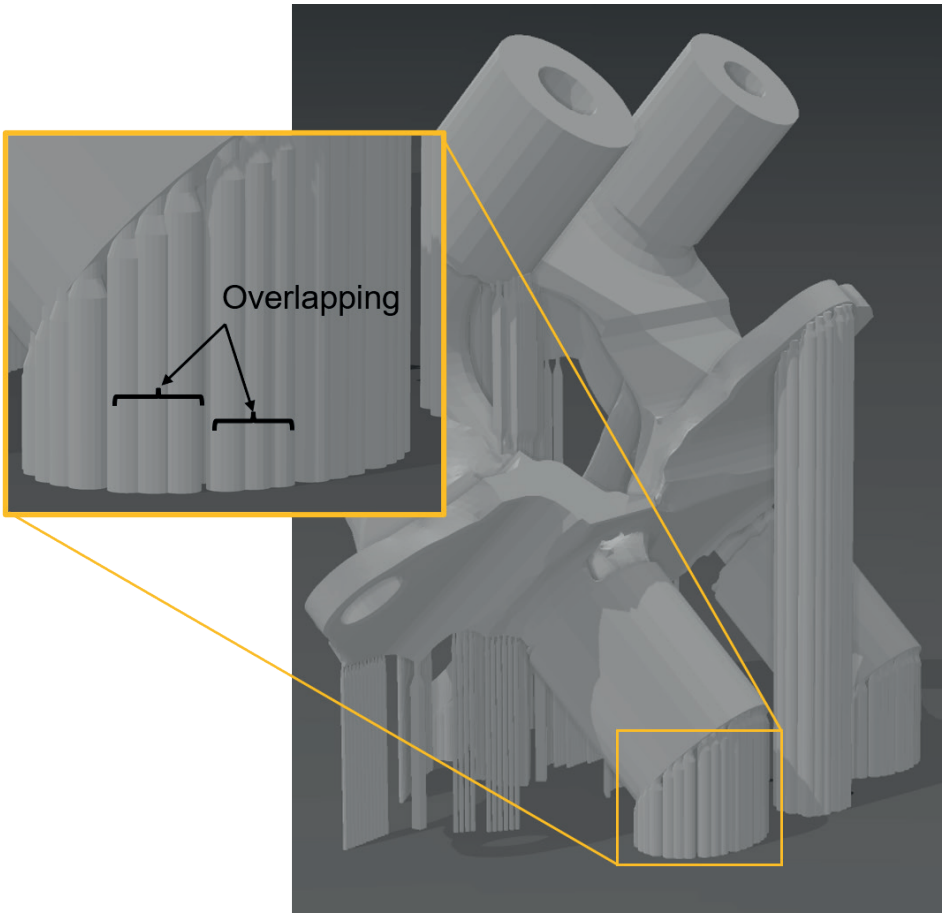

Figure 3.18 : Hydraulic joint STL file: zoom on overlapping supports region.

The numerical results are summarized in Table 3.6, it can be seen that adding horizontal links through the 1D beams results in very similar results as the 3D model. This observation seems to be verified for all directions of the applying force. Indeed, adding horizontal connections to the 1D beams may reinforce the global structure as the overlapping does.

However, in the case of the hydraulic joint model, too many supplementary instances and elements were generated while adding automatically (with a python script) horizontal connections to the supports. It looks like the memory on the computer was not sufficient to handle the hundreds of new instances, and the automatic

scripts could not complete.

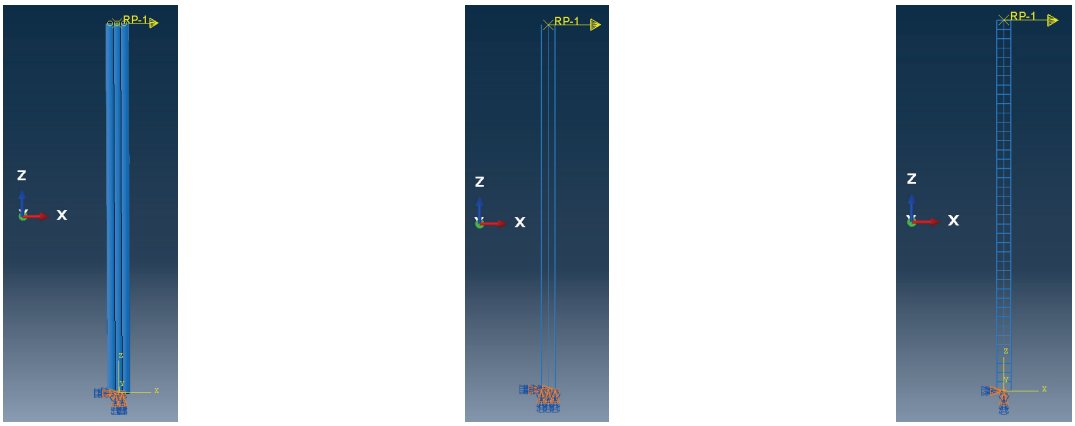

(a) 3D overlapping-beams (b) 1D unlinked-beams (c) 1D linked-beams

Figure 3.19: Simplified models of three beams, locked at the base, connected at the top, and a X-directed force applied at the top.

Then, the solution of adding horizontal connections to the beam supports that are overlapping was not applied in the following sections.

There may be a certain level of errors linked to this assumption, however, only the widest the supports were overlapping, and the ones that broke during the manufacturing (Figure 3.9) did not overlap. Also, it is expected that the tensile solicitation would lead to fracture, hence an error for a force along X direction would not be of paramount importance practically. A further improvement would be to write better python scripts for generating these supports structures (with horizontal links) on dense supporting structures without the memory management issues.

Table 3.6: Displacements and relative errors of the 3D overlapping model and both 1D models with and without horizontal links.

	Displacements 3D model	Displacements 1D model without links	Displacements 1D model with links	Relative error 3D/1D without links	Relative error 3D/1D with links
Force along X	0.255 mm	0.617 mm	0.250 mm	142%	2%
Force along Y	1.78 mm	1.73 mm	1.80 mm	3%	1%
Force along Z	0.223 µm	0.202 µm	0.210 µm	9%	6%

3.4.1.4. Overcoming buckling-based numerical instabilities: proposed solutions

Whereas the simulation in which the supports are meshed using voxel elements completed with no incident, the model which makes use of beam elements to mesh the supports has generated numerous instabilities and convergences issues.

From the different trials to determine the origin of the instabilities, it was concluded that using 2 mm diameter supports without teeth allowed to convergence. But in fact, using these instances, no plasticity was observed on the supports at the end of the simulation. Supplementary models allowed to define the origin of the instabilities: the buckling phenomena using an elasto-plastic behaviour.

Indeed, some supports are sometimes under compression loading, leading to buckling and the static problem becomes unstable. Using a perfect elastic material, the analysis remained linear, hence no instabilities occur. The Newton's method used with the ABAQUS/Standard solver is not able to overcome buckling instabilities while in

plasticity (i.e., non-linear analysis) [104]. The instability comes from the load-displacement response, where a release in strain energy is represented by a negative stiffness [105].

From [105], it is assumed that a dynamic resolution would follow the buckling phenomenon, however, it is chosen to keep a static resolution since a dynamic would lead to too huge computational durations.

Also, the problem may have been stabilised using damping [104]: viscous forces must be sufficiently large to prevent buckling instabilities. But they must be small enough to yield similar results overall. Because of the number of support instances suffering compression within the model and the challenges that represent defining well-suited parameters for damping, this solution was not chosen.

In this study, two strategies have been tested to tackle these problems in a static resolution : using another resolution method or using simplifying hypotheses to prevent the buckling phenomenon.

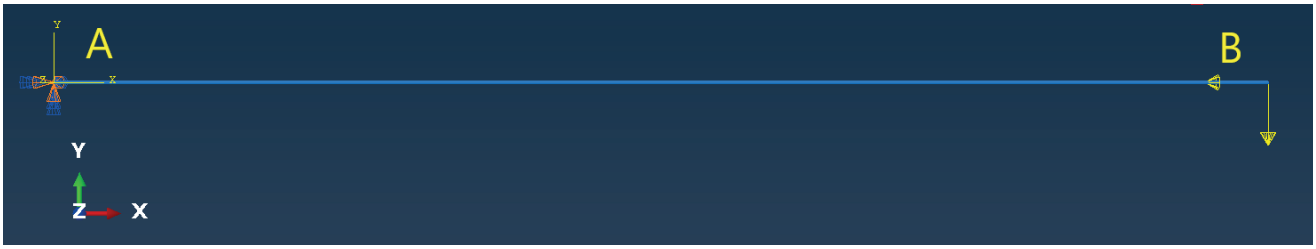

(a) Individual beam model locked at the base (Point A), under compression loading (Point B). The force applied in -Y direction (to avoid numerical issues) was ten times lower than the force along -X.

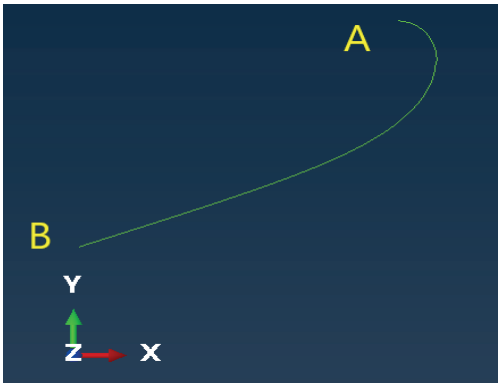

(b) Newton's method: elastic material.

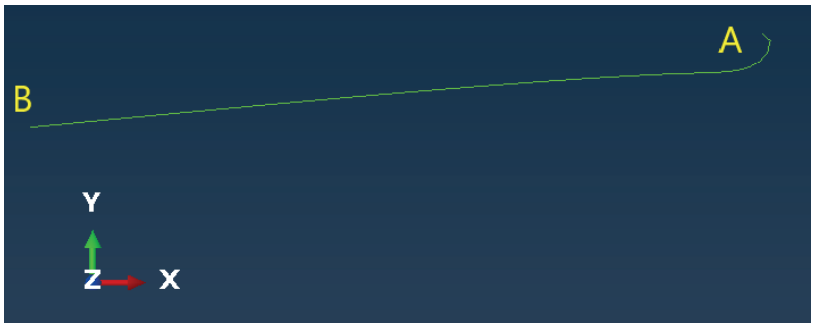

(c) Modified Riks method: elasto-plastic material.

Figure 3.20 : Simplified model (a) and deformed shapes (b & c) of an individual beam under compression.

Some tests on a single beam under compression have been launched and showed that the ABAQUS/Standard modified Riks method was able to converge for a single beam in compression while using elasto-plastic material properties. The results can be observed in Figure 3.20.

Although the displacement vector is the only unknown in the Newton's method used by ABAQUS/Standard to solve nonlinear equilibrium equations; in the modified Riks method (implemented in ABAQUS/Standard also), both the load magnitude and the displacement are unknown [104]-[106].

Hence, in this method, a novel measure must be used in the load-displacement space: the «arc length» through the static equilibrium path [105]. It is then assumed that the loading is proportional and that the response is smooth [107]. The full algorithm description is available in [107].

However, from the Restrictions section in [105], the *Activation* tool (mandatory for progressively adding layers one above the others in our models) is not available using this method in ABAQUS/Standard. Mixing both standard Static and Riks solvers in specific steps was tried, but it requires to restart the analysis at each step (see [105]). As for the dynamic resolution, this solution is not recommended because of the computation efforts

required.

The second strategy consists in preventing all the rotations at each node of the beams, preventing any possible buckling phenomena. Hence, the beams are only able to suffer traction / compression and shear solicitations. This strong assumption artificially stiffens the structure for compressive and some lateral loads, but it is expected from experimental trials that the main damage come from traction loadings at the tooth area. This assumption will be used in the following models.

3.4.2. Numerical results and experimental comparison

3.4.2.1. 3D-voxel elements simulation results

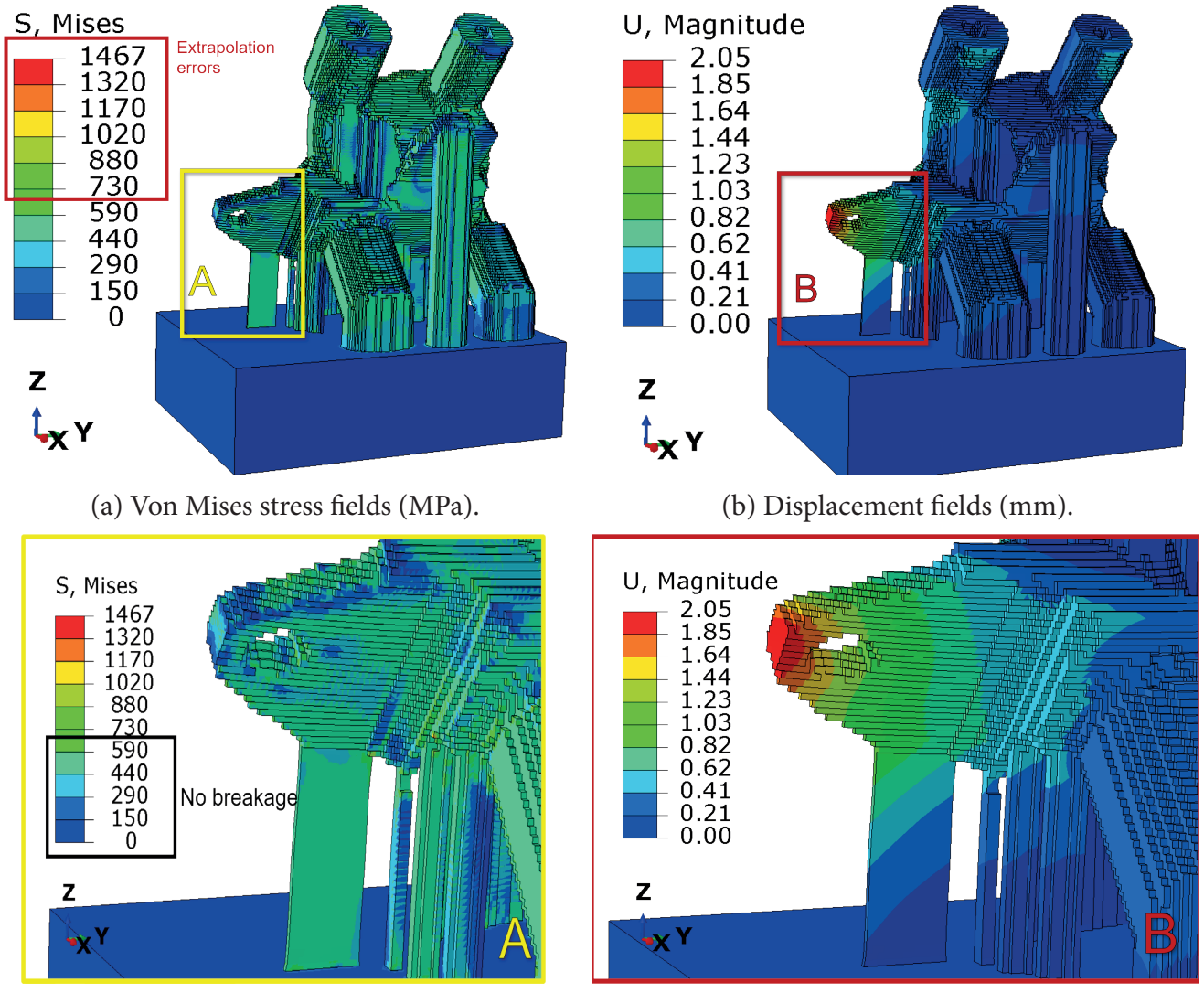

(a) Von Mises stress fields (MPa).

(b) Displacement fields (mm).

(c) Von Mises stress (MPa), zoom on supports and hydraulic joint arm.

(d) Displacement fields (mm), zoom on supports and hydraulic joint arm.

Figure 3.21: 3D-voxel simulation results: stress and displacement fields.

Von Mises stress and displacement fields using 0.5 mm voxel elements to mesh the supports are displayed in Figure 3.21. No supports were detached from the part using voxel elements (as seen in Figure 3.21(c)); however, the maximum displacement value (2.05 mm) is significant and would lead to invalidate the part. It can also be

seen from Figure 3.21(a) that some excessive stress values were obtained.

All these excessive values (significantly higher than the tensile strength of 614 MPa, mentioned in Table 3.5) are due to the large mesh size. Indeed, the stresses are computed at the elements integration points, however, the contouring algorithm used by ABAQUS to fill the contour plot (i.e. the stress fields) makes use of the nodal values. The nodal values are then extrapolated from the integration points values [103].

In fact, while extracting the von Mises stress values at the integration points of the hydraulic joint elements, the value did not exceed 614 MPa.

The stress levels of interest are those of the supports, shown in the black frame in Figure 3.21(c) in the range 0−614 MPa (see Table 3.5). It could be noted that the stress distribution within the voxel supports looks homogeneous.

The global displacement fields are displayed in Figure 3.21(b) and the maximum displacement values are located at the hydraulic joint arm, as shown in Figure 3.21(d). It corresponds to the location of the supports breakages and significant distortion of the manufactured part. The maximum displacements is in the (wide) interval of the commercial codes results tested, see Table 3.4.

The computation time for this simulation is about 1.6 day using 12 core AMD Opteron™ 6376 2.3 GHz – 128 Gb RAM.

3.4.2.2. 1D-beam elements simulation results

Figure 3.22(a) and Figure 3.22(b) display the whole ABAQUS assembly using 1D-beam supports, with render beam profile option activated (this option would show the 1D-beam elements with a 3D profile, as previously mentioned for Figure 3.14(b)). Figure 3.22(c) and Figure 3.22(d) display the supports only, also with *render beam profile* deactivated.

Just like the voxel model, excessive stress values were artificially extrapolated by Abaqus at some part elements. However, the stress range within the supports does not exceed the tensile strength from Table 3.5.

Unlike the voxel supports, the 1D cone supports stress fields are not homogeneous through the supports for several reasons: the main stress values are located at the teeth while using the 1D-beam elements since the section reduction is considered. Also, in our study, each beam is independent from its beam neighbours, contrarily to the voxels, connected one to the others.

Although both models (voxel and beam elements) integrate damage and fracture, only beam supports have been detached from the part during the simulation. The detached support elements are those for which the damage was completed, they were deleted during the simulation.

Simulation results using beam elements to mesh the 354 supports are displayed on Figure 3.22. The computation times for this model were about 1.8 day on 12 core AMD Opteron™ 6376 2.3 GHz – 128 Gb RAM. The computations are a bit slower, however in this case, the software had to handle some instabilities such as the damage and the element deletions. Also, the boundary conditions on the rotations may have slowed the computations.

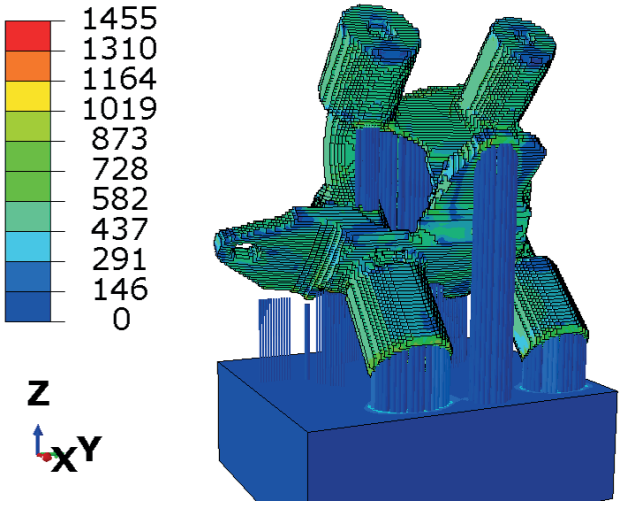

(a) Von Mises stress fields (MPa).

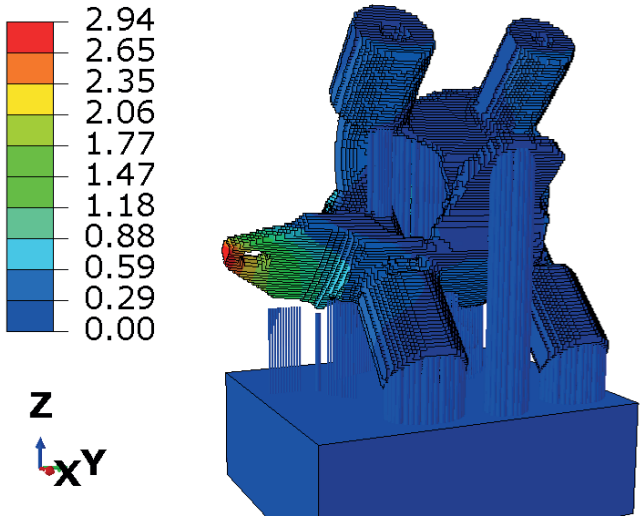

(b) Displacement fields (mm).

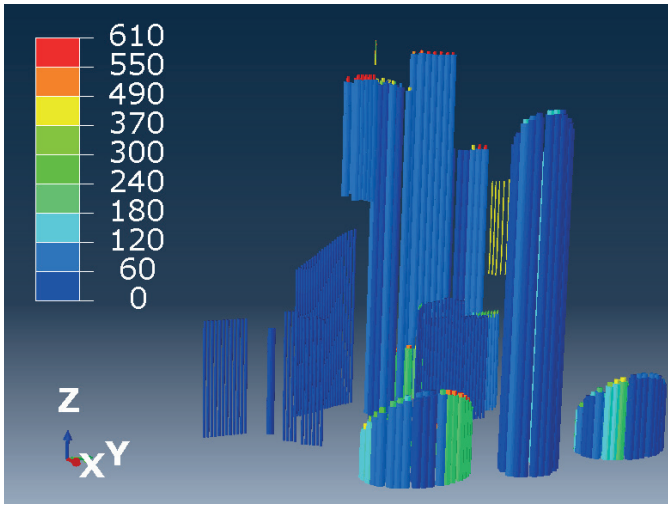

(c) Von Mises stress fields (MPa) on beam supports.

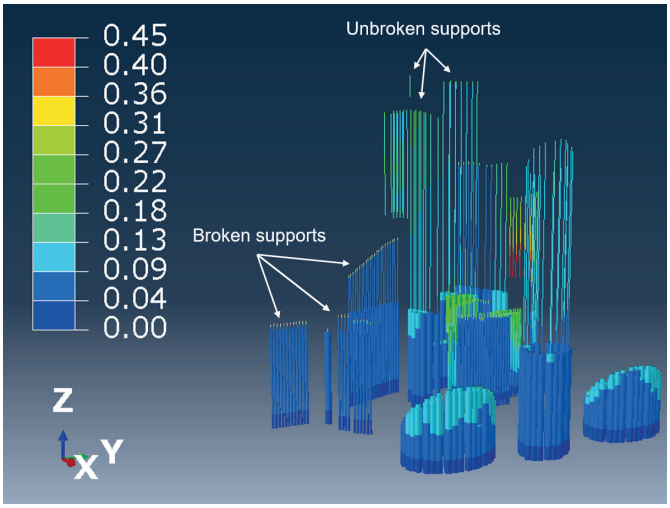

(d) Displacement fields (mm) on beam supports

Figure 3.22: Beam elements simulation results: stress and displacement fields.

It could also be noticed that all the breakages appeared at the tooth location, no supports have been detached from the build plate or at a midsection. This behaviour is due to the radius shrinkage at the tooth area which results in a stress concentration area.

There are 126 detached supports. This number of detached supports is significantly higher than the experimental production (supports breakages were located on the hydraulic joint arm as shown in Figure 3.9).

It is worth mentioning that some supports have completed the damage and their teeth have been detached while suffering compression solicitations. This behaviour is not representative since the cracks may not propagate as they could in traction. These compression loadings are the reason for hindering all the rotations, they lead to buckling phenomena and convergence issues.

Regarding the overall displacement results in Figure 3.22(b), it can be seen that the maximum displacement is higher than the value range of the commercial software, see Table 3.4. This discrepancy must be due to the large number of detached supports, which allowed for the part to wrap more freely.

The number of detached supports is too large compared to the experimental results (13supports experimentally instead of 126 detached supports in the simulation).

It is necessary to understand the reasons of such discrepancy and eventually to better calibrate the model parameters to fit the actual supports behaviour. Hence, in the next sections, investigations are performed to identify the main parameters within the model that generate such discrepancies in the simulation results.

First, we will look at the mechanical behaviour of the supports as a group, in a controlled loading case. Hence, a self-developed multi-support set up will be tensile tested and the force-displacement measurements will be compared to a numerical simulation.

3.4.2.3. Multi-supports set up: supports group's mechanical behaviour

The previous 1D-beam elements supports model have converged and some of the beam supports detached from the part, including those at the arm of the hydraulic joint (the location we expect from the experimental results shown in Figure 3.9). However, too many beams have been detached from the part and it may be due to numerous factors (i.e. too weak material properties, damage during compression phase, non-representative temperature conditions, abrupt section reduction for teeth radius, bending phenomenon in the supports, stiffening from the neighbourhood supports, etc.).

At first, we will compare the behaviour of an experimental set up having several cone supports with a tensile test at room temperature and compare the results with a simulation. The same parameters as in the previous models will be used.

A multi-supports set up (shown in Figure 3.23) is additively manufactured for tensile testing. Its objective is to compare the maximum force applied to detach the beam supports from a part, experimentally and numerically, using literature material properties.

Seventy-nine supports of base diameter 1.10 mm were meshed with B31 beam elements, their teeth having a uniform diameter of 0.75 mm (the minimum diameter of the real teeth). The section variation from 1.10 mm to 0.75 mm is abrupt, and a smoother variation might be implemented using non-standard beam elements in a future work. As in the hydraulic joint case, both the diameter values of 1.10 mm and 0.75 mm were proposed as standard by the manufacturer software QuantAM®.

The numerical model was established with the same file used for the production. The part was meshed using 305 434 linear hexahedral elements of type C3D8I (mesh size of 250 µm). The mesh size applied to the supports was finer, 0.1 mm, in order to accurately retrieve the force magnitude and the displacement fields. Supports were meshed using 5 530 linear B31 beam elements.

The set up consisted of a part that could be pulled from a central hole. The contact on the central hole was idealised through the superior surface of the hole, this assumption having no impact on the teeth loadings.

To keep the same conditions as the hydraulic joint model, the beams rotations were also artificially frozen. A vertical displacement boundary condition of 0.7 mm was set at the hole's upper surface to simulate the experimental loading.

A reduced build plate of dimensions 22.5 mm* 10 mm* 9.3 mm was used to numerically attach the supports. An elastic foundation was set on the lower side of the build plate (see red triangles in Figure 3.23(b)). In order to simulate a quasi-rigid attachment of the build plate, a large rigidity value was set for the elastic foundation.

From the experimental data shown in Figure 3.24, it can be observed that the maximum applied force was approximately of 20 kN. From the experiment, a displacement of the build plate of 1.25 mm was observed before the breakage.

The stiffness is defined as the resistance to deflection, and in this case, the estimated stiffness value was of 16 kN/mm. Since the models did not converge with this stiffness value, it was decided to use a stiffness comparable to a rigid body, multiplying the original stiffness by a factor 1 000.

Hence, the magnitude of the force applied on the system was retrieved by measuring the averaged vertical displacement of the build plate bottom face, and multiplying it by the stiffness value. Vertical displacements at the end of the teeth were compared to the displacement of the build plate to define the strains in Figure 3.24.

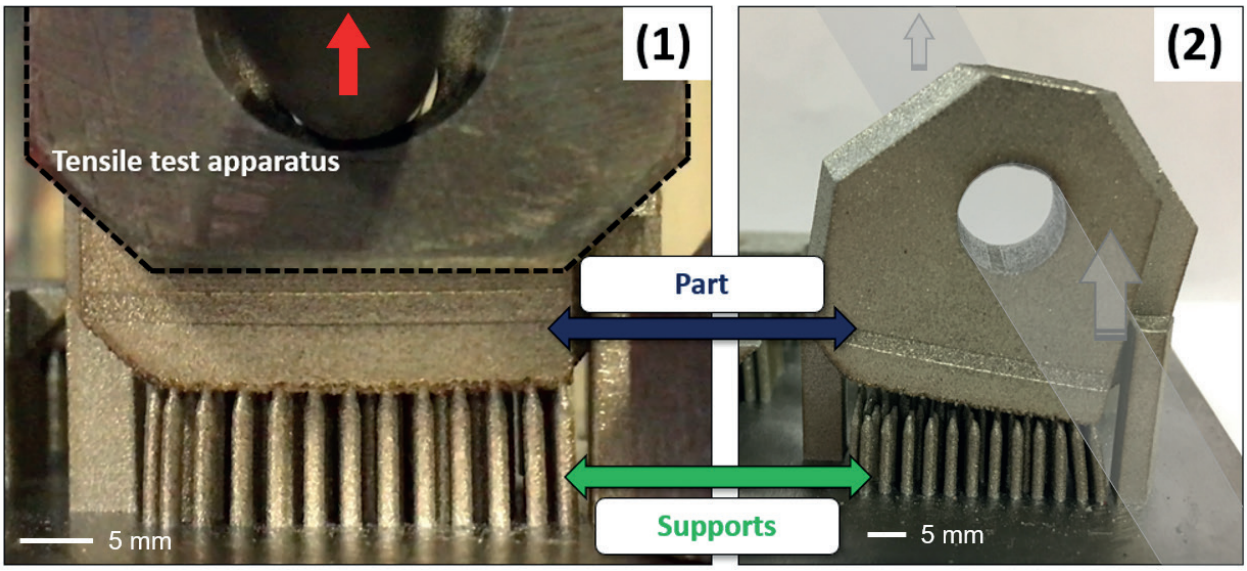

(a) Experimental multi-supports set-up: (1) During loading, dashed lines delimit the tensile test apparatus tied to the part. (2) After supports detachment and unloading, all breakages were located at the teeth. Grey areas and arrows show the position of the rod and the pulling direction.

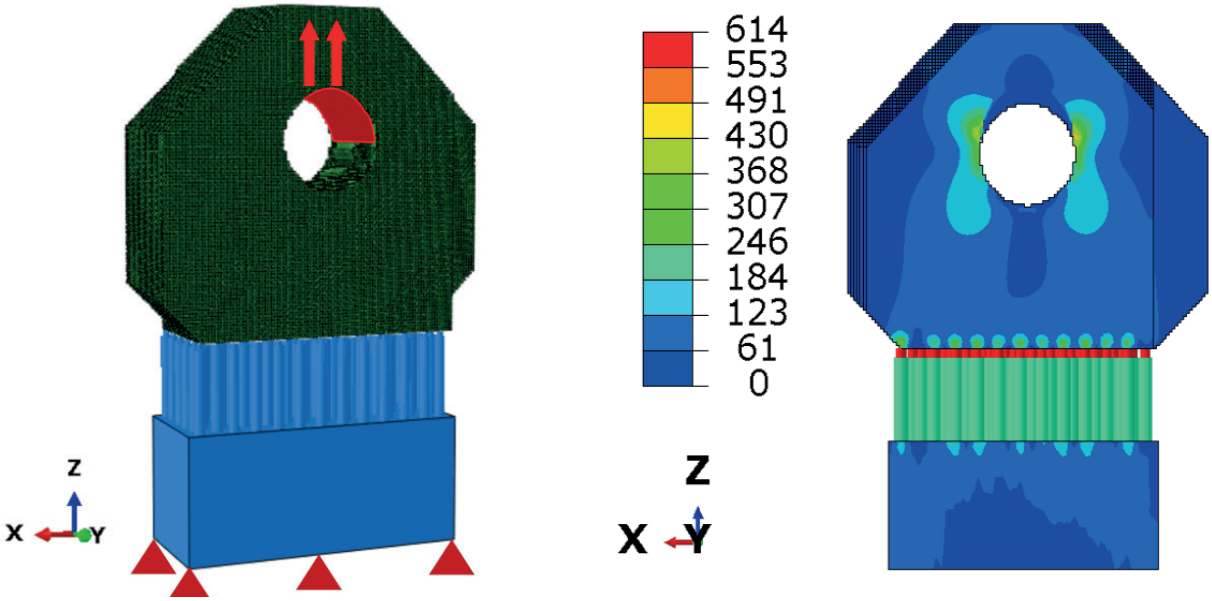

(b) Abaqus model of the multi-support set-up. (c) Von Mises stress fields at the peak stress value.

Figure 3.23: Multiple cone supports experimental and model set-up, as well as simulation results at the peak stress value.

The multi-supports set up model and simulation at a specific displacement increment (for which the peak stress value is attained) are displayed on Figure 3.23. From Figure 3.23(c), it could be seen that the main stresses are located at the tooth area. The underlying supports having a larger diameter (1.10 mm compared to 0.75 mm at the tooth location) suffer less than half the stress magnitude than the teeth.

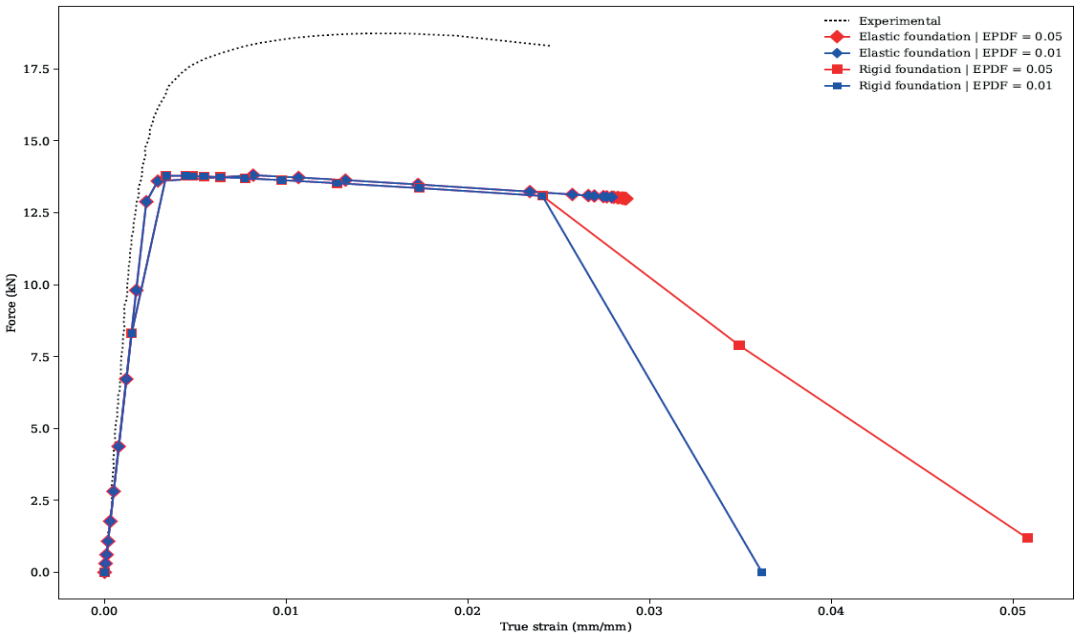

Figure 3.24: Multi-supports set up experimental (dashed) and simulated force-strain tensile test results with different stifness (elastic foundation: stiffness 16 kN/mm, and rigid foundation: stiffness 16.10^6 N/mm); and for both stifnesses, two values of the effective plastic displacement at the point of failure (EPDF) parameter.

The whole force-strain curves from the experimental tensile test and the simulation are shown on Figure 3.24. The simulated curves are shown with two different values of the effective plastic displacement at the point of failure (EPDF), presented in Section 3.4.1.

In the hydraulic joint model (Section 3.4.2), the 0.05 parameter value was used. Indeed, it was not possible for the simulation to converge while using a most suitable effective plastic displacement parameter (such as 0.01 and lower).

Hence, while using a EPDF value of 0.05, 126 supports were detached from the hydraulic joint model. Using the degradation variable, it was possible to estimate the number of additional detached supports with a value of 0.01: only 7 more would have been detached. Then, increasing the number of supports increases the risk of having several damaged supports, and the risk for the simulations to fail to converge.

Using a rigid foundation (1 000 times larger than the elastic foundation), the damage pursued through a large strain range, which does not behave like the experimental supports. On the contrary, with an elastic foundation (of stiffness 16 kN/mm), at the instant the force would decrease significantly due to the damage initiation, the restoring force from the build plate foundation would lead to an instantaneous breakage of the supports. The experimental observations are similar. Hence, it is necessary to consider the elasticity of the set up to retrieve an equivalent damage behaviour. A lower value of the EPDF parameter may lead to closer behaviour to the experiments.

It can be observed in Figure 3.24 that the simulated mechanical behaviour is below the experimental. The difference between the maximum force of the simulated test (13.79 kN) and the experimental one (18.74 kN) was about 26%. Hence, the mechanical behaviour of the cone supports needs to be further tuned to imitate the experimental behaviour.

Equally, the damage behaviour may need to be tuned for the supports to break at the same strain as the experiment. However, extracting data about the damage of the supports using the Figure 3.24 looks challenging. It is possible that an exponential evolution of the damage variable (as detailed in Equation (3.13)) would help to better fit the evolution of the simulated force in the plastic domain. Tests using this parameter were not

launched in this study.

To observe the impact of the plastic parameters set within the model, a simulation test has been performed rising the tensile strength and the yield strength values by 26%. The model used for this test was using an elastic foundation (stiffness 16 kN/mm) under the build plate and the same two EPDF values as before. The simulation results are shown with the experiment in Figure 3.25.

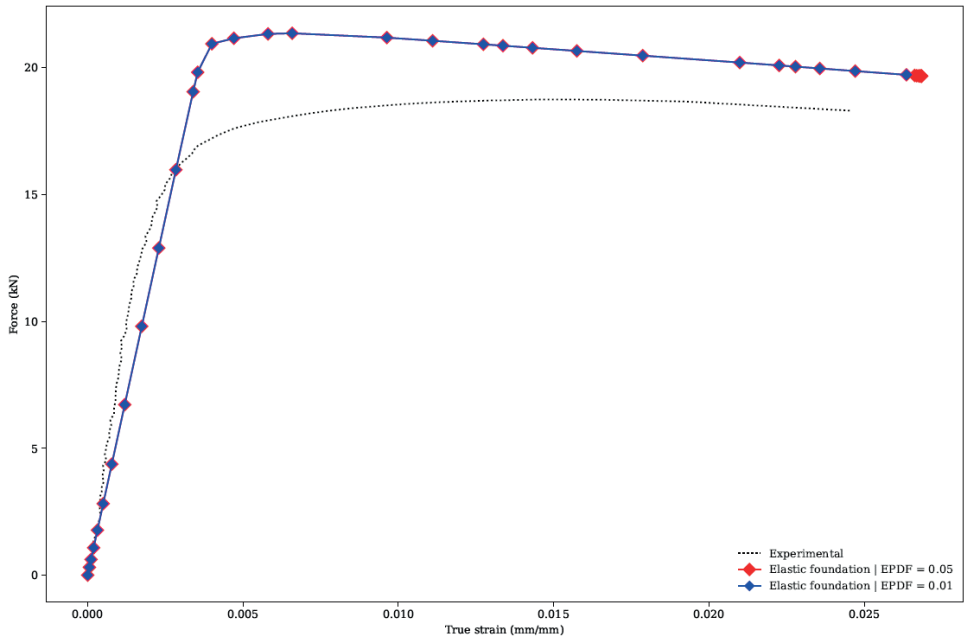

Figure 3.25: Multi-supports set up experimental (dashed) and simulated force-strain tensile test results using artifically larger tensile strength and yield strength (+26%) and two values of the effective plastic displacement at the point of failure (EPDF) parameter.

It can be seen in Figure 3.25 that the maximum simulated force in larger than the experimental (13% discrepancy), while previously lower (26% discrepancy, see Figure 3.24). Hence, the plastic parameters set within the model have a strong impact on the behaviour of the cone supports and need to be thoroughly characterised.

However, the discrepancy in the maximum force between the experiment and the simulations can hardly be explained only by plastic parameters set within the model. It is assumed that the actual beam diameter manufactured by LPBF are a little larger than the nominal values, hence they may suffer larger force magnitudes before breakage.

Also, in the experimental set-up, not all supports broke at the same time, whereas the modelled supports did experience similar damage through the simulation and broke at the same time. Simulating this specific behaviour looks challenging since it also depends on internal flaws due to the manufacturing process.

In the next section, the individual supports mechanical response is considered under tensile loading.

3.4.2.4. Individual beam support mechanical characterisation

In the previous section, several supports were considered as a whole (numerous identical supports of the same height and diameter, all connected to the same part surface). Seventy-nine supports together were tested using a specific experimental set up, in order to have realistic supports.

In this section, the behaviour of an individual cone support will be looked upon. It is assumed that the mechanical characteristics of the manufactured cone supports may differ greatly from the bulk part because of their specific thermal history. In particular, cone supports are surrounded by thermally insulating powder particles, causing the heat to be mostly diffused in the vertical direction. Also, the part's manufacturing would

generate a large extent of thermal energy that would diffuse through the cone supports below.

The thermal history difference between the cone supports and the part could lead to specific microstructures or even defects (i.e. porosity). Hence, the literature mechanical characteristics listed in Table 3.5 may not be suited to the supports.

In order to perform tensile tests on individual supports, i.e. at least a bar with a small diameter, another specific set up was designed, as can be seen in Figure 3.26.

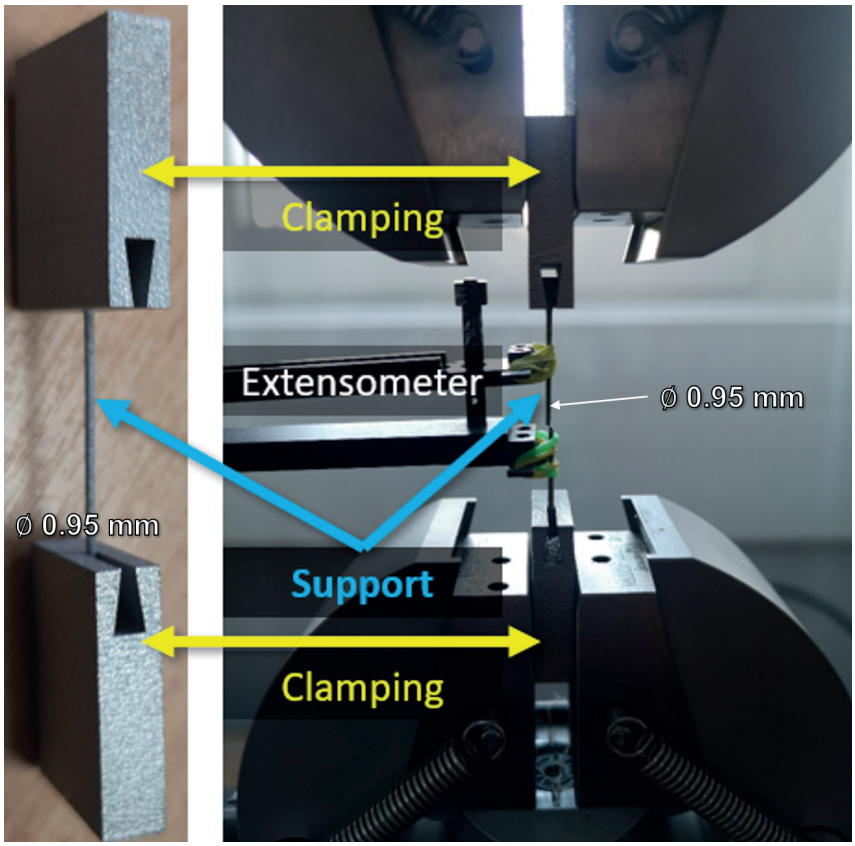

Figure 3.26: Individual support set up (left) and inside the tensile test apparatus with the extensometer (right).

The tensile tests were performed on an Instron Electropulse 3kN apparatus, and the distortion was measured using mechanical extensometry with an 2620-604 Instron extensometer. A specific set up was manufactured in three parts and assembled as shown in Figure 3.26.

The supports had a uniform diameter of 0.95mm (supports with diameters below this limit shown manufacturing issues when built with great heights). The total supports height was of 33mm and an operating length (outside the clamping) was of 23 mm. A 5mm lid was designed at the support edges for the assembly within the clamping (see Figure 3.26).

The resulting tensile test curves for nine individual supports are displayed in Figure 3.27.

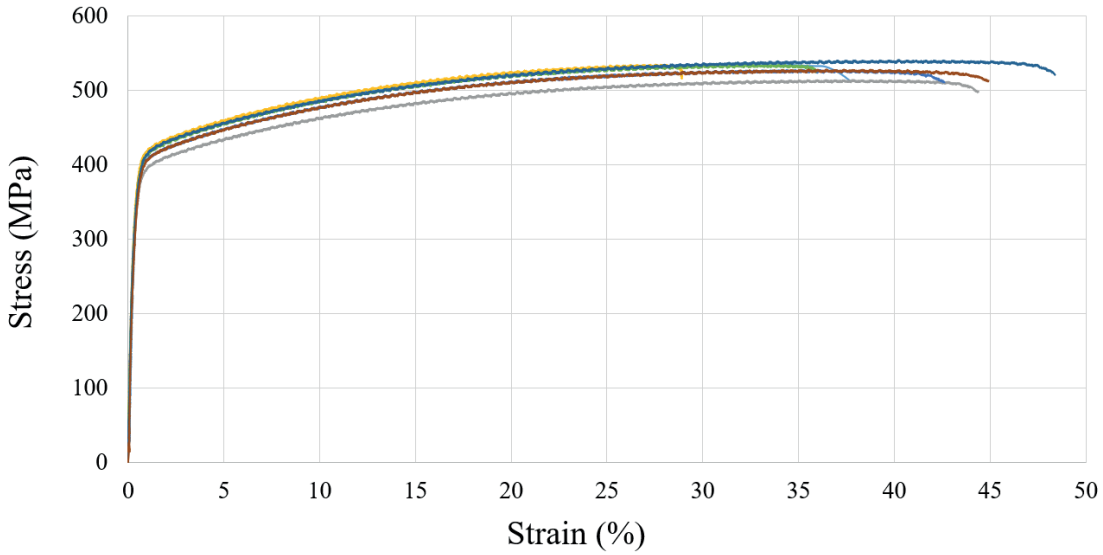

Figure 3.27 : Individual beam support tensile test stress-strain results.

It can be seen from the stress-strain curves in Figure 3.27 that the results are homogeneous between the samples. Regarding the mechanical properties, the mean Young modulus was about 106 GPa (instead of 180 GPa from literature values, see Table 3.5). The yield strength was about 400 MPa (instead of 496 MPa) and the tensile strength is estimated at 520 MPa (instead of 614 MPa).

Thus, it can be concluded that the material properties assigned to the part differ significantly from individual cone supports.

It is worth mentioning that only one support broke below a strain of 30%, and the other ones broke at a strain above 35% (the maximum measured fracture strain being 48%).

Hence, in the following section, specific support mechanical properties will be assigned within the hydraulic joint model and several scenarios compared. The objective is to compare the number of broken supports by the end of the simulation and identify the key parameters. A complementary objective would be to fully characterise the mechanical behaviour of the support teeth.

At the moment, these ranges of diameters (below 0.9 mm) are difficult to manufacture by LPBF on a sufficient height. These experimental teeth characterisation will be the topic of a future study.

3.4.2.5. Beam supports mechanical sensibility

In the previous section, individual support tensile tests have been performed, showing that the bulk part mechanical properties differ significantly from the supports.

In the current section, two separate cases are performed to understand the key parameters to be assigned to the modelled supports. These cases are compared with the reference (Ref. in Table 3.7), for which the simulation results have already been analysed (see Section 3.4.2). For the reference case, the bulk material characteristics found in the literature have been assigned to the supports.

The second case ”Case 2” has a higher fracture strain parameter than the reference case: the fracture strain is set at 45% instead of 34%. All the other parameters are equal to those of the reference case.

The third case ”Case 3” has equal fracture strain to the reference case (34%), but its elasto-plastic properties are lowered: Young Modulus is set at 106GPa, the yield and tensile strengths are set at 400MPa and 520MPa respectively. The changes are driven by the experimental results of the individual cone supports (Figure 3.27).

The different parameters are listed in Table 3.7.

While using weakened mechanical properties for the supports (Case 3), and keeping the same fracture strain

(34%), the number of broken supports remained the same (125 instead of 126 in Reference case, Section 3.4.2). On the contrary, while keeping the same elasto-plastic properties as the part, and providing a greater fracture strain (45% instead of 34%, Case 2), the number of broken supports diminishes to 105.

Hence, the fracture strain could be considered as one of the key parameters to precisely characterise in order to simulate the supports breakage.

Considering the three material characteristics cases (see Table 3.7) and the number of broken supports, it can be concluded that assigning greater fracture strain parameter improves fairly the simulation results.

Table 3.7: Mechanical properties and number of broken supports for the different cone support sensibility cases.

Characteristics	Ref.	Case 2	Case 3
Young Modulus E (GPa)	180	180	106
Yield strength Re (MPa)	496	496	400
Tensile strength Rm (MPa)	614	614	520
Fracture strain A% (%)	34	45	34
Broken supports / Exp	126/13-44	105/13-44	125/13-44

We then decided to modify the compression damage behaviour modifying the triaxiality parameter in ABAQUS. While the damage beginning of the elements in tensile solicitation remains at a strain value of 34%, we set the damage beginning of the elements under compression at 110%. The experiment is summarized in Table 3.8.

In this case, delaying the damage of compressed elements had a significant result on the number of broken supports: only 53 of them were separated. Hence, a large number of previously broken supports were deleted while being in compression soliciation. Precise compressive characterisations are necessary for simulating beam supports breakage.

In this case, the computation times were about 18h36min, hence significantly faster than the previous Reference model (42h49min). The discrepancy in computation durations may be due to the fact that the solver does not need to consider the various damage variables and the numerous element deletions.

Table 3.8: Mechanical properties and the number of broken supports with a delayed damage behaviour for elements under compression soliciation.

Characheristics	Ref.	Compressive damage delayed
Young Modulus E (GPa)	180	180
Yield strength Re (MPa)	496	496
Tensile strength Rm (MPa)	614	614
Tensile fracture strain A% (%)	34	34
Compressive fracture strain (%)	34	110
Broken supports / Exp	126/13-44	53/13-44

3.5. Conclusions and perspectives

The laser powder bed fusion (LPBF) process is one of the most studied additive manufacturing processes, both in the industry and academic research fields. A significant challenge of this process is anticipating the various flaws before manufacturing the parts, including distortions and fractures.

While using numerous supports to anchor the part, some may be damaged and even detached, during the manufacturing or during the final cool down. At this point, the part can warp freely and collide with the recoating system, interrupting the whole manufacturing process.

In some cases, the breakage of the supports does not invalidate the part. Simulating the damage of the sup-

ports and being able to track the ongoing deflection was the scope of this study.

An industrial part was chosen as a case study. Its manufacturing completed, but some supports have broken, allowing the part to warp and slightly collide with the layering system. However, the manufacturing process completed.

Firstly, five commercial software were used to simulate the manufacturing process, and all the results show a significant distortion of the part. However, none of the codes was able to predict the breakage of the supports.

A deeper investigation into one of these commercial codes allowed to suggest a possible collision with the layering system; and also, a potential breakage of the supports. The software provided probabilities that cannot be explained (the code is the property of the software editor and is not accessible); and overall, the supports damage is not explicitly modelled.

Every developed model was strictly quasi-static mechanical. And, for sake of simplicity, loads were assigned as constant temperature increments along the activated macro layers. However, full thermal modelling could be considered.

Since most of the commercial codes use voxel elements, and as a comparison basis, two types of models were developed to mesh the supports: 3D-voxel elements and 1D-beam elements.

The main reason for modelling supports using the 1D-beam elements is their inherent ability to accurately incorporate the shrinkage in the teeth section, in contrast with the 3D-voxels.

To approximate the shrinkage in the voxels model, a local change in the material properties would have been necessary. However, identifying the location of the specific shrinkage material properties in the voxels model could be delicate to perform using a global STL file containing both the supports and the part.

Some numerical instabilities and convergence issues were encountered with the 1D-beam elements model. We managed to identify the buckling phenomena (from some supports suffering compression solicitations) as the origins of the instabilities. Then, we listed a series of possible ways to overcome the issue, and their respective drawbacks: mainly the overwhelming computational times and the difficulty to identify suitable parameters for each support of the model.

Finally, it was chosen to freeze all the supports' rotations, preventing the buckling from happening. This way, we managed to use a static resolution, elasto-plastic material behaviour and also the *Activation* feature in ABAQUS, essential for modelling the LPBF process.

We also found a way to model the supports overlapping using horizontal instances to connect each of them. However, due to the size of the resulting model and the physical memory limitations, this solution (yielding promising results on small examples) could not be implemented.

In an initial simulation campaign using the previously mentioned assumptions and initial non-calibrated damage parameters, both models (voxel and beam support elements) managed to converge, in large computational durations though (almost two days for the beam elements simulation).

While using 1D-beam elements to mesh the cone supports, a whole supported region was detached. However, no fracture was observed in the voxel elements model. The difference between voxel and 1D-beam elements could be explained by the absence of geometrical narrowing corresponding to the teeth while using voxel elements. Also, there is a strong connection between the voxel elements, although the beam supports were not connected to each other.

The maximum displacement results of the voxel elements model were comprised in the range of those of the commercial codes, and like the commercial codes, none of these supports broke away. The maximum displacement results of the beam elements model were higher than those of the commercial software, however, in

contrast to these codes, using beam elements and teeth-narrowing, some supports broke away. Hence, in this case, the maximum displacement result could hardly be compared to the commercial codes.

The number of supports that broke away during the simulation was too large compared to the experiment. The supports mechanical behaviour was then characterised. To do so, two configurations were studied, and specific set-ups were LPBF manufactured: a multi-supports set-up (to comprise the behaviour of the supports as a group) and an individual support set-up.

Regarding the group of supports, it was observed that the difference in the maximum force applied in the simulation and experimentally was large (26%). The simulated plastic behaviour did not follow the experiment and it seems necessary to characterise the behaviour of the group of supports more accurately in the future.

Then, the individual cone support behaviour was characterised using another specific set-up. The fracture strain was slightly greater, but the Young modulus and the strengths were significantly weaker than the values reported from the literature for bulk 316L. It is assumed that the specific thermal history of the supports influences the microstructure and consequently, the mechanical behaviour. Hence, it has been shown that the supports mechanical properties differ significantly from the bulk parts and needs to be thoroughly characterised to be modelled.

Regarding the hydraulic joint 1D-beam elements simulation, a potential improvement solution resides in precisely characterising the fracture strain parameter for both the supports and the bulk material. Indeed, using a value of 45% (instead of 34%) led to a decreased number of detached supports down to 105.

Also, the mechanical characterisation of the teeth seems primordial since the teeth constitute the fracture site in every case (experimentally and simulated). For now, it is technically challenging to LPBF-manufacture individual supports with suitable diameters. Indeed, it was managed to manufacture beams of 0.95 mm in diameter for the individual supports set-up; however, the teeth that broke away had a diameter of 0.20 mm and 0.50 mm. Developing a method for producing long beam with the suitable diameters will be the focus of a complementary study. However, the thermal history of this individual beam may be different than the one of a support linked to (and heated by) the part, even more when there are multiple supports connected to the part. Identifying the characteristics to implement within the finite element code from individual and multiple beam testing remains a challenging task.

Lastly, while hindering the supports suffering compression solicitation to damage, it was noticed that the number of broken supports decreased significantly (from 126 to 53). However, supports may damage from compression, and their behaviour regarding these solicitations should be thoroughly characterised in the future.

Also, it was noticed that with an increasing number of cone-supports in the hydraulic joint model, it could reveal more and more challenging to find suitable damage evolution parameters and boundary conditions allowing the simulations to complete. This is due to the numerous numerical instabilities while using a static resolution and non-linear characteristics.

It is expected that running a simulation of several parts, each of them with hundreds of cone-supports (such as the present application), would make a global convergence inaccessible because of the numerous supports cracking. Using equivalent homogeneous material properties to approximate the support structures may help to tackle the convergence issues.

As for the previous chapter, it seems that the thermal history has a paramount importance within the process since it is assumed that the differences between the supports and the bulk material comes from the potentially different thermal history. The next chapter of this manuscript will focus on the thermal resolution of the LPBF process using a specific multiscale method.

3.6. References

[1] ISO/TC. PR NF EN ISO/ASTM 52911- 1:2018-01 Additive manufacturing - Technical design guideline for powder bed fusion - Part 1: Laser-based powder bed fusion of metals, 2018.

[2] Jingchao Jiang, Xun Xu, and Jonathan Stringer. Support Structures for Additive Manufacturing: A Review. Journal of Manufacturing and Materials Processing, 2(4):64, 2018.

[3] M. X. Gan and C. H. Wong. Practical support structures for selective laser melting. Journal of Materials Processing Technology, 238:474-484, 2016.

[4] V. Benoist. Topological optimization design for additive manufacturing, taking into account flexion and vibrations during machining post processing. University of Toulouse. 2020.

[5] Inigo Flores, Niklas Kretzschmar, Abdul Hadi, Sergei Chekurov, David Bue, and Atanu Chaudhuri. Implications of lattice structures on economics and productivity of metal powder bed fusion. Additive Manufacturing, 31(November 2019):100947, 2020.

[6] VELO3D Website, 2020.

[7] Trumpf Website. Option de préchauffage à 500 ° C : First time right, 2021, [Online]. Available: https://www.trumpf.com/fr_FR/solutions/avantages-des-machines-trumpf/les-avantages-des-systemes-de-fabrication-additive/prechauffage-a-500-c/.

[8] Paramita Das, Ramya Chandran, Rutuja Samant, and Sam Anand. Optimum Part Build Orientation in Additive Manufacturing for Minimizing Part Errors and Support Structures. In Procedia Manufacturing, volume 1, pages 343–354. Elsevier B.V., 2015.

[9] Kaifei Zhang, Guang Fu, Peng Zhang, Zhibo Ma, Zhongfa Mao, and David Z. Zhang. Study on the geometric design of supports for overhanging structures fabricated by selective laser melting. Materials, 12(27):1-16, 2018.

[10] Kamran Mumtaz, P. Vora, and Neil Hopkinson. A method to eliminate anchors supports from directly laser melted metal powder bed processes. In Proceedings of the Solid Freeform Fabrication Symposium, pages 55-64, Austin, Texas, 2011.

[11] Owen J. Hildreth, Abdalla R. Nassar, Kevin R. Chasse, and Timothy W. Simpson. Dissolvable metal supports for 3D direct metal printing. 3D Printing and Additive Manufacturing, 3(2):91-97, 2016.

[12] Christopher S. Lefky, Brian Zucker, David Wright, Abdalla R. Nassar, Timothy W. Simpson, and Owen J. Hildreth. Dissolvable Supports in Powder Bed Fusion-Printed Stainless Steel. 3D Printing and Additive Manufacturing, 4(1):3-11, 2017.

[13] Subbarao Raikar, Meredith Heilig, Avinash Mamidanna, and Owen J. Hildreth. Selfterminating etching process for automated support removal and surface finishing of additively manufactured Ti-6Al-4V. Additive Manufacturing, 37(June 2020):101694, 2021.

[14] Qiqiang Cao, Yuchao Bai, Jiong Zhang, Zhuoqi Shi, Jerry Ying Hsi Fuh, and Hao Wang. Removability of 316L stainless steel cone and block support structures fabricated by Selective Laser Melting (SLM). Materials and Design, 191:108691, 2020.

[15] Daniel Thomas. The Development of Design Rules for Selective Laser Melting. PhD thesis, University of Wales Institute, Cardiff, 2012.

[16] F. Calignano. Design optimization of supports for overhanging structures in aluminum and titanium alloys by selective laser melting. Materials and Design, 64:203–213, 2014.

[17] Martin Leary, Tobias Maconachie, Avik Sarker, Omar Faruque, and Milan Brandt. Mechanical and thermal characterisation of AlSi10Mg SLM block support structures. Materials and Design, 183:108138, 2019.

[18] Lourdes D. Bobbio, Shipin Qin, Alexander Dunbar, Panagiotis Michaleris, and Allison M. Beese. Characterization of the strength of support structures used in powder bed fusion additive manufacturing of Ti-6Al- 4V. Additive Manufacturing, 14:60–68, 2017.

[19] Kai Zeng. Optimization of support structures for selective laser melting. PhD thesis, University of Louisville, 2015.

[20] Altair Inspire™ Print3D Website, 2020.

[21] Additive Works GmbH Website, 2020.

[22] Netfabb® Website, 2020.

[23] Simufact Additive Website, 2020.

[24] ESI Group Website, 2018.

[25] J. Zhang, Y. Zhang, W. H. Lee, L. Wu, H. H. Choi, and Y. G. Jung. A multi-scale multi-physics modeling framework of laser powder bed fusion additive manufacturing process. Met. Powder Rep., vol. 73, no. 3, pp. 151–157, 2018, doi: 10.1016/j.mprp.2018.01.003.

[26] C. Li, C.H. Fu, Y.B. Guo, and F.Z. Fang. A multiscale modeling approach for fast prediction of part distortion in selective laser melting. Journal of Materials Processing Technology, 229:703-712, 2016.

[27] Matthias Markl and Carolin Körner. Multiscale Modeling of Powder Bed-Based Additive Manufacturing. Annual Review of Materials Research, 46(1):93-123, jul 2016.

[28] Rishi K. Ganeriwala, Neil E. Hodge, and Jerome M. Solberg. Towards improved speed and accuracy of laser powder bed fusion simulations via multiscale spatial representations. Computational Materials Science, 187(November 2020):110112, 2021.

[29] Peter Mercelis and Jean Pierre Kruth. Residual stresses in selective laser sintering and selective laser melting. Rapid Prototyping Journal, 12(5):254-265, 2006.

[30] T. Mukherjee, J. S. Zuback, A. De, and T. DebRoy. Printability of alloys for additive manufacturing. Scientific Reports, 6:1-8, 2016.

[31] T Mukherjee, V Manvatkar, A. De, and T. DebRoy. Mitigation of thermal distortion during additive manufacturing. Scripta Materialia, 127:79-83, 2017.

[32] Paul A. Hooper. Melt pool temperature and cooling rates in laser powder bed fusion. Additive Manufacturing, 22(May):548â€“559, 2018.

[33] Michael F Zaeh and Gregor Branner. Investigations on residual stresses and deformations in selective laser melting. Production Engineering, 4(1):35-45, 2010.

[34] Ratnadeep Paul, Sam Anand, and Frank Gerner. Effect of Thermal Deformation on Part Errors in Metal Powder Based Additive Manufacturing Processes. Journal of Manufacturing Science and Engineering, 136(3):031009, 2014.

[35] Erik R. Denlinger and Pan Michaleris. Effect of stress relaxation on distortion in additive manufacturing process modeling. Additive Manufacturing, 12:51–59, 2016.

[36] L. Parry, I. A. Ashcroft, and R. D. Wildman. Understanding the effect of laser scan strategy on residual stress in selective laser melting through thermo-mechanical simulation. Additive Manufacturing, 12:1-15, 2016.

[37] T. Mukherjee, W. Zhang, and T. DebRoy. An improved prediction of residual stresses and distortion in additive manufacturing. Computational Materials Science, 126:360-372, 2017.

[38] R.K. Ganeriwala, M. Strantza, W.E. King, B. Clausen, T.Q. Phan, L.E. Levine, D.W. Brown, and N.E. Hodge. Evaluation of a thermomechanical model for prediction of residual stress during laser powder bed fusion of Ti-6Al-4V. Additive Manufacturing, 27(April):489-502, may 2019.

[39] Lars Erik Lindgren, Henrik Runnemalm, and Mats O. Näsström. Simulation of multipass welding of a thick plate. International Journal for Numerical Methods in Engineering, 44(9):1301-1316, 1999.

[40] Panagiotis Michaleris. Modeling metal deposition in heat transfer analyses of additive manufacturing processes. Finite Elements in Analysis and Design, 86:51-60, 2014.

[41] C. Li, Z. Y. Liu, X. Y. Fang, and Y. B. Guo. On the Simulation Scalability of Predicting Residual Stress and Distortion in Selective Laser Melting. Journal of Manufacturing Science and Engineering, 140(4):041013, 2018.

[42] J. Goldak, A. Chakravarti, and M. Bibby. A new finite element model for welding heat sources. Metall. Trans. B, vol. 15, pp. 299–305, 1984.

[43] Yukio Ueda, Keiji Fukuda, and Masayuki Tanigawa. New Measuring Method of Three Dimensional Residual Stresses Based on Theory of Inherent Strain(Welding Mechanics, Strength & Design). Transactions of JWRI, 8(2):249-256, 1979.

[44] Nils Keller and Vasily Ploshikhin. New method for fast predictions of residual stress and distortion of AM parts. In Solid Freefrom Fabrication, pages 1689-1699, 2014.

[45] Nils Keller. Nils Keller verfahren durch Multi-Skalen-Simulation Verzugsminimierung bei selektiven Laserschmelzverfahren durch. PhD thesis, Universität Bremen, 2016.

[46] Matteo Bugatti and Quirico Semeraro. Limitations of the inherent strain method in simulating powder bed fusion processes. Additive Manufacturing, 23(May):329–346, 2018.

[47] Marvin Siewert, Fabian Neugebauer, Jérémy Epp, and Vasily Ploshikhin. Validation of Mechanical Layer Equivalent Method for simulation of residual stresses in additive manufactured components. Computers and Mathematics with Applications, 78(7):2407-2416, 2019.

[48] Xuan Liang, Lin Cheng, Qian Chen, Qingcheng Yang, and Albert C. To. A modified method for estimating inherent strains from detailed process simulation for fast residual distortion prediction of singlewalled structures fabricated by directed energy deposition. Additive Manufacturing, 23(August):471-486, 2018.

[49] Katharina Bartsch, Fritz Lange, Melanie Gralow, and Claus Emmelmann. Novel approach to optimized support structures in laser beam melting by combining process simulation with topology optimization. Journal of Laser Applications, 31(2):022302, 1–7, 2019.

[50] Zhi-Dong Zhang, Osezua Ibhadode, Usman Ali, Chinedu Francis Dibia, Pouyan Rahnama, Ali Bonakdar, and Ehsan Toyserkani. Topology optimization parallel-computing framework based on the inherent strain method for support structure design in laser powder-bed fusion additive manufacturing. International Journal of Mechanics and Materials in Design, 0123456789, 2020.

[51] Xuan Liang, Wen Dong, Shawn Hinnebusch, Qian Chen, Hai T Tran, John Lemon, Lin Cheng, Zekai Zhou, Devlin Hayduke, and Albert C To. Inherent strain homogenization for fast residual deformation simulation of thin-walled lattice support structures built by laser powder bed fusion additive manufacturing. Additive Manufacturing, 32(October 2019):101091, 2020.

[52] Hai T Tran, Qian Chen, Jonathan Mohan, and Albert C To. A new method for predicting cracking at the interface between solid and lattice support during laser powder bed fusion additive manufacturing. Additive Manufacturing, 32(January):101050, 2020.

[53] Jukka Pekka Järvinen, Ville Matilainen, Xiaoyun Li, Heidi Piili, Antti Salminen, Ismo Mäkelä, and Olli Nyrhilä. Characterization of effect of support structures in laser additive manufacturing of stainless steel. Physics Procedia, 56(C):72-81, 2014.

[54] Qiqiang Cao, Zhuoqi Shi, Yuchao Bai, Jiong Zhang, Cuiling Zhao, Jerry Ying Hsi Fuh, and Hao Wang. A novel method to improve the removability of cone support structures in selective laser melting of 316L stainless steel. Journal of Alloys and Compounds, 854:157133, 2021.

[55] Sebastian Weber, Joaquin Montero, Christoph Petroll, Tom SchÂ¨afer, Matthias Bleckmann, and Kristin Paetzold. The Fracture Behavior and Mechanical Properties of a Support Structure for Additive Manufacturing of Ti-6Al-4V. Crystals, 10(5):343, 2020.

[56] I. Ainsworth, G. D. Rayner, M. J. Mcclelland, R. Revanur, and B. I. Ferrar. US20160306901A1. Improvements in or relating to the building of supports in additive manufacturing, 2016.

[57] M. R. Burhop, D. Madeley, S. Musuvathy, E. Arisoy, E. Slavin, and H. Bank. US9844917B2 Support structures for additive manufacturing of solid models, 2017.

[58] ZhipingWang, Yicha Zhang, Shujie Tan, Liping Ding, and Alain Bernard. Support point determination for support structure design in additive manufacturing. Additive Manufacturing, 47(August):102341, 2021.

[59] Florian Markus Barth. US20180304541A1. 3D Lattice supports for additive manufacturing, 2018.

[60] E. M. A. Marte, T. Sinnett, D. Joerger, and N Dunham. US10486362B2. Method and connecting supports for additive manufacturing, 2019.

[61] Daniel Joerger. US10799951B2. Method and conformal supports for additive manufacturing, 2017.

[62] E.M.A. Marte, Z.D. Fieldman, T. Sinnett, D. Joerger, N. Dunham, and M. Miller. US10549478B2. Methods and surrounding supports for additive manufacturing, 2020.

[63] Z.D. Fieldman, D. Joerger, and N Dunham. US10391753B2. Methods and keyway supports for additive manufacturing, 2019.

[64] Z.D. Fieldman. US10744713B2. Methods and breakable supports for additive manufacturing, 2017.

[65] Z.D. Fieldman, T. Sinnett, D. Joerger, and N. Dunham. US10357828B2. Methods and leading edge supports for additive manufacturing, 2019.

[66] D. Joerger and N Dunham. US10583606B2. Method and supports with powder removal ports for additive manufacturing, 2020.

[67] Z.D. Fieldman and C. Hall. US20180141122A1. Methods and spoke supports for additive manufacturing, 2018.

[68] Pantcho Stoyanov. US9975182B2. Cutting Tool Made by Additive Manufacturing, 2018.

[69] Jan Van Espen. US10843412B2. Support structures in additive manufacturing, 2018.

[70] Vasily Ploshikhin. DE102017113485A1. Method for the additive production of at least one component, support structure or element of a support structure, component with the same and installation for carrying out such a method, 2018.

[71] Scott Alan Gold and Patrick Michael Kenney. US20180029306A1. Methods using ghost supports for additive manufacturing, 2018.

[72] Jamasp Jhabvala, Eric Boillat, Cédric André, and Rémy Glardon. An innovative method to build support structures with a pulsed laser in the selective laser melting process. International Journal of Advanced Manufacturing Technology, 59(1-4):137â€“142, 2012.

[73] M. Cloots, A.B. Spierings, and K. Wegener. Assessing new support minimizing strategies for the additive manufacturing technology SLM. In Solid freeform fabrication symposium, pages 631–643, 2013.

[74] G. Strano, L. Hao, R. M. Everson, and K. E. Evans. A new approach to the design and optimisation of support structures in additive manufacturing. International Journal of Advanced Manufacturing Technology, 66(9-12):1247-1254, 2013.

[75] Ratnadeep Paul and Sam Anand. Optimization of layered manufacturing process for reducing form errors with minimal support structures. Journal of Manufacturing Systems, 36:231-243, 2015.

[76] Jie Song, Youxiang Chew, Xiling Yao, Lishi Jiao, Guijun Bi, and Seung Ki Moon. Numerical study of temperature and cooling rate in selective laser melting with functionally graded support structures. Additive Manufacturing, 24(August):543-551, 2018.

[77] Grégoire Allaire and Beniamin Bogosel. Optimizing supports for additive manufacturing. HAL, 2018.

[78] Mingdong Zhou, Yichang Liu, and Zhongqin Lin. Topology optimization of thermal conductive support structures for laser additive manufacturing. Computer Methods in Applied Mechanics and Engineering, 353:24-43, 2019.

[79] Yuka Kajima, Atsushi Takaichi, Takayuki Nakamoto, Takahiro Kimura, Nuttaphon Kittikundecha, Yusuke Tsutsumi, Naoyuki Nomura, Akira Kawasaki, Hidekazu Takahashi, Takao Hanawa, and Noriyuki Wakabayashi. Effect of adding support structures for overhanging part on fatigue strength in selective laser melting. Journal of the Mechanical Behavior of Biomedical Materials, 78(September 2017):1-9, 2018.

[80] Ö. Poyraz, E. Yasa, G. Akbulut, A. OrhangÂ¨ul, and S. Pilatin. Investigation of support structures for direct metal laser sintering (DMLS) of IN625 parts. In Solid Freeform Fabrication (SFF) Symposium, pages 560-574, Austin, Texas, 2015.

[81] Lin Cheng, Xuan Liang, Jiaxi Bai, Qian Chen, John Lemon, and Albert To. On Utilizing Topology Optimization to Design Support Structure to Prevent Residual Stress Induced Build Failure in Laser Powder Bed Metal Additive Manufacturing. Additive Manufacturing, 27(November 2018):290–304, 2019.

[82] T. A. Krol, M. F. Zaeh, and C. Seidel. Optimization of supports in metal-based additive manufacturing by means of finite element models. In 23rd Annual International Solid Freeform Fabrication Symposium - An Additive Manufacturing Conference, SFF 2012, pages 707-718, Austin, Texas, 2012.

[83] Mattia Mele, André Bergmann, Giampaolo Campana, and Tony Pilz. Experimental investigation into the effect of supports and overhangs on accuracy and roughness in laser powder bed fusion. Optics and Laser Technology, 140(November 2020), 2021.

[84] Vincent Benoist, Lionel Arnaud, Maher Baili, and Pierre Faye. Topological optimization design for additive manufacturing , taking into account flexion and vibrations during machining post processing operations. In 14Th International Conference on High Speed Machining, pages 1–4, San Sebastian, Spain, 2018.

[85] GE. Stainless Steel 316L (powder). [Online]. Available: https://www.ge.com/additive/additive-manufacturing/machines/dmlm-machines/mlab-family, 2021.

[86] Renishaw. SS 316L-0407 powder for additive manufacturing, 2020.

[87] Outokumpu. Handbook of stainless steel. Technical report, 2013.

[88] Itziar Tolosa, Fermin Garciandia, Fidel Zubiri, Fidel Zapirain, and Aritz Esnaola. Study of mechanical properties of AISI 316 stainless steel processed by selective laser melting, following different manufacturing strategies. International Journal of Advanced Manufacturing Technology, 51(5-8):639-647, 2010.

[89] A. Mertens, S. Reginster, Q. Contrepois, T. Dormal, O. Lemaire, and J. Lecomte- Beckers. Microstructures and mechanical properties of stainless steel aisi 316l processed by selective laser melting. Materials Science Forum, 783-786:898-903, 2014.

[90] Arman Ahmadi, Reza Mirzaeifar, Narges Shayesteh Moghaddam, Ali Sadi Turabi, Haluk E. Karaca, and Mohammad Elahinia. Effect of manufacturing parameters on mechanical properties of 316L stainless steel parts fabricated by selective laser melting: A computational framework. Materials and Design, 112:328–338, 2016.

[91] H Alsalla, L Hao, and CW Smith. Effect of build orientation on the surface quality, microstructure and mechanical properties of selective laser melting 316L stainless steel. Rapid Prototyping Journal, 2016.

[92] R. Casati, J. Lemke, and M. Vedani. Microstructure and Fracture Behavior of 316L Austenitic Stainless Steel Produced by Selective Laser Melting. Journal of Materials Science and Technology, 32(8):738–744, 2016.

[93] Yuan Zhong, Leifeng Liu, Stefan Wikman, Daqing Cui, and Zhijian Shen. Intragranular cellular segregation network structure strengthening 316L stainless steel prepared by selective laser melting. Journal of Nuclear Materials, 470:170-178, 2016.

[94] Jyoti Suryawanshi, K. G. Prashanth, and U. Ramamurty. Mechanical behavior of selective laser melted 316L stainless steel. Materials Science and Engineering A, 696(April):113-121, 2017.

[95] Wei Chen, Guangfu Yin, Zai Feng, and Xiaoming Liao. Effect of Powder Feedstock on Microstructure and Mechanical Properties of the 316L Stainless Steel Fabricated by Selective Laser Melting. Metals, 8(9):729, 2018.

[96] Md Shamsujjoha, Sean R. Agnew, James M. Fitz-Gerald, William R. Moore, and Tabitha A. Newman. High Strength and Ductility of Additively Manufactured 316L Stainless Steel Explained. Metallurgical and Materials Transactions A: Physical Metallurgy and Materials Science, 49(7):3011-3027, 2018.

[97] Michael J. Heiden, Lisa A. Deibler, Jeff M. Rodelas, Josh R. Koepke, Dan J. Tung, David J. Saiz, and Bradley H. Jared. Evolution of 316L stainless steel feedstock due to laser powder bed fusion process. Additive Manufacturing, 25(November 2018):84â€“103, 2019.

[98] Philipp Stoll, Adriaan Spierings, and Konrad Wegener. Impact of a process interruption on tensile properties of SS 316L parts and hybrid parts produced with selective laser melting. International Journal of Advanced Manufacturing Technology, 103(1-4):367-376, 2019.

[99] Paul Wood, Tomasz Libura, Zbigniew L. Kowalewski, Gavin Williams, and Ahmad Serjouei. Influences of Horizontal and Vertical Build Orientations and Post-Fabrication Processes on the Fatigue Behavior of Stainless Steel 316L Produced by Selective Laser Melting. Materials, 12(4203):1-19, 2019.

[100] A. Röttger, J. Boes, W. Theisen, M. Thiele, C. Esen, A. Edelmann, and R. Hellmann. Microstructure and mechanical properties of 316L austenitic stainless steel processed by different SLM devices. International Journal of Advanced Manufacturing Technology, 108(3):769-783, 2020.

[101] ASTM International. A666-15, Standard Specification for Annealed or Cold-Worked Austenitic Stainless Steel Sheet, Strip, Plate, and Flat Bar, 1999.

[102] Simulia. Abaqus Analysis User's Manual 24.2.2 Damage initiation for ductile metals Products: Abaqus/Standard Abaqus/Explicit Abaqus/CAE, 2014.

[103] Simulia. Abaqus Analysis User's Manual 24.2.3 Damage evolution and element removal for ductile metals Products: Abaqus/Standard Abaqus/Explicit Abaqus/- CAE. ABAQUS Manual, pages 1-10, 2015.

[104] Simulia. Abaqus Analysis User's Manual. Static stress analysis. [Online]. Available: https://abaqus-docs.mit.edu/2017/English/SIMACAEANLRefMap/simaanl-c-static.htm.

[105] Simulia, Abaqus 6.13 Anal. User's Guid. Vol. II Analysis. Unstable Collapse and Postbuckling Analysis Riks. [Online]. Available: https://abaqus-docs.mit.edu/2017/English/SIMACAEANLRefMap/simaanl-c-postbuckling.htm. vol. II, pp. 1–7, 2013.

[106] Simulia, Abaqus Anal. User's Guid. Nonlinear solution methods in Abaqus / Standard. [Online]. Available: https://abaqus-docs.mit.edu/2017/English/SIMACAETHERefMap/simathe-c-nonlinearsol.htm. 2017

[107] Simulia. Abaqus Anal. User's Guid Modified Riks algorithm. [Online]. Available: https://abaqus-docs.mit.edu/2017/English/SIMACAETHERefMap/simathe-c-modifiedriks.htm. pp. 1–4. 2017.

Chapter IV

Table of contents

IV. Simulate the thermal history using a multiscale finite element method

4.1. Introduction . . . 118
4.2. State of the art . . . 119
4.2.1. Relation between thermal history and characteristics of parts . . . 119
4.2.2. Modelling methods . . . 119
4.3. Methodology . . . 121
4.3.1. General principles . . . 121
4.3.1.1. Parameter-driven approach . . . 121
4.3.1.2. Level definition . . . 122
4.3.2. Rules . . . 125
4.3.2.1. Definition of space and time domains . . . 125
4.3.2.2. Heat source modelling . . . 126
4.3.2.3. Boundary and initial conditions . . . 128
4.4. Study case . . . 128
4.4.1. Context, parameters, and levels . . . 128
4.4.2. Level 1 . . . 131
4.4.3. Level 2 . . . 133
4.4.4. Level 3 . . . 136
4.4.5. Level 4 . . . 138
4.4.6. Level 5 . . . 139
4.5. Discussions . . . 140
4.6. Conclusions and perspectives . . . 142
4.7. References . . . 143

Chapter IV

Simulate the thermal history using a multiscale finite element method

4.1. Introduction

The LPBF process is complex because most phenomena occur on different spatial and temporal scales [1]. It is commonly classified into three separate scales: microscale, mesoscale, and macroscale [2]-[4].

The microscale comprises phenomena occurring in the laser-matter vicinity, notably the melt pool generation, the role of the interfacial forces in its evolution and fluid convection, and the generation of plumes, plasma, and spatters. At this scale, it is possible to retrieve the formation of defects such as denudation and keyholes, as well as to capture the thermal cooling rates generating specific microstructures.

Mesoscale is a scale in which the entire layer or regions of this layer, such as the scanning pattern (i.e. a group of islands), is scanned. It can be used to observe the mesoscale factors influencing the local cooling time (such as the length of the scan vector and the width of the scanning pattern).

The last scale is the macroscale, or the part scale, which accounts for diverse factors such as the part geometry (overhangs, feature thickness), conduction through the supports and the surrounding powder, and the influence of the build plate acting as a heat sink. At this scale, it is possible to observe defects, such as overall distortion, cracks, and support detachment. Residual stresses are generally measured at this scale.

Even though different phenomena occur at different scales, nearly all of them share a common origin, the laser-matter interaction, whose direct effects are thermal in nature [5]-[7]. Hence, nearly all phenomena and characteristics (melt pool shape, denudation, keyholes, spatters, microstructural defects, distortion, cracks, and residual stresses) are linked to the thermal history of the process.

The current process parameter development stages (mostly trial errors) are costly because one needs to manufacture samples, characterise the main indicators such as density and mechanical characteristics, and validate the suitability of these parameters for several types of geometries and configurations. The medical, aeronautics, and oil domains would also be influenced by the final chemical composition.

Hence, there are several indicators for validation, which could also depend on the end-user application. The final surface quality, feature thickness, and dimensional requirements are important for the jewellery and similar

domains.

Since all validation processes are time-consuming and costly, the ability to simulate most of the phenomena and anticipate some results in a shorter time period would result in significant savings.

Given that most phenomena have a thermal origin, the thermal history and its influencing factors should be thoroughly considered.

In this study, a novel simulation method is presented to account for almost every influencing factor of the thermal history. First, the state-of-the-art method is presented in Section 4.2, then the methodology framework is introduced in Section 4.3. The method is applied to industrial application in Section 4.4 and the results are discussed in Section 4.5. Finally, the conclusions are provided in Section 4.6.

4.2. State of the art

4.2.1. Relation between thermal history and characteristics of parts

The correlation between thermal history and the characteristics of parts has been extensively discussed in the last decade for both thermally induced distortions and porosities.

Residual stress formation and distortions are strongly linked to the thermal history because matter tends to expand and constrict consecutively at a local scale near the melt pool [5][8]-[10] with the laser beam path.

Several types of porosities can be encountered, such as lack of fusion, keyholes, denudation, and entrapped gas [11]. This excludes entrapped gas, which may already be present within the powder particles before the AM process.

These mechanisms are directly linked to the thermal history of the scanned region [9][11]-[15]. Mitchell *et al.* [14] confirmed the position of the porosities in the part with in-situ pyrometry measurements, revealing a clear link between porosity formation and thermal history.

Hence, the local distributed energy should not be too high to prevent the formation of keyholes. In addition, if the temperature is too high, the melt pool may be unstable, and denudation may occur.

An excessively low melt pool temperature may induce a lack of fusion porosity. Hence, a temperature window should be maintained to manufacture dense parts and to prevent the formation of pores.

4.2.2. Modelling methods

All the modelling methods resolve the thermal problem [16]:

$$\frac{\partial^2 T}{\partial x^2}+\frac{\partial^2 T}{\partial y^2}+\frac{\partial^2 T}{\partial z^2}+\frac{1}{k}\,g(x,y,z,t)=\frac{1}{\alpha}\,\frac{\partial T}{\partial t} \tag{4.14}$$

where $T(x,y,z,t)$ is the temperature, t is the time, $g(x,y,z,t)$ is the rate of energy generation per unit volume (W/m^3), $\alpha = k/\rho c$ is the thermal diffusivity (m^2/s), k is the conductivity of the material (W/(m.K)), c is the specific heat, and ρ is the density of the material. This problem formulation is accompanied by boundary and initial conditions, as detailed in a previous report [16].

Green's function can be used to analytically resolve the partial differential equation (Equation (4.14)). Considering a unidimensional infinite body, and to further simplify, only conduction is considered as a heat transfer mechanism, and Green's function is in the form [16]

$$G(x,t\,|\,x',\tau) = K(x-x',t-\tau);$$
$$K(x-x',t-\tau) = [4\pi\alpha(t-\tau)]^{-1/2}\exp\left(-\frac{(x-x')^2}{4\alpha(t-\tau)}\right); t \geq \tau \quad \textbf{(4.15)}$$

where τ is the instant at which the heating phase occurs, and x' is the location where it occurs. Using this formulation and considering an initial temperature of $T(x,t_0) = 0\,°C$, for simplicity, and the generation term $g(x,t) = q_{x_0}\,\delta(x-x_0)$, where δ is the Dirac function, the temperature field can be expressed as [16] (eq. 1.87)

$$T(x,t) = \frac{q_{x_0}\sqrt{\alpha t}}{k}\,ierfc\left[\frac{|\,x-x_0\,|}{\sqrt{4\alpha t}}\right] \quad \textbf{(4.16)}$$

where ierfc is the integral of the complementary error function [16]:

$$ierfc(z) = \int_z^\infty erfc(u)\,du$$
$$ierfc(z) = \frac{1}{\sqrt{\pi}}\exp(-z^2) - z\,erfc(z) \quad \textbf{(4.17)}$$

Different approaches can be used to numerically simulate the global part-scale thermal history of LPBF. Regarding non-finite element methods (FEM), several studies use semi-analytical approaches [17], whereas others use superposition approaches [18] or graph theory-based approaches [19][20].

Finite element (FE)-based approaches can also be used. However, to capture the complex physics and small scales at which several phenomena occur, it is necessary to use a fine mesh size and time increments.

These requirements hinder the simulation of the entire process without strongly simplifying the assumptions, such as using macrolayers (bundling of several layers) [21]-[25] or powder [26]-[31] and heat source modelling simplifications [30][32]-[38].

Several techniques have also been used, such as adaptive meshing [30][37], and recently, graphics processing units (GPUs) and matrix-free approaches have also been used [30].

Another type of FE-based approach is a multiscale simulation. The phenomena are separated according to the scale to which they belong, and each scale simulation, linked to one another, is launched sequentially.

This enables various phenomena to be considered while adapting the simulation resolution to the scale at which these phenomena occur.

This method is the main framework of the thermomechanical simulation methods of inherent strain (IS) [3] [39] and modified IS (MIS) [34][40][41]. However, the IS and MIS methods do not complete the thermal resolution at the part-scale, leading to some assumptions regarding the thermal boundaries and initial conditions. Geometry has a major impact on thermal fields [42][43].

Li *et al.* [44][45] developed a multiscale method to resolve this thermomechanical problem. The thermal behaviour was simulated at all three scales (microscale, mesoscale, and macroscale).

Most of these methods compute the thermal history at the macroscale (part-scale) and directly use it in a thermomechanical resolution. Hence, the local thermal history is not considered.

Most studies that model the heating process at the microscale (melt pool scale) do not use the global thermal history as an initial or boundary condition. These conditions can be highly heterogeneous depending on the location of the layer and the topology of the part.

All the phenomena that affect the thermal history should be considered. Phenomena that generate dwell

times typically have a significant impact on the thermal fields [31][46][47], such as the recoating process or the time necessary to scan other parts of the build plate.

In this study, a multiscale method driven by all phenomena affecting the thermal history is presented. The number of simulation scales depends on the user objective; this method can easily be used for other AM processes, implying similar thermomechanical phenomena.

4.3. Methodology

4.3.1. General principles

4.3.1.1. Parameter-driven approach

The objective of this approach is to consider the impact of all parameters on the thermal history of LPBF parts. Owing to the complex physics and fine resolution required to consider all these parameters together, the overall process was divided into several levels. Each level is the site of a specific simulation, which communicates with other levels.

All phenomena can be defined using temporal and spatial domains. The groups of phenomena involve the mutual overlap of the spatial and temporal domains.

Table 4.1 lists the principal parameters that affect the thermal history and the corresponding temporal and spatial domains. These groups are regarded as the levels, which are defined using general rules, as described later.

Figure 4.1 depicts the coupling between the temporal and spatial domains for the three main levels. The levels shown in Figure 4.1 will help the reader with the following application (in which five levels will be used (Section 4.4)).

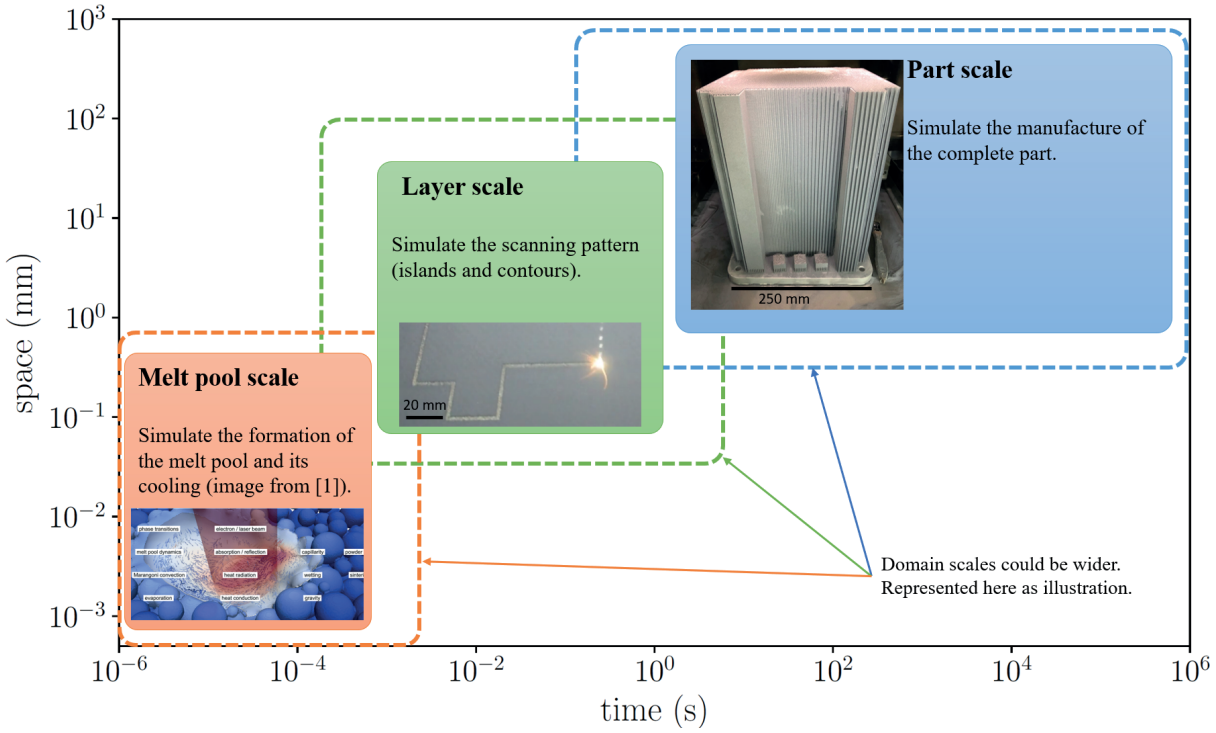

Figure 4.1: Illustration of the domains of three different scales. Dashed lines represent the size of the domains that a user may define for his application. All sizes are provided as illustration.

Table 4.1: Parameters driven time and space domains of the simulation levels (D-S: discretization - scope).

Levels	Parameters	Time domain (D-S)	Space domain (D-S)
Level 1 - Full build		3 min - 100 h	$(15mm)^3$ - $(500mm)^3$
	Layer thickness		
	Layering delays		
	Interlayer rotational angle		
	Interlayer shifting		
Level 2 - Inside one layer		0.1 s - 5 min	$(1mm)^2$ - $(250mm)^2$
	Pattern type (islands, stripes, etc.)		
	Pattern dimensions		
	Instance sequence (supports, parts)		
	Pattern sequence		
Level 3 - Inside the scanning pattern		50 ms - 5 s	$(0.5mm)^2$ - $(5mm)^2$
	Filling direction		
	Filling angle		
	Unique way or 2 ways		
	Hatch distance		
Level 4 - Following the scanning vector		0.5 ms - 50 ms	0.1 mm - 5 mm
	Direction		
	Acceleration/deceleration delays		
	Scanning speed		
Level 5 - Melt pool		0.05 ms - 1 ms	0.05 mm - 0.120 mm
	Energy density profile		
	Beam diameter		

The temporal and spatial ranges of the phenomena enable the groups of phenomena and their levels to be defined. Each level is simulated. The first level is always the widest, and the subsequent levels are finer than previous levels.

The first level had the widest scale. It could also be the part scale or build plate scale, for instance, considering several parts on the build plate. This level should be able to comprise every macro phenomenon, from the beginning to the end of the process.

The last level is the finest, and its precise definition depends on the user's needs. The computed thermal information is transferred from the first to the last level and progressively refined at each modelling level. The information can also be sent in another way for verification processes depending on the user's needs.

4.3.1.2. Level definition

A level is defined by both a spatial scale and the temporal scale linked with the selected phenomena. The level contains the modelling information, such as the heat transfer mechanisms, the heat source model, the thermal boundary conditions (BCs), and the thermal initial conditions (ICs).

Certain rules to define the heat source model are subsequently discussed. Regarding the IC and BC, the information contained within the level originate from the previous (wider) level.

The results computed at a specific level must be sent to the next level to be used as ICs and BCs at the precise instant and location considered at this finer level.

Since the next level (Level n+1) has spatial and temporal resolutions that are smaller than the previous level (Level n), the results computed at Level n are considered as averaged thermal information.

For instance, considering multiple instantaneous heat sources Q_{in} applied at the same region at different instants, and comparing them with an averaged heat source Q_{av}, illustrates a model where each area of the layer is sequentially scanned, and a model where the entire layer is heated using an average heat source.

The total energy injected is the same for each model, as illustrated in Figure 4.2. For simplicity, this analysis will be analytically conducted using one-dimensional (1D) semi-infinite bodies heated at the same point x_0.

The average heating illustrates the heating of a macrolayer, and the discrete heatings represent the island heating on the surface of physical layers. The volume of the subsequent physical layers is the same as the volume of the macrolayer.

Using the 1D semi-infinite body assumption must respect the criterion $\alpha t/L^2 < 0.05$, with α the thermal diffusivity (Equation (4.14)), t is the duration considered and L is the length of the body. In the analytical study, the only thermal exchanges considered are from the conduction within the body (convection heat transfer and radiation are not considered).

For the whole section, the thermal loadings are applied at different instant t, but at only one location x_0. Hence, the temperature difference at the order of a layer thickness is assumed not significant. It also implies that the cooling resulting from the powder deposition (the layering process) does not impact significantly the temperature fields.

The average heating was considered continuous, and the discrete island heatings were considered discontinuous. Because the only heat transfer mechanism considered here is conduction, the total injected energy remains within the system and is denoted E_{tot} in Figure 4.2. The same energy was applied in both cases during the overall heat period ($t_{heat} = t_1 - t_0$), and an observation period Δt corresponding to the layering process (here, $t_{cool} = 15\ s$) is expected.

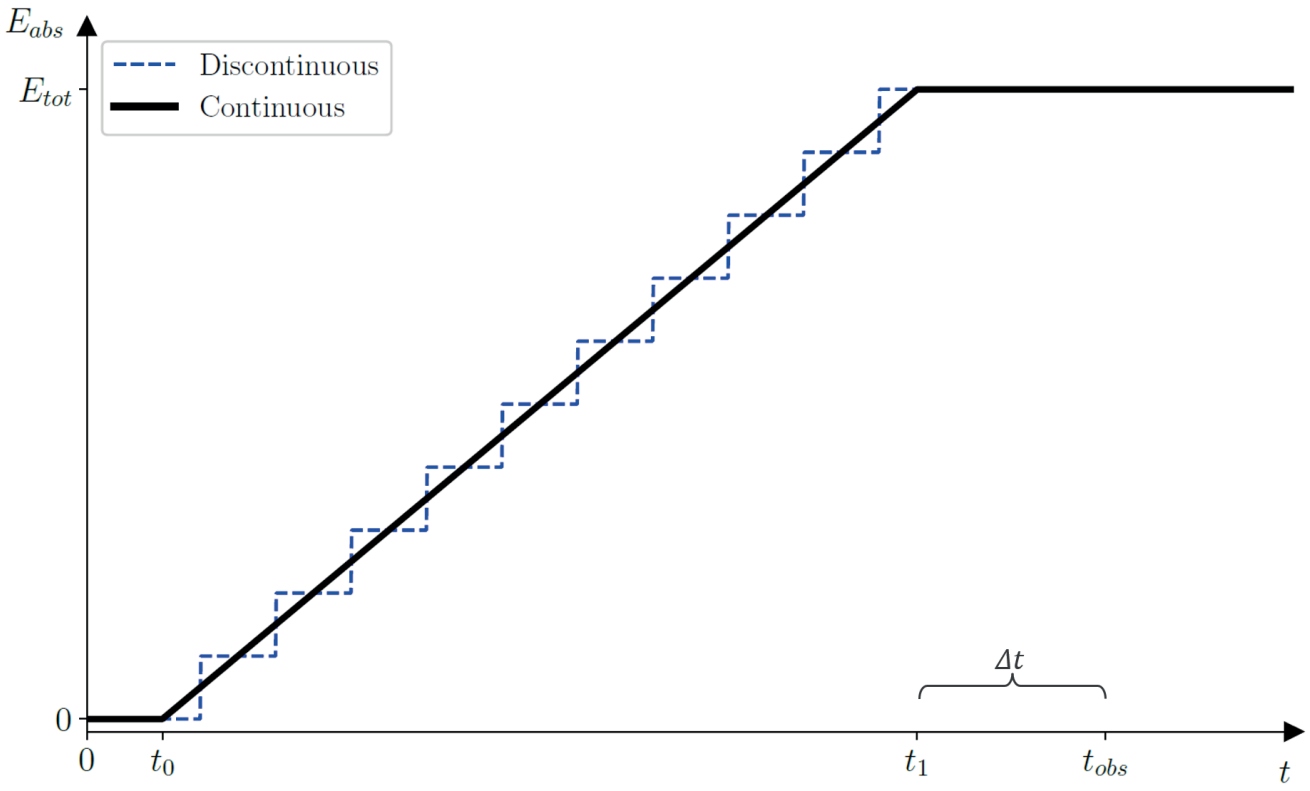

Figure 4.2: Absorbed energy Eabs for different types of heat generation: continuous (averaged) and discontinuous (instantaneous). The total absorbed energy E_{tot} is equivalent for both models.

From Equation (4.16), considering a sequence of n_h heatings of the same duration theat, spaced by n_{cool} cooling (mirror term), each of duration t_{cool}, the discrete heat source formulation for a 1D semi-infinite body is

$$T^{n_h}_{discrete}(x,t) = \frac{2E_s}{t_{heat}\sqrt{k\rho c}}\left(\sum_{i=1}^{n_h}\sqrt{t_{heat}}\ ierfc\left[\frac{|x-x_0|}{2\sqrt{\alpha t_{heat}}}\right] - \sum_{j=1}^{n_{cool}}\sqrt{t_{cool}}\ ierfc\left[\frac{|x-x_0|}{2\sqrt{\alpha t_{cool}}}\right]\right);$$

$$t_{heat} = t-(i-1)t_{heat}-(i-1)t_{cool}; \qquad (4.18)$$
$$t_{cool} = t-jt_{heat}-(j-1)t_{cool};$$
$$E_s = q_{x_0}\,t_{heat}$$

Its equivalent averaged heating is written as

$$T^{n_h}_{averaged}(x,t) = n_h q_{x_0}\sqrt{\frac{t-t_0}{k\rho c}}\ ierfc\left[\frac{|x-x_0|}{2\sqrt{\alpha(t-t_0)}}\right] - q_{x_0}\sqrt{\frac{t-t_1}{k\rho c}}\ ierfc\left[\frac{|x-x_0|}{2\sqrt{\alpha(t-t_1)}}\right];\quad t_1 > t_0 \qquad (4.19)$$

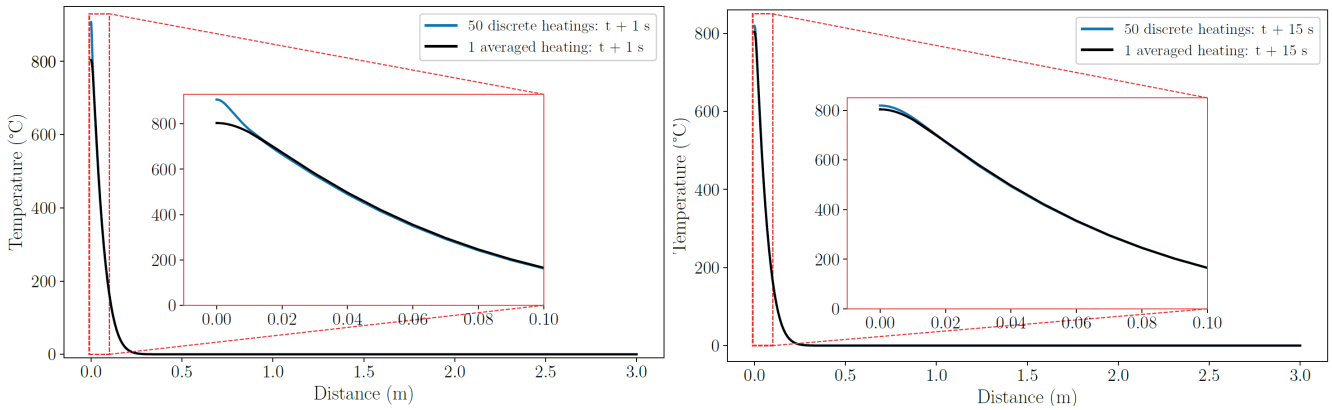

(a) $\Delta t = 1\ s$ (b) $\Delta t = 15\ s$

Figure 4.3: Temperature field in the 1D semi-infinite body with two types of loading: averaged and discrete.

Figure 4.3 depicts the two temperature fields, depending on the heat source type (averaged or discrete), with two different observation periods. The observation period was the period after the last heat source was applied.

Figure 4.3 shows that there is very little difference between the temperature fields of several discrete heat sources ($T^{n_h}_{discrete}$, Equation (4.18), where n_h is the number of discrete heating occurrences) and an equivalent averaged source ($T^{n_h}_{averaged}$, in Equation (4.19)).

As shown in Figure 4.3(a) and Figure 4.3(b), the observation period Δt has a significant impact on the temperature difference. As the period value increases, the difference decreases.

Hence, at a wider scale (Level n), the temperature fields are considered homogenised and averaged, compared to the temperature fields at finer levels (Level n+1). As they are far from the heat source site, these homogenised temperatures were used as the boundary conditions.

Hence, a level is well defined if

- It is clearly limited by spatial and temporal domains;
- It is associated with manufacturing parameters;
- ICs and BCs are clearly defined;
- Thermal results can be provided to the next level.

4.3.2. Rules

4.3.2.1. Definition of space and time domains

The spatial domain must contain the instances (parts and build plate) of heat transfer. Areas without significant temperature variations may not be considered within the simulation to reduce the computational effort.

These areas can be identified at the previously simulated level and approximated by thermal BCs at the level of interest.

The model should also contain a reasonable number of elements regarding the available computational effort. For instance, regarding the available computational power of the authors, the number of elements above one million appears too high, leading to excessively long computations.

To prevent the simultaneous use of too many elements, one should consider splitting the studied level or using coarser elements within the model.

The boundaries of the temporal domain were directly linked to the durations of the studied parameters. The minimum boundary should be set to limit computation errors while simulating the thermal impact of the studied parameters.

The minimum boundaries may partially overlap the domain of the next level, but should not entirely cover it. As illustrated in Figure 4.4, the next level should cover a temporal domain, which is not fully covered by the studied level.

A convergence study should always be conducted to precisely define the boundaries of the temporal domain and time increment values. The rule of thumb is to avoid having an excessively wide temporal domain: the ratio between the maximum and minimum boundaries should be ≤ 100.

To reduce the computational effort regarding the temporal domain, intermediate levels should be inserted, or supplementary approximations of the heat flux can be used. Notably, the BCs placed on the boundaries of the spatial domain (i.e. to replace areas with small temperature variations) should be valid throughout the entire temporal domain.

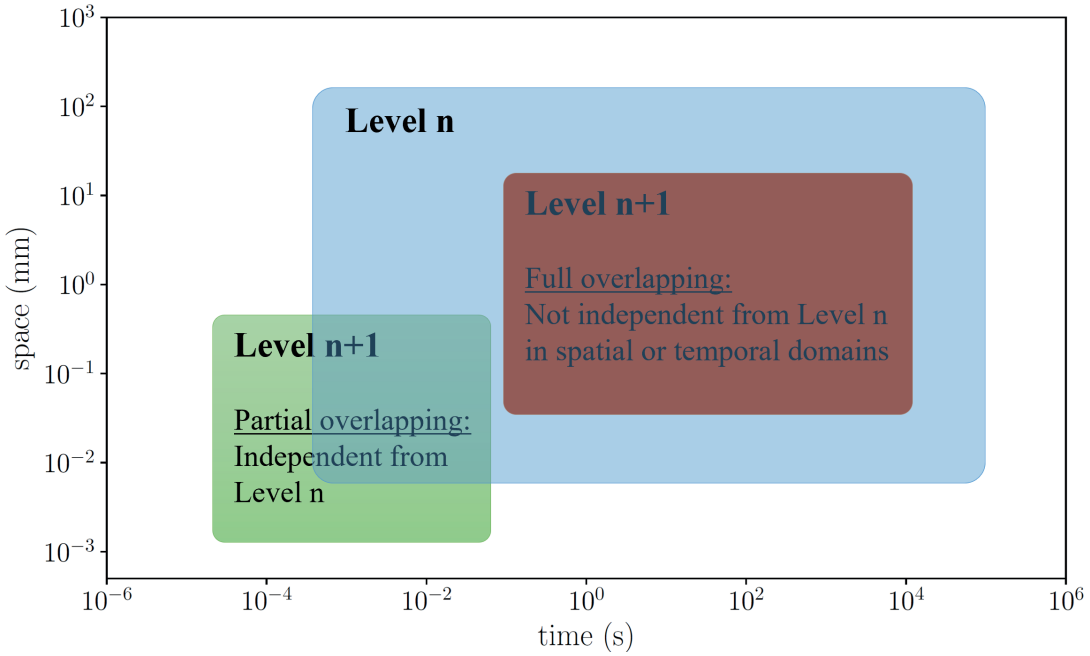

Figure 4.4: Overlapping temporal domains of Level n and Level n+1.

The temporal and spatial boundaries as well as the time increments should deliver results within reasonable durations. For practical use, the duration of all level simulations, one after the other, should not last more than 24 h overall.

4.3.2.2. Heat source modelling

The objective of this section is to provide rules to avoid inserting non-physical transitions within the levels and to yield enormous computational efforts. The first choice is to determine the type of heat source (HS) provided: surface or volumetric.

A surface HS is preferred when no matter is introduced into the system at the time of loading and when some simplifying assumptions are necessary for the heat source. Using a surface HS allows the user to simplify the numerous melt pools into an averaged heat source that delivers the same energy within the system.

Gaussian-shaped surface heat sources have been used previously. For example, Li *et al.* and Wolff *et al.* [2][48] used a surface Gaussian-distributed moving HS.

When matter is introduced into the system (such as other metal AM processes like directed energy deposition (DED), where powder is molten and deposited on the part), a volumetric HS may be more suitable than a surface HS because the energy is brought along with the volume of matter in contact with the previously existing body.

In addition, defining an average volumetric HS avoids heating a surface that does not exist as yet. For the same reasons, it may be better to consider a volumetric HS while handling macrolayers. Then, thermal results should be considered only beneath the macrolayer for the duration of the loading.

Overall, when the objective is to finely model the heat source (at finer levels, for instance), some volumetric distributions may be more precise than surface distributions, because of the actual penetration of the laser beam between the powder particles. Various distributions of the volumetric heat sources are listed in previous reports [41][49]-[51].

Considering volumetric or surface HS models, while injecting thermal energy, one should also consider the cooling delay involved in the process (owing to the layering time, scanning of all the other parts, and laser vector jumps).

There should be no fine localised modelling at the part scale (when macrolayers are considered) because the volumetric heat sources in the macrolayer volumes are used. One should consider that there is no benefit to injecting more precise (and unsteady) phenomena if they cannot be considered with high time increments or a large mesh size.

The objective is to define the right heat source approximations with acceptable accuracy and computational effort.

As discussed in the previous sections, FE computational efforts must be reasonable, and the quality of the approximation can be estimated using specific numerical trials and simple analytical results.

For instance, regarding HS modelling, the difference between one averaged source and several discrete sources can be approximated analytically using Green's functions (Equation (4.15)).

In Equation (4.16), the generation term was an impulse in space only, meaning the heat source was applied to a single point x_0, but was continuous for a certain period Δt. In its impulse form, $g(x,t) = 2\,E_s\,\delta(x-x_0)\,\delta(t-t_0)$, where δ is the Dirac function, and E_s is the surface energy (in J/m^2), both space and time are an impulse.

The temperature field can be retrieved from the general formulation in Equation (4.20). The first part is linked with the initial temperature T_0, which is assumed to be 0 for simplification. The second part is K from the Equation (4.15), multiplied by the heat generation term.

$$T(x,t) = \int_{-\infty}^{\infty} [4\pi\alpha t]^{-1/2} \exp\left[-\frac{(x-x')^2}{4\alpha t}\right] T_0(x')\,dx' + \frac{\alpha}{k} \int_{\tau=0}^{t} \int_{x'=-\infty}^{\infty} [4\pi\alpha(t-\tau)]^{-1/2} * \exp\left[-\frac{(x-x')^2}{4\alpha(t-\tau)}\right] g(x',\tau)\,dx'd\tau \quad \textbf{(4.20)}$$

The temperature fields of a 1D semi-infinite body corresponding to this type of loading are formulated as

$$T(x,t) = \frac{E_s}{\sqrt{k\rho c}\sqrt{\pi t}} \exp\left[-\frac{(x-x')^2}{4\alpha t}\right] ;\ t \geq 0 \quad \textbf{(4.21)}$$

$T_{imp=2}^{n_h=2}$ in Equation (4.22) is the thermal field after two impulsions at the same, with an energy n_h of $n_h = 2$ heatings. Both impulsions occurred at $x_0 = 0$ and at different instants of $t_0 = 0$ and $t_2 = 2\delta$.

$$T_{imp=2}^{n_h=2}(x,t_{obs}) = \frac{E_s}{\sqrt{\pi k\rho c}} \frac{1}{\sqrt{t_{obs}}} \exp\left(-\frac{x^2}{4\alpha t_{obs}}\right) + \frac{E_s}{\sqrt{\pi k\rho c}} \frac{1}{\sqrt{t_{obs}-2\delta}} \exp\left(-\frac{x^2}{4\alpha(t_{obs}-2\delta)}\right) \quad \textbf{(4.22)}$$

$T_{imp=1}^{n_h=2}$ in Equation (4.23) delivers the same energy as $T_{imp=2}^{n_h=2}$ from Equation (4.22), with only one impulse, at $x_0 = 0$ and at the instant $t_1 = \delta$.

$$T_{imp=1}^{n_h=2}(x,t_{obs}) = \frac{2E_s}{\sqrt{\pi k\rho c}} \frac{1}{\sqrt{t_{obs}-\delta}} \exp\left(-\frac{x^2}{4\alpha(t_{obs}-\delta)}\right) \quad \textbf{(4.23)}$$

The limited development ε at order 2 in $\delta \to 0$ is

$$\varepsilon = T_{imp=2}^{n_h=2}(x,t_{obs}) - T_{imp=1}^{n_h=2}(x,t_{obs}) \quad \textbf{(4.24)}$$

yielding:

$$\varepsilon = E_s \exp\left(-\frac{x^2}{4\alpha t}\right) \frac{(12\alpha^2t^2 - 12\alpha t x^2 + x^4)\delta^2}{32\sqrt{\pi}\ t^2\ (t\alpha)^{5/2}} + o(\delta^3) \quad \textbf{(4.25)}$$

This formulation is divided between an exponential term in $-x^2/t$ and a polynomial term in $x^4\ \delta^2\ /\ t^{2,5}$, using only the highest orders. With $x \to 0$, the exponential term tends to 1, and $\delta^2/t^{2,5}$ drives the polynomial term.

From Equation (4.25), at $x_0 = 0$, the relative error formulation is $0.75\,\delta^2/t^2$.

To maintain a 10% relative error, it is necessary to consider the temperature field at $\simeq$ 2.73 times the layer island-scanning duration. This value of 2.73 is not constant with the number of heatings: it converges to 1.03.

In other words, the longer the surface is heated, the more precise the approximations are after the heating phase.

Figure 4.3 shows the temperature fields at two different instants. As the number of heatings increases, the period Δt required to reduce the error between the discrete and averaged sources decreases.

4.3.2.3. Boundary and initial conditions

The boundary conditions can be used to replace regions with small temperature variations, thereby limiting the computational efforts, replacing the impact of the powder material, or representing specific heat transfer mechanisms (such as convection).

Temperature boundary conditions can be used in this method because they are used to replace regions with small temperature variations.

Convective flux or constant flux boundary conditions can also be used, but the final energy within the system must be coherent. In the following application, the boundary conditions were set based on the results computed from the previous level.

The initial conditions were also computed at previous levels and used to set a correct temperature field around the area that will be loaded at the studied level.

The initial conditions used in this method were an averaged value of the temperature computed at the mesh nodes because the meshes of the next levels were finer than those used in the previous levels.

4.4. Study case

4.4.1. Context, parameters, and levels

This study focuses on peak temperatures to identify regions that may contain thermally induced porosities. The part is a Ti-6Al-4V hydraulic joint from the aeronautic industry, which is shown in Figure 4.5 with its voxel meshed version.

The part is identical to the one used in the previous chapter, except for its supports, generated in ABAQUS with volumetric (3D brick) elements. As a recall, in the previous chapter, supports generated in ABAQUS were beam supports with 1D-elements.

The FEM model was constructed using the ABAQUS CAE 2018 FE package. All parameter values are listed in Table 4.3.

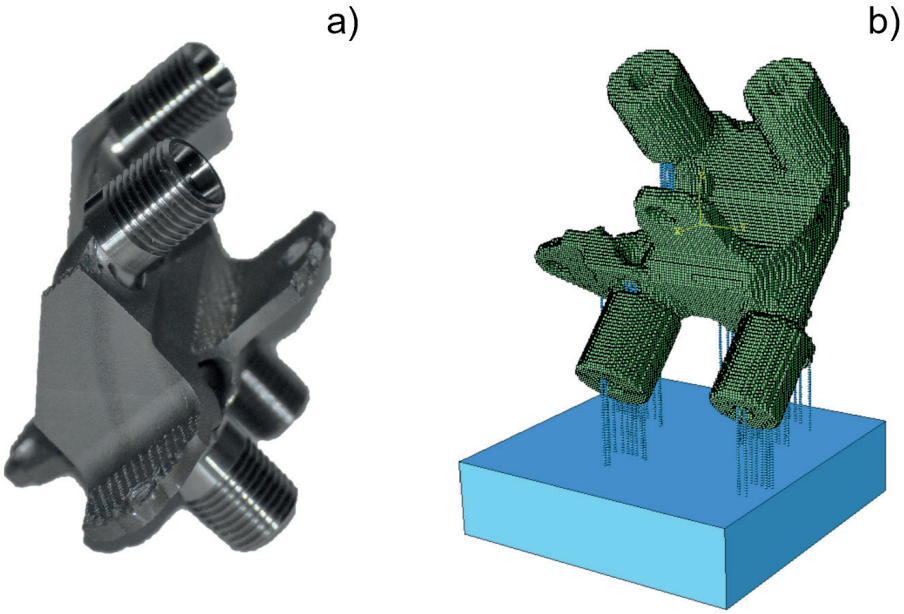

Figure 4.5: Hydraulic joint (a) and ABAQUS model with supports and build plate (b).

An overall simulation was required to detect the potential regions where porosity could form. This will be performed at five distinct levels, as described in Table 4.3.

It will also be necessary to zoom into a near-melt-pool level. There is no need to model the precise porosity formation because only the surrounding region temperature is of interest.

Hence, to estimate the temperature in the vicinity of the melt pool, there is no need to model the phase change (liquid-solid, although it would lead to more precise results).

For simplicity, only one part is simulated in this study. The approach for several parts is the same. For the material properties, temperature-dependent Ti-6Al-4V material parameters from [8] were fitted, as shown in Figure 4.6.

The model and process parameter values from the DMP ProX320 system, listed in Table 4.2, were affected to specific levels based on their temporal and spatial domains, as illustrated in Table 4.3.

Depending on the domain, some parameters may be directly simulated (i.e. in a specific step), averaged (i.e. several occurrences are grouped together and have an overall influence on step time or load magnitude) or could not be considered.

The absorption coefficient was estimated based on separate calibration simulations to fit the melt pool boundaries from a previous report [52].

Table 4.2: Parameter values set to the models.

Model parameters	Value
Mesh element size	0.5 mm
Scan speed	1200 mm/s
Acceleration delay	0.1 ms
Deceleration delay	0.075 ms
Laser power	195 W
Absorption coefficient	0.18
Hatch distance	82 µm
Layer thickness	60 µm
Layering delay	10 s
Macrolayer thickness	0.5 mm
Powder-transfer convection	4 W/(m^2.K)
Gas-flow convection	200 W/(m^2.K)
Build-plate temperature	170 °C
Boiling point [13]	3287 °C
Latent heat of evaporation [53]	9.83 10^6 J/kg

Table 4.3: Parameter consideration and corresponding levels used for the study case of the hydraulic joint. (□ averaged impact; ● simulated; - not considered at this level)

Parameters	Level 1	Level 2	Level 3	Level 4	Level 5
Power	□	□	□	□	□
Melt pool length	□	□	□	□	●
Melt pool width (hatch)	□	□	□	□	●
Speed	□	□	□	●	●
Inter-vector jump delay	□	□	□	●	-
Vector direction	□	□	□	●	-
Vector length	□	□	●	●	-
Vector sequence	□	□	●		-
Additional delays	□	●	●	-	-
Island size	□	●	-	-	-
Island sequence	□	●	-	-	-
Recoating delay	□	●	-	-	-
Supports/parts sequence	□	●	-	-	-
Parts sequence	□	●	-	-	-
Parts & supports heights	●	-	-	-	-
Parts shape & orientations	●	-	-	-	-

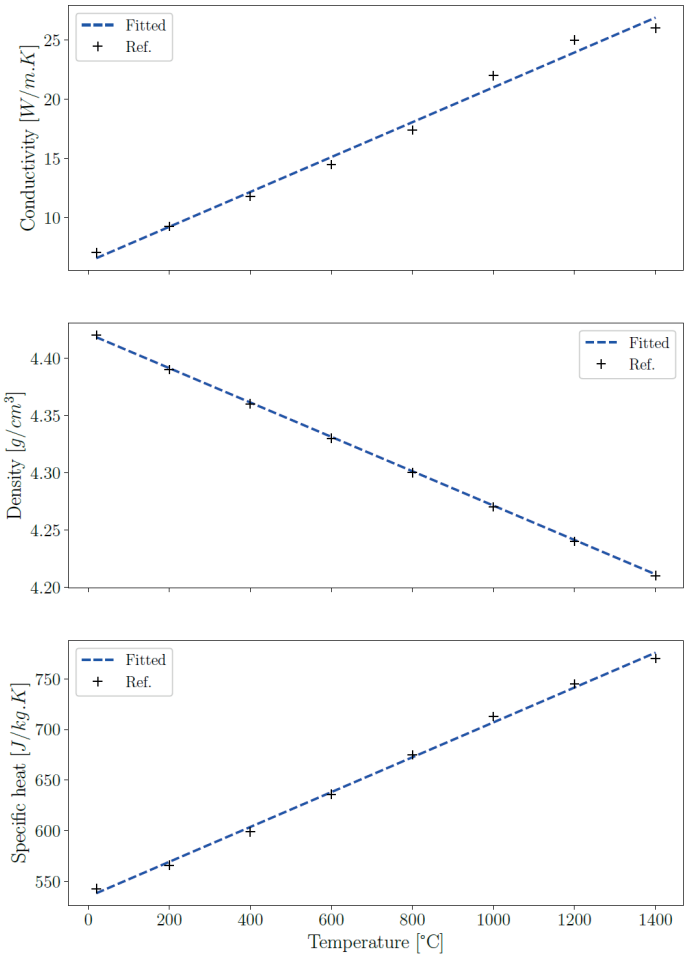

Figure 4.6: Fitted material properties from Parry *et al.* [8] used within the models.

4.4.2. Level 1

The first simulation level included the geometry of the entire part, its supports, and a small build plate. The part is meshed with voxel elements of the size of the macrolayer (0.5 mm in this application). The supports used were cone supports with a diameter of 0.5 mm.

The teeth were considered using weaken material properties to model the effect of the geometric striction from the actual support tooth area. Indeed, different material properties on elements of supports connected to the part, compared to the other elements of supports. All elements were assigned to cylinder shape geometries, as shown in Figure 4.5.

Since the tooth support geometry is a truncated cone, and the modelled support structure has a cylindric shape, the density, and the conductivity should be affected. Therefore, it was necessary to compute the conic shape's density and conductivity ratios.

Considering a truncated cone shape of height 0,5 mm, an upper diameter $D_2 = 2\,R_2 = 0.2\,mm$ and a lower diameter $D_1 = 2\,R_1 = 0.5\,mm$.

The truncated cone volume is equal to $V_{cone} = \pi/3 * H(R_1^2 + R_2^2 + R_1R_2)$ and the cylinder volume is $V_{cylinder} = \pi\,R_1^2 H$.

The volume ratio leads to the density ratio between the density of the material and the cylinder density

$$\frac{V_{cone}}{V_{cylinder}} = \frac{\pi H}{3\pi H} * \frac{R_1^2 + R_2^2 + R_1R_2}{R_1^2} = 0.52$$
$$\rho_{eq} = \frac{V_{cone}}{V_{cylinder}}\,\rho_{material} \tag{4.26}$$

From Fourier's law, considering that the temperature gradient is only dependent on the vertical position z (heat is expected to diffuse from the part to the supports mainly in a vertical fashion), and the flux constant within the tooth:

$$Q(z) = \int_S \lambda \frac{\partial T}{\partial z} dS = \lambda\, S(z)\, \frac{\partial T}{\partial z} \tag{4.27}$$

The equivalent conductivity could be estimated as the sum of the inverse of each small element conductivity as:

$$\int_{z_1}^{z_2} \frac{Q(z)}{S(z)} dz = \lambda\,(T_2 - T_1) \Rightarrow Q = K_{eq}\Delta T;$$
$$\frac{1}{K_{cone}} = \frac{1}{\lambda_{material}} \int_0^H \frac{1}{S(z)} dz = \frac{1}{\lambda_{material}} \frac{1}{\pi} \int_0^H \frac{1}{\left[\left(\frac{R_2 - R_1}{H}\right) z + R_1\right]^2} dz = \frac{1}{\lambda_{material}} \frac{H}{\pi R_1 R_2} \tag{4.28}$$
$$\frac{1}{K_{eq}} = \frac{1}{K_{cylindre}} = \frac{1}{\lambda_{eq}} \int_0^H \frac{1}{S(z)} dz = \frac{1}{\lambda_{eq}} \frac{H}{\pi R_1^2}$$

$$Q_{eq} = Q_{cone} \Longleftrightarrow \frac{\pi R_1^2}{H} \lambda_{eq} \Delta T = \frac{\pi R_1 R_2}{H} \lambda_{material} \Delta T \qquad (4.29)$$

$$\lambda_{eq} = \frac{R_2}{R_1} \lambda_{material}$$

The powder has a very low conductivity and a lower density than the solid material. The surrounding powder was thus modelled using convective heat transfer through the exterior faces of the part.

To model the preheating of the build plate and its regulation, a temperature boundary condition of 170 °C was set at its bottom surface.

Except for the first macrolayer elements and the build plate, all the above-mentioned elements were deactivated in the first step. There was no thermal transfer with deactivated elements.

The first macrolayer was then heated using a volumetric heat source during a specific heating step. The next macrolayer was then activated in another step with specific material properties (using a USDFLD subroutine) to obtain the temperature of the underlying elements.

At the scale of a 60 µm thick layer, the energy absorbed by the recoated powder is of the order of 1 mJ/mm², which is negligible compared to the laser power or the energy transferred by convection. Simple small models confirmed that the powder particles acquire the underlying solid temperature quasi-instantly in the Level 1 temporal domain.

Based on the hypothesis that powder is immediately heated by the solid material below when the powder is spread across the build plate, an artificial cooling that does not occur in the process is prevented. Hence, the subsequent steps are the heating and activating steps, which are similar to the previous ones.

The magnitude of the loads was computed based on the fraction absorbed by the material. The step time was computed from the actual scanning time, layering time, and delays (Table 4.2).

An additional USDFLD subroutine was used to extract the maximum temperature of the heated macrolayer. A map of the maximum temperatures is shown in Figure 4.7.

The regions experiencing higher temperatures are in the lower region of the part. This is mainly because of an insufficient amount of support connected to the part.

Owing to the convection coefficients, the temperature tended to decrease with the height of the part, even below the build plate temperature (170 °C). This shows that the impact of build plate preheating is limited to the first macrolayers.

Here, the region with the highest temperature was directly connected to the support cones. These regions are usually machined or polished after detachment of the supports.

Hence, a nearby macrolayer was used as the study site for the Level 2. In this case, macrolayer 33 was selected, to illustrate this method.

The temperature fields after heating this macrolayer are shown in Figure 4.8. The temperatures were homogeneous owing to the slow average loading.

Level 2 facilitates consideration of both the scanning strategy and the part scanning sequence.

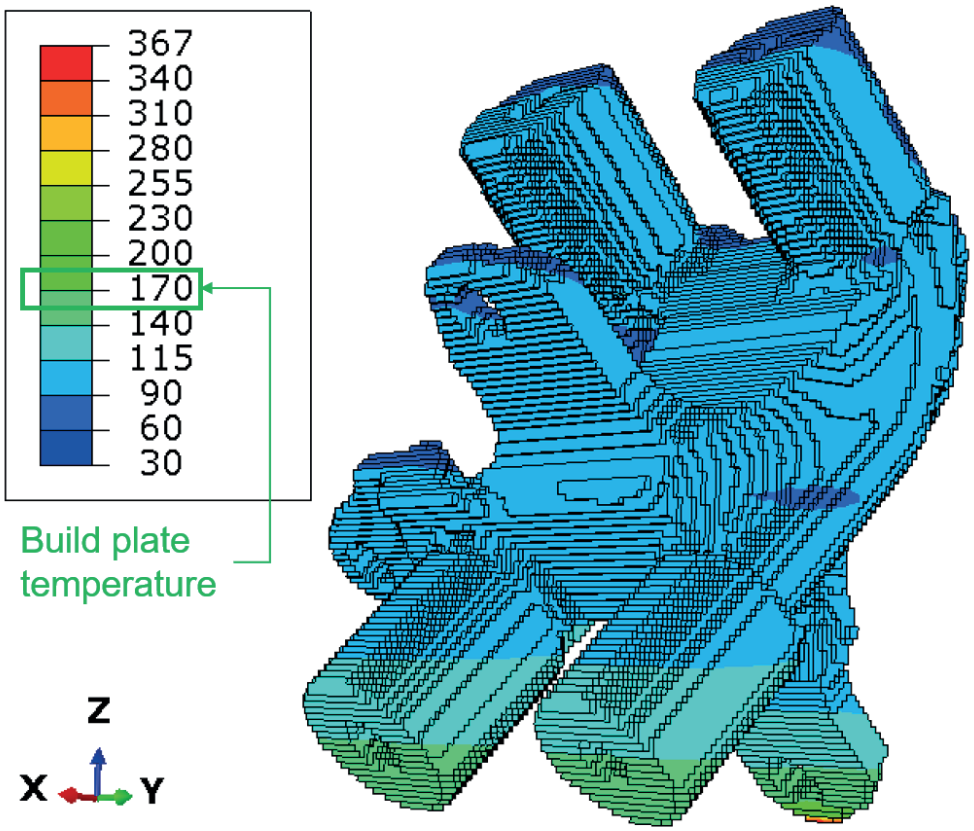

Figure 4.7: Level 1 map of maximum temperatures.

4.4.3. Level 2

Level 1 macrolayer 33 results were selected for further analysis at Level 2.

At Level 2, it is possible to consider the recoating delay and to heat only one 60 µm layer from within macrolayer 33. Hence, for the upper area of the model, regions above macrolayer 32 were removed.

For the lower region, regions that did not exhibit significant temperature variations were eliminated before Level 2 analysis. Hence, regions with little temperature variation (i.e. constant gradients) are removed and replaced by a thermal field boundary condition.

This hypothesis can be verified by running a Level 2 analysis and observing the temperature variations at the identified steady regions. If the gradient differs significantly during a simpler analysis, the region does not satisfy the steady condition and cannot be omitted, so the boundary should be placed in a distant region.

In our case, the temperature variations through the supports and build plate were significant (> 10%). Hence, all the lower regions were retained. This hypothesis can be tested once more at Level 3, where the temporal domain is refined compared with Level 2.

For simplicity, we considered the same mesh, particularly without remeshing the borders of the part. The initial temperature field was set from the result of Level 1 at the end of the heating step of macrolayer 32.

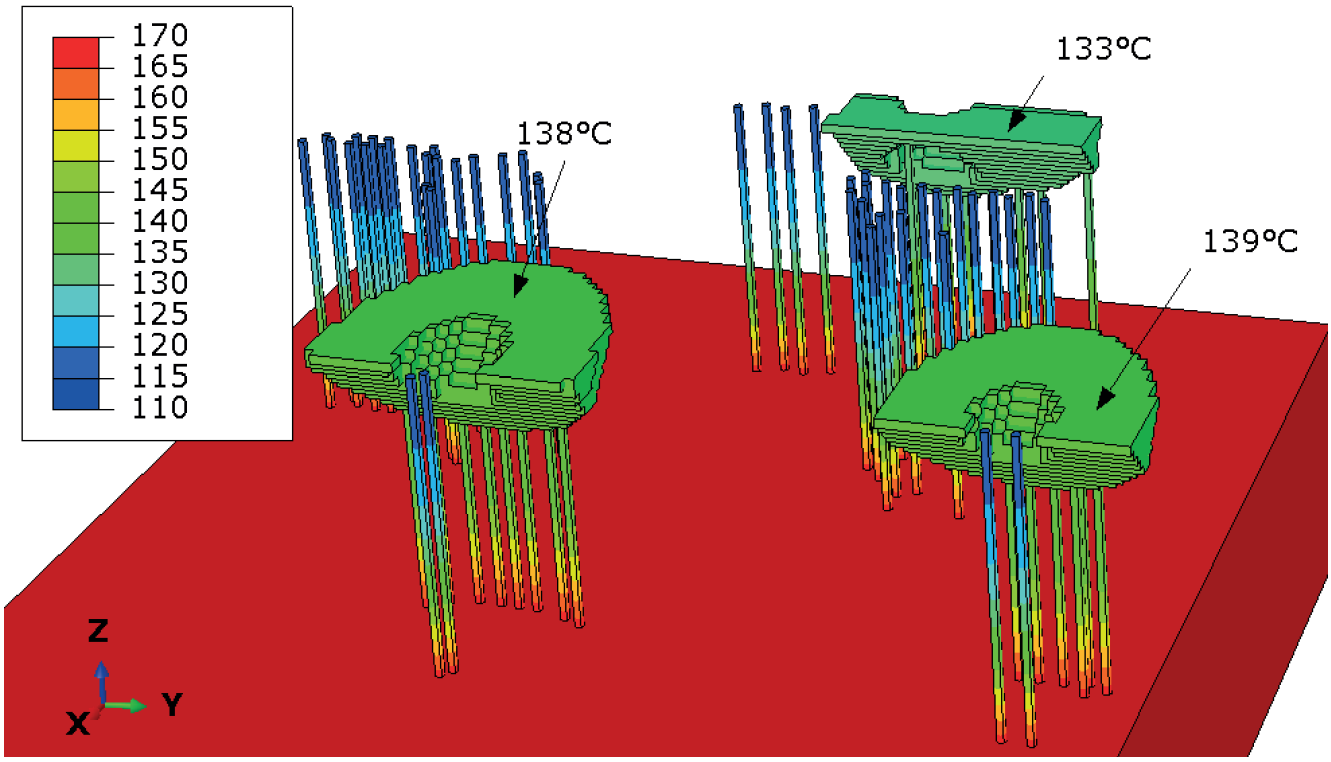

Figure 4.8: Level 1 temperature fields after heating macrolayer 33.

The scanning strategy selected in this study was the island pattern. Other geometric patterns, such as stripes or hexagons, can also be easily used.

Hence, the upper surface was divided into multiple islands with a maximum size of 4 mm × 4 mm. These islands were consecutively used as surface heat sources during specific heating steps.

The sequence of these islands is important because it affects the minimum and maximum temperatures obtained on the part. For the example, a randomly generated sequence was used, as shown in Figure 4.9.

Several islands are sometimes close to the next heated island in the sequence and are sometimes not similar to real production sequences. By optimising the sequence, the temperature fields may be more homogeneous, and peak temperatures may be diminished.

The supports were also heated as in the real process. Because they are isolated by powder and can only diffuse heat in the vertical direction, it is expected that during their production, they will suffer higher temperatures than the part.

However, they were not reported in the maximum temperature results because we focused on the parts. During their manufacturing, some support regions exhibited the highest temperatures (up to 1 421 °C).

A map of the maximum temperatures in this part is shown in Figure 4.10. Regions on the border of the part generally experience higher temperatures than those in the bulk regions.

The maximum temperature field of the part with a peak temperature of 454 °C is shown in Figure 4.11. The maximum temperature was reached on island 25, close to island 24.

In addition, island 25 has a small surface compared to the other islands and is at the edge of the part on two sides. Hence, heat cannot diffuse effectively, and the maximum temperature is observed there.

We focus on the heating of this region using the Level 3 model.

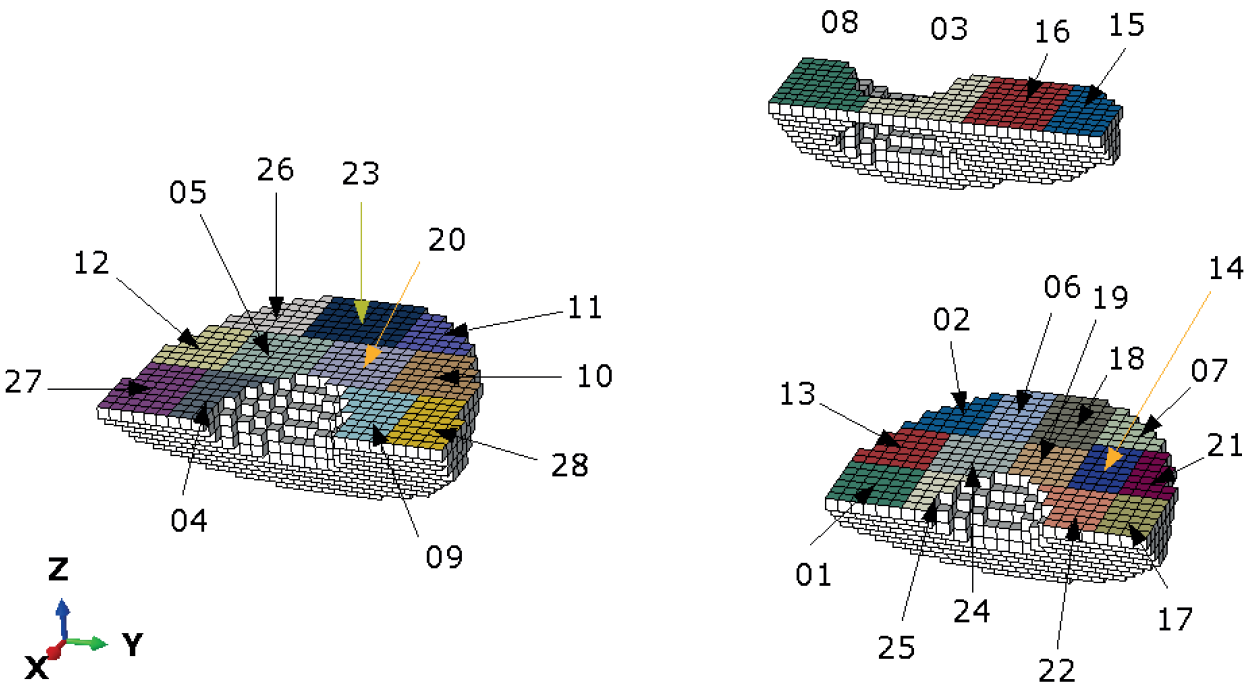

Figure 4.9: Level 2 islands randomly-generated sequence (supports and build plate are not shown for better clarity).

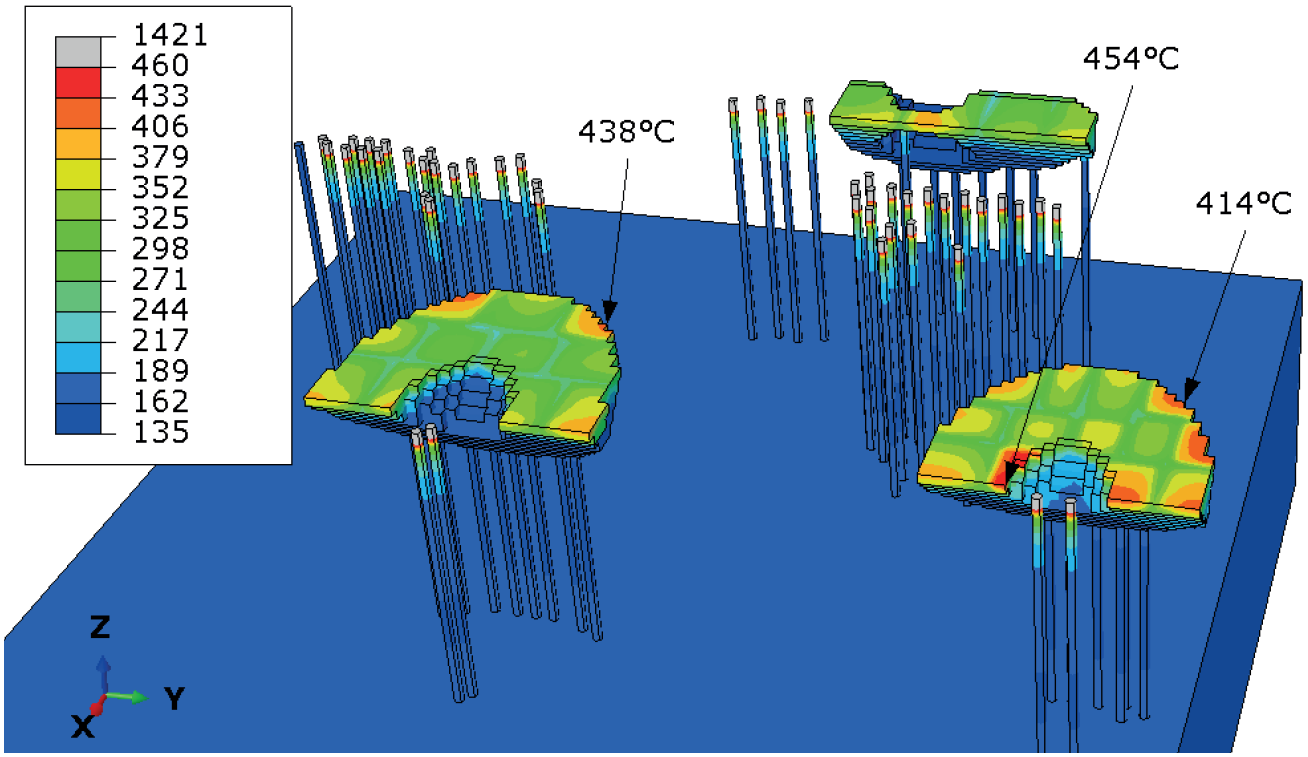

Figure 4.10: Level 2 map of maximum temperatures.

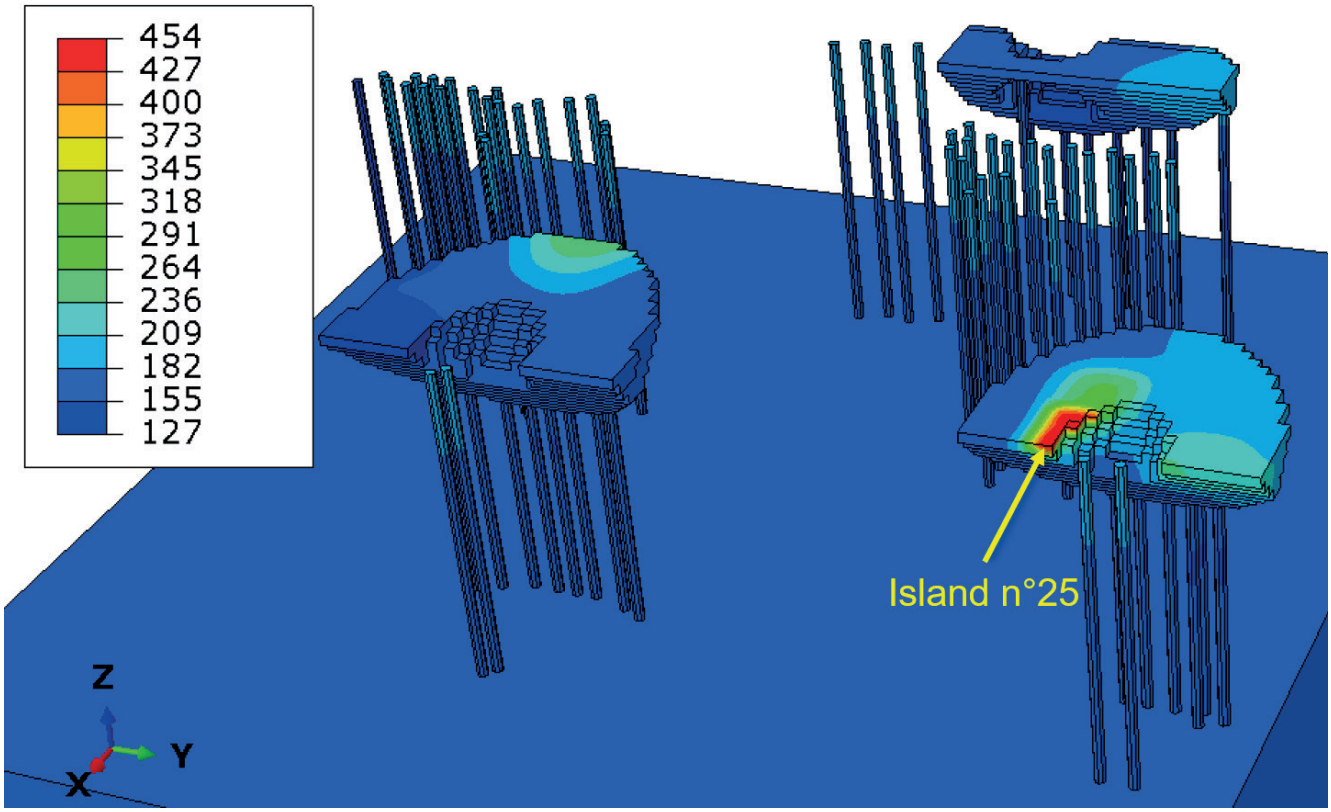

Figure 4.11: Level 2 zoom of maximum temperature.

4.4.4. Level 3

Level 2 analysis was used to identify the island site of the Level 3 analysis. Level 3 analysis permits the user to explore the effect of the filling direction for this particular island.

At Level 3, lines the size of the scanning vectors are heated to progressively fill the island. From Level 2, only the hydraulic joint region containing island 25 (Figure 4.9) and the top of its supports were maintained.

Using the Level 2 temperature field, a fixed temperature BC was set on the lower surface. Macrolayer 32 is replaced by refined FE on island 25.

An overview of the Level 3 model is displayed in Figure 4.12, with a zoom on one of the thermal line load that will fill island 25.

Among the numerous possible directions to fill the island, we selected lines aligned in the X-direction, and activated opposite to the Y-direction, as seen in Figure 4.12.

All lines were consecutively heated in one step of the calculus, to simulate the effect of all vectors. The durations of the heating steps considered the delays in the vector jumps (before and after scanning).

For the other levels, the mesh was optimised to yield small computation times (110 730 elements as shown in Figure 4.12). However, in this case, the mesh should be further optimised because of the non-physical "wave effect" seen in Figure 4.13.

As previously discussed, the temperature variations, that is, the gradients, are negligible near the BC at the bottom, indicating that the reduced model is acceptable. The overall maximum temperatures attained at Level 3 are displayed in Figure 4.13(a). The temperature field while reaching the peak temperature is displayed in Figure 4.13(b).

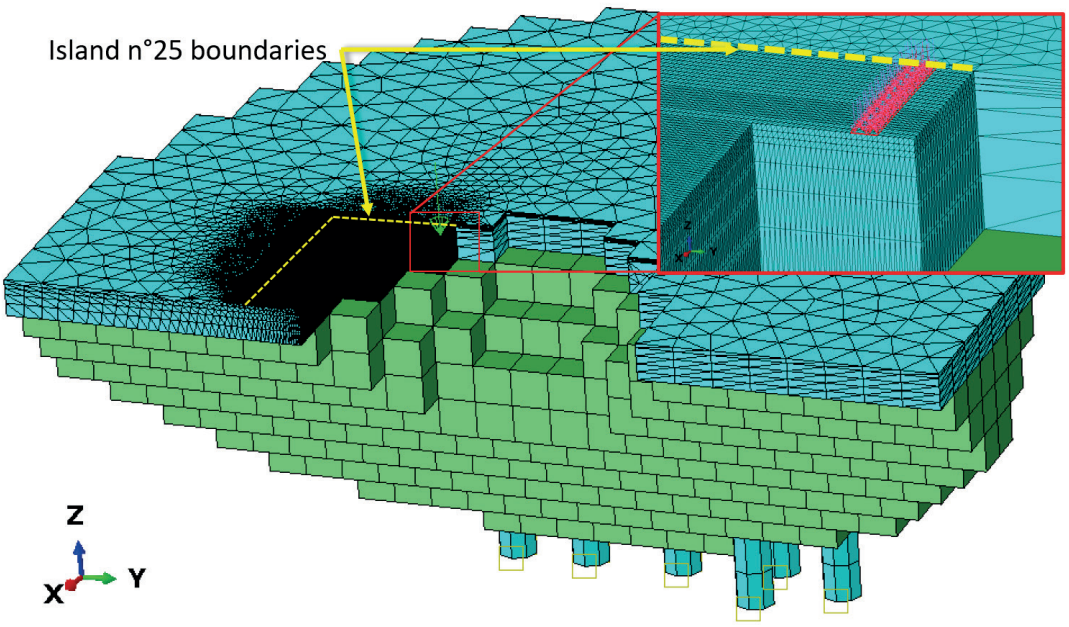

Figure 4.12: Level 3 model. Temperature BC assigned to the bottom of the supports. The red surface in the zoom panel shows a line-heat source.

The maximum temperature was reached near the edge of the part at the corner of the voxel element. The site of maximum temperature was not located on the site where the heat source was applied; it was located on an isolated corner. This is because the heat cannot be diffused more efficiently in this area than in other regions.

For simplicity, the size of the voxels is maintained at Level 1, and it would be more accurate to refine the mesh. However, the global method of analysis remains the same.

In Level 3, the entire vector line is used as a single heat source; hence, it is an averaged form of the melt pools, forming the entire vector. In addition, the peak temperature is close to the Ti-6Al-4V melting point. The model used may not be the best fit for this simulation, as it only comprises a homogeneous solid, with material properties which do not consider phase change.

The peak temperature itself may have some errors; however, the position of the maximum temperature is probably the same. The step displayed in Figure 4.13(b) will be used for Level 4 analysis.

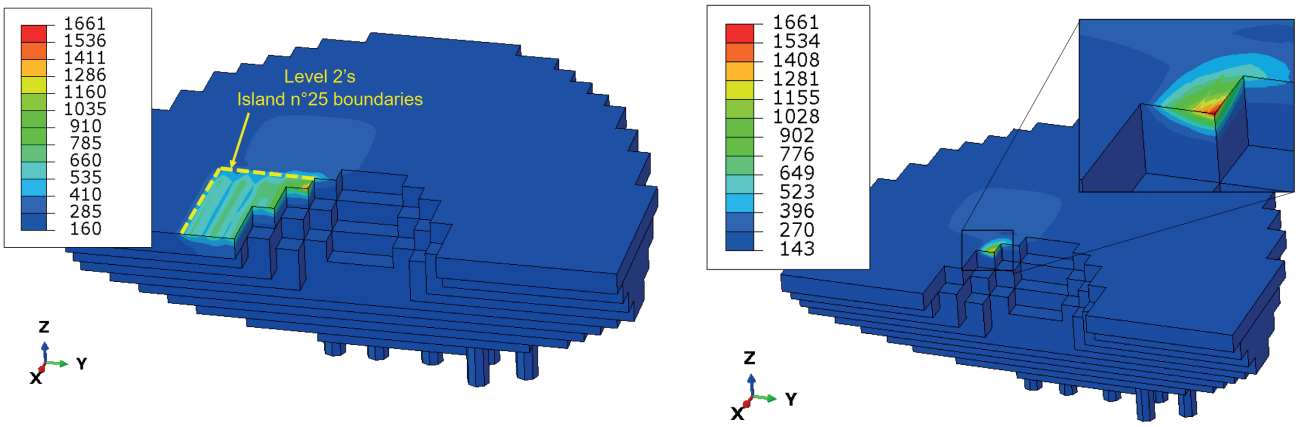

(a) Map of maximum temperatures. (b) zoom of maximum temperature.

Figure 4.13: Level 3 temperature results.

4.4.5. Level 4

From Level 3, it was possible to consider a direction to fill island 25 (selected from Level 2 results) with lines of the size of the scanning vectors. However, the directions of these vectors were not considered.

This can be done at Level 4, by progressively heating the entire line vector. The geometry from Level 3 is reduced for a few macrolayers because the temperature field does not vary significantly. Temperature BCs were also considered at the bottom of the model using the temperature field from Level 3.

The first step of Level 4 is a delay step to simulate the acceleration delay of the laser mirrors. At this stage, the laser spot accelerates without emission, and at its nominal speed, the laser heats the powder. The stage duration value is described as the acceleration delay in Table 4.2.

For this specific model, the considered scanning direction is -X. The level 4's model is shown in Figure 4.14.

Because the line identified at Level 3 is small, the heating sequence is made by heating blocks the size of a few melt pools (two melt pools in this case). For longer scan lines, it is possible to generate blocks with several melt pools grouped together to maintain a short computation time.

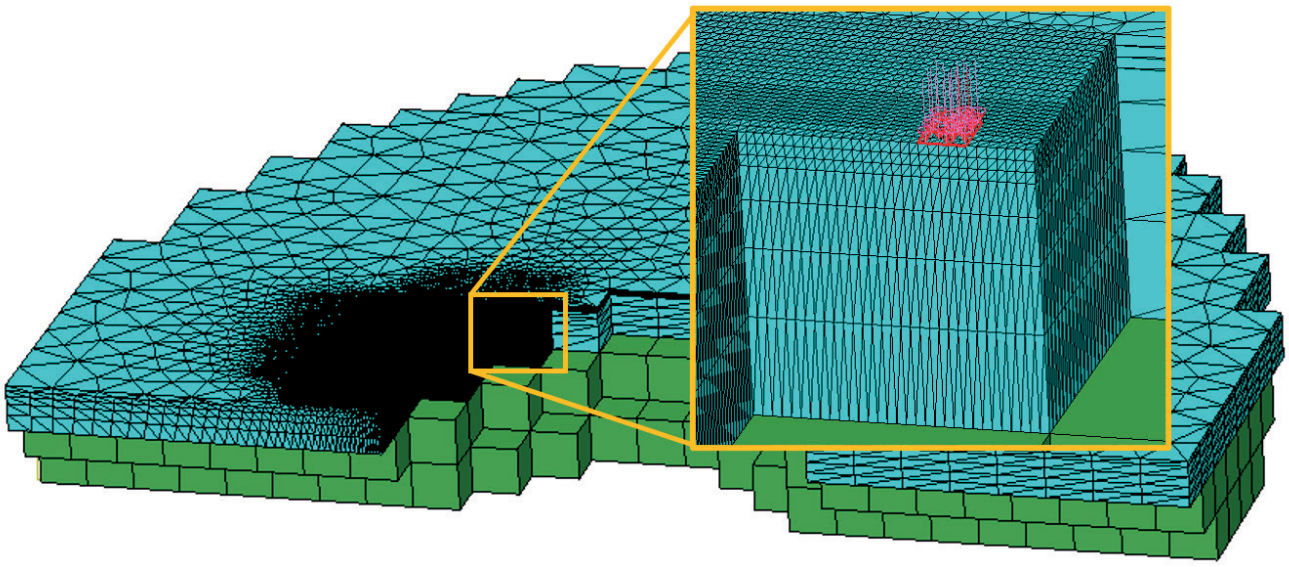

Figure 4.14: Level 4 model. Temperature boundary conditions are applied on the lower side. The red surface in the zoom panel shows a group of point-like heats sources.

A map of the maximum temperatures is shown in Figure 4.15(a). The peak temperature was reached at the very first heating step, at the border of the part, because the heat could not diffuse efficiently. The temperature fields at the peak temperature are shown in Figure 4.15(b).

The peak temperature was large near the boiling point of titanium (3287 °C [13]). This is because the model does not account for the changing material properties in different phases (solid to liquid or solid to gas). Using the linear material properties (i.e. density, see Figure 4.6) above the melting temperature is irrelevant.

The step in which the peak temperature was obtained (Figure 4.15(b)) was used for the Level 5 study. When the peak temperature reached a step other than the first heating step, the method is identical: the initial temperatures would be set from the field of the previous heating, and the BCs would be set in regions where the thermal temperature is constant.

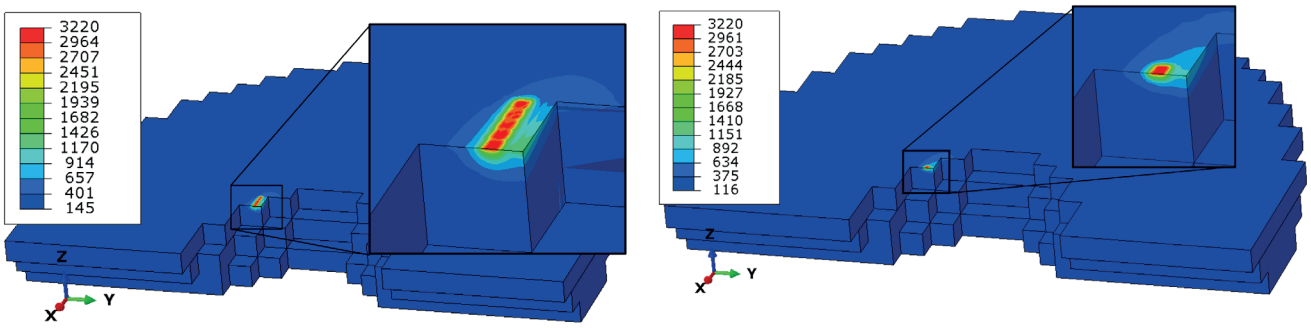

(a) Map of maximum temperatures. (b) zoom of maximum temperature.

Figure 4.15: Level 4 temperature results.

4.4.6. Level 5

Level 4 enabled the user to identify the most suitable scanning direction for the vector. For the first time, laser scanning may be directly simulated in Level 5 using this method.

From Level 1 to Level 4, laser scanning was averaged to a greater surface than that of the melt pool. Hence, the user may set the initial temperature fields approximated from the previous results and use the relevant BCs. Compared with Level 4, the temporal increments were refined.

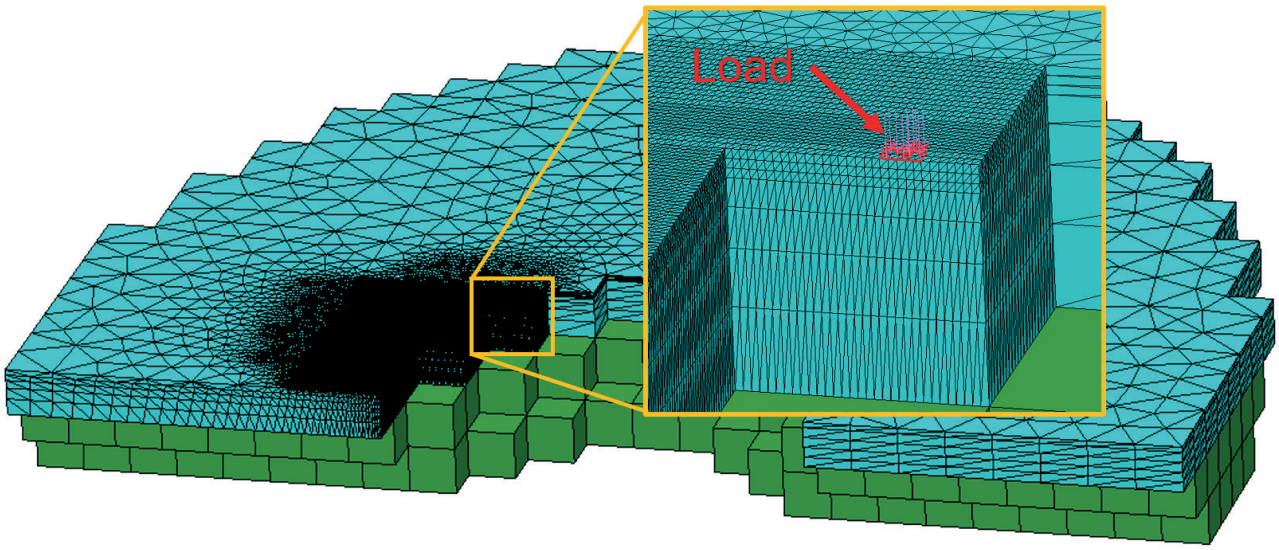

Figure 4.16: Level 5 model. Temperature boundary conditions are applied on the lower side. The red surface in the zoom panel exhibit a point-like heat source.

At this level, the loads are the size of single melt pools, and each melt pool has a specific heating step. In this manner, a punctual laser heat source was simulated.

The Level 5 model is shown in Figure 4.16, revealing a constant heat source applied to the entire melt pool area. Any other type of HS model and material phase change can be employed.

Here, the main advantage of the method is that the ICs and BCs were set from the previous simulation results. A map of the maximum temperatures is shown in Figure 4.17.

Because the employed model is not suitable for microscale simulations, the peak temperature is large com-

pared to the boiling point of the material. Hence, the temperatures above the boiling point were filtered, as shown by the grey areas in Figure 4.17.

The region around the peak temperature may contain a large amount of porosity owing to thermal instabilities of the melt pool (i.e. keyhole) and evaporation.

The method exhibited great potential because the computations took approximately 14 h, each using 12 core AMD OpteronTM 6376 2.3 GHz-128 Gb RAM.

This method can also be used to simulate specific scanning strategies linked to the geometry of the part, scanning sequences, and pattern (e.g. islands and stripes) sizes.

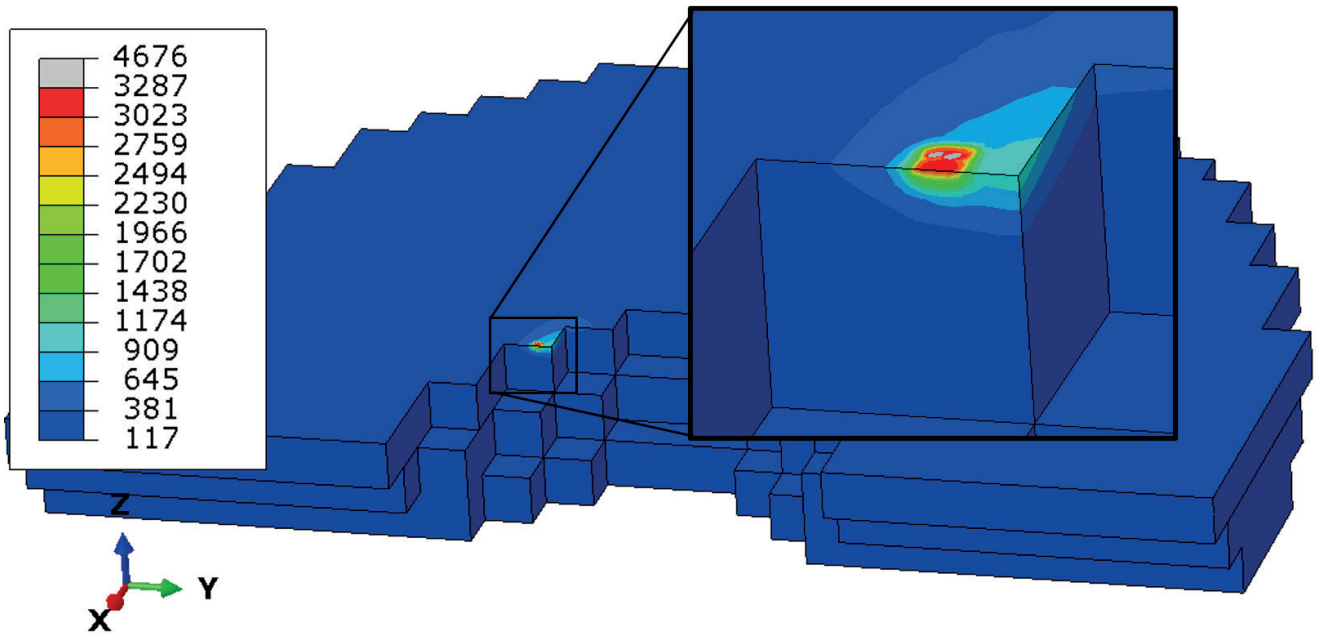

Figure 4.17: Level 5 map of maximum filtered temperatures.

4.5. Discussions

Using the presented multiscale thermal method, it was possible to simulate thermal fields through hydraulic joint manufacturing (Level 1). It was also possible to zoom into the details of the scanning pattern (Level 2), scanning strategy (Level 3), scanning direction (Level 4), and to model the vicinity of some melt pools prior to melting.

Because all levels are linked to one another, it was possible to use initial thermal fields and BCs that were not homogeneous and computed from the previous level.

The total computational duration for all levels was approximately 14 h on 12 core AMD OpteronTM 6376 2.3 GHz-128 Gb RAM, as shown in Table 4.4.

Level 1 is much slower than the other levels. This was due to the number of activation and heating steps (301 steps in total).

The first approximation to drastically reduce the Level 1 computational duration is to use thicker macrolayers. For instance, using 0.6mm thick voxels instead of 0.5 mm, the total number of total steps would be 258 (instead of 301), and by using 1mm thick voxels, there would be 171 steps in total.

Also, the Level 2 model made use of 28 individual island surfaces with a maximum surface area of 4mm×4 mm. Using larger islands or stripes scanning pattern at Level 2, the number of total steps would be reduced and

the computational durations would also be reduced.

Table 4.4: Computation duration for each level of the multiscale method.

Levels	Computation duration
1	10 h 27 min 23s
2	2 h 09 min 06 s
3	1 h 06 min 31 s
4	11 min 28 s
5	3 min 25 s

As discussed in the Level 3 results section (Section 4.4.4), the location of the peak temperature identified at Level 3 differed from those of Levels 4 and 5. This is due to the modelling of the heat sources at Levels 4 and 5. Level 3 used the entire vector line to heat the surface, although Level 4 only heated portions of the line.

In addition, the peak temperatures reached at Level 5 were above the material boiling point. This is because the model does not consider the change in material while changing the phase from solid to liquid and gas; the thermal properties of the material are extrapolated for higher temperature values. Hence, the bodies can reach non-physical temperatures.

In addition, according to Khairallah *et al.* [54], fluxes linked to metal vapour, which increase exponentially with temperature, should be considered at the microscale.

In our case, the same convective flux as the previous levels was used (Table 4.2), which may explain the excessively large remaining energy within the system. Hence, at this level, more complex thermal models should be used; however, the global method would be the same.

A further possible approach would be to use the Level 5 results to precisely define the HS and energy brought to the system. This energy is then applied to the other levels as a closed loop.

Exploring several Level 5 models at different sites (identified in previous models) would enable the supervision of local temperatures under different initial thermal conditions. This stage can be used to ensure that the energy is not excessive and induces melt-pool instabilities. This control of the melt pool condition was performed by Khairallah *et al.* [12] for a turnaround vector scan strategy.

Keeping Level 5 results in a library format, it is possible to estimate the energy effectively absorbed within the solid at previous levels.

In the previous levels (Level 1 to Level 4), the absorption coefficient can be adjusted from Table 4.2. This coefficient roughly estimated thermal losses, which were not modelled in this study and remained constant at every level.

In the previous levels (Levels 1 to 4), the coefficient can be calibrated considering the resulting supplementary energy at Level 5, leading to peak temperatures above the boiling point. These temperatures were obtained using the initial conditions computed at previous levels.

Hence, while reaching similar temperatures at these levels, the absorption coefficient can be adjusted to account for the supplementary energy obtained from previous Level 5 computations.

In the case presented here, from Level 3, it appeared that the area of interest was small (corner of the island). For presentation purposes, a general method was developed: Level 4 used portions of the line as heat sources, and Level 5 used heat sources the size of the melt pools.

However, in this specific case, since Level 4 made use of only five heat sources, it could have been interesting to group together Levels 4 and 5. In other words, the user may heat the Level 5 heat sources (melt pool size) along the entire line (Level 4 range), and the method would only have four levels in total.

Given the limitations of the method, owing to the current computational potential, it is impossible to zoom into every melt pool by manufacturing all parts.

Hence, this method is only useful for selecting regions at the highest levels and zooming into these regions at lower levels. The user must make choices regarding the regions to be zoomed in.

In addition, the temperature fields computed at a specific level depend on the assumptions made at higher levels. Hence, approximation errors were generated at a high level and cannot be diminished by zooming in because the initial temperature fields and BCs depend directly on the previous level.

4.6. Conclusions and perspectives

A novel method for simulating the thermal history of the LPBF process is proposed. This method considers every parameter that influences the thermal fields within reasonable computation times. This was achieved using specific modelling assumptions and zooming in on specific interest regions of the part.

The proposed method is sequential multiscale FE analysis. It begins at the macroscale, and each subsequent level enables zooming down into a part. The thermal fields computed at the previous level were used as the ICs and BCs in the next level. Methods to model the heat source, initial conditions, and boundary conditions, as well as the spatial and temporal boundaries of each level, were methodically defined. This is shown analytically in a simplified case in which the error linked to the heat source approximation can be estimated.

Using macrolayers and volumetric HS the size of the macrolayer, it was demonstrated with a simplified analytical case (1D semi-infinite body with conduction only) that using a greater observation duration after the heating process yielded less errors. Also, when more layers are bundled together, the error tends to diminish. The error decay was estimated analytically with an exponential and a polynomial term.

An industrial application was selected for the proposed method with five distinct levels employed to zoom down to a scale near the melt pool. The impacts of all identified parameters on the thermal fields were modelled in a specific simulation step.

The proposed method cannot be used to simulate the entire part at the microscale or mesoscale. In addition, in this specific study, for Levels 4 and 5, a homogeneous solid body assumption does not suit the physical behaviour; a more complex model incorporating fluid dynamics should also be considered.

The proposed method can first be used to identify the porosity location and to compute the thermal history. Such a thermal history is required for residual stress formation, simulation of the melt pool, and generated metallurgy, which mainly depends on the thermal history.

Using this method, the user can modify the parameters (such as pause durations, island sequences, and vector length) to limit the local rise in temperatures and obtain more homogeneous thermal fields in the entire part. In addition, this method may be used to manually adapt the laser power to limit the extreme temperatures locally with regard to the initial temperature fields.

In addition, with the possible ways to use the method, it can be enhanced using specific simulation method while refining the space and time domains. Indeed, the entire method was performed using FE analysis with homogeneous solids. However, one may use spectral graph techniques for macroscale levels [20], for instance; and a discrete element method (to simulate the powder particles) coupled with a lattice Boltzmann method (as detailed in [55]) to simulate the liquid-solid interface and the thermal fields.

Also, the estimated error was analytically estimated using 1D semi-infinite bodies. Future works may tackle the challenge of estimating the macrolayer assumption errors with 3D bodies for simple cases. The objective is to approximate the errors and be able to define optimal macrolayer thicknesses for each application, depending on the user's error requirements.

Finally, microscale libraries may help estimate the amount of energy effectively received by the matter at macroscale, and adapt the absorption coefficient depending on the material, the power, the loading duration and the macrolayer size.

4.7. References

[1] Markl, M. & Körner, C. Multiscale Modeling of Powder Bed–Based Additive Manufacturing. Annu. Rev. Mater. Res. 46, 93–123 (2016).

[2] Li, C., Fu, C. H., Guo, Y. B. & Fang, F. Z. A multiscale modeling approach for fast prediction of part distortion in selective laser melting. J. Mater. Process. Technol. 229, 703–712 (2016).

[3] Keller, N. Nils Keller verfahren durch Multi-Skalen-Simulation Verzugsminimierung bei selektiven Laserschmelzverfahren durch. PhD Universität Bremen (Universität Bremen, 2016).

[4] Meier, C., Penny, R. W., Zou, Y., Gibbs, J. S. & Hart, A. J. Thermophysical Phenomena in Metal Additive Manufacturing By Selective Laser Melting: Fundamentals, Modeling, Simulation, and Experimentation. Annu. Rev. Heat Transf. 20, 241–316 (2018).

[5] Mercelis, P. & Kruth, J. P. Residual stresses in selective laser sintering and selective laser melting. Rapid Prototyp. J. 12, 254–265 (2006).

[6] Rubenchik, A. M., King, W. E. & Wu, S. S. Scaling laws for the additive manufacturing. J. Mater. Process. Technol. 257, 234–243 (2018).

[7] Leung, C. L. A. *et al.* In situ X-ray imaging of defect and molten pool dynamics in laser additive manufacturing. Nat. Commun. 9, 1–9 (2018).

[8] Parry, L., Ashcroft, I. A. & Wildman, R. D. Understanding the effect of laser scan strategy on residual stress in selective laser melting through thermo-mechanical simulation. Addit. Manuf. 12, 1–15 (2016).

[9] Ali, H., Ghadbeigi, H. & Mumtaz, K. Effect of scanning strategies on residual stress and mechanical properties of Selective Laser Melted Ti6Al4V. Mater. Sci. Eng. A 712, 175–187 (2018).

[10] Liu, Y., Yang, Y. & Wang, D. A study on the residual stress during selective laser melting (SLM) of metallic powder. Int. J. Adv. Manuf. Technol. 87, 647–656 (2016).

[11] Stef, J. Fusion Laser Selective de poudres de TA6V : microstructure et mécanismes de formation des porosités en lien avec les paramètres du procédé SLM et les propriétés structurales. Thèse de Doctorat de l'Université de Bordeaux (2018).

[12] Khairallah, S. A. *et al.* Controlling interdependent meso-nanosecond dynamics and defect generation in metal 3D printing. Science. 368, 660–665 (2020).

[13] Hooper, P. A. Melt pool temperature and cooling rates in laser powder bed fusion. Addit. Manuf. 22, 548–559 (2018).

[14] Mitchell, J. A., Ivanoff, T. A., Dagel, D., Madison, J. D. & Jared, B. Linking pyrometry to porosity in additively manufactured metals. Addit. Manuf. 31, 100946 (2020).

[15] Teng, C. *et al.* A review of defect modeling in laser material processing. Addit. Manuf. 14, 137–147 (2017).

[16] Cole, K. D., Beck, J. V., Haji-Sheikh, A. & Litkouhi, B. Heat conduction using Green's functions. (Taylor & Francis Group, 1992).

[17] Yang, Y., Keulen, F. Van & Ayas, C. A computationally efficient thermal model for selective laser melting. Addit. Manuf. 31, 100955 (2020).

[18] Moran, T. P., Warner, D. H. & Phan, N. Scan-by-scan part-scale thermal modelling for defect prediction in metal additive manufacturing. Addit. Manuf. 37, 101667 (2021).

[19] Reza Yavari, M., Cole, K. D. & Rao, P. Thermal modeling in metal additive manufacturing using graph theory. J. Manuf. Sci. Eng. Trans. ASME 141, 1–20 (2019).

[20] Yavari, R., Williams, R., Cole, K., Hooper, P. & Rao, P. Thermal Modeling in Metal Additive Manufacturing using Graph Theory: Experimental Validation with In-situ Infrared Thermography Data from Laser Powder Bed Fusion. J. Manuf. Sci. Eng. 142, 1–43 (2020).

[21] Ganeriwala, R. K. *et al.* Evaluation of a thermomechanical model for prediction of residual stress during laser powder bed fusion of Ti-6Al-4V. Addit. Manuf. 27, 489–502 (2019).

[22] Zaeh, M. F. & Branner, G. Investigations on residual stresses and deformations in selective laser melting. Prod. Eng. 4, 35–45 (2010).

[23] Williams, R. J., Davies, C. M. & Hooper, P. A. A pragmatic part scale model for residual stress and distortion prediction in powder bed fusion. Addit. Manuf. 22, 416–425 (2018).

[24] Desmaison, O. *et al.* Influence of computational grid and deposit volume on residual stress and distortion prediction accuracy for additive manufacturing modeling. in Proceedings of the 4th World Congress on Integrated Computational Materials Engineering (ICME 2017) vol. Part F4 365–374 (The Minerals, Metals & Materials Series, 2017).

[25] Setien, I. *et al.* Empirical methodology to determine inherent strains in additive manufacturing. Comput. Math. with Appl. 78, 2282–2295 (2019).

[26] Wei, L. C. *et al.* Thermal conductivity of metal powders for powder bed additive manufacturing. Addit. Manuf. 21, 201–208 (2018).

[27] Alkahari, M. R. *et al.* Thermal Conductivity of Metal Powder and Consolidated Material Fabricated via Selective Laser Melting. Key Eng. Mater. 523–524, 244–249 (2012).

[28] Denlinger, E. R., Jagdale, V., Srinivasan, G. V., El-Wardany, T. & Michaleris, P. Thermal modeling of Inconel 718 processed with powder bed fusion and experimental validation using in situ measurements. Addit. Manuf. 11, 7–15 (2016).

[29] Li, C., Gouge, M. F., Denlinger, E. R., Irwin, J. E. & Michaleris, P. Estimation of part-to-powder heat losses as surface convection in laser powder bed fusion. Addit. Manuf. 26, 258–269 (2019).

[30] Dugast, F. *et al.* Part-scale thermal process modeling for laser powder bed fusion with matrix-free method and GPU computing. Addit. Manuf. 37, 101732 (2021).

[31] Zhang, W., Tong, M. & Harrison, N. M. Resolution, energy and time dependency on layer scaling in finite element modelling of laser beam powder bed fusion additive manufacturing. Addit. Manuf. 28, 610–620 (2019).

[32] Lindwall, J., Malmelöv, A., Lundbäck, A. & Lindgren, L. E. Efficiency and Accuracy in Thermal Simulation of Powder Bed Fusion of Bulk Metallic Glass. Jom 70, 1598–1603 (2018).

[33] Luo, Z. & Zhao, Y. A survey of finite element analysis of temperature and thermal stress fields in powder bed fusion Additive Manufacturing. Addit. Manuf. 21, 318–332 (2018).

[34] Chen, Q. *et al.* An inherent strain based multiscale modeling framework for simulating part-scale residual deformation for direct metal laser sintering. Addit. Manuf. 28, 406–418 (2019).

[35] Foroozmehr, A., Badrossamay, M., Foroozmehr, E. & Golabi, S. Finite Element Simulation of Selective Laser Melting process considering Optical Penetration Depth of laser in powder bed. Mater. Des. 89, 255–263 (2016).

[36] Tran, H. C. & Lo, Y. L. Heat transfer simulations of selective laser melting process based on volumetric heat source with powder size consideration. J. Mater. Process. Technol. 255, 411–425 (2018).

[37] Luo, Z. & Zhao, Y. Numerical simulation of part-level temperature fields during selective laser melting of stainless steel 316L. Int. J. Adv. Manuf. Technol. 104, 1615–1635 (2019).

[38] Luo, Z. & Zhao, Y. Efficient thermal finite element modeling of selective laser melting of Inconel 718. Comput. Mech. 65, 763–787 (2020).

[39] Keller, N. & Ploshikhin, V. New method for fast predictions of residual stress and distortion of AM parts. in Solid Freefrom Fabrication 1689–1699 (2014).

[40] Tran, H. T., Chen, Q., Mohan, J. & To, A. C. A new method for predicting cracking at the interface between solid and lattice support during laser powder bed fusion additive manufacturing. Addit. Manuf. 32, 101050 (2020).

[41] Bayat, M., Dong, W., Thorborg, J., To, A. C. & Hattel, J. H. A review of multi-scale and multi-physics simulations of metal additive manufacturing processes with focus on modeling strategies. Addit. Manuf. 47, 102278 (2021).

[42] Paudel, B. J. & Thompson, S. M. Localized Effect of Overhangs on Heat Transfer during Laser Powder Bed Fusion Additive Manufacturing. in Solid Freeform Fabrication 2019: Proceedings of the 30th Annual International Solid Freeform Fabrication Symposium – An Additive Manufacturing Conference (2019).

[43] Keller, N., Neugebauer, F., Xu, H. & Ploshikhin, V. Thermo-mechanical Simulation of Additive Layer Manufacturing of Titanium Aerospace structures. Light. Conf. (2013) doi:10.1128/AAC.36.7.1525.

[44] Li, C., Liu, J. F., Fang, X. Y. & Guo, Y. B. Efficient predictive model of part distortion and residual stress in selective laser melting. Addit. Manuf. 17, 157–168 (2017).

[45] Li, C., Liu, Z. Y., Fang, X. Y. & Guo, Y. B. On the Simulation Scalability of Predicting Residual Stress and Distortion in Selective Laser Melting. J. Manuf. Sci. Eng. 140, 041013 (2018).

[46] Williams, R. J. *et al.* In situ thermography for laser powder bed fusion: Effects of layer temperature on porosity, microstructure and mechanical properties. Addit. Manuf. 30, 100880 (2019).

[47] Denlinger, E. R., Heigel, J. C., Michaleris, P. & Palmer, T. A. Effect of inter-layer dwell time on distortion and residual stress in additive manufacturing of titanium and nickel alloys. J. Mater. Process. Technol. 215, 123–131 (2015).

[48] Wolff, S. J. *et al.* A framework to link localized cooling and properties of directed energy deposition (DED)-processed Ti-6Al-4V. Acta Mater. 132, 106–117 (2017).

[49] Mirkoohi, E., Seivers, D. E., Garmestani, H. & Liang, S. Y. Heat source modeling in selective laser melting. Materials (Basel). 12, 1–18 (2019).

[50] Hocine, S., Van Swygenhoven, H. & Van Petegem, S. Verification of selective laser melting heat source models with operando X-ray diffraction data. Addit. Manuf. 37, 101747 (2021).

[51] Yang, Y. & Zhou, X. A Volumetric Heat Source Model for Thermal Modeling of Additive Manufacturing of Metals. Metals (Basel). 10, 1406 (2020).

[52] Dilip, J. J. S. *et al.* Influence of processing parameters on the evolution of melt pool, porosity, and microstructures in Ti-6Al-4V alloy parts fabricated by selective laser melting. Prog. Addit. Manuf. 2, 157–167 (2017).

[53] Le, T. N., Lo, Y. L. & Tran, H. C. Multi-scale modeling of selective electron beam melting of Ti6Al4V titanium alloy. Int. J. Adv. Manuf. Technol. 105, 545–563 (2019).

[54] Khairallah, S. A., Anderson, A. T., Rubenchik, A. & King, W. E. Laser powder-bed fusion additive manufacturing: Physics of complex melt flow and formation mechanisms of pores, spatter, and denudation zones. Acta Mater. 108, 36–45 (2016).

[55] Markl, M. Numerical Modeling and Simulation of Selective Electron Beam Melting Using a Coupled Lattice Boltzmann and Discrete Element Method. Ph.D. Thesis Universität Erlangen-Nürnberg (Universität Erlangen-Nürnberg, 2015).

Conclusions

Table of contents

V. Conclusions

5.1. Contributions 148
5.2. Perspectives 150

Chapter V
Conclusions

5.1. Contributions

During this work, several aspects of the Laser Powder Bed Fusion (LPBF) process have been investigated: the oxidation sources, the simulation of supports breakages and the simulation of the thermal history.

First, owing to the rise of parts oxygen content, numerous users in the medical, dental, and aeronautics industries throw away used powders (most of the time Ti-6Al-4V).

Indeed, the Ti-6Al-4V chemical content is constrained by two standards, notably limiting the oxygen content. The factors influencing the oxidation kinetics have already been well identified in the literature, namely time, temperature, and oxygen sources.

Both oxygen sources and heat are in play during the process, so the objective of the first part of this work was to identify the main stage (hence, the main factor) of the oxidation, between the recycling and the heating stages. From the experimental results, it was shown that the heating phase had the most significant impact on the oxygen rise, while powders manually handled and recycled did not show any specific variation.

Hence, it should be assumed that the oxidation mainly occurs during the scanning, and, according to our observations, spatters may play a major role since they originate from the melt pool (originally in liquid state, they solidify when cooled). Also, particles flying through the laser beam, and condensates linked to the metal evaporation above the melt pool may contaminate the surrounding powders. A study may be conducted to identify the specific influence of these factors.

Two strategies were suggested to limit the spatters generation: increasing the dwell time (interlayer cooling time), or reducing the scanned surface at each layer.

The first strategy (increasing the dwell time, to enable the parts to cool down before subsequent scanning) did not reduce the number of generated spatters. The dwell times varied from 0 to 50 s, but results were similar. These dwell times variations may not be large enough, however, increasing significantly the dwell times has a significant impact on the final manufacturing durations.

The second strategy (reducing the scanned surface for each layer) seemed to yield good results regarding the

reduction of generated spatters. It seems that the amount of spatters increases with the scanned surface. This result can be directly used by the user, since he selects an orientation of the part. The orientation selection may incorporate the minimisation of the surface scanned at each layer. This way, defects generated by the spatters (i.e. porosities) and oxidation may be limited. However, it may have an influence on the parts cost, since more layers are needed to manufacture the parts, leading to longer manufacturing durations. Hence, explorations at the melt pool scale and studies optimising the gas flow may allow to reduce the number of contaminated particles (spatters from the melt pool, flying particles through the laser beam, and condensation/evaporation-originated particles) .

In the second study, it was considered that using five commercial software it was not possible to simulate the breakage of supports observed experimentally with an industrial application.

It was shown that using large voxel elements (> 0.5 mm) to mesh the supports and part stiffens the structures, even more at the teeth location. Supports being attached to the part with a narrowing geometry called tooth, such geometry cannot be modelled using large voxel elements.

Using 0.5 mm 1D-beam elements in place of the voxels to mesh the supports, it was possible to simulate the breakage of the supports.

However, some numerical instabilities took place and were identified. The major instability originates from some supports suffering from compression solicitations, leading to the buckling phenomenon. Solutions to overcome this issue were discussed, and one was chosen for this study: freezing the rotations of the beam elements. Using this solution, supports can only suffer from compression and traction solicitations. The main assumption was that the observed experimental breakages originate from traction solicitations.

Also, from our simulations, numerous supports broke from compression solicitations, which may not occur on real supports because of buckling. Preventing the breakage of compressed supports, the number of broken supports was reasonable.

Tensile test set-ups were then manufactured to characterise the mechanical behaviour of the supports as a group, and individually. It was shown that the tensile behaviour of supports material was significantly different from the parts.

The thermal history is assumed to be the reason explaining the discrepancy between supports and parts mechanical behaviour. Supports are quite thermally insulated owing to the surrounding powder, although parts may conduct heat away from various directions depending on the geometry.

From the results of the two previous studies, the heat seems to have a significant influence on the overall oxidation behaviour, and on the mechanical characteristics. Hence, thoroughly simulating the thermal history seems to have a paramount importance.

In the last study, a novel method to simulate the process thermal history is proposed and detailed with an industrial application. The method is driven by the process parameters influencing the thermal history, each of them is simulated in a specific step, leading us to consider five modelling scales. The first level is at macroscale (one or several parts, the supports, and the build plate), and uses both macrolayer assumption and volumetric heat sources.

The method allows to use large elements (0.5 mm voxels in this case) as heat sources at macroscale, using the macrolayer approximation. Ways to limit the errors using this type of assumption is discussed, using analytical transient conduction results of a 1D semi-infinite body.

The initial and boundary conditions of all levels from Level 2 to Level 5 were set from the previous simulation results. From Level 2 to Level 5, the models used the finite elements method to resolve the transient thermal analysis. Each specific scale had a time and spatial domains, refined from one level to the next.

With this method, some regions of the parts can be studied individually, and it is assumed that regions with extreme temperatures may yield some defects such as porosities.

Using this method, the user can vary process parameters to obtain more homogeneous thermal fields. Indeed, process parameters are usually tuned with costly experimental trials, and this method may accelerate the findings of optimum scanning parameters. Also, generally, four types of parameters are developped (core, skin, upskin and downskin parameters), depending on the overhang aspect of the scanned surface. Using this method, more parameters may be developped and integrated, considering also the size of the part and the overhang angle.

Also, regions where porosity defects may rise due to thermal instabilities (i.e. keyholes) are suggested from the method results. Hence, the laser power during scanning should vary according to the surrounding temperatures, the ability to conduct heat away (hence, the part shape), the vector length and the position of the beam on the vector. With such considerations, it may be possible to obtain homogeneous temperature fields for each layer.

The findings of this work show the fundamental need to understand and simulate accurately the thermal history of the parts in the LPBF process.

Regarding the industrial aspects of the oxidation behaviour, this work allows to focus on the heating stages while designing methods to limit the oxidation. It also provides a first step to limit the amount of generated spatters, which may cause several types of defects (i.e. porosity, high-oxygen content).

For the simulations aspects, several strong assumptions and methods are discussed, with their influence on the final results. Sources of numerical instabilities are identified, and methods to tackle them are discussed.

Also, the multiscale method presented in the final study was developed on a general finite element code, and, using the same assumptions as our application, computational durations can be significantly reduced using less steps (with larger macrolayers, or larger scanning patterns for instance). Hence, the entire computation durations for an industrial build plate may fall under a working day.

5.2. Perspectives

From the first study, a preferential landing side of the spatters was observed with different locations of the samples on the build plate. This behaviour needs to be investigated in the future, since only assumptions regarding the gas flow and the scanning directions have been made. Indeed, since the spatters generation phenomenon was different from one layer to another, the scanning direction may explain such behaviour.

From the same study, the method used to quantify the amount of generated spatters deposited on the last layer was misleading in some cases, and sensible to the brightness during the measurement. Hence, the comparison must have been done visually. A more robust method should be used to quantify and approve the visual interpretations of this study.

The proposed strategy to reduce the amount of generated spatters (minimising the scanned surface at each layer from rotating the part) should be validated measuring the oxygen evolution with the number of reuses of the same part using different orientations and different scanned surface sizes.

From the second study, it seems important to thoroughly characterise the compressive mechanical behaviour of cone supports. Indeed, preventing the breakage of compressed supports led to a more reasonable number of broken supports. However, these supports may effectively damage, and this behaviour needs to be understood.

Also, in this study, the minimum sample diameter was too large compared to the actual teeth of the supports. Future works should investigate ways to manufacture such thin geometries in the LPBF, with the adequate

thermal history, since the defects (i.e. porosities) may have a greater influence with reduced diameters.

In addition, the thermal-related loadings were manually set in this application. A primary thermal analysis should be launched before the mechanical analysis to provide correct thermal inputs as loadings.

In the last study, a closed loop can be implemented from Level 5 results, to calibrate the absorption coefficient used by each scale. Indeed, this coefficient may not be constant, and should represent the energy effectively absorbed by the material.

Some other techniques than finite element method may be used at different scale to yield faster and more reliable results. For instance, at macroscale, investigating the spectral graph techniques may lead to significantly faster results. Also, at microscale, modelling powder particles with discrete element method, and simulate the melt flow with a lattice Boltzmann method should yield accurate results.

Novel methods using neural networks may be used to replace microscale levels (Levels 4 and 5 for instance), since they may be relatively similar from one simulation to another. Also, neural networks guided by physical laws may conduct to fast results and may be used to replace the finite elements calculations.

Appendices

Table of contents

VI. Appendices

6.1. Parameters of the heat-incorporated experiment 153
6.2. Scanning parameters of the spatter-limitation experiment 155
6.3. Non-dispersive infrared method. 156

CHAPTER VI
APPENDICES

6.1. Parameters of the heat-incorporated experiment

Supports parameters (Grid custom)	
Cross section	Grid
Diameter	3.6 mm
Critical angle	46°
Teeth diameter	3.6 mm
Teeth height	0.1 mm
Penetration length	0 mm
Cone angle	70°
Groups spacing	300 mm
Number of supports	1
Supports spacing	1.25 mm
Zone spacing	2
Angle shifting	0.5
Grid supports	On
Grid X spacing	5
Grid Y spacing	5
Grid orientation	0
Support distance	0

Supports parameters (coarse supports custom)	
Cross section	Circle
Diameter	1.10 mm
Critical angle	46°
Teeth diameter	0.75 mm
Teeth height	0.4 mm
Penetration length	0 mm
Cone angle	70°
Groups spacing	1.8 mm
Number of supports	2
Supports spacing	1.1
Zone spacing	1.8
Angle shifting	0.37
Grid supports	Off

Scanning parameters (AlSi10Mg_0503_3177_AM400_30_M_02_B)	
Layer thickness	30 µm
Strategy	Meander
Volume border	1
Total filling	0
Filling volume contours	0
Hatching volume	1
Jump optimisation	1
Top skin	1
Top skin border	0
Lower skin	1
Blocked trajectory borders	0
Hatching compensation	0

Hatching parameters	
Hatching shifting	30 µm
Hatching power	350 W
Hatching exposition time	40 µs
Distance between hatching points	90 µm
Distance between hatching	90 µm
Initial angle	0
Increment angle	67°
Volume filter length	0
Hatching compensation threshold	30
Blocked trajectory corner angle	62°
Internal corner angle threshold	28.5°

Border parameters	
Beam compensation	- 0.065 µm
Number of borders	1
Border power	350 W
Border exposition time	40 µs
Distance between border points	60 µm
Border distance	40 µm
Additional border power	300 W
Additional border exposition time	50 µs
Additional border points distance	60 µm

Filling contour parameters	
Number of contours	3
Filling contour power	200 W
Filling contour exposition time	50 µs
Filling contour points distance	70 µm
Contours distance	60 µm
Contour shifting	50 µm

Supports contour parameters	
Power	275 W
Focus	0 mm
Supports contour points distance	80 µm
Supports contour exposition time	40 µs
Contour shifting	130 µm

6.2. Scanning parameters of the spatter-limitation experiment

Laserform Ti Gr23

Build style	Part LT30
Mid face	
Final contour (C1)	
Laser power	75 W
Mark speed	445 mm/s
Final contour (C2)	
Laser power	145 W
Mark speed	1 000 mm/s
Hatch	
Laser power	145 W
Mark speed	1 000 mm/s
Down face	
Final contour (C1)	
Laser power	50 W
Mark speed	850 mm/s
Final contour (C2)	
Laser power	50 W
Mark speed	850 mm/s
Hatch	
Laser power	50 W
Mark speed	850 mm/s

6.3. Non-dispersive infrared method

The following description was provided by EAG laboratory to describe the measuring method.

Original:

Principe de mesure

Technologie d'infrarouge non-dispersif (NDIR)
Les capteurs infrarouge non-dispersifs sont des capteurs optiques qui sont souvent utilisés dans l'analyse de gaz.

Les composants principaux sont la source infrarouge, la chambre d'absorption, un filtre de longueur d'ondes et un détecteur infrarouge.

Dans le détecteur de gaz GIR-10, l'air aspiré est pompé vers la chambre d'absorption La concentration de gaz SF_6 est déterminée de manière électro-optique au moyen de l'absorption de SF_6 à 947cm^{-1}. Le signal de sortie du détecteur est directement proportionnel à l'absorption de la lumière infrarouge au numéro d'onde en question. Le GIR-10 ne nécessite pas de matières consommables ni d'entretien dans le cycle d'étalonnage.

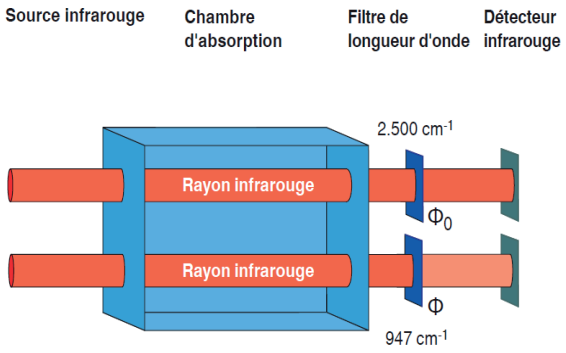

La loi de Lambert–Beer

$$A = -\lg \frac{\Phi}{\Phi 0} = \varepsilon \cdot c \cdot l$$

A : Absorption
Φ : Intensité de la lumière après absorption de gaz SF_6
Φ0 : Intensité de la lumière sans absorption
ε : Coefficient d'extinction
c : Concentration
l : Longueur de la chambre irradiée (chambre d'absorption)

Translated:

Non-dispersive infrared sensors are optical sensors commonly used in gas analysis. The principal components are the infrared source, the wavelength filter, and an infrared detector.

In the gas detector GIR-10, air is pumped through the absorption chamber. SF_6 gas concentration is electro-optically estimated from absortpion of SF_6 at 947 cm^{-1}. The detecor output signal is directly propotional to the absorption of the infrared light. The GIR-10 does not require consumables or maintenance during the calibration cycle.

Résumé:

L'adoption de la fabrication additive (FA), comme moyen de production de pièces en série, s'accélère dans le tissu industriel français. Parmi les méthodes de FA, le procédé fusion laser sur lit de poudre métallique est le plus mature. Malgré la maîtrise croissante du procédé par les industriels, celui-ci reste complexe avec des phénomènes multi-physiques intervenant à des échelles d'espace et de temps très différentes. Dans cette thèse, l'importance du rôle de l'histoire thermique est démontrée au travers de deux études distinctes, et une méthode numérique basée sur les éléments finis avec le logiciel Abaqus pour simuler l'histoire thermique aux diverses échelles a été proposée. La première étude visait à identifier le facteur majeur de contamination des poudres et des pièces avec l'utilisation, et de déterminer à quel moment cette contamination intervenait. Il a été montré que le recyclage et la manipulation de la poudre ne conduisaient pas en eux-mêmes à une augmentation significative du taux d'oxygène. En revanche, la chaleur apportée durant le procédé (par le plateau et le laser) s'accompagnait d'une augmentation sensible de la quantité d'oxygène dans les échantillons solides. Il est supposé que les scories générées durant le procédé ont un rôle majeur dans cette élévation du taux d'oxygène, et des stratégies pour réduire le nombre de scories ont été explorées. La deuxième étude visait à simuler par éléments finis l'endommagement et la rupture d'un certain type de supports, sans avoir à diminuer la taille du maillage, ce qui en pratique aurait été hors de portée. Des éléments 1D ont été proposés pour mailler ces supports, et une étude de cas a été réalisée avec une pièce industrielle. Les étapes de caractérisation mécanique des supports ont montré que les structures fines isolées dans la poudre lors du procédé avaient un comportement mécanique différent des pièces solides. Il a été supposé que l'histoire thermique spécifique à ces structures était responsable de la différence entre ces comportements mécaniques. De plus, certaines limitations liées à la construction d'éprouvettes de type dent de supports, et leur caractérisation expérimentale ont été identifiées. Dans la dernière partie, quir représente le coeur de la thèse, une méthode éléments finis multi-échelles à cinq niveaux a été développée. La méthode permet de simuler l'histoire thermique à l'endroit et à l'instant choisi, et elle est pilotée par les tous paramètres procédé, du plateau complet aux motifs de lasage jusqu'à l'échelle d'un vecteur laser. L'objectif de la méthode est d'utiliser les champs de températures hétérogènes simulés aux échelles plus macro comme conditions initiales et conditions aux limites des échelles plus micro. L'évolution temporelle et spatiale des erreurs liées à l'utilisation de l'hypothèse macro-couche ont été étudiées analytiquement. Cette méthode peut être utilisée pour détecter les régions avec de potentielles porosités, engendrées par des températures extrêmes, et pour optimiser les paramètres du procédé en vue d'homogénéiser les champs de température durant la construction de la pièce. Cette méthode, construite de façon générique, est potentiellement applicable aux autres procédés de FA avec apport de chaleur.

Mots clés:

Fabrication additive métallique ; Simulation thermique ; Éléments finis multi-échelles ; Rupture des supports ; Oxydation ; Poudres métalliques.

Abstract:

The adoption of additive manufacturing (AM), as a means of mass production of parts, is accelerating in the French industry. Among the AM methods, the laser powder bed fusion process is the most mature. Despite the growing mastery of the process by manufacturers, it remains complex with multi-physical phenomena occurring on very different space and time scales. In this thesis, the importance of the role of thermal history is demonstrated through two separate studies; and a numerical method based on finite elements with Abaqus software to simulate thermal history at various scales has been proposed. The first study aimed to identify the major factor of contamination of powders and parts with use, and to determine when this contamination occurred. It has been shown that the recycling and handling of the powder do not lead to a significant increase in the oxygen level. On the other hand, the heat provided during the process (by the build plate and the laser) was accompanied by a significant increase in the quantity of oxygen in the solid samples. It is assumed that spatters generated during the process have a major role in this elevation of the oxygen level, and strategies to reduce the number of spatters have been explored. The second study aimed to simulate by finite elements the damage and the rupture of a certain type of supports, without having to decrease the size of the mesh, which in practice would have been out of reach. 1D elements have been proposed to mesh these supports, and a case study has been carried out with an industrial part. The mechanical characterisation stages of the supports showed that the fine structures isolated in the powder during the process had different mechanical behaviours from the solid parts. It was assumed that the specific thermal history of these structures was responsible for the difference between these mechanical behaviours. In addition, some limitations related to the manufacturing of support tooth specimens, and their experimental characterisation have been identified. In the last part, which represents the heart of the thesis, a five-level multi-scale finite element method has been developed. The method makes it possible to simulate the thermal history at the place and at the chosen moment, and it is controlled by all the process parameters, from the complete build plate scale to the scanning patterns, up to the scale of a laser vector. The objective of the method is to use the heterogeneous temperature fields simulated at more macro scales as initial and boundary conditions at more micro scales. The temporal and spatial evolution of the errors related to the use of the macro-layer hypothesis have been studied analytically. This method can be used to detect regions with potential porosities, generated by extreme temperatures, and to optimise the process parameters in order to homogenise the temperature fields during the construction of the part. This method, constructed in a generic way, is potentially applicable to other AM processes with heat input.

Keywords:

Metal additive manufacturing ; Thermal simulation ; Multiscale finite element method ; Supports breakage ; Oxidation ; Metallic powders.